



PHD

**Numerics and Theory of High-Energy Relativistic Astrophysical Transients
(Alternative Format Thesis)**

Ayache, Eliot

Award date:
2021

Awarding institution:
University of Bath

[Link to publication](#)

Alternative formats

If you require this document in an alternative format, please contact:
openaccess@bath.ac.uk

Copyright of this thesis rests with the author. Access is subject to the above licence, if given. If no licence is specified above, original content in this thesis is licensed under the terms of the Creative Commons Attribution-NonCommercial 4.0 International (CC BY-NC-ND 4.0) Licence (<https://creativecommons.org/licenses/by-nc-nd/4.0/>). Any third-party copyright material present remains the property of its respective owner(s) and is licensed under its existing terms.

Take down policy

If you consider content within Bath's Research Portal to be in breach of UK law, please contact: openaccess@bath.ac.uk with the details. Your claim will be investigated and, where appropriate, the item will be removed from public view as soon as possible.



PHD

Numerics and Theory of High-Energy Relativistic Astrophysical Transients

Ayache, Eliot

Award date:
2021

Awarding institution:
University of Bath

[Link to publication](#)

Alternative formats

If you require this document in an alternative format, please contact:
openaccess@bath.ac.uk

General rights

Copyright and moral rights for the publications made accessible in the public portal are retained by the authors and/or other copyright owners and it is a condition of accessing publications that users recognise and abide by the legal requirements associated with these rights.

- Users may download and print one copy of any publication from the public portal for the purpose of private study or research.
- You may not further distribute the material or use it for any profit-making activity or commercial gain
- You may freely distribute the URL identifying the publication in the public portal ?

Take down policy

If you believe that this document breaches copyright please contact us providing details, and we will remove access to the work immediately and investigate your claim.

Numerics and Theory of High-Energy Relativistic Astrophysical Transients

submitted by

Eliot Ayache

for the degree of Doctor of Philosophy

of the

University of Bath

Department of Physics

April 2021

COPYRIGHT

Attention is drawn to the fact that copyright of this thesis rests with the author. A copy of this thesis has been supplied on condition that anyone who consults it is understood to recognise that its copyright rests with the author and that they must not copy it or use material from it except as permitted by law or with the consent of the author.

This thesis may be made available for consultation
within the University Library and may be
photocopied or lent to other libraries for the purposes
of consultation with effect from (date)

Signed on behalf of the Faculty of Science

Summary

Recent years have seen massive breakthroughs in the observations of gamma-ray bursts and other high-energy astrophysical transients. Dynamical jet simulations have progressed to a point where it is now becoming possible to fully numerically resolve gamma-ray burst (GRB) jet evolution across scales. However, the modeling of radiative emission is currently lagging behind and makes for a bottleneck severely limiting our efforts to fully interpret the physics of GRBs in the multi-messenger era. In this thesis, I present new numerical developments to resolve this discrepancy and focus on providing insights into GRB afterglow physics. Using numerical simulations, I set out to understand the impact of the presence of multiple emission sites on afterglow light curves. I also investigate the trans-relativistic evolution of the jet and poorly understood behaviour of the spectral breaks in the radiation as the jet decelerates. In order to do this, I develop a new method for the local numerical calculation of non-thermal emission in relativistic shocks. This method combines a moving mesh finite-volume code with the a local description of particle acceleration and corresponding Synchrotron process. In order to inform the theoretical models to simulate, I investigate the GRB X-ray afterglow sample variability using Machine-Learning-based data visualisation techniques.

In more details, I first investigate the mechanism responsible for flares in the early X-ray afterglow. Using a one-dimensional Lagrangian relativistic dynamics code, I carry out simulations to show that an erratic shutdown of the central engine in the first few hundred seconds after the burst can produce flares at arbitrarily late times. This erratic shutdown leads to stratification in the ejecta. The radiative flux of the external reverse shock increases when it encounters this stratification. We show that the limitation in the angular extent of the perturbations from transverse causal connection is directly responsible for the observed flare timescale in this scenario. These findings rely on the ability to locally evolve the non-thermal particle populations responsible for emission which is made possible by the increased spatial resolution resulting from the behaviour of the moving mesh.

Summary continues on next page...

Secondly, I apply the same methods to the study of the trans-relativistic phase of jet evolution. For this multi-dimensional problem, I develop a massively parallel code, **GAMMA**, in which hydrodynamics are computed on discrete tracks that follow the fluid motion. This code can accurately capture the jet spreading with very high computational efficiency. Thanks to the local particle evolution calculation, it can accurately simulate the afterglow spectral evolution from early to late times. We show that the spectral cooling break shifts by a factor of ~ 40 compared to previous approaches. The evolution of this break during jet deceleration is also different as it does not shift with time between the relativistic and Newtonian asymptotes when computed from our local algorithm

Finally, I investigate the question whether differences in features between events can be explained by the same model or it is a marker of differences in the phenomenology, and thus separates distinct populations. I explore prospects for acquiring physical inference from Machine Learning models by clustering light curves in an unsupervised manner, and investigate the resulting level of segregation in the *Swift* X-ray afterglow dataset. We find that the data creates over-densities in the encoded latent space suggesting the presence of dominant light curve types. However, the observed gradual transition in between unifies the prevalent classification of GRBs based on their X-ray data into a single continuum, supporting the idea that light curves of different types should be unified under a single model.

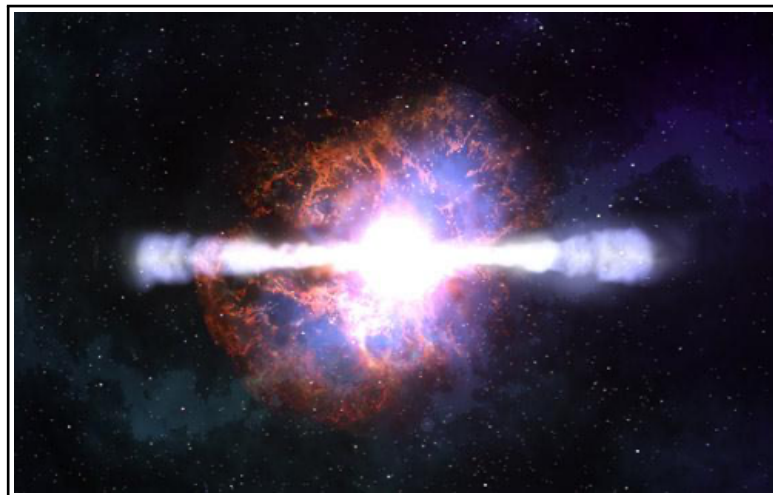


Figure 1: Artist's impression of a gamma-ray burst jetted outflow (credits NASA/Dana Berry/Skyworks Digital¹).

Acknowledgements

I could never have completed this thesis without the support and the help of such a great number of people.

First I would like express my deep gratitude to my Ph.D. supervisor, Hendrik van Eerten, not only for giving me the opportunity to work on such an exciting topic, but also for his intense dedication to the success of this project and my research career. This thesis is owes a lot to his great mentorship.

I also want to state how grateful I am to my current and past mentors and collaborators who trusted me and taught me all they could: Zakaria Meliani and Frédéric Daigne, who introduced me to this topic, and the ones before them. I especially want to acknowledge Tanmoy Laskar for his support as a mentor, colleague and a friend whom I have learnt from more than I can count.

Most importantly, I would like to thank my parents, Isabelle and Nicholas, for providing me with everything I needed to follow my dreams, and for believing in me. I would simply not be here if it were not for their love. To Emily, I am deeply indebted to you for your unconditional support through the whole of my Ph.D.

Finally, thanks to all my friends and colleagues on campus and in Bath, and the WH3.54 crew, which made working in Bath such an enriching experience.

Declaration

This dissertation is the result of work carried out in the Astrophysics Group at the University of Bath, between October 2017 and July 2021. The work in this thesis is my own except where stated otherwise. No part of this dissertation has been submitted for a degree, diploma or other qualification at this or any other university.

Contents

1	Introduction	15
1.1	Motivation and outline	17
1.1.1	General context	17
1.1.2	Numerical modeling challenges	20
1.1.3	Thesis objectives and outline	23
1.2	Gamma-ray Bursts	25
1.2.1	Historical context	25
1.2.2	Observational features	25
1.2.3	Phenomenology and currently accepted paradigm	30
1.3	Modeling GRB afterglows	34
1.3.1	Relativistic blast-wave hydrodynamics	34
1.3.2	Synchrotron emission in shocks	37
2	Numerical Methods: from Dynamics to Radiation	43
2.1	Special Relativistic Hydrodynamics theory	47
2.1.1	Hydrodynamics equations	47
2.1.2	Conservative formulation	48
2.1.3	The 3+1 Valencia formulation of SRHD equations	48
2.1.4	Equation of State	50
2.1.5	Rankine-Hugoniot jump conditions	52
2.1.6	Riemann problem	53
2.2	Numerical Hydrodynamics with finite volumes - The Godunov Scheme	54
2.2.1	First order scheme	55
2.2.2	Riemann solvers	57
2.2.3	Recovering primitive variables	59
2.2.4	Time-integration - the CFL condition	60
2.2.5	HRSC method	60
2.3	Moving mesh	63

2.3.1	Advantages and drawbacks	63
2.3.2	New fluid update	64
2.3.3	Adaptive mesh refinement	67
2.4	Numerical radiative transfer for non-thermal processes	67
2.4.1	Shock detection and particle injection	67
2.4.2	Local synchrotron cooling	70
2.4.3	Flux reconstruction - linear radiative transfer	71
3	Late X-ray Flares from the Interaction of a Reverse Shock with a Stratified Ejecta in GRB Afterglows: Simulations on a Moving Mesh	77
3.1	Introduction	81
3.2	Numerical Methods	83
3.2.1	Relativistic hydrodynamics on a moving mesh	83
3.2.2	Simulation setup	86
3.3	Hydrodynamical evolution	88
3.4	Emission - Flares from a LLRS in a stratified ejecta	92
3.4.1	Radiative prescription - local cooling	92
3.4.2	Synthetic light-curves and spectra	97
3.4.3	Short flares from a localised angular emission region	101
3.4.4	Evolution and influence of the shocked external medium	103
3.4.5	Late flares	106
3.5	Discussion	110
3.5.1	Limitations to dynamical simulations	110
3.5.2	Validity of the flaring setup	111
3.6	Conclusions	113
3.7	Article appendix	114
3.7.1	Code validation	114
3.7.2	Shock detection algorithm	117
3.8	Additional information	119
3.8.1	Implementation specifics	119
3.8.2	Flux integration	119
4	GAMMA: A New Method for Modeling Relativistic Hydrodynamics and Non-thermal Emission on a Moving Mesh	123
4.1	Introduction	127
4.2	Code description	129
4.2.1	Special relativistic hydrodynamics	130
4.2.2	Riemann solver	131

4.2.3	Moving mesh and parallelisation	132
4.2.4	Spatial reconstruction	134
4.2.5	Time-stepping and adaptive mesh refinement	136
4.3	Tests	136
4.3.1	1D relativistic shock tubes	137
4.3.2	Isentropic wave	138
4.3.3	2D Riemann problem	138
4.3.4	1D GRB jet - Blandford Mckee blast wave profile	141
4.3.5	2D GRB jets - Rayleigh-Taylor instabilities in afterglows	141
4.4	Local synchrotron cooling	144
4.4.1	Tracing of accelerated particles	145
4.4.2	Radiative flux calculation	146
4.4.3	Shock detection algorithm	147
4.5	Synthetic GRB afterglow light curves with local cooling	149
4.5.1	Initial setup	149
4.5.2	Grid parameters	149
4.5.3	Results	151
4.6	Discussion	156
4.7	Additional information	160
4.7.1	Implementation specifics	160
4.7.2	Interfacing with radiation code	162
5	Machine Learning Insights into Gamma-ray Burst X-ray Emission	165
5.1	Introduction	169
5.2	Data description	171
5.2.1	<i>Swift</i> -XRT light curves	171
5.2.2	Synthetic light curves	173
5.2.3	Sample pre-processing	175
5.3	Convolutional variational autoencoder	177
5.4	Preliminary Results	181
5.5	Discussion	190
6	Conclusion and Outlook	193
A	GAMMA readme	221
A.1	Requirements	221
A.2	Installation	221
A.3	Usage	222
A.3.1	running a simulation	222

A.3.2	choice of module to use	222
A.3.3	environment variables	222
A.3.4	initial setup	222
A.4	License	223
A.5	Contact	223

Introduction

In this world, there are things you can only do alone, and things you can only do with somebody else. It's important to combine the two in just the right amount.

— HARUKI MURAKAMI, *After Dark*

1.1 Motivation and outline

1.1.1 General context

Gamma-ray bursts (GRBs) are the most powerful explosions ever observed in the Universe. An artist's impression of a GRB event is shown in figure 1. They are the result of the collapse of a rapidly rotating massive star (Woosley, 1993; MacFadyen & Woosley, 1999) or of a binary neutron star (BNS) or neutron star - black hole (NS-BH) merger (Eichler et al., 1989; Mochkovitch et al., 1995), a scenario very recently confirmed (Abbott et al., 2017; Goldstein et al., 2017; Hallinan et al., 2017; Savchenko et al., 2017; Troja et al., 2017) with the joint detection of GW170817 and GRB170817a¹. Both these scenarios are linked to the formation of a compact object, either a BH or a NS. These explosions produce an extremely powerful ultra-relativistic jetted outflow best observed (and consequently most often only detected) when pointing towards the observer. In the first milliseconds to a few seconds, an initial burst of gamma rays (the prompt emission) can be measured, followed after a few hundred seconds by an afterglow (at lower wavelengths). The afterglow, originally peaking at X-ray energies, decreases in luminosity and increases in wavelength with time until it disappears. Depending on the energy of the GRB, the radio emission can be observed from days up to years after the initial burst. Internal dissipation processes are thought to be responsible for the prompt emission (Rees & Meszaros, 1994), though this is still debated, whereas the afterglow is produced by a forward shock - reverse shock (FS-RS) system created by the interaction of the outflow, or blast-wave (BW), with the external medium surrounding the burster (the circumburst medium, CSM) (Rees & Meszaros, 1992; Meszaros & Rees, 1997). At the shock fronts, accelerated electrons, interacting with tangled magnetic fields generated in shock instabilities, are responsible for synchrotron emission. A schematic view of basic GRB phenomenology is given in figure 1.1 and the FS-RS system is represented in figure 1.2, along with typical distance scales for such events. The GRB phenomenon is described in more details in the rest of this chapter (§1.2).

GRB research benefits to various fields of astrophysics, as well as theoretical physics. In observational cosmology, GRBs can be used as cosmic probes, since their very powerful radiation imprints the absorption properties of the intergalactic medium at very early cosmic times (see e.g. Schady, 2017, for a recent review). They also are natural large-scale high-energy physics laboratories where fundamental physics can be put to the

¹Gravitational wave (GW) events and GRBs follow the same name attribution convention. GW events are named GW<YYMMDD> and GRBs are named GRB<YYMMDD>. If two events of the same nature happen on the same day, a letter is added at the end of the name in alphabetical order. GRB170817A hence was the first (of two) GRB detected on August 17th 2017. Since 2009, GRBs automatically have the 'A' suffix added even if they are the only burst on this day.

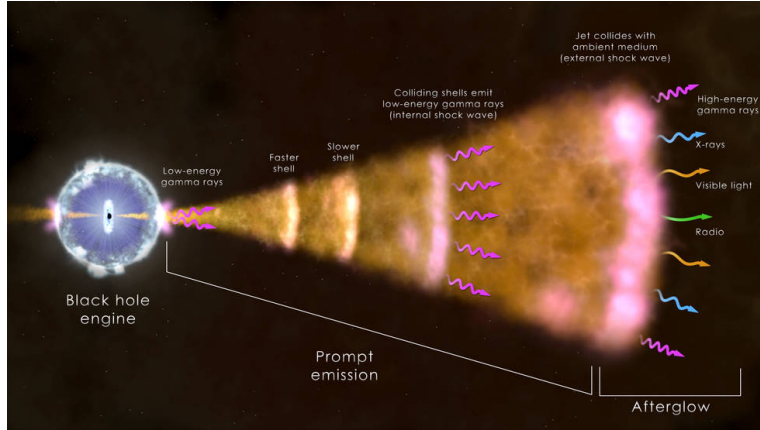


Figure 1.1: Schematic view of the phenomenology of a GRB. The prompt emission is produced by internal shocks appearing when faster regions of the flow catch up with slower regions ahead. The afterglow is the result of the collision with the external medium. All the radiation is produced by non-thermal synchrotron processes, observable at all wavelengths throughout GRB evolution. (credits: NASA GSFC)

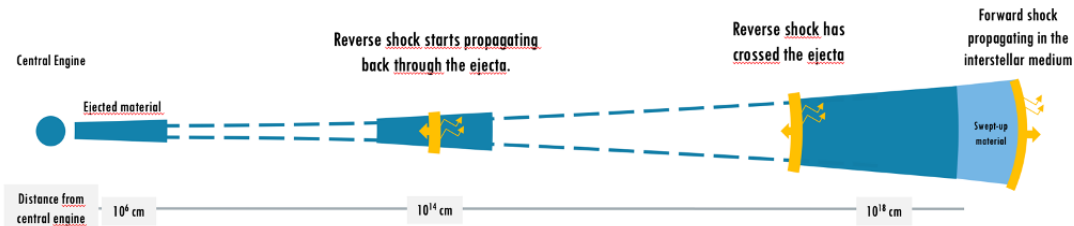


Figure 1.2: Schematic representation of the propagation of a GRB blast wave. With this orientation, the reverse shock moves leftwards in the fluid frame, but rightwards in the lab frame as it is carried outwards by the ejecta. The reverse shock forms as soon as the material is launched, but it takes the shell several orders of magnitude in space before the reverse shock traverses a significant fraction of the ejecta. The spatial dynamics range covered is immense. In addition, the spatial scales that have to be resolved inside the shell are as small as 10^5 times smaller than the radial location.

test.

Today, the basic phenomenology of these events is mainly understood. Analytical and numerical modeling of the dynamical and emission processes of both in the prompt emission (see e.g. Zhang, 2014, for a review) and afterglow phases (see e.g. van Eerten, 2018, for a review) have been carried out. However, many questions still remain unanswered. The exact nature of the progenitor, usually investigated by studying the impact of the CSM structure on the afterglow light curve (observed electro-magnetic flux as a function of time), is still unclear in many cases. The nature of the remnant (BH, magnetar², NS) is also often debated as features such as flares and re-brighthenings appear in the light curve and need to be explained. More importantly, the micro-physics involved in the emission processes associated with GRB afterglows are still poorly understood. Involved quantities such as the amount of energy injected in the population of accelerated electrons at a shock front, or the amplification factor of the magnetic field in the shocked regions are still very loosely constrained today and can vary by up to several orders of magnitude depending on the level of detail of the modeling carried out (Granot & Sari, 2002; van Eerten et al., 2010b; Guidorzi et al., 2014). With new spectral windows opening in the near future (e.g. CTA - Acharya et al. (2013), SKA - Carilli et al. (2003)), understanding of the radiative contribution of the RS in radio, as well as Compton upscattering processes at high energies, becomes urgent. More recently, observations of GW170817/GRB170817A unearthed a large number of questions: what is the nature, origin and influence of the jet structure on the early and late-time dynamics and emission? What spectral contributions can we expect from the different geometrical components present in a BNS merger, and how do they interact with one another?

The use of over-simplistic dynamics and emission models are responsible for our current difficulty in pinning down the workings of all these processes. Improved accuracy and precision of synthetic afterglow light curves, when compared to observations, would significantly reduce the uncertainty around the behavior of the radiative micro-physical quantities. In light of the recent observations of the aftermath of 170817, where we anticipate the contribution from the associated kilonova (KN) afterglow to dominate the signal that is still visible almost 4 years later (Hajela et al., 2019; Troja et al., 2020) and where the contribution from the GRB afterglow has to be accurately subtracted, such improvements actually become vital.

²Magnetars are a class of young neutron stars with extremely powerful magnetic fields (10^{13} to 10^{15} G). They display bursts of X-ray activity with a wide dynamic range in temporal variability. They are candidates as the central engine powering gamma-ray burst jets.

1.1.2 Numerical modeling challenges

The dynamics and radiative transfer involved in the afterglow phenomenon exhibit complex behaviors that are extremely challenging to model, both analytically and numerically. Historically, semi-analytical approaches have been very successful in modeling the ultra-relativistic and non-relativistic limits, assuming radial flows and simple central engine activity (the physical mechanism powering the base of the jets) (Rees & Meszaros, 1992; Frail et al., 2000). Various approaches to simulating the evolution of the jet across time-scales from early to late times have been proposed (Rhoads, 1999a; van Eerten et al., 2010b; Wygoda et al., 2011; van Eerten & MacFadyen, 2012; Granot & Piran, 2012; van Eerten & Macfadyen, 2013; Duffell & Laskar, 2017; Ryan et al., 2020). However, these approaches fail to accurately capture the features of the trans-relativistic evolution, and the associated lateral spreading of the jet as it decelerates. They are also ill-suited to identifying and modeling flux from multiple emission sites, which is crucial to understand light curve features induced by erratic central engine activity.

In turn, numerical simulations offer better chances at improving our understanding the complex multi-scale behavior of the blast wave. There is thus a need for efficient, accurate and precise numerical schemes to produce synthetic light curves for comparison with observations. Current simulation methods however have yet to overcome challenges seriously crippling their computational efficiency and level of accuracy (van Eerten, 2018). Indeed, the dynamical setup of a GRB afterglow mostly consists in following the evolution of a conical shell of ejected material of radial width $\Delta R \sim R/\Gamma^2$ where R is the distance of the shell from the burster, propagating with a Lorentz factor³ Γ . Since the values of Γ are contained between 100 and 1000, this already highlights the need for a grid of effective resolution of at least $10^{-4}R_0$, where R_0 is the radius at which the blast-wave is launched. Moreover, this shell has to be followed for distances spanning up to 9 orders of magnitude, with the best possible resolution in order to resolve shocks, where particle acceleration and emission takes place. This brings the resolution to at least 13 orders of magnitude lower than the total grid size, not accounting for the additional constraints associated with a local calculation of radiation which we described later in this chapter. Finally, propagation happens inside an non-moving external medium of mass density as much as 14 orders of magnitude lower than that of the ejecta, responsible for the need of efficient highly conservative schemes, due to the high discrepancy in velocity and density between neighboring parts of the flow.

³The Lorentz factor Γ measures how relativistic the motion of an object of velocity v is. It is given by $\Gamma = 1/\sqrt{1 - v^2/c^2}$, with c the speed of light in a vacuum. For non-relativistic motion, Γ approaches 1.

This extreme resolution leads to enormous memory requirements. Additionally, such refinement of the grid contracts time-steps in the simulation to such an extent that accurate simulations can simply not be run in reasonable time using common numerical hydrodynamics techniques.

Today, the most widely adopted approach to modeling the dynamical evolution is to use finite-volume methods with Adaptive Mesh Refinement (AMR) techniques on a fixed grid, such as in the codes RAMSES (Teyssier, 2001), AMRVAC (Nool & Keppens, 2002; Meliani et al., 2007), RAM (Zhang & MacFadyen, 2006), and more recently PLUTO (Mignone et al., 2012), all benefiting from relativistic hydrodynamics extensions. These techniques have been applied to the modeling of GRB afterglows with relative success (Kumar & Granot, 2003; Cannizzo et al., 2004; Zhang & MacFadyen, 2009; van Eerten et al., 2010a; Meliani & Keppens, 2010; De Colle et al., 2011; Wygoda et al., 2011; van Eerten et al., 2012) but still display some difficulties in resolving the extreme sharpness of the shocks satisfyingly, even with very long computation times and many levels of refinement, as shown in figure 1.3. This figure shows the maximum fluid Lorentz factor Γ in the blast wave as a function of time, for various levels of spatial refinement, in simulations from De Colle et al. (2012). The numerical method only converges on the analytical solution for very low Γ values. Keeping in line with these methods, significant improvement was introduced by switching the computation to a boosted frame moving along with the fluid (van Eerten & Macfadyen, 2013). This approach relaxed the constraints arising from relativistic length contraction and allowed for lower resolution and increased time-steps. The boosted frame approach (fig. 1.4) improves precision but still needs half the spreading time (where sudden deceleration occurs) to converge properly. Getting an accurate value for this maximum fluid Lorentz factor is crucial to accurately compute synchrotron emission, and vital to simulate the correct lateral expansion of the jet when it decelerates.

From this boosted frame setup, it is a logical step to full moving-mesh approaches. As gains from arbitrary Lagrangian-Eulerian (ALE) methods had already been demonstrated in the context of Newtonian astrophysical flows with e.g. AREPO (Springel, 2010; Weinberger et al., 2020), this approach was implemented for relativistic hydrodynamics by Duffell & MacFadyen (2011) in their ALE Voronoi-tesselation-based code TESS. These methods provide a range of benefits when the mesh is set up to follow the motion of the flow. Firstly, they directly enhance shock resolution as the mesh naturally contracts with increasing fluid density. Secondly, the time-step is significantly increased when the flow is dominated by motion in one direction. In this particular case, additional improvement in terms of computational efficiency can be found by limiting the expensive re-gridding operations normally associated with moving meshes.

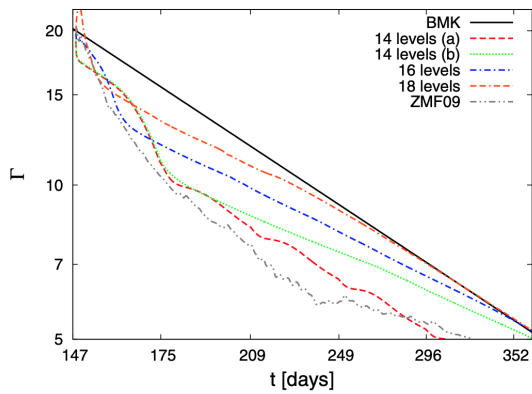


Figure 1.3: (from De Colle et al. (2012)) Maximum fluid Lorentz factor Γ in the blast wave as a function of time for simulations with various levels of AMR for the code MezcalsRHD. BMK stands for "Blandford-McKee" (also written BM), the analytical solution for a point-like explosion (Blandford & McKee, 1976) which corresponds to the simulations setup. ZMF09 is the same setup from Zhang & MacFadyen (2009) using their code RAM (Zhang & MacFadyen, 2006).

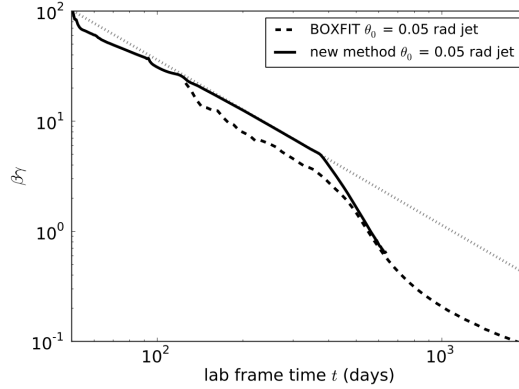


Figure 1.4: (from van Eerten & Macfadyen (2013)) Maximum fluid four-velocity $\beta\gamma$ (β is the fluid velocity in units of c the speed of light, γ is the fluid Lorentz factor) as a function of time. The dotted line is the BM solution. The simulations are carried out using RAM (Zhang & MacFadyen, 2006). The solid line is the boosted frame solution. The dashed line is the fixed frame solution. The BM solution is not valid after ~ 300 s and the simulations converge together.

By only allowing the mesh to move in one direction (say the main direction of motion), mesh entanglement is suppressed and AMR operations can be run independently along tracks moving in this direction. This is the approach implemented in JET (Duffell & MacFadyen, 2013) and DISCO (Duffell, 2016) for radial and azimuthal flows, respectively.

These recent improvements on the treatment of the dynamics mean that the current bottleneck lies in the radiative prescriptions used so far. This bottleneck severely limits our ability to interpret broadband emission from GRB afterglows using numerical simulations. As previously mentioned, the afterglow is produced by synchrotron emission directly downstream of the shock fronts formed by the blast wave as it collides with the CSM. The modeling done by the community of the evolution of the micro-physical fluid state (parameters describing the local characteristics of the emission) downstream of the shocks relies on approximations (usually the "global cooling" approximation) that significantly impact the spectral flux density computed by current simulations by up to a decade (van Eerten et al., 2010a; Guidorzi et al., 2014). Ideally, one would want to locally numerically compute the evolution of the electron population downstream of shocks to accurately account for cooling from adiabatic expansion and synchrotron losses. This second approach requires extreme resolution as the particle population (as well as the fluid quantities) evolve on very short time-scales downstream of the shock.

For high frequencies, the region contributing to the flux is so small that reconstructing the total flux from local emissivity requires us to capture this evolution precisely (van Eerten & Wijers, 2009). Local and global cooling are described in more detail in §1.3.2.

1.1.3 Thesis objectives and outline

We set out, in this Ph.D. project, to tackle two major aspects of GRB afterglow research. The first one concerns the consequences of the presence of **multiple emission sites**, with the objective of explaining some of the short time-scale variability observed in X-ray afterglow light curves. This will help us to better understand the origin of flares and re-brightenings, and put constraints on energy injection processes and central engine activity. The second aspect is the detailed study of the evolution of afterglow radiation *as a whole*, in order to **unearth the underlying complex processes responsible for its spectral properties**, and currently hindering our ability to properly analyse observations. Like other GRB afterglows, recent observations of GRB170817A suggest that the radiative processes are more complex than what state-of-the-art models currently account for, with e.g. an influence from the evolution of the shock strength on the particle injection index (Troja et al., 2020). The afterglow remaining on a single spectral regime from radio to X-ray is also surprising and needs to be investigated. This thesis takes the first steps towards explaining the deviations of GRB afterglows from the current models and investigates these processes. It also paves the way towards future observations at very high energies (MAGIC Barrio et al. (1998), CTA Acharya et al. (2013)) as it explores local descriptions of radiative processes essential to the study of inverse Compton processes in GRBs.

The questions reported above all rely on **local modeling of the synchrotron process**. In this thesis I present the combination of the recent moving-mesh developments in relativistic hydrodynamics with the local calculation of the emissivity from high-energy relativistic outflows. The moving mesh naturally provides the increase in resolution needed by the local cooling prescription and allows fast, accurate and precise calculation of broadband time-dependent emission. There are different ways of implementing such calculation. One could focus on developing an extension for a pre-existing ALE code like TESS or JET, or even update a purely Eulerian code such as PLUTO, RAM or AMRVAC to an ALE description. However, considering the versatility in terms of geometries and applications we want from such code, and the full control we require over the interfacing between the dynamical radiative modules, the numerical code presented in this thesis, **GAMMA**, is developed from scratch. This approach allows complete freedom in the algorithmic choices and total independence from other software. It also provides the community with a full independent code that can be used in

a wide range of contexts involving radiative emission from relativistic flows, and allows cross-checking of results from other similar dynamics code. In this thesis, **GAMMA** is applied to the modeling of GRB afterglows.

As such, **GAMMA** allows one to experiment with various GRB afterglow theoretical models. However, these models need to be informed by observational data. As more and more data is collected, physical inference can now be obtained by making use of the recent advances in machine learning and data visualisation. State-of-the-art dimensionality reduction techniques allow one to finally assess the relevance of unified theories (or separation in classes) of a given phenomenon, in a data-driven approach that does not introduce model biases. They also extract the most discriminatory characters of such phenomenon in order to explain the observed variability. While the work presented in this thesis mostly focuses on developing an accurate and efficient tool for the numerical modeling of the dynamics and emission from high-energy relativistic astrophysical transients, we also set out to investigate the intrinsic structure of the current GRB X-ray afterglow sample. This complementary angle we adopt for the study of the mechanisms underpinning the behavior of these events completes our comprehensive approach to the modeling of the GRB afterglow phenomenon.

In the rest of this first chapter, I present an overview of current state of GRB afterglow research, focusing on the aspects that will be of interest in the rest of the thesis. In chapter 2, I introduce the theoretical framework of numerical relativistic hydrodynamics on a moving mesh, local emissivity calculation for synchrotron radiation, as well as time-dependent flux reconstruction for synthetic light curve production. I also present the implementation of these aspects in the code **GAMMA** I developed as part of this project. Chapter 3 puts forward a first application of this code to the study of the flaring behavior in the early X-ray afterglow for a scenario in which complex dynamics and multiple emission sites are responsible for the features observed in the light curve. In the published journal article reported there, we confirm the validity of the scenario involving the interaction of the reverse shock with a stratified ejecta and show that it can produce flares at arbitrary late times with the expected duration. Chapter 4 is devoted to the work submitted for publication and in review at this time (July 2021), in which **GAMMA** is used for 2D simulations of trans-relativistic blast-waves and the calculation of associated emission. I report on the results from this work in which we observe a significant difference in the behavior of one of the characteristic frequencies of the time-dependent spectrum between our approach and previous works. I choose to present chapters 3 and 4 unchanged from their journal form, since it allows the experienced reader to tackle them independently, and include an introductory and concluding section to explain in more detail how they fit in the general argument

of this thesis. In chapter 5, I present the draft manuscript of an ongoing machine-learning project in which we use advanced unsupervised data visualisation techniques in order to gain physical insight into the cause of the wide range of GRB afterglow light curve morphologies, and question whether the physics responsible for differing temporal behaviours signal a difference in phenomenology or a simple gradual change of regime.

1.2 Gamma-ray Bursts

1.2.1 Historical context

The story of Gamma-Ray Bursts (GRB) begins during the cold war, in the late 1960's. In the context of the race for nuclear weapons, the *Nuclear Test Ban Treaty* was signed in 1963. Consequently, the United States military developed a nuclear test monitoring program: the fleet of *Vela* spacecrafts, specifically designed to detect radiation produced by atmospheric nuclear tests. In 1967 two of the few satellites in operation at the time detected a flash of gamma-rays of cosmic origin (Klebesadel et al., 1973). Following this event, the *Vela* spacecrafts' detector sensitivity was improved and led to the detection of 16 gamma-ray bursts of cosmic origin in 3 years, between 1969 and 1972, opening a whole new field of research in high-energy astrophysics.

1.2.2 Observational features

Over the following decades, as detector sensitivity was improved, and as more dedicated missions were launched, the number of detections increased significantly. Follow-up campaigns were carried out in order to cover the whole time-scale and spectral features of these events.

Distance scale

One of the first questions about these events is to determine the distance at which they occur. Measuring this distance allows one to estimate the intrinsic power of the source. The debate between the galactic and extra-galactic models was settled in the 1990's. The the distribution of these events was first shown to be isotropic (Hartmann & Blumenthal 1989; Hartmann et al. 1991; Meegan et al. 1992; Briggs et al. 1996; Tegmark et al. 1996; more recently Andrade et al. 2019). A recent all-sky distribution of GRBs from the Fermi Gamma-ray Burst Monitor Burst catalogue (Gruber et al., 2014; von Kienlin et al., 2014; Bhat et al., 2016) is shown in figure 1.5. The gradual growth of the sample slowly started confirming the extra-galactic origin until the first observation of

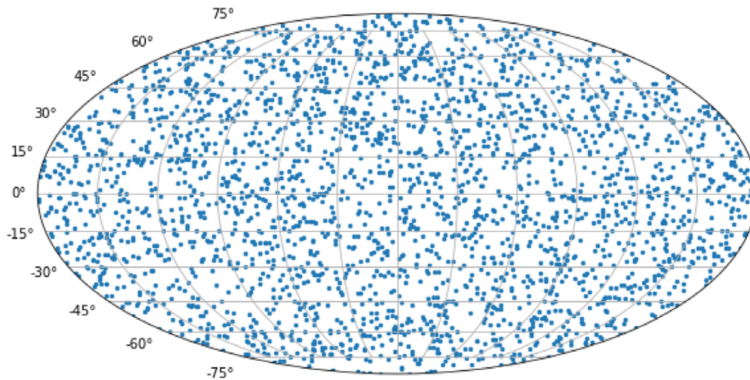


Figure 1.5: Mollweide projection of the GRB sky positions of the FER-MIGBRST catalogue (figure from [Andrade et al., 2019](#)). Their recent analysis suggests there is no significant deviation from an isotropic distribution.

afterglows enabling redshift measurements ([Costa et al., 1997](#); [van Paradijs et al., 1997](#)), confirming the vast distance at which GRBs are produced. Today, the increased sample of redshift measurements from GRB afterglows has a median of $z \sim 2$ ([Jakobsson et al., 2006](#); [Fynbo et al., 2009](#); [Perley et al., 2016](#)). The redshift distribution of various afterglow samples is shown in figure 1.6. Nevertheless, even at such large distances, the flux observed still implied an unprecedented intrinsic isotropic energy for these events at 10^{51} erg to 10^{53} erg, which we now know is explained by the collimated character of the cataclysmic explosion.

Long/Short GRB

Another characteristic statistical feature of the GRB population is the bimodal distribution of the duration of the events, with a clear separation at ~ 2 s. This led to divide the population of GRBs into two types: the *short* (shorter than 2s) and *long* (longer than 2s) GRBs ([Kouveliotou et al., 1993](#)). While well identified on the BATSE sample, The position and significance of this divide varies with the observing band, and is less visible for narrower/softer energy bandpass instruments such as the *Neil Gehrels Swift* space telescope. However, the validity of the bimodal distribution is further supported by larger BATSE samples and identification with other instruments such, as Fermi GBM (e.g. [Bissaldi et al., 2011](#); [Zhang et al., 2012](#); [Qin et al., 2013](#)). Moreover, recent work has been able to show an unambiguous separation between the two populations by using the complete prompt emission information ([Jespersen et al., 2020](#)). We will see later that this can be explained by a different phenomenology for these two types.

Measuring the duration of an event is actually not as straightforward as one might

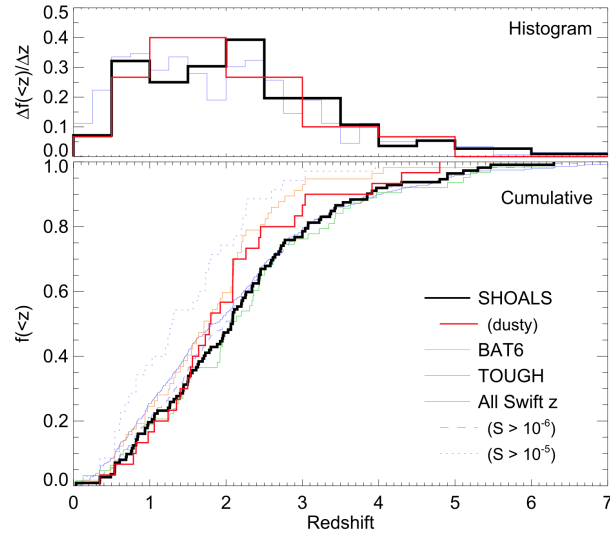


Figure 1.6: Redshift distribution for various afterglow surveys (figure from [Perley et al., 2016](#)).

expect. Indeed there is a great complexity in the light curve with multiple showers of photons arriving at various times. The time of duration, T_{90} , is thus defined as the time elapsed between when 5% and 95% of the total energy above the background level was received. Even though the temporal evolution is really complex, the spectral features are much simpler, showing a decreasing power-law, characteristic of non-thermal emission. The physical origin of this non-thermal emission is however still debated. While some bursts can be fit using a synchrotron shock model, a majority display a low-energy power-law photon number spectral index that exceeds the "line of death" ([Preece et al., 1998](#)) over which the synchrotron model can be ruled out. Additionally, new components have been identified: a most-likely thermal component at low energies, and a separate component at very high energies (most likely the result of a scattering process) showing a different temporal evolution (for a review see e.g. [Pe'er, 2015](#)). While having been able to separate these contributions allows for easier interpretation of each component, the models now have to explain the variability observed across the GRB population.

GRB Afterglow

In 1997, the picture about GRBs changed completely with the first discovery of an optical counterpart for GRB970228 ([van Paradijs et al., 1997](#)). These counterparts, called afterglows, had been predicted by a class of models (the *fireball* model) ([Rees & Meszaros, 1992](#); [Meszaros & Rees, 1997](#)). The discovery was made possible by the launch the preceding year of the *Beppo-SAX* gamma-ray and X-ray space observatory

(Boella et al., 1997). This instrument both benefited from the improved localization information from X-ray measurements, and the ability to broadcast this information to the Earth in only a couple of hours for rapid follow-up. The afterglow flux decreased following a power-law to disappear within a few weeks (Wijers et al., 1997), revealing the presence of a host galaxy. Later detections of *afterglows*, and measurements of their redshifts confirmed the cosmological origin of these objects (Djorgovski et al., 1997; Metzger et al., 1997). Observations of these afterglows, as well as the study of the host galaxies eventually proved to be a gold mine of information used to constrain our understanding of GRBs.

The high variability of the early X-ray afterglow

The launch of the NASA-led *Neil Gehrels (Swift)* space observatory (Gehrels et al., 2004) in 2004, dedicated to GRB detection and early X-ray/optical afterglow observations, disrupted our earlier understanding of the afterglow phenomenon by revealing the great variability present in the light curve at early times. Indeed, previous observations at later stages of the afterglow appeared to suggest that the radiated power decreased with time as a power-law with parameter $1 < \alpha < 1.5$. After the launch of *Swift*, the picture changed radically with the discovery of new regimes of the afterglow, with a canonical behaviour showing a steep decay ($3 < \alpha_1 < 5$) before ~ 300 s, a plateau ($0.2 < \alpha_2 < 0.8$) until 10^3 s to 10^4 s, eventually followed by the "normal" decay ($1 < \alpha_3 < 1.5$) observed before *Swift* (Nousek et al., 2006). All the questions that arose from the observations of *Swift* are summarized in figure 1.7. These questions include e.g. finding the underlying physical explanation for these new regimes and explaining the statistical occurrence of some features such as the jet break (see §1.2.3).

For 17 years now, *Swift* has been detecting GRBs and measuring the properties and spectra of their early X-ray afterglow at a rate of around 90 detections a year (Evans et al., 2009), revealing even more features of the light curves, such as flaring and re-brightening behaviors. These flares are detected in about a third of GRBs (Burrows et al., 2005b; Falcone et al., 2007; Chincarini et al., 2010; Margutti et al., 2011) and display a characteristic shape with a sharp jump in luminosity followed by a smoother decay, eventually going back to the original luminosity level (Chincarini et al., 2007). They can happen at any time during the afterglow, growing longer with time following $\Delta t_{\text{flare}}/t_{\text{flare}} = 0.1 - 0.3$ (e.g. Burrows et al., 2005b). We will see in chapter 3 that being able to explain the features of these flares in detail can help to strongly constrain GRB phenomenology, and we will show that flares can be the result of an erratic shutdown of the central engine.

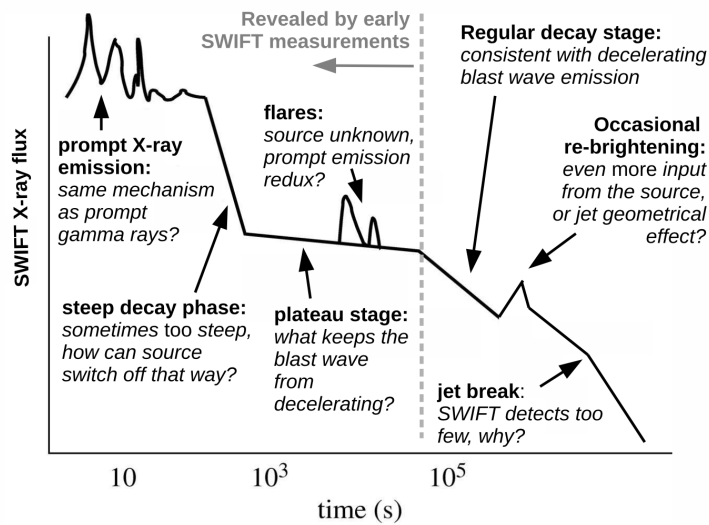


Figure 1.7: The pending questions about the high variability of early X-ray afterglow light curves. (credits: [van Eerten \(2018\)](#))

Host galaxy type and progenitor association

The study of GRB host galaxies can provide a lot of information about the GRB itself. A striking characteristic is the association of *long GRBs* with *young star-forming galaxies* ([Fruchter et al., 2006](#)) (for a recent review see e.g. [Schady, 2017](#)). Moreover, these GRBs are generally located inside or close to the star-forming regions of these galaxies, gathered towards the center. This supports the idea of the association of long GRBs with type Ic supernovae, corresponding to *the core-collapse of a massive star*. This was later confirmed by observations ([Galama et al., 1998](#); [Hjorth et al., 2003](#)).

On the other hand, short GRBs appear to occur in any galaxy type, with no predominance in any particular region of their galaxy, favoring a mechanism happening on much longer time-scales (e.g. [Berger, 2013](#), for a review). Moreover there is no correlation between the rate of short GRBs and the star formation rate in their vicinity. Thus, *short GRBs* could be explained by the *merger of a neutron star (NS) with another compact object (NS or BH)* ([Paczynski, 1986](#); [Eichler et al., 1989](#)). Indeed, the long time-scale of the mechanism could be well explained by the length of the inspiraling phase before the merger. This scenario was amazingly confirmed in 2017 by the simultaneous detection of a gravitational wave event GW170817 originating from the merger of two NS by the *LIGO-Virgo* collaboration ([Abbott et al., 2017a](#)) and a short gamma-ray burst GRB170817a by the *Fermi* and *INTEGRAL* satellites ([Goldstein et al., 2017](#); [Savchenko et al., 2017](#); [Abbott et al., 2017](#)). However, GRB170817a was abnormally

dim compared to the population of short GRBs at cosmological distances (d'Avanzo et al., 2014), and it was unclear whether the two events were related. Eventually, the discovery of an optical counterpart, AT2017gfo, in the direction of the GRB and its identification as a kilonova resulting from a binary neutron star merger, followed by the late apparition of the GRB afterglow (because of an off-axis structured jet), left no doubt as to the connection between the two events (e.g. Troja et al., 2017; Hallinan et al., 2017).

1.2.3 Phenomenology and currently accepted paradigm

Today, the main evolutionary scenario corresponding to GRBs is generally agreed upon and will be described in the following section. Simple considerations on the orders of magnitude involved can already strongly constrain the phenomenology of the event.

General constraints: a massive explosion

By first considering the variability time-scale of the prompt emission as small as a few ms, associated with emitted isotropic energies of up to 10^{53} erg, corresponding to a large fraction of stellar rest-mass energy, it is clear that the source has to involve a compact object of stellar mass. Long GRBs are thus associated with the core-collapse of a massive star in what is called the *collapsar* model (Woosley, 1993; MacFadyen & Woosley, 1999). This is also able to explain the correlation with star-forming regions, and thus massive stars. Indeed, the collapse of the core of a massive star at the end of its life leads to the birth of a black hole. Some of the surrounding matter can create an accretion disc, swallowed at a very high rate. This type of system is already known to be able to give rise to radiation at very high energies, such as in jets produced by Active Galactic Nuclei (AGN) (see e.g. Blandford et al., 2019, for a review of AGN jets). The very short duration of short GRBs entails the need to think of another way of creating a compact object with very fast accretion of matter. This can be achieved with the merger of two neutron stars (Paczynski, 1986), for which the time-scale of the burst is going to be smaller.

Another strong constraint is the necessity of a relativistic ejection responsible for the gamma-ray emission, arising from *the compactness problem* (Piran, 1996). This problem comes from the ability of high energy photons to pair-annihilate, creating an electron-positron pair following the reaction $\gamma\gamma \rightarrow e^+e^-$. Moreover, computing the cross-section of this reaction shows that MeV photons can annihilate together for angles of interactions that are not too small (which is not unrealistic in the case of isotropic emission). Moreover, the intrinsic variability (and deduced very small size) of the

source associated with the very high energy of the emission suggests that the density of photons in the source is extremely high. All of these aspects should cause MeV photons to annihilate thus leading to a discrepancy between the expected and the observed spectrum. The solution lies in a relativistic ejection at very high Lorentz factor Γ . This causes the size of the source deduced from variability to be increased by a factor Γ^2 , decreasing the photon density estimate by a factor Γ^4 . Additionally, blue-shifting of the emitted photons leads to an over-estimate of photon energy by a factor Γ , leading to a change in the fraction of electrons participating in pair production by a factor $\Gamma^{-2\alpha}$, where α is the photon energy distribution power-law index. Overall, the optical depth decreases by a factor $\Gamma^{4+2\alpha}$. For $\alpha = 2$, both effects eventually allow for MeV gamma-ray production for Lorentz factors $\Gamma \gtrsim 100$.

Evidence for a jetted outflow

We will see later that this explosion can be modeled in the early stages assuming spherical symmetry. However, some observational features hint at the fact the the observed outflows are actually collimated into jets. We will see in chapter 4 that this collimation hinders our ability to interpret and accurately model the electro-magnetic flux at late times. Since GRBs are located at vast distances, it is impossible to resolve them observationally. As a result, any indication about their geometry has to come from indirect measurements. Luckily the observation of a *jet break* (see fig. 1.7 for schematic representation) in the afterglow emission of these objects is a clear signature of a collimated ejection (Rhoads, 1999b; Sari et al., 1999; Panaitescu & Kumar, 2003).

Indeed, since the outflow propagates at relativistic speeds with very high Lorentz factor Γ , any radiation moving towards the observer will be beamed into a solid angle of opening $\sim \frac{1}{\Gamma}$. As a result, it is impossible for an observer to distinguish a spherical from a jetted outflow, as they can only see fraction $\frac{1}{\Gamma^2}$ of the surface of the ejected shell. However, as the shell decelerates, the opening angle increases. For a jetted outflow of opening angle θ_0 , the received flux displays a break when $\frac{1}{\Gamma} > \theta_0$, as the deceleration (and thus the Doppler beaming) is not counteracted by the increase of observable emitting surface area anymore.

On top of the the Doppler effect, the jet starts to spread sideways at around the same time as the causal contact across the jet is reinstated (Sari et al., 1999). This causes Γ to decrease even faster, sharpening the observed jet break. Sari et al. calculate that the jet break is expected to happen at:

$$t_{\text{jet}} = 6.2(E_{52}/n_1)^{1/3}(\theta_0/0.1)^{8/3}\text{hrs}, \quad (1.1)$$

where E_{52} is the burst equivalent isotropic energy in units of 10^{52} erg, n_1 is the surrounding homogeneous interstellar medium (ISM) number density in cm^{-3} and θ_0 is the jet opening angle in radians. It is thus possible to derive the jet opening angle from the measurement of the jet break time. A standard value is usually $\theta_0 \sim 0.1\text{rad}$.

As predicted, these jet breaks have now been observed in a fraction of GRBs, at times ranging from a few hours to a few days (depending on the energy of the burst), proving the jetted character of the ejected outflows (e.g. [Evans et al., 2009](#); [Racusin et al., 2009](#); [Kann et al., 2010](#)). As a result the required intrinsic energy of GRBs can be significantly decreased to more reasonable values clustered around 10^{51} erg ([Frail et al., 2001](#); [Bloom et al., 2003](#)).

Step by step scenario

Initial burst and the fireball model: As mentioned earlier, a GRB involves the creation of a compact object (BH or NS). During the system's collapse, some of the matter forms a very hot accretion disk around the newly created compact object. This matter is accreted at a super-Eddington⁴ rate and can give rise to relativistic outflows. This system is thus referred to as the *central engine* (for a review see e.g. [Piran, 2005](#)).

Even though these outflows are collimated into jets (with opening angles as narrow as $\theta_0 \sim 0.1\text{rad}$) (see e.g. [Ghirlanda et al., 2013](#)), assuming spherical symmetry in the early stages of their evolution is a very good approximation, as there is no causality across the jet due to the very high velocities. Their expansion can thus be modeled with a very simple approach where the initial system is a sphere of radius R_0 of the same scale as the central engine, containing a mass M_0 and an initial amount of thermal energy E_0 . This is the *fireball model* first proposed and described by [Paczynski \(1986\)](#) for a fireball of pure energy. [Goodman \(1986\)](#) argues that the fireball has to originally be optically thick in order to model GRB behavior. Eventually, [Shemi & Piran \(1990\)](#) describe the first consistent acceleration model for a GRB by considering a fireball of completely ionized hydrogen plasma.

If the fireball remains optically thick for long enough, all the thermal energy will eventually be converted into kinetic energy. The flow then accelerates to a final bulk Lorentz

⁴The Eddington limit is the maximum power that can be radiated by a source with a static photosphere, and is set to $L_{\text{Edd}} \simeq 3.4 \times 10^4 \left(\frac{M}{M_{\odot}}\right) L_{\odot}$, with M the mass of the object, M_{\odot} and L_{\odot} the mass and luminosity of the Sun. A source is accreting at super-Eddington rate if the accretion luminosity is above the Eddington limit.

factor given by:

$$\Gamma_0 \simeq \frac{E_0}{M_0 c^2}. \quad (1.2)$$

In reality, the acceleration processes are much more complex and involve the understanding of the behavior of the magnetic fields around the central engine (e.g. Piran, 2005). However, the relation derived in equation 1.2 is very helpful in understanding the later dynamical evolution of the ejecta.

Prompt emission: Once the flow has been accelerated and eventually becomes optically thin again, radiation can eventually escape and produce the actual GRB observed. Rees & Meszaros (1994) first proposed the internal shocks model for the production of gamma-rays. Considering that the central engine can display variability on very small time-scales, the power injected in the ejecta is certainly not constant, leading to a variable profile of velocity. Faster regions of the flow will eventually catch up with slower regions, eventually leading to the formation of shocks (see §2.1.5). In the case of highly magnetized flows, these shocks are good candidates for the production of radiation (see §1.3.2). Some of the kinetic energy is converted into thermal and magnetic energy, which is characterized by an accelerated non-thermal population of electrons injected in the flow, and an amplification of the magnetic field. In turn, these electrons are able to produce *synchrotron emission* and *inverse-Compton scattering*. This Doppler boosted emission corresponds to the gamma-ray prompt emission produced in the observer's rest-frame.

Afterglow: Eventually, the outflow is going to be influenced by the external medium it propagates into. Typically, in what is called the thin shell case (initially small fireball with large baryon loading, see §1.3.1), this happens when the amount of matter swept up by the blast wave has an effective mass energy including internal energy $\Gamma_0 M_{\text{sw}} c^2$ in the frame comoving with the ejecta comparable to the total energy of the blast wave E_0 , which eventually gives $M_{\text{sw}} \sim M_0/\Gamma_0$. In the thick shell case (initially large fireball and low baryon loading) however, the ejecta has only marginally slowed down at this stage and deceleration of the ejecta happens later (see §1.3.1). At this point, a forward shock / reverse shock system forms at the head of the ejecta (Rees & Meszaros, 1992). The forward shock (FS) propagates in the external medium, and its dynamics are described analytically by Blandford & McKee (1976) in the relativistic case, until it slows down and adopts the self-similar solution independently described by Sedov&Taylor (Sedov, 1946). In the commonly accepted paradigm, the emission processes usually observed in shocks occur in the FS and are responsible for the emission of the afterglow (Meszaros

& Rees, 1993). The reverse shock (RS) propagates back in the ejecta. In the case of weakly magnetised ejecta, its contribution to the total radiation is visible from optical to radio at early times (Kobayashi, 2000; Zhang & Kobayashi, 2005) and has been shown to be able to dominate (Uhm & Beloborodov, 2007) in X-ray when the FS is radiatively inefficient. We will analyse the competition between FS and RS when studying the flaring mechanism in chapter 3.

1.3 Modeling GRB afterglows

1.3.1 Relativistic blast-wave hydrodynamics

One last aspect of the theory of relativistic hydrodynamics to address is the analytical dynamical evolution of a relativistic blast-wave (or fireball). This will indeed be of crucial importance in order to interpret the numerical results we get from our simulations. We will report here the most important aspects of such evolution, referring the reader to the excellent review by Kobayashi et al. (1999) for more information.

As explained in §1.2.3, Shemi & Piran (1990) developed a model for fireballs with baryonic component, showing that the acceleration of such fireballs under their own pressure eventually leads to a relativistic, freely propagating, expanding, baryonic shell. The evolution involves an acceleration phase where thermal energy is converted into kinetic energy carried by the baryons, followed by a coasting phase when this conversion has been completed (Mészáros et al., 1993). Eventually, the blast-wave will feel the influence of the external medium (Rees & Meszaros, 1992), leading to the formation of a FS/RS system separated by a contact discontinuity (CD). This CD stands between the regions of shocked ejecta and shocked ISM. Once the shell has lost most of its energy to the shocked ISM, the FS eventually converges towards the self-similar relativistic Blandford&McKee (BM) solution (Blandford & McKee, 1976). When that shock has decelerated enough, the solution moves towards the non-relativistic self-similar Sedov&Taylor solution (Sedov, 1946).

In the following paragraphs of this section, we describe the adiabatic evolution of a baryonic shell of initial energy E_0 , mass M_0 and radius R_0 . For the sake of simplicity, we consider an homogeneous fireball. Inhomogeneous fireballs (such as the setups presented in chapter 3) will lead to the formation of internal shocks. However, these shocks are not capable of converting a significant part of the total kinetic energy of the blast-wave (Kobayashi et al., 1997; Daigne & Mochkovitch, 1998), and can thus be neglected as a first approach. The quantities r , ρ , p and Γ are naturally the radius, rest-mass density, pressure (in the comoving frame) and Lorentz factor, respectively,

of a fluid element belonging to this shell. We should recall here that the final Lorentz factor after acceleration Γ_0 is given by equation 1.2. We will refer to the position of the narrow shell with R . Finally, we still have $c = 1$ in this section, as in the rest of the chapter.

Free acceleration and coasting

During the *acceleration phase*, the fluid variables in the shell scale as follows (Kobayashi et al., 1999):

$$\Gamma \propto r, \quad \rho \propto r^{-3}, \quad p \propto r^{-4}. \quad (1.3)$$

When the shell reaches the coasting radius $R_L \equiv \Gamma_0 R_0$, it stops accelerating and transitions to the *coasting phase* for which:

$$\Gamma = \text{constant}, \quad \rho \propto r^{-2}, \quad p \propto r^{-8/3}. \quad (1.4)$$

In this phase, the shell behaves like a *frozen pulse* of energy of width $\Delta = R_0$ (in the central engine rest-frame) with a constant radial profile, propagating at almost the speed of light.

Spreading and Influence of the ISM

As all fluid elements in the shell move at slightly different velocities, the *frozen pulse approximation* that enabled the derivation of the scalings for the acceleration and the coasting phase starts to break down (Piran et al., 1993). This happens when the shell reaches the spreading radius $R_s \equiv R_0 \Gamma^2$ where the width ΔR of the shell starts to increase such that $\Delta R \propto R/\Gamma^2$.

As the shell sweeps up ISM material, a RS starts propagating inside the ejecta. Several important transitions happen throughout the evolution for this RS (Sari & Piran, 1995). One of these transitions occurs when the RS becomes relativistic with regard to the unshocked ejecta, which causes it to convert a significant fraction of the kinetic energy of the shell into thermal energy and radiation, eventually slowing it down. This transition happens for a radius $R_N \equiv l^{3/2}/\Delta^{1/2}\Gamma_0^2$, where $l = (E/n_0 m_p)^{1/3}$ is the Sedov length, with n_0 the ISM number density and m_p the proton mass⁵. Another transition happens when the reverse shock has entirely crossed the ejecta. This occurs at a radius $R_\Delta \equiv l^{3/4}\Delta^{1/4}$. Finally, another critical radius is crossed when the mass of the shocked ISM reaches M_0/Γ_0 and is given by $R_\Gamma \equiv l/\Gamma_0^{2/3}$.

⁵The rest-mass energy of the ISM contained in l^3 is E .

The question is now to identify when each transition occurs relative to the others. Thankfully, all these radii can actually be linked together using the dimensionless variable $\xi \equiv (l/\Delta)^{1/2}\Gamma_0^{-4/3}$:

$$\xi^2 R_s = \xi^{1/2} R_\Delta = R_\Gamma = \xi^{-1} R_N. \quad (1.5)$$

This allows to distinguish two different cases depending on the value of ξ . If $\xi < 1$ initially, then $R_N < R_\Gamma < R_\Delta < R_s$. The RS quickly becomes relativistic and is able to substantially slow down the ejecta. However, only a fraction of the energy will have been transferred to the ISM at R_Γ , and the blast-wave only decelerates (has transferred most of its energy to the external medium) at R_Δ , before spreading at R_s . In this case, this deceleration can actually occur before the coasting phase (and so before all of the thermal energy of the fireball has been converted into kinetic energy). This is called the *thick shell* model. The cases simulated in chapter 3 correspond instead to the *thin shell* model where $\xi > 1$ initially. This entails that $R_s < R_\Delta < R_\Gamma < R_N$. In this case, the RS is initially Newtonian, before gradually becoming mildly relativistic. The shell starts spreading first and the width now satisfies $\Delta = r/\gamma^2$. This causes ξ to decrease towards unity. When $\xi = 1$, all remaining critical radii coincide such that $R_\Delta = R_\Gamma = R_N$, which is the deceleration radius in this case. As the blast wave decelerates, the forward shock transitions to the Blandford&McKee (BM) self-similar solution (see next paragraph). Simulations in the thin shell limit are shown in §4.3.5.

The Blandford&McKee self-similar solution

[Blandford & McKee \(1976\)](#) derived an analytical self-similar solution for the dynamics of an ultra-relativistic spherical blast-wave enclosed by a strong shock. It describes the evolution of a point explosion, where a given amount of energy is inserted at a point location in the CSM. The solution is based on the shock-jump conditions presented in §2.1.5. In the simulations presented in this thesis, we will assume a homogeneous ISM (the Blandford-McKee (BM) solution can also be derived for stellar wind environments). Assuming that the evolution of the blast-wave is adiabatic, one can write the Lorentz

factor, density and pressure downstream of the shock as follows:

$$\Gamma(t, r) = \frac{1}{\sqrt{2}}\Gamma_{\text{sh}}\chi^{-1/2}, \quad (1.6)$$

$$\rho(t, r) = 2\sqrt{2}\rho_0\Gamma_{\text{sh}}\chi^{-5/4}, \quad (1.7)$$

$$p(t, r) = \frac{2}{3}\rho_0\Gamma_{\text{sh}}^2\chi^{-17/12}, \quad (1.8)$$

$$\chi(t, r) \equiv 1 + 8\Gamma_{\text{sh}}^2(1 - r/R) \quad \text{the similarity variable,} \quad (1.9)$$

with $\Gamma_{\text{sh}}(t) \equiv (17/8\pi)^{1/2}(R/l)^{-3/2}$ the Lorentz factor of the shock itself, $R(t) = (1 - 1/8\Gamma_{\text{sh}})t$ its radius and ρ_0 the rest-mass density of the ISM. A solution in this form also exists for non-homogeneous external medium (e.g. stellar wind).

In the fireball model, as the initial mass and radius of the initial fireball become negligible in comparison with the swept-up mass, the evolution naturally transitions towards the solution of a point-like explosion i.e. the BM solution. Eventually, at radius l the blast-waves becomes non-relativistic and the evolution then follows the Sedov&Taylor solution.

1.3.2 Synchrotron emission in shocks

As mentioned earlier, the emission observed from GRB afterglows is interpreted as synchrotron radiation produced at shock fronts propagating in the fluid (for a recent review see e.g. [van Eerten, 2018](#)). Indeed, looking from the shock co-moving frame, an observer will see some of the kinetic energy upstream of the shock converted into internal energy at the shock front. Some of this energy is non-thermal and manifests in an accelerated non-thermal population of electrons. These electrons can radiate by interacting with a locally generated magnetic field (see [Rybicki & Lightman \(1979\)](#) for synchrotron emission theory).

In order to compute the overall spectrum of radiation emitted behind a shock, one needs to know, at any point downstream of the shock front, the information related to the hydrodynamics and the micro-physical state: the strength of the magnetic field, and the distribution in energy of accelerated electrons. Assuming no influence of the radiation on the hydrodynamics is a good approximation, as a very small fraction of the total energy of the fluid is eventually radiated. However, when running simulations, the effect of cooling on the dynamics can be implemented straightforwardly at runtime if the medium is optically thin. With this information, the synchrotron emissivity can thus be calculated at any point of the fluid.

While we can compute the emissivity at shock locations (where particles are acceler-

ated) directly from the fluid states, the emissivity downstream of these shocks requires that we compute the evolution of the micro-physical state with time. In the approach synchrotron emission from shocks is usually modeled by, the shock-accelerated population of electrons is parametrized by a truncated power-law in energy of slope p (the spectral index), such that $n_e(\gamma_e) \propto \gamma_e^{-p}$, with $p \sim 2.-2.5$ (e.g. [van Eerten, 2015](#)), where γ_e is the electron Lorentz factor expressed in the comoving frame of the fluid. From the shock-jump conditions that we will present in §2.1.5, one can derive the variation of internal energy between the upstream and downstream regions of the fluid. A fraction ϵ_e (order of magnitude $\epsilon_e \sim 0.1$, [Beniamini & van der Horst \(2017\)](#)) of this energy will be transferred to a fraction ζ of the total population of electrons. Based on this parametrization, one can derive the lower cut-off γ_{\min} for the distribution by equating the integrated electron population energy with the energy available for emission. The higher cut-off is originally fixed to $\gamma_{\max} \rightarrow \infty$, before decreasing with cooling, but its precise initial value is immaterial when $p > 2$ as long as it is sufficiently high. The last needed piece of information is the magnetic energy $B^2/8\pi$ coming from the tangled shock-generated magnetic field, that is usually modeled as a fraction ϵ_B of the internal energy of the fluid. These parameters allow the calculation of the synchrotron spectrum from a single-location power law electron distribution, as first derived by [Gleeson et al. \(1974\)](#), that features a broken power-law with an exponential drop for $\nu(\gamma_{\max})$ (with $\nu(\gamma) \propto \gamma^2 B$ the synchrotron frequency corresponding to energy γ).

Behind the shock, the evolution of the Lorentz factor of a single electron is driven by the following equation ([Granot & Sari, 2002](#)):

$$\frac{d\gamma_e}{dt'} = \underbrace{-\frac{4\sigma_T\gamma_e^2}{3m_e c}\epsilon_B q_e}_{\text{synchrotron cooling}} + \underbrace{\frac{\gamma_e}{3n} \frac{dn}{dt'}}_{\text{adiabatic cooling}}, \quad (1.10)$$

where σ_T is the Thomson cross-section, n the number density in the fluid frame, t' the time in the fluid frame, m_e the electron mass and q_e its electric charge. This equation involves losses from the emitted radiation, as well as cooling from the adiabatic spherical expansion of the fluid (the blast-wave in our case) and allows access to the local population of accelerated electrons downstream of the shock. It also shows that γ_{\max} is going to decrease with time for the population of a given fluid particle. This implies an evolution of the single-location synchrotron spectrum as the electrons cool down behind the shock.

The evolution of the particle population in a region of fluid is driven by the following

continuity equation:

$$\frac{\partial}{\partial t'} N(\gamma_e, t') + \frac{\partial}{\partial \gamma_e} \left[N(\gamma_e, t') \frac{d\gamma_e}{dt'} \right] = I(\gamma_e, t'), \quad (1.11)$$

where $N(\gamma_e, t')$ is the particle distribution function and $I(\gamma_e, t')$ is the particle injection term modeling particle acceleration at the shock front if the considered region contains one. Different approaches to solving this equation can be considered. The *global cooling* approach assumes a single zone with a steady state for equation 1.11, no internal structure and a single cooling time in the plasma. Integrating the equation leads to two different asymptotic behaviors on both sides a critical electron Lorentz factor; the cooling break particle Lorentz factor γ_c is computed by equating the electron energy with the time-integrated emitted synchrotron power from this electron in the observer frame (Granot et al., 2000):

$$\Gamma \gamma_c m_e c^2 = P_{\text{syn}}(\gamma_c) t, \quad (1.12)$$

with Γ the fluid Lorentz factor, $P_{\text{syn}}(\gamma_e)$ the bolometric synchrotron power from an electron of Lorentz factor γ_e and t the time since the shock appeared. γ_c is the Lorentz factor above which electrons have lost all of their energy to radiation at a given time t . This approach leads to the following expression for γ_c :

$$\gamma_c = \frac{6\pi m_e c}{\sigma_T \Gamma B'^2 t} = \frac{3m_e c}{4\sigma_T \Gamma \epsilon_B e' t}, \quad (1.13)$$

with e' the internal energy density in the fluid frame (and B' the magnetic field in the fluid frame). The full spectrum can be computed making use of the steady state assumption. This method presents the advantage of being very efficient, while preserving the shape of the light curve and spectrum (van Eerten et al., 2010a). The observed flux at a given observer time consists in a broken smoothly connected power-law schematically represented in figure 1.8, with breaks positionned at $\nu_m = \nu(\gamma_{\text{min}})$ and $\nu_c = \nu(\gamma_c)$. The obtained global cooling spectra for a single time t_{obs} , in the fast-cooling ($\nu_c < \nu_m$) and slow-cooling ($\nu_m < \nu_c$) regimes give a good idea of the spectrum that can be expected from a blast-wave. The peak flux of emission F_{peak} happens for ν_m in the slow-cooling regime, and ν_c , the cooling break, in the fast-cooling regime. However, in the slow-cooling case, most of the energy is radiated at ν_c and not ν_m for the typical values of $p \sim 2.5$. For emission from the forward shock of an afterglow blast-wave propagating into a uniform interstellar environment, these two frequencies evolve with observer time as $\nu_m \propto t_{\text{obs}}^{-3/2}$ and $\nu_c \propto t_{\text{obs}}^{-1/2}$ (the scalings can also be derived for a wind environment following the same method). This leads to a transition from fast-cooling

to slow-cooling eventually, but the most important is that the peak frequency ν_{peak} decreases with time. As a result, one will expect different behaviors when observing in a high or low-frequency band⁶. When observing at high frequencies, and when the blast wave already started following the BM solution, the power in the observing band can only decrease, leading to a monotone light curve (before deceleration, the light curve can rise due to continuous energy injection into the forward shock). At lower frequencies however, the flux will first increase before dropping after reaching the peak. Both evolutions are reported in figure 1.9.

Building on numerical hydrodynamical simulations, hybrid approaches have also been used in which γ_c is computed globally, but the rest of the emissivity quantities (e.g. ν_m , peak flux) are calculated locally (van Eerten, 2015). The resulting observed spectrum is going to be the superposition of the spectra from all the points in the flow with the same photon arrival time $t_{\text{obs}} = t - r/c$, t being the time in the lab frame, and r the radius at which the emitting region considered is located. This hybrid approach also recovers the correct spectral shape and scalings, however, multi-band analysis is jeopardized by the change offset introduced on the value of ν_c (Guidorzi et al., 2014).

A more accurate approach involves *local cooling*. We will discuss local cooling in details in chapters 2, 3 and 4. However with this approach, equation 1.10 is re-cast into an advection equation for γ_{min} and γ_{max} . The electron population is then initialized right behind the shock and can evolve with the fluid. In numerical simulations however, this approach requires extreme resolutions (van Eerten et al., 2010b). Combining a moving mesh with local cooling is thus a way to improve this resolution limitation.

Eventually, once one is able to model the evolution of both γ_{min} and γ_{max} , they can integrate over the whole fluid evolution taking into account beaming effects and arrival times in the relativistic context.

⁶Frequencies are compares to the critical frequency $n_0 = \nu_m(t_0) = \nu_c(t_0)$ where t_0 is the time for which $\nu_m = \nu_c$.

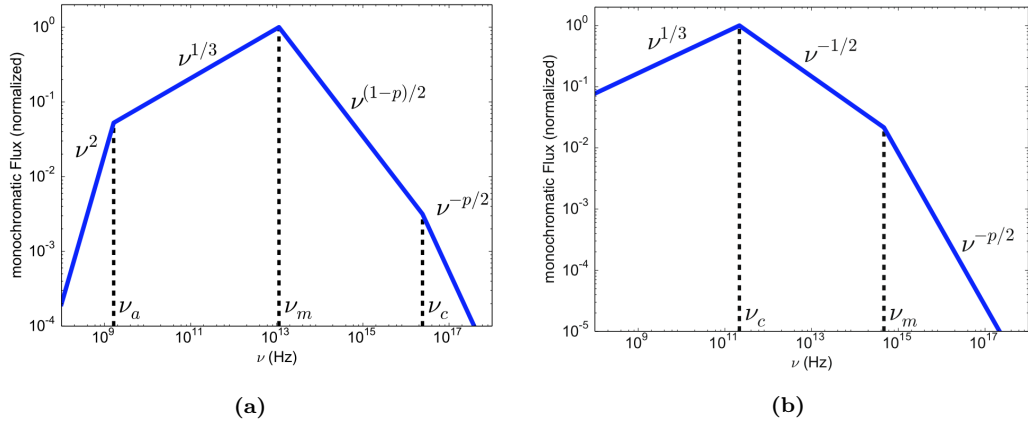


Figure 1.8: Expected instantaneous snapshot of the integrated synchrotron spectrum of a modeled GRB. (a) Slow-cooling regime. (b) fast-cooling regime. (credits: van Eerten (2015))

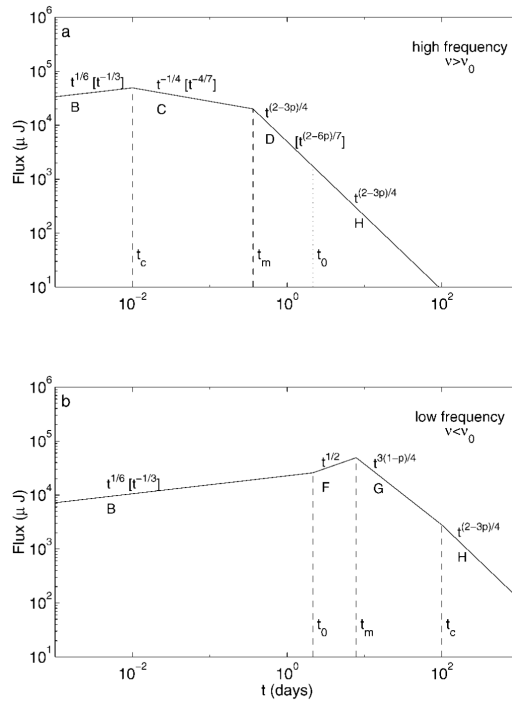


Figure 1.9: Light curve scalings for high and low frequencies. t is the observer time. The scalings without brackets are the ones describing an adiabatic expansion. The scalings in between brackets describe a radiation dominated expansion. (credits: Sari et al. (1998))

Numerical Methods: from Dynamics to Radiation

What I cannot create, I cannot understand

— RICHARD FEYNMAN

Preamble

As explained in the previous chapter, understanding of the underlying dynamical evolution explaining the various features observed in GRB afterglows lies in the ability to run accurate, precise and efficient numerical simulations of the outflow ejected by these events. These simulations can be carried out in a purely hydrodynamical setup as they will follow the evolution of collisionless shocks in propagating in a barely magnetized external medium (Rees & Meszaros, 1992). In that regard, we will introduce in this chapter the theoretical context and notation of special relativistic hydrodynamics (SRHD), before presenting the specificities of the numerical approach that we used to model the dynamics. We also introduce the formalism and present the numerical methods used to model the non-thermal emission and calculate the received flux from these dynamical simulations.

2.1 Special Relativistic Hydrodynamics theory

2.1.1 Hydrodynamics equations

The special relativistic hydrodynamics (SRHD) theory describes the dynamics of relativistic fluids moving with relativistic speeds in a flat space-time. We will carry out simulations far enough from the central engine that the curvature is negligible. Throughout the rest of this thesis, space-time will thus be described by a flat Minkowski metric tensor $g = \eta = \text{diag}(-1, 1, 1, 1)$. We will also consider perfect fluids for which any viscous effects and heat conduction can be neglected, leading to a diagonal pressure tensor. The speed of light will be set to $c = 1$.

We can start from the general relativistic description of the evolution of an arbitrary fluid, which is constrained by the conservation of only two quantities: rest-mass and energy-momentum. These conditions can be cast into two differential equations:

$$\nabla_{\mu} D^{\mu} = 0, \quad (2.1)$$

$$\nabla_{\nu} T^{\mu\nu} = 0, \quad (2.2)$$

where D is the rest-mass density flux (which can also be written as $D^{\mu} = \rho u^{\mu}$ with ρ the rest mass density and u the 4-velocity of the fluid) and T is the energy-momentum tensor. Deriving the expression of the energy-momentum tensor in the case of perfect fluids in Minkowski's metric is the key to establishing the set of scalar conservation equations describing the evolution of the fluid. In the case of perfect fluids, T can be expressed as follows:

$$T^{\mu\nu} = (e + p)u^{\mu}u^{\nu} + pg^{\mu\nu}, \quad (2.3)$$

where p is the isotropic pressure in the comoving frame and e the total internal energy¹. g is the metric tensor, equal to η in the case of special relativity. This gives for the conservation equations:

$$\nabla_{\mu} D^{\mu} = \nabla_{\mu}(\rho u^{\mu}) = u^{\mu}\nabla_{\mu}\rho + \rho\nabla_{\mu}u^{\mu} = 0, \quad (2.4)$$

$$\nabla_{\nu} T^{\mu\nu} = \nabla_{\mu}[(e + p)u^{\mu\nu} + p\eta^{\mu\nu}] = 0. \quad (2.5)$$

¹The total internal energy e includes the rest mass energy ρ (since $c = 1$) as well as the (thermal, magnetic...) internal energy usually written per unit of mass as ϵ .

2.1.2 Conservative formulation

Equations 2.4 and 2.5 can be cast in the generic first-order-in-time form:

$$\partial_t \mathbf{U} + \mathbf{A} \cdot \nabla \mathbf{U} + \mathbf{B} = 0, \quad (2.6)$$

where \mathbf{U} is the state vector of the fluid². [Wilson \(1972\)](#) first derived the expression of the conservation equations by introducing the following dynamical variables:

$$D \equiv \rho u^t, \quad (2.7)$$

$$S_\mu \equiv \rho h u^t u_\mu, \quad (2.8)$$

$$E \equiv \rho u^t \epsilon, \quad (2.9)$$

where $h = (e + p)/\rho$ is the specific enthalpy and ϵ the specific internal energy. These variables are the components of $\mathbf{U} = (D, S_\mu, E)^T$.

In the case of relativistic hydrodynamics, equation 2.6 is hyperbolic, and $\mathbf{A}(\mathbf{U})$ can be seen as the Jacobian of a flux vector $\mathbf{F}(\mathbf{U})$ with respect to the state vector \mathbf{U} . The homogeneous version of the conservation equations can hence be written in conservative form:

$$\partial_t \mathbf{U} + \nabla \mathbf{F}(\mathbf{U}) = 0. \quad (2.10)$$

This formulation is crucial in the case of discontinuous flows (as reviewed in [LeVeque, 1992, 1998](#)), and hence in the case of shock propagation, as non-conservative numerical formulations will lead to incorrect solutions, with inaccurate shock-propagation velocities, if a discontinuity is present in the flow ([Hou & Le Floch, 1994](#)). On the other hand, [Lax & Wendroff \(1960\)](#) showed that any convergent conservative numerical scheme will converge towards a solution of the problem.

In the case of SRHD, this requirement will lead to establish the *3+1 Valencia formulation* ([Martí et al., 1991](#)) of the equations of relativistic hydrodynamics (§2.1.3).

2.1.3 The 3+1 Valencia formulation of SRHD equations

General formulation

Stepping away from the Wilson formulation, the fluid can more intuitively be described by a state vector of *primitive variables* $\mathbf{V} = (\rho, \vec{v}, p)^T$, where ρ and p are the rest-mass

²A bold font will be used throughout the rest of this thesis to refer to any vector in state-variables-space (D, S_μ, E) .

density and pressure in the co-moving frame, and \vec{v} is the fluid velocity in the lab frame. Using the 3+1 decomposition of space-time³ (Misner et al., 1973), the Valencia formulation enables the derivation of a conservative form, in three dimensions (x, y, z) by using a set of *conserved* variables \mathbf{U} , and corresponding flux vector $\mathbf{F}(\mathbf{U})$ (Banyuls et al., 1997):

$$\mathbf{U} = \begin{pmatrix} D \\ \vec{m} \\ \tau \end{pmatrix} \equiv \begin{pmatrix} \rho\Gamma \\ \rho h\Gamma^2\vec{v} \\ \rho h\Gamma^2 - p - D \end{pmatrix} \quad \begin{array}{l} \text{(Rest-mass density)} \\ \text{(Momentum)} \\ \text{(Energy)} \end{array}, \quad (2.11)$$

$$\mathbf{F}_i(\mathbf{U}) = \begin{pmatrix} Dv_i \\ \vec{m}v_i + p\hat{i} \\ m_i - Dv_i \end{pmatrix}, \quad \forall i \in \{x, y, z\}, \quad (2.12)$$

where \hat{i} is the unit vector in the i -direction, h is the specific enthalpy including rest-mass energy in the co-moving frame, Γ is the Lorentz factor, and the speed of light is set to $c = 1$. Using the conserved variables, the relativistic hydrodynamics equation can be cast into the compact form:

$$\partial_t(\mathbf{U}) + \partial_x(\mathbf{F}) = \mathbf{S}, \quad (2.13)$$

where x is the spatial dimension and \mathbf{S} is the source term.

Angular momentum conserving formulation

Unfortunately, the previous expression in conservative form is only correct in Cartesian coordinates, and obtaining a conservative expression in cylindrical (r, θ, z) and spherical (r, θ, ϕ) coordinates needs a bit more work, leading to a non-zero (geometrical) source term. However, the expression can be greatly simplified by not considering the conservation of linear momentum (as done in eq. 2.11) but instead the conservation of angular momentum in the θ -direction (Mignone & McKinney, 2007). In this new

³The distinction of the time coordinate from the spatial ones is the most natural in describing physical processes. This is possible within the formulation of General Relativity by foliating space-time into a set of non-intersecting space-like hypersurfaces. Each hypersurface is thus parametrized by a constant value of t .

formulation:

$$\vec{m} = \rho h \Gamma^2 \begin{pmatrix} v_r \\ r v_\theta \\ v_{z/\phi} \end{pmatrix}. \quad (2.14)$$

The expression of the flux of momentum in the θ -direction, $F_{i\theta}$ also changes, as we are now advecting angular momentum instead of linear momentum, and becomes:

$$F_{i\theta} = r(m_\theta v_i + p \delta_\theta^i), \quad \forall i \in (r, \theta, z/\phi). \quad (2.15)$$

With this form of the equations, the following source terms appear in 2D:

$$\text{cylindrical} \quad \mathbf{S} = (0, p/r, 0, 0)^T, \quad (2.16)$$

$$\text{spherical} \quad \mathbf{S} = (0, (\rho h \Gamma^2 v_\theta^2 + 2p)/r, p/\tan \theta, 0)^T, \quad (2.17)$$

where the pressure terms compensate our inclusion of p in the divergence and the other term is a "geometrical" source term. In the rest of this thesis, whenever presenting results in cylindrical or spherical coordinates, this angular momentum conserving formulation will have been used. However, the linear momentum conserving form can also be expanded to any set of curvilinear coordinates, albeit with more complex geometrical source terms, as presented in the appendix of [Mignone et al. \(2005\)](#). The corresponding derivation for spherical and cylindrical coordinates in the case of SRHD is reported in the appendix of [Zhang & MacFadyen \(2006\)](#), which is equivalent to the approach we just described. The full conservation equations can also be derived in any curved metric using the "Valencia formulation" directly ([Banyuls et al., 1997](#)), but the calculation is more complex there.

2.1.4 Equation of State

In order to close the hyperbolic system of equations 4.1, one has to provide a closure equation in the form of an Equation of State (EoS). This equation describes the evolution of the fluid on a microscopic level and links the state variables to one another, without having to rely on the microscopic distribution function of the particles forming the fluid. As a result, there are as many EoS as fluid systems that can exist. Choosing the right EoS is thus crucial in order to accurately describe the evolution of a hydrodynamical system.

In the case of GRB outflows, since the energy is mostly carried by the baryons ([Rees & Meszaros, 1992](#)), the ejecta can be considered as an ideal, monoatomic, ultra-

relativistic, non-degenerate fluid⁴. The EoS giving the expression of the pressure p as a function of rest-mass density ρ and specific internal energy ϵ is written as follows:

$$p(\rho, \epsilon) = \rho\epsilon(\gamma - 1), \quad (2.18)$$

where γ is the *adiabatic index of the fluid*. This equation can be rewritten in terms of the specific enthalpy such that:

$$h = 1 + \gamma\epsilon. \quad (2.19)$$

The advantage of using this description is that it can be applicable to non-relativistic, relativistic and ultra-relativistic non-degenerate monoatomic fluids by simply adjusting the value of γ . In the non-relativistic case, $\gamma = 5/3$. In the case of GRB ejecta and before the fluid cools down, the gas is ultra-relativistic with $\gamma = 4/3$.

Eventually, the trans-relativistic case can be captured with a Synge-like ideal monoatomic fluid equation of state (EOS). Careful however, in situations involving a sub-relativistic shock with efficient induced particle acceleration, the electron temperature can become much higher than the proton temperature, which will have a direct influence on the pressure inside the shock. The fluid would then need to be described by a multi-temperature EOS. However, in keeping with the common approach seen in the literature, we keep the monoatomic description and keep the multi-fluid implementation for future work. We use the formulation from [Meliani et al. \(2004\)](#) based on the relativistic perfect gas law ([Synge, 1957](#); [Mathews, 1971](#)):

$$p(\rho, \epsilon) = \rho\epsilon(\gamma_{\text{eff}} - 1), \quad (2.20)$$

where ϵ is the specific internal energy and γ_{eff} the effective polytropic index of the fluid given by:

$$\gamma_{\text{eff}} = \gamma - \frac{\gamma - 1}{2} \left(1 - \frac{1}{e^2} \right). \quad (2.21)$$

⁴The state of degeneracy of a fluid is indicated by the fugacity $\alpha_f \equiv \frac{m}{k_B T} \left(\frac{e+p}{\rho} - Ts \right)$ where $e = \rho(c^2 + \epsilon)$ is the total energy density and $s \equiv \frac{S}{Nm}$ is the specific entropy. The value of α_f gives an idea of the importance of the quantum corrections that have to be applied to the EoS. If $\alpha_f \ll 1$ then the fluid is non-degenerate. If $\alpha_f \gg 1$ the fluid is degenerate.

The importance of the relativistic corrections to the EoS are quantified by the coldness $\zeta_c \equiv \frac{mc^2}{k_B T}$ that measures the thermal energy of the fluid. $\zeta_c \ll 1$ will designate a relativistic fluid, where the thermal energy is much greater than the rest-mass energy. On the other hand, $\zeta_c \gg 1$ designates a non-relativistic fluid.

e is the proton mass and specific internal energy including rest-mass. $\gamma = 5/3$ is the fixed adiabatic index for a non-relativistic (cold) fluid. We can verify that we have $\gamma_{\text{eff}} = \gamma = 5/3$ for a cold fluid and $\gamma_{\text{eff}} = 4/3$ in the ultra-relativistic case. This description is a very good approximation to the Synge gas equation. It avoids having to tabulate the Bessel functions that are costly to evaluate and that would have to be used otherwise.

2.1.5 Rankine-Hugoniot jump conditions

The equations of relativistic hydrodynamics form a hyperbolic system that thus features both wave motion and advective transport. This can give rise to different types of waves involving linear acoustic waves, as well as non-linear simple (compression and rarefaction) waves, and discontinuous waves (generally referred to as *shock waves*) (see e.g. Rezzolla & Zanotti, 2013). A good description of the latter is crucial in understanding both the dynamics of blast-waves involved in GRBs (see §1.3.1), but also for understanding the Godunov numerical scheme for hydrodynamics (see §2.2). Understanding the physics of shocks is also vital to accurately modeling the resulting Synchrotron emission.

A discontinuous wave is, unsurprisingly, an infinitesimally thin interface across which at least one of the fluid properties is discontinuous (it can also be said that it experiences a *jump*, hence the name *jump conditions*). They can be divided into *contact waves* separating two parts of the fluid with no flow through the interface, and *shock fronts* when the fluid does flow across the interface. Physically, the variables involved in the jump do not actually display a discontinuity, but rather a very steep gradient on the length-scale of the mean free path ℓ_{mfp} of the particles forming the fluid (in the case of a non-viscous perfect fluid). When ℓ_{mfp} is small compared to the typical length-scale of the evolution of the fluid properties, the jump can be mathematically modeled as a discontinuity, which actually provides a very handy simplification to the treatment of these features, by the use of the aforementioned *jump conditions*.

These Rankine-Hugoniot jump conditions simply state the conservation of rest-mass, energy and momentum across the surface. They are written as follows in the discontinuity rest-frame:

$$\llbracket \rho u^\mu \rrbracket n_\mu = 0, \quad (2.22)$$

$$\llbracket T^{\mu\nu} \rrbracket n_\nu = 0, \quad (2.23)$$

with the double-bracket notation $\llbracket X \rrbracket \equiv X_b - X_a$ describing the jump of an arbitrary

quantity X across the discontinuity (with a and b denoting the side of the discontinuity X refers to).

This eventually translates to the set of following conditions:

$$\rho_a \Gamma_a v_a = \rho_b \Gamma_b v_b, \quad (2.24)$$

$$\rho_a h_a \Gamma_a^2 v_a^2 + p_a = \rho_b h_b \Gamma_b^2 v_b^2 + p_b, \quad (2.25)$$

$$\rho_a h_a \Gamma_a^2 v_a = \rho_b h_b \Gamma_b^2 v_b, \quad (2.26)$$

where v is the velocity perpendicular to the shock front. This relativistic version of the Rankine-Hugoniot jump conditions is also called the *Taub adiabat*, after Abraham Taub who first derived it (Taub, 1948). These conditions represent the starting point of the derivation of a solution to a Riemann problem which will be introduced in the next section.

2.1.6 Riemann problem

A Riemann problem is the study of the decay of an interface between two fluid states in differing thermodynamical states (or more specifically, with different values of (ρ, v, p)). We will see later that the commonly used Godunov scheme solves this exact problem at each interface in the computational grid for each time-step. Mathematically, it is written as follows:

$$\mathbf{U}(x, 0) = \begin{cases} \mathbf{U}_L & \text{if } x < 0, \\ \mathbf{U}_R & \text{if } x > 0, \end{cases} \quad (2.27)$$

where L stands for *left* state and R for *right* state. The solutions of the Riemann problem in SRHD have been investigated by Martí & Müller (1994) (1D analytical solution), Pons et al. (2000) (tangential velocities), and Rezzolla et al. (2003a) (multidimensional solution). Phenomenologically, the solution gives rise to a self-similar 3-wave pattern, with the propagation of 3 non-linear waves on either side of the original discontinuity. The center wave is a contact discontinuity \mathcal{C} , showing a jump in density only, whereas the left and right waves (respectively \mathcal{W}_\leftarrow and \mathcal{W}_\rightarrow) can be rarefaction waves or shock waves (written \mathcal{R} and \mathcal{S} respectively) indifferently, with a change in all 3 primitive variables in the relativistic case. The waves delimit 4 regions of space in various thermodynamical states (L, L_*, R_*, R) , with L and R equal to the original left and right

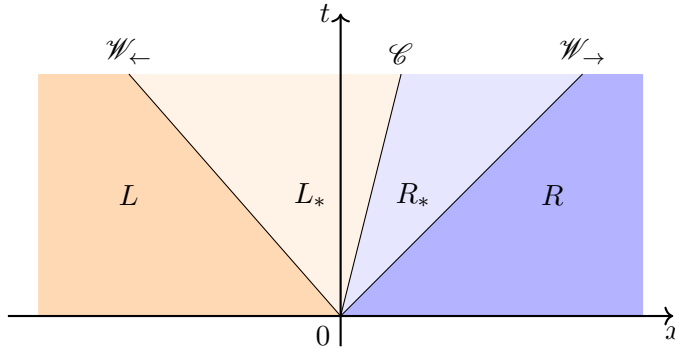


Figure 2.1: Space-time diagram of the 1D general Riemann problem in the x direction. Two non-linear waves and a contact wave separating 4 thermodynamical states propagate on either side of the original discontinuity. The velocities of all waves can be negative or positive (depending on the initial state) such that they can be on either side of the original discontinuity position.

states respectively) such that the Riemann problem is written as follows:

$$LR \quad \text{at } t = 0, \quad (2.28)$$

$$L\mathcal{W}_{\leftarrow}L_*\mathcal{C}R_*\mathcal{W}_{\rightarrow}R \quad \text{at } t > 0. \quad (2.29)$$

This evolution is reported in a space-time diagram in figure 2.1 for one dimension in the general case.

The Riemann problem can be solved iteratively to any desired degree of precision (Rezzolla & Zanotti, 2013) (the so-called *exact solution*). We will see however that numerical simulations requiring a Riemann problem to be solved will make extensive use of approximate solvers rather than exact solutions, mostly in order to optimize algorithmic complexity. This will be developed in §2.2.2.

2.2 Numerical Hydrodynamics with finite volumes - The Godunov Scheme

In the previous section, we derived the analytical tools necessary to model the dynamics of relativistic fluid flows. As explained in chapter 1 however, analytical models fail to capture the full details of multidimensional flows, and numerical approaches are thus needed. There are two major approaches for numerically describing the evolution of a fluid. The smoothed particle hydrodynamics method (SPH), is a Lagrangian scheme similar to N-body approaches, where interacting fluid particles evolve freely. This approach is particularly well suited for multi-dimensional situations with no obvious symmetries. However, they do not allow precise capturing of shocks as they rely on

a smoothing kernel in order to compute field gradients. As a result, we will favor for our work *grid-based methods*. A discussion on the advantages and drawbacks of SPH compared to grid-based methods is given in [Bodenheimer et al. \(2007\)](#).

The grid-based numerical approaches rely on a discretization of space and time into a finite number of points (finite-differences approach), or volumes (finite-volumes approach). The normally continuous fields describing the dynamics of a fluid flow are then only defined at the location of these elements/volumes in space. A good aspect of the 3+1 space-time description (see §2.1.3) is that it allows us to globally evolve a whole spatial grid from one time increment to the next. Any numerical simulation built like this thus consists in a collection of space-like grids $(\mathbf{U}_i)_{i \in \llbracket 1, N \rrbracket}^n$ of size $N \in \mathbb{N}$ at various time increments $(t^n)_{n \in \mathbb{N}}$. Again, the system we propose to study involves shocks that lead to deviation from total conservation when using finite-difference methods. Interfaces between volumes in the finite-volumes approach, on the other hand, represent a perfect setup to modeling discontinuities, provided that they can track the motion of these discontinuities. We will thus develop a finite-volume scheme based on the Godunov approach ([Godunov, 1959](#)) which has proven to be very efficient, accurate and is very well documented in the literature. As introduced in §1.1.3, we will adapt this method to a multi-dimensional ALE approach.

This section focuses on explaining the basics of the Godunov numerical method, and dives into the details of the associated schemes we favored for our work. Any chosen method will have to be conservative and keep sufficient resolution in order to model shock fronts appearing in the flow as accurately as possible.

2.2.1 First order scheme

As stated earlier, the Godunov scheme is a *finite-volume* method that can be used in order to solve second order hyperbolic problems. In an orthonormal system of coordinates, the simulated domain is divided into a series of cells $(\mathcal{C}_i)_{i \in \llbracket 1, N \rrbracket}$ for which all intensive hydrodynamical quantities have been averaged over their volume (fig. 2.2b), enabling us to thus refer to *cell-averaged values*, written \mathbf{U}_i^n . For the rest of this section, and for the sake of clarity, we will consider a 1D grid (but multi-dimensional velocity). However, all the concepts introduced can be easily extended to higher dimension as we will see at the end the chapter, since the algorithms described here are unchanged regardless of the direction considered. As a result, cells are separated by a set of $N - 1$ interfaces designated by half space indexes $\mathcal{I}_{i+1/2}$ (staggered grid). These interfaces are orthogonal to the chosen dimension (aligned with the coordinate system, and can be chosen to remain so even when considering a multi-dimensional moving mesh). In

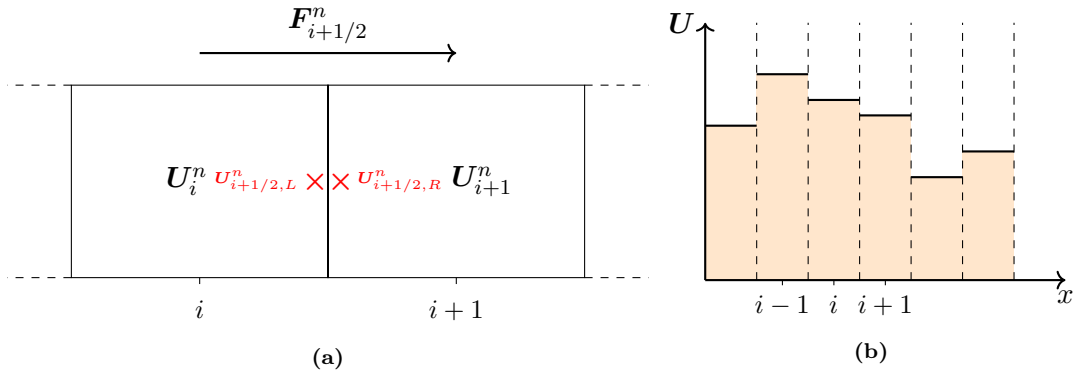


Figure 2.2: 1-D representation of a Godunov scheme. The left and right state at interface $\mathcal{I}_{i+1/2}$ are noted $U_{i+1/2,L}^n$ and $U_{i+1/2,R}^n$. The arrow indicates the flux through the interface, as computed by the Riemann solver using these states as an input.

the rest of the thesis, let us use i to refer to an integer index and j to refer to a half integer index ($j = i + (2k + 1)/2$, $k \in \mathbb{N}$). This way, we can refer to interfaces with the notation \mathcal{I}_j or $\mathcal{I}_{i+1/2}$ depending on whether we focus on the interface itself, or define it with respect to one of its neighboring cells. Whenever unambiguous, we will allow ourselves to drop the indexes i , j or n .

For every time-step Δt^n , cell \mathcal{C}_i is updated by computing the *inter-cell fluxes* $F_{i-1/2}^n$ and $F_{i+1/2}^n$ (eq. 2.30), that is, the amount of every physical quantity crossing from one cell to another. This operation is repeated for every cell in the grid. The clever idea in the Godunov scheme is to notice that every cell interface \mathcal{I}_j is a discontinuity whose evolution is directed by a Riemann problem. Solving this Riemann problem allows to compute the corresponding flux across the interface. The scheme thus can be summarized in the following three simple steps:

1. **Reconstruct:** the left and right interface states $U_{i+1/2,L}^n$ and $U_{i+1/2,R}^n$ are computed from the neighboring cell-averages (fig. 2.2a). In the first order scheme, these are calculated in a piece-wise constant manner, setting their value to the cell-average value of the cell they belong to ($U_{i+1/2,L}^n = U_i^n$ and $U_{i+1/2,R}^n = U_{i+1}^n$ respectively, see fig. 2.2b). Higher-order reconstruction is described in §2.2.5.
2. **Solve:** The Riemann problem is solved (exactly or approximatively) at the interface, allowing to compute the flux across the interface $F_{i+1/2}^n$. The Riemann solvers used are described in §2.2.2.
3. **Update:** The new cells are updated using the fluxes calculated in the previous

step following equation 2.30:

$$\mathbf{U}_i^{n+1} = \mathbf{U}_i^n + \frac{\Delta t^n}{dV_i^n} (\mathbf{F}_{i-1/2}^n dA_{i-1/2}^n - \mathbf{F}_{i+1/2}^n dA_{i+1/2}^n), \quad (2.30)$$

where dA_j^n is the surface area of interface \mathcal{I}_j^5 , and dV_i^n is the volume of cell \mathcal{C}_i , both at time t^n .

This approach ensure that the scheme is conservative and upwind. It also guarantees monotone evolution, and thus non-oscillatory behavior (for piece-wise constant interface reconstruction, see §2.2.5). These aspects make of the Godunov approach a very good starting point for trying to develop more elaborate numerical schemes.

2.2.2 Riemann solvers

The phenomenology of the Riemann problem has already been described in §2.1.6. Here we focus on the numerical approaches based on the Riemann problem in order to compute inter-cell fluxes. These solvers compute a so-called "Riemann fan" (recall figure 2.1). As mentioned earlier, exact solutions are rather computationally expensive to obtain, this to a particularly prohibitive extent as soon as one moves towards multidimensional problems. Approximate solvers achieve better computational efficiency. *Complete* solvers (as opposed to *incomplete*) will compute velocities and intermediate states for all three waves emerging from the discontinuity (in the case of the SRHD equations), giving a solution in the following form:

$$\mathbf{U}(x, t) = \begin{cases} \mathbf{U}_L & \text{if } x/t < \lambda_L, \\ \mathbf{U}_{L^*} & \text{if } \lambda_L < x/t < \lambda_*, \\ \mathbf{U}_{R^*} & \text{if } \lambda_* < x/t < \lambda_R, \\ \mathbf{U}_R & \text{if } x/t > \lambda_R. \end{cases} \quad (2.31)$$

where λ_L , λ_* and λ_R are the velocities (normal to the discontinuity) of \mathcal{W}_{\leftarrow} , \mathcal{C} and $\mathcal{W}_{\rightarrow}$, respectively. The incomplete solvers on the other hand will generally only focus on the fastest waves in the Riemann fan, overlooking the intermediate waves (\mathcal{C} in our case).

The HLLC solver for SRHD

As our main objective is to be able to model blast-waves and capture shocks, we need a

⁵Depending on the dimension of the grid, dA can be 1D in the 2D case, and 2D in the 3D case. In the special case of 1D Cartesian coordinates, we arbitrarily choose $dA = 1$.

⁶In a fixed mesh approach, dA_j and dV_i are constant with time, and we can drop the n exponent.

complete solver able to model the contact discontinuity accurately. Most importantly, building pseudo-lagrangian approaches require us to move mesh interfaces at the contact discontinuity velocity. A pseudo-lagrangian approach maximises mass conservation and minimises diffusion around shocks. We focus especially on the relativistic HLLC solver for relativistic hydrodynamics developed by Mignone & Bodo (2006) which has the advantage of accurately describing the contact discontinuity (CD). This is particularly important as we will combine the scheme with a moving mesh following the motion of these contact waves when in the purely Lagrangian configuration (see §2.3).

The HLLC Riemann solver for relativistic hydrodynamics is based on the incomplete HLL solver first presented by Harten, Lax, & van Leer 1983. This solver considers only 3 states (\mathbf{U}_L , \mathbf{U}^{hll} and \mathbf{U}_R) in the fan, delimited by two waves. By using estimated velocities for these waves, one can apply the Rankine-Hugoniot conditions across them and thus reconstruct the values of these states. The corresponding interface numerical flux is given by:

$$\mathbf{F} = \begin{cases} \mathbf{F}_L & \text{if } \lambda_L \geq 0, \\ \mathbf{F}^{\text{hll}} & \text{if } \lambda_L \leq 0 \leq \lambda_R, \\ \mathbf{F}_R & \text{if } \lambda_R \leq 0, \end{cases} \quad (2.32)$$

with $\mathbf{F}_L = \mathbf{F}(\mathbf{U}_L)$, $\mathbf{F}_R = \mathbf{F}(\mathbf{U}_R)$ (see eq. 4.3) and:

$$\mathbf{F}^{\text{hll}} = \frac{\lambda_R \mathbf{F}_L - \lambda_L \mathbf{F}_R + \lambda_R \lambda_L (\mathbf{U}_R - \mathbf{U}_L)}{\lambda_R - \lambda_L}. \quad (2.33)$$

It should be noted that there are various ways of estimating the wave velocities, some relying on direct estimates, and others on the estimation of the pressure in the *hll* region (Toro, 2009). For the sake of simplicity, we use in our setup the wave speed estimates from Mignone & Bodo (2006). These are direct estimates of the upper and lower bounds of the signal velocities first derived for the relativistic gas dynamics case by Davis (1988) and have since then been the popular choice for SRHD numerical simulations.

As mentioned earlier, the HLLC solver is a modification of the HLL solver that restores the contact discontinuity in the Riemann fan. The fluxes corresponding to the $*$ states given in equation 2.31 are derived using the Rankine-Hugoniot jump conditions:

$$\mathbf{F}_{L^*} - \mathbf{F}_L = \lambda_L (\mathbf{U}_{L^*} - \mathbf{U}_L), \quad (2.34)$$

$$\mathbf{F}_{R^*} - \mathbf{F}_R = \lambda_R (\mathbf{U}_{R^*} - \mathbf{U}_R). \quad (2.35)$$

After imposing that $\mathbf{F}_{L_*} = \mathbf{F}(\mathbf{U}_{L_*})$ and $\mathbf{F}_{R_*} = \mathbf{F}(\mathbf{U}_{R_*})$ (see eq. 2.11 for the expression of $\mathbf{F}(\mathbf{U})$) this becomes a system of $2n$ equations (where n is the number of components of \mathbf{U}) with $2n + 3$ unknowns λ_* , D_* , $v_{\perp,*}$, $\vec{m}_{//,*}$, E_* , p_* , where $v_{\perp,*}$ is the velocity normal to the interface, $\vec{m}_{//,*}$ the momentum aligned with the interface, and all starred quantities are duplicated to describe both L and R sides of the interface. Note that we have made use of the relation $m = (E + p)v$ (eq. 2.11) such that the normal component of the momentum is not an unknown. By imposing $v_{\perp,L_*} = v_{\perp,R_*} = v_{\perp,*} = \lambda_*$ and $p_{L_*} = p_{R_*} = p_*$ across the contact discontinuity, and rewriting the equations in terms of λ_* and p_* , we get the 3 necessary relations to close the system. The method to solve this system is well described in [Mignone & Bodo \(2006\)](#) and [Toro \(2009\)](#).

As explained earlier in the case of the HLL solver, the interface numerical flux will be the one corresponding to the region that contains the interface ($x/t = 0$ in the case of a fixed mesh).

2.2.3 Recovering primitive variables

The computation of the numerical inter-cell fluxes by the Riemann solvers presented earlier requires the knowledge of the values of the vector of primitive variables \mathbf{V} . These fluxes allow for the update of the values of the conserved variables \mathbf{U} for every cell. It is then necessary to recover the values of \mathbf{V} from \mathbf{U} between each update. [Martí & Müller \(2003\)](#) dedicate a whole section to the various ways this can be done. In the case of SRHD, the main issue is that this involves solving a non-linear equation for p :

$$E + p - D\Gamma - \frac{\gamma}{\gamma - 1}p\Gamma^2 = 0, \quad (2.36)$$

where $\Gamma = (1 - m^2/(E + p)^2)^{-1/2}$. In order to do this, we chose to implement a simple iterative Newton-Raphson method.

Sometimes however, unphysical results for \mathbf{U} can be produced for ultra-relativistic flows. A solution to this is to decrease the value of the CFL factor (see §2.2.4), but this causes the computation to slow down, which cannot be allowed past a given extent. A *fall-back* procedure, such as the one described in [Zhang & MacFadyen \(2006\)](#), moving the evolution for the problematic time-step to more diffusive solvers has proved to be an efficient method to deal with this issue, and is used in the work presented in chapter 3. A more straightforward approach however is setting a floor value for pressure, depending on the setup that we are simulating. This is equivalent to injecting energy in the problematic cells, and requires monitoring of the total energy of the system to ensure that the simulation is not too affected by this solution.

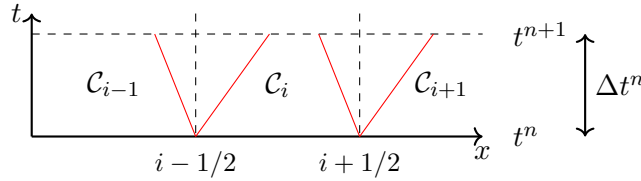


Figure 2.3: The value of the CFL factor a_{CFL} is chosen in such a way that waves emerging from two adjacent interfaces (in red) do not interact over one time-step Δt^n . As a result we have $a_{\text{CFL}} < 0.5$ in general.

2.2.4 Time-integration - the CFL condition

Time integration is driven by the *Courant-Friedrichs-Lewy (CFL) condition* (Courant et al., 1928). This condition guarantees that the numerical domain of dependence of a cell \mathcal{C}_i^{n+1} is wider than its physical domain of dependence. A schematic representation of the condition is given in figure 2.3. As inter-cell fluxes are computed only between direct neighbors (numerical dependence), the time-step has to be small enough such that any wave emerging from an interface does not hop over to the next cell within Δt^n . Mathematically, the condition writes:

$$\Delta t^n = a_{\text{CFL}} \min_i(\Delta t_i^n) \quad \text{with} \quad \Delta t_i^n = \frac{\Delta x_i^n}{\max(|\lambda_{R,i-1/2}^n|, |\lambda_{L,i+1/2}^n|)}, \quad (2.37)$$

where, $a_{\text{CFL}} \in [0, 1]$ is the CFL factor. We give the updated expression for a moving mesh in §2.3.1. In practice $a_{\text{CFL}} \in [0.2, 0.5]$ to ensure that waves emerging from neighboring interfaces do not interact either. When working with multiple dimensions, the time-step can simply be chosen as the minimum value obtained from the application of this criterion in each dimension independently. The lower the value of the CFL factor, the more conservative and stable the scheme is. Moreover, being able to choose a time-step as small as possible ensures that the order of precision of the simulation is limited by the spatial order of precision only. Higher order time-integration employing Runge-Kutta approaches is still possible and increases the scheme's stability, but is very expensive in terms of memory as intermediate states of the simulated grid need to be stored before the final grid update.

2.2.5 HRSC method

The Godunov scheme as it has been presented is only of first order in space (and thus referred to as only first-order accurate). As a result, the shock fronts expected to appear in simulations of blast-waves are smeared out over multiple cells. This constitutes a problem as the light emitted by GRBs is directly produced in these shocks via the acceleration of particles. An impossibility to resolve the shock fronts with sufficient

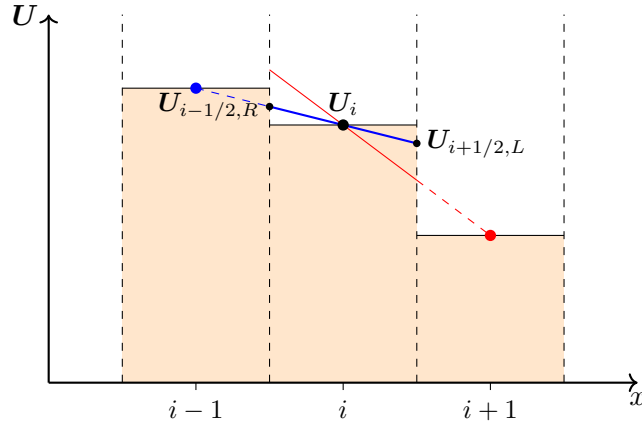


Figure 2.4: Schematic representation of the piece-wise linear reconstruction with the minmod slope limiter. Interface states are reconstructed using linear interpolation between neighboring cells. Since there are two neighboring cells, the slope with minimum gradient is chosen, in order to limit spurious oscillations. For cell C_i , the minimum gradient with a neighboring cell is $\frac{\Delta U}{\Delta x}|_{i,i-1/2}$ (in blue). The red slope is not used for the computation of $U_{i-1/2,R}$ and $U_{i+1/2,L}$.

precision would represent a double obstacle to the production of synthetic light curves as, on top of the difficulty of computing the injected power accurately, the ability to detect these shocks would itself become challenging.

Hence, we need a way to increase the spatial order of precision of our numerical scheme and devise a *high-resolution shock-capturing (HRSC) method*. One strategy for doing so is to include a *reconstruction* step in the calculation of the fluid states on both sides of an interface between two cells (step 1 in §2.2.1). In the first order scheme, this reconstruction step is simply done using a piece-wise constant function for U (fig. 2.2b). However, this discretization is not representative of the physical continuous state of the fluid and introduces errors in the treatment of the fluid evolution. In modern Godunov schemes, more accurate methods such as the *piece-wise parabolic reconstruction* or the *piece-wise linear reconstruction* are used. These methods are accurate as long as they remain conservative, meaning that cell-averages before and after reconstruction are conserved. In this process, one also, needs to be careful about introducing spurious oscillation and instability in the scheme. This will be done by ensuring that the scheme is *Total-Variation Diminishing (TVD)*⁷, using what is called *flux-limiters* or *slope-limiters*.

⁷The total variation of a differentiable function f of several variables on a domain Ω is: $TV(f, \Omega) = \int_{\Omega} |\nabla f(x)| dx$. A scheme is TVD if the total variation decreases with each iteration. In practice this means that oscillations and spurious features around discontinuities cannot appear.

Piece-wise linear reconstruction

Even though this method is not the most commonly used in the literature, with the piecewise parabolic method usually favored, it is the most computationally efficient and most straightforward to implement. It is also a good example in order to explain the principles of higher order reconstruction. To this date, it is thus the method we have chosen to use in the simulations presented in chapters 3 and 4. It works by following a linear interpolation in a given cell from the cell-centered value to any position x within that cell such that:

$$\mathbf{U}_i^n(x) = \mathbf{U}_i^n + \boldsymbol{\sigma}_i^n(x - x_i), \text{ with } x_{i-1/2} \leq x \leq x_{i+1/2}, \quad (2.38)$$

where $\boldsymbol{\sigma}_i^n$ is the *slope* of the interpolation. The advantage of this description is that it is clearly conservative and that it only requires to specify the slope to use. As several choices exist for these slopes, it is important to make sure that the choice of slope conserves the TVD aspect of the elected scheme. This the reason why slopes are also often directly referred to as *slope limiters*. These slope limiters are mathematically equivalent to the flux limiters, the difference in denomination only coming from the stage at which these limiters intervene (reconstruction for slope limiters, update for flux limiters). Again, for the sake of simplicity, we describe and implement in our work the minmod slope limiter.

Minmod slope limiter

The minmod slope limiter is given by the following equation:

$$\boldsymbol{\sigma}_i^n \equiv \text{minmod} \left(\frac{\mathbf{U}_i^n - \mathbf{U}_{i-1}^n}{x_i^n - x_{i-1}^n}, \frac{\mathbf{U}_{i+1}^n - \mathbf{U}_i^n}{x_{i+1}^n - x_i^n} \right), \quad (2.39)$$

where $\text{minmod}()$ is applied to every component of its arguments individually and writes:

$$\text{minmod}(\alpha, \beta) \equiv \begin{cases} \alpha & \text{if } |\alpha| < |\beta| \text{ and } \alpha\beta > 0, \\ \beta & \text{if } |\beta| < |\alpha| \text{ and } \alpha\beta > 0, \\ 0 & \text{if } \alpha\beta \leq 0. \end{cases} \quad (2.40)$$

This guarantees that the scheme stays TVD and reaches 2nd order accuracy (however reduced to 1st order at local extrema). This allows for a better resolution of non-linear waves, such as shock fronts. An example of interface reconstruction using a piece-wise linear approach with a minmod slope limiter is shown in figure 2.4. In this sketch, interface $\mathcal{I}_{i-1/2}$ and $\mathcal{I}_{i+1/2}$ are reconstructed in blue and red, respectively, and the slope is constrained by the left interface for which the interacting cells have the lowest

gradient. At this point, it is crucial to point out that the reconstruction on all faces of a single cell (not to confuse with left and right states of a single interface) should use the same slope in order to fulfill the conservative criterion of reconstruction.

2.3 Moving mesh

2.3.1 Advantages and drawbacks

Thus far, we have described the mathematics of HRSC finite-volume methods but have not mentioned moving meshes. This is because all the methods introduced in the previous sections of this chapter usually are applied to fixed meshes. However, the extension to moving meshes is surprisingly straightforward provided that one is ready to tackle the associated mesh distortion.

As briefly mentioned in chapter 1, moving meshes provide a range of advantages. Let us consider in this section a setup in which the mesh follows the fluid motion. First, for similar grid resolutions, the time-step for every fluid update will increase in comparison with a fixed mesh. The performance will at worst as bad as the fixed mesh (in the presence of high-velocity gradients), and at best limited by the speed of sound. Let's examine how the CFL condition (see §2.2.4) changes for a moving mesh. A schematic representation is given in figure 2.5. Instead of using the cell size to compute the maximum time-step allowed for each wave in the Riemann fan, we instead evaluate the distance each wave can travel before it hits the moving opposite boundary. The expression for the time-step becomes:

$$\Delta t^n = a_{\text{CFL}} \min_i(\Delta t_i^n) \quad \text{with} \quad \Delta t_i^n = \max \left(\frac{\Delta x_{R,i-1/2}^{\text{CFL}}}{|\lambda_{R,i-1/2}^n|}, \frac{\Delta x_{L,i+1/2}^{\text{CFL}}}{|\lambda_{L,i+1/2}^n|} \right) \quad (2.41)$$

where Δx^{CFL} is the distance a given wave can travel before interacting with its opposite interface. This unwinding approach works in all directions and all interface velocities. For a flow with small velocity gradients but high bulk velocity, the time-step will, with this new condition, be limited by the speed of sound in the co-moving frame, instead of by the speed of the bulk motion.

Another significant advantage is that a mesh moving at the fluid velocity will cause the resolution to increase when subjected to compression waves, leading a naturally shock-capturing method. There will be plenty of opportunities to highlight and take advantage of this behavior in the applications presented in chapters 3 and 4.

Finally, setting interface velocities to the CD velocity in the Riemann fan ensures that

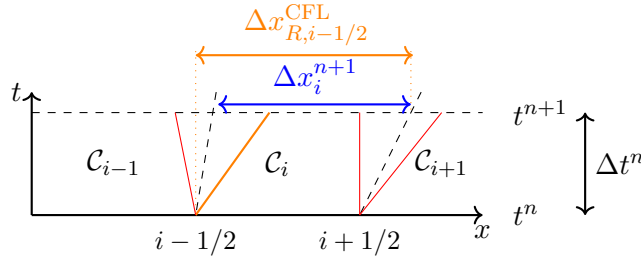


Figure 2.5: CFL condition schematic representation for a moving mesh. Notation is identical to fig. 2.3 and we have added the cell width in blue. The moving interfaces translate to oblique dashed lines now. We consider each wave subsequently and compute a maximum time-step based using not the cell width, but the distance between the original wave position and the position of the opposite interface after time Δt^n . We report this distance Δx_{CFL} for the orange wave.

there is no mass flux across the interface, making the code pseudo-Lagrangian⁸. This minimises numerical errors in mass conservation and reduces diffusion in regions of large gradients, provided that the gradient is aligned with the direction of mesh motion. As we will see later, the calculation of the local synchrotron emissivity directly relies on our ability to accurately enforce mass conservation which makes this advantage from the moving mesh very attractive.

However, these improvements come at the cost of mesh complexity. Mesh entanglement is a well known issue which is usually solved by very expensive re-gridding operations. However, entanglement itself can be circumvented in highly directional flows in which motion is dominant in one direction. JET (Duffell & MacFadyen, 2013) and DISCO (Duffell, 2016) take advantage of this for radial and polar flows, respectively, and allow the mesh to move along tracks oriented following these directions only in each of these cases. This means that the only re-gridding needed is done inside individual tracks. We will tackle adaptive mesh refinement (AMR) in §4.2.5. Another challenge is that we lose mesh regularity. This means that bookkeeping operations become much more intensive as we now need to keep track of cell position and geometry as well as their varying number of neighbours and associated inter-cell interfaces. We explain how to overcome this challenge in the next section.

2.3.2 New fluid update

In two dimensions we follow the same approach as JET and DISCO in which we allow the mesh to move only in one direction. This means that the simulation domain is a set of tracks along which cells are allowed to move. Let us call x the moving direction

⁸We can talk of pseudo-Lagrangian character in a given direction if we allow the mesh to move only in one direction, resulting in mass flux in the transverse directions (see next paragraph).

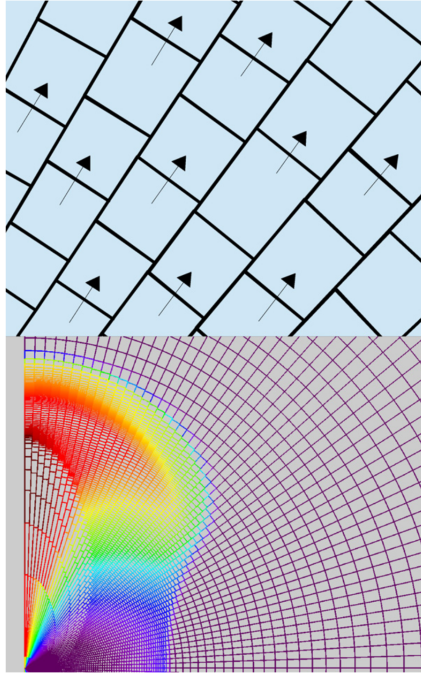


Figure 2.6: Low-resolution snapshot from the code JET of a blast-wave propagating in a diffuse medium. The mesh is only allowed to move along tracks in the radial direction. The resolution naturally increases downstream of the shock. Figure from [Duffell & MacFadyen \(2013\)](#). Figure 4.2 shows a similar setup for GAMMA.

and y any non-moving dimension (the treatment stays the same in 2D or 3D). Figure 2.6 shows an example of such a mesh with radial tracks. Already, one notices that, for a given cell, while the number of neighbours stays identical in x , it is variable in y . This means that while the expression of the flux for each x -interface will change, it is the number of y -interfaces and not the expression of their flux that will be modified in the y direction. However, while spatial reconstruction for x -interfaces follows the same procedure as before, the loss of regularity in the y direction means that we are going to need to update the spatial reconstruction process for y -interfaces. In the rest of this section we describe the updates that need to be done to the procedures described earlier in the chapter. Methods not mentioned here remain unchanged from a fixed mesh approach.

Geometry update

We follow the movement of interfaces on a given track. For an interface at position \vec{x}_i^n moving at velocity \vec{v}_i^n and for time-step Δt^n , the new position with first order time integration is simply:

$$\vec{x}_i^{n+1} = \vec{x}_i^n + \vec{v}_i^n \Delta t^n. \quad (2.42)$$

For each iteration we first move the interfaces and then re-compute the cell centers,

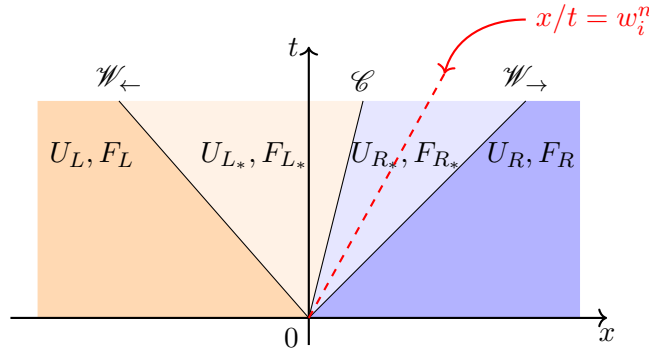


Figure 2.7: Example of flux correction determination in the case of a moving interface with velocity w_i^n . In this case, the interface will travel in the (R_*) region during the n update, as shown in this representation of the Riemann fan (see §2.1.6). The values used in the flux correction presented in eq. 2.43 are thus U_{R*} and F_{R*} .

the cell centroids, volumes and corresponding cell neighbours in adjacent tracks.

Spatial reconstruction across tracks (y -direction)

Interface spatial reconstruction is not as straightforward in the y -direction (direction transverse to mesh movement) as in the x -direction (moving dimension), for the simple reason that cells have multiple neighbours on each side in y . To solve this, one must bear in mind that the gradient used in a piecewise-linear approach as described in §2.2.5 must be set at the cell level to ensure conservation of fluid quantities. A thorough description of how to carry out such reconstruction is given in §4.2.4.

Cell update

Once the new kinematics of the mesh have been updated, the cell values can be updated by taking into account the velocity of their interfaces. Figure 2.7 gives an example of the organization of the Riemann fan and interface movement. The fluxes used for cell update will be corrected for the advection across the interface of the quantities in the region of the fan that the it propagates into. Mathematically, this writes:

$$\mathbf{F}_{\text{corr},j} = \mathbf{F}_j - \mathbf{U}_{\text{corr}} w_j, \quad (2.43)$$

with $\mathbf{U}_{\text{corr}} \in \{\mathbf{U}_L, \mathbf{U}_{L*}, \mathbf{U}_{R*}, \mathbf{U}_R\}$ set to the state the interface propagates into (\mathbf{U}_{R*} in the case of figure 2.7). The cells are then updated like in equation 2.30 but their values are also multiplied by the ratio between the former and the new volume of the cell.

2.3.3 Adaptive mesh refinement

The introduction of the ability for cells to change size means that their dimensions need to be capped. The bounds can be respected by introducing adaptive mesh refinement (AMR) methods that will merge and split cells to meet the target size. If not doing so, two main issues may arise. First, the time-step can find itself limited by cells of unreasonably small size in comparison to the rest of the fluid and the computation can grind to a halt because of the compression in strong shocks. In this situation, merging cells on the same track can restore higher time-step values. Second, regions where the fluid expands can become insufficiently resolved. In this case, splitting cells increases the resolution without impacting the time-step as it will be limited by other regions of the flow. The criteria for merging and splitting depend on the geometry of the problem, the dynamic range of the features to capture, as well as the chosen resolution in the y dimension. For example, chapters 3 and 4 introduce two different sets of criteria and we refer the reader to them to get an understanding of how these AMR criteria are chosen in practice.

The simpler operation is merging. There, the two neighbouring cells selected for merging, \mathcal{C}^- and \mathcal{C}^+ , see their conserved variables volume-averaged in the new cell:

$$\mathbf{U}^{\text{new}} = (\mathbf{U}^- dV^- + \mathbf{U}^+ dV^+) / (dV^- + dV^+) \quad (2.44)$$

For splitting, we can carry out a linear interpolation from the mother cell centroid to the new daughter cells centroid positions. To enforce conservation, we choose the same gradient for both sides of the interpolation using the same procedure at that used for interface state spatial reconstruction (see §2.2.5 and make use of the minmod slope limiter).

2.4 Numerical radiative transfer for non-thermal processes

In §1.3.2 I briefly introduced the processes involved in modeling synchrotron emission from astrophysical shocks. Here I describe in more detail our approach to numerically capture the synchrotron process and accurately compute the emissivity downstream of the shocks present in moving-mesh SRHD simulations.

2.4.1 Shock detection and particle injection

Accurate shock detection is essential to the computation of non-thermal emission. [van Eerten et al. \(2010b\)](#) show that the region around the shock contributing to the emission is extremely narrow. As a result, inaccurate shock position measurement can lead to

a high degree of error in the computed emission when using a local cooling approach, as described later in this section. While in [Ayache et al. \(2020\)](#) (chap. 3) make use of a shock detector based on the calculation of the limiting relative velocities at cell interfaces in 1D from [Rezzolla et al. \(2003b\)](#) and [Zanotti et al. \(2010\)](#), we use in chapter 4 the more complex multi-dimensional version of this detector, introduced by the same authors. Both chapters 3 and 4 give the details of the calculation. We introduce here basic the philosophy behind these shock detectors in order to be able to present the particle injection process in the rest of the section.

Historically, shock detection methods have relied on measurements of the gradients of the fluid quantities in the simulation domain. One such method involves measuring the spatial gradients of the rest-mass density. When this gradient overshoots a certain threshold the jump in density can be interpreted as a shock. the most widely used method, improving on the density gradient approach, checks for negative divergence of the velocity in a given cell: $\vec{\nabla} \cdot \vec{v} < 0$. This cell is marked as shocked if the difference in pressure with at least one of its neighbours is greater than the difference prescribed by the Rankine-Hugoniot shock jump conditions (see §2.1.5) for an arbitrarily decided shock Mach Number. These approaches have shown relatively satisfying results in detecting very strong shocks. However, complex dynamics such as that that studied in chapter 3 require us to detect shocks of all strengths and we must implement a more robust approach.

The calculation of *limiting relative velocities* at cell interfaces takes advantage of the Godunov scheme by measuring the threshold on relative velocities between adjacent fluid states for the formation of a shock in the Riemann fan. Let us consider a candidate discontinuity in fluid quantities in which we observe a jump in density, pressure and velocity between two regions denoted 1 and 2. The relative velocity orthogonal to the discontinuity is $v_{12} \equiv (v_1 - v_2)/(1 - v_1 v_2)$. Chapters 3 and 4 give the expression of the threshold for the formation of one shock and one rarefaction (\mathcal{SR}), or two shocks ($2\mathcal{S}$) in the resulting Riemann fan, in the 1D and multi-D cases, respectively. By checking for this criterion on all the interfaces of the grid we can map the location of the shocks in all directions.

This procedure can be run for every iteration on all the interfaces in the simulation domain. Once the shocks have been mapped, initialisation of the accelerated particle population can be done in the cells on the downstream side of these shocks. As mentioned in §1.3.2, this population is modeled by a power-law distribution in energy of spectral index p bounded by γ_{\min} (lower bound) and γ_{\max} (higher bound). Particle-in-cell simulations have shown that p directly downstream of the shock varies with shock

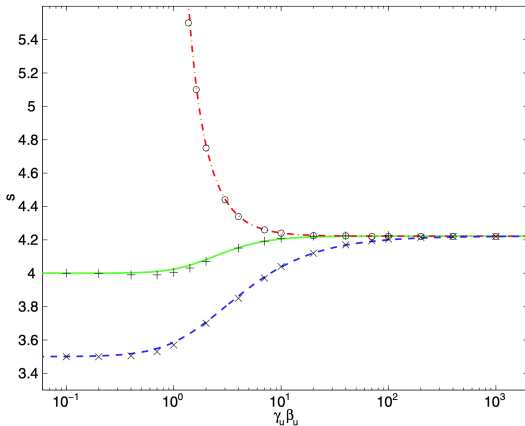


Figure 2.8: Analytically and numerically calculated spectral index $s = p + 2$ as a function of upstream four-velocity in the shock frame of reference for three different types of shocks: a strong shock with the Jüttner-Synge EOS (solid curve and crosses), a strong shock with fixed adiabatic index $\gamma = 4/3$ (dashed curve and x marks) and a shock in a relativistic gas where $\beta_u \beta_d = 1/3$ (dash-dotted and circles). Figure from [Keshet & Waxman \(2005\)](#).

strength (for recent reviews see e.g. [Sironi et al., 2015](#); [Marcowith et al., 2020](#)). [Kirk et al. \(2000\)](#) and [Keshet & Waxman \(2005\)](#) measure the evolution of p for a strong shock (fig. 2.8) with a trans-relativistic equation of state similar to the one described earlier in §2.1.4. As long as one can measure the upstream velocity in the shock frame it is possible to initialise p directly downstream of the shock following their result. In chapter 4 however, we resort to an approximation to facilitate this calculation and equate the upstream velocity in the shock frame to the fluid velocity in the lab frame directly downstream of the shock. Even though this approach over-estimates the value of p we will still observe the trans-relativistic behavior expected with our simulations.

Once the spectral index has been set, the bounds of the distribution can be initialised. As long as $p > 2$, γ_{\max} can actually be set to infinity. In practice, it just needs to be set to a high enough value such that the contribution of the upper end of the distribution to the flux in the observer frame is above the highest frequency of interest. Since we know the shape of the distribution and have now initialised p and γ_{\max} , we can set γ_{\min} by simply equating the integrated energy from the population (provided we know the fraction ζ of electrons participating to the synchrotron process) with that available for emission calculated from the microphysical parameters ϵ_e and ϵ_B . In practice, ζ , ϵ_e and ϵ_B are ignorance parameters fitted to observations using analytical models (e.g. [Granot & Sari, 2002](#)). Once p has been measured from the afterglow spectral decay and temporal decay using the afterglow closure relations, the remaining microphysical parameters (ϵ_e , ϵ_B) can only be determined without degeneracy if the afterglow is observed in every one of its 4 spectral regimes. For this reason, the microphysics are still poorly constrained with ϵ_B spanning a few orders of magnitude across the GRB population ([Barniol Duran, 2014](#); [Santana et al., 2014](#)). In the simulations presented in this thesis we will set them to sensible values in comparison to those measured in the literature.

Let's place ourselves directly downstream of a shock, in the co-moving frame and drop the prime exponent for readability. Let us remind the reader that the energy distribution of accelerated particles follows:

$$n(\gamma_e) \propto \begin{cases} (\gamma_e)^{-p} & \text{if } \gamma_{\min} < \gamma_e < \gamma_{\max}, \\ 0 & \text{otherwise,} \end{cases} \quad (2.45)$$

The number of electrons contributing to radiation is:

$$n_e = \zeta \rho / m_p. \quad (2.46)$$

Since the bulk of the energy is contained in the electrons close to the lower bound γ_{\min} , we can assume infinity for γ_{\max} (for $p > 2$) and get (Granot et al., 1999):

$$\gamma_{\min} = \frac{p-2}{p-1} \frac{\epsilon_e e}{n_e m_e}. \quad (2.47)$$

Notice that ϵ_B does not influence γ_{\min} . Only the spectral index p and the amount of energy going into particle acceleration ϵ_e impact the position of the lower bound of the population.

2.4.2 Local synchrotron cooling

We now have an initialised micro-physical state directly downstream of shocks. To evolve this state we have to consider how individual electrons lose energy with time. In this regard, equation 1.10 driving the evolution of an electron's Lorentz factor in the fluid frame γ'_e can be re-cast into an advection equation by making use of the continuation equation:

$$\frac{\partial}{\partial t} \left(\frac{\Gamma \rho^{4/3}}{\gamma'_e} \right) + \frac{\partial}{\partial x^i} \left(\frac{\Gamma \rho^{4/3}}{\gamma'_e} v^i \right) = \frac{\sigma_T}{6\pi m_e c} \rho^{4/3} (B')^2. \quad (2.48)$$

The advantage of this formulation is that a hydrodynamics code can simply treat the new quantity $\hat{\gamma} = \rho^{1/3} / \gamma'_e$ as a passive scalar with a source term. To numerically capture the evolution of the accelerated particle population, one would ideally need to split the distribution into a large number of energy bins and advect the bin boundaries during the dynamical evolution. As a first approach, one can simply advect the upper and lower bounds γ_{\max} and γ_{\min} and assume that the distribution remains a power-law throughout the evolution.

2.4.3 Flux reconstruction - linear radiative transfer

Eventually, we have everything at our disposal to carry out the calculation of the local emissivity in the co-moving frame at any point of the fluid. The radiative flux can then be reconstructed in the observer frame by means of a linear radiative transfer approach. Let us first focus on the emissivity.

Assuming an isotropic distribution of electrons, a single average electron of energy γ_e (where we have dropped the primed exponent for legibility) radiates at a characteristic frequency (Rybicki & Lightman, 1979):

$$\nu_{\text{syn}}(\gamma_e) = \frac{3\gamma_e q_e B}{16m_e}. \quad (2.49)$$

The spectral power P_ν follows a 1/3 slope asymptotic behavior below this frequency and decreases exponentially above:

$$P_\nu(\nu) = \frac{4}{3}\sigma_T\beta^2 \frac{\epsilon_e e}{n_e m_e} F\left(\frac{\nu}{\nu_{\text{syn}}(\gamma_e)}\right), \quad (2.50)$$

with

$$F(x) \sim \frac{4\pi}{\sqrt{3}\Gamma(\frac{1}{3})} \frac{x^{1/3}}{2}, \quad x \ll 1, \quad (2.51)$$

$$F(x) \sim \left(\frac{\pi}{2}\right)^{1/2} e^{-x} x^{1/2}, \quad x \gg 1, \quad (2.52)$$

where $\Gamma(z) = \int_0^{+\infty} x^{z-1} e^{-x} dx$ is the gamma function.

As introduced in §1.3.2, we know that the synchrotron emission from a truncated power-law distribution of electrons produces a smoothly connected broken power-law spectrum in the co-moving frame that peaks for $\nu_{\text{min}} = \nu_{\text{syn}}(\gamma_{\text{min}})$. The volumetric spectral emitted power in the co-moving frame (where quantities are denoted with a prime) is simply the convolution of single average electron emissivity with the electron energy distribution, and can be approximated by a broken power-law (Sari et al., 1998; Granot et al., 1999):

$$P'_\nu = \begin{cases} P'_{\nu, \text{max}} \left(\frac{\nu}{\nu'_{\text{min}}}\right)^{1/3}, & \nu < \nu'_{\text{min}}, \\ P'_{\nu, \text{max}} \left(\frac{\nu}{\nu'_{\text{min}}}\right)^{-(p-1)/2}, & \nu > \nu'_{\text{min}}, \end{cases} \quad (2.53)$$

$$\text{with } P'_{\nu, \text{max}} = \frac{4(p-1)}{3p-1} \times n' \sigma_T \frac{4}{3} \frac{B'}{6\pi} \frac{16m_e c}{3q_e}. \quad (2.54)$$

Notice that $P'_\nu(\nu)$ retains the 1/3 slope from the single electron contribution below ν_{\min} which is expected since $\nu_{\text{syn}}(\gamma_e) \propto \gamma_e$.

Up until now, no influence of cooling has been added in this prescription. In the local cooling approach, cooling is implemented by tracking the evolution of the higher bound of the electron population, γ_{\max} . [van Eerten & Wijers \(2009\)](#) compute the emissivity for this local cooling approach. Let us declare another characteristic frequency $\nu_{\max} = \nu_{\text{syn}}(\gamma_{\max})$. While the local spectrum remains approximately unchanged for $\nu < \nu_{\max}$, the introduction of a higher cutoff in the particle population distribution leads to a fast decay in emissivity above ν_{\max} :

$$P'_\nu(\nu) \propto \left(\frac{\nu}{\nu'_{\max}} \right)^{p-1} \exp \left(-\frac{\nu}{\nu'_{\max}} \right), \quad \frac{\nu}{\nu'_{\max}} \gg 1. \quad (2.55)$$

This means that for $\nu \gg \nu_{\max}$ the emissivity is effectively zero because of the exponential term. Calculating the accurate emissivity in the vicinity of the characteristic frequencies involves numerically solving a complex integral. [van Eerten & Wijers \(2009\)](#) tabulate the result and use it to compute the corresponding emissivity from the local fluid state. However, in our applications of the code, we will instead use a simple broken power-law prescription as described above and introduce a sharp cut-off at ν_{\max} . In summary, the numerical volumetric spectral power is thus given by:

$$P'_\nu(\nu) = \begin{cases} P'_{\nu,\max} \left(\frac{\nu}{\nu'_{\min}} \right)^{1/3}, & \nu < \nu'_{\min}, \\ P'_{\nu,\max} \left(\frac{\nu}{\nu'_{\min}} \right)^{-(p-1)/2}, & \nu > \nu'_{\min}, \\ 0, & \nu > \nu'_{\max}, \end{cases} \quad (2.56)$$

where $P'_{\nu,\max}$ is unchanged from eq. 2.53. We address in chapter 4 the potential impact of our approximation when producing light curves and spectra from multidimensional simulations.

Flux reconstruction implies solving the radiative transfer equation:

$$\frac{dI_\nu}{dz} = \epsilon_\nu - \alpha_\nu I_\nu. \quad (2.57)$$

In this equation, the specific intensity I_ν at frequency ν evolves along a path length s following the emissivity coefficient ϵ_ν and extinction coefficient α_ν . Note that for an optically thin medium, α_ν vanishes and the equation is left with only emissivity to integrate on the line of sight (l.o.s).

So this integration can be done from the dynamical output as long as we have a pre-

scription for local emissivity. Let us consider the output of a numerical simulation for which we have dynamical snapshots including micro-physical information at different lab times (time for a static observer with regard to the central engine). We are interested in computing the observed flux for a static observer at a given *observer frequency* ν_{obs} and *observer time* t_{obs} (for a given lab time and location, the corresponding observer time is the arrival time of a photon emitted at this location at this lab time). Since we are considering relativistic flows, the frequency of interest in the frame co-moving with the fluid ν'_{obs} will be related to the observer frequency ν_{obs} following the relativistic Doppler effect valid for all frequencies:

$$\nu' = \nu\Gamma(1 - \beta\mu_\nu) \quad (2.58)$$

where μ_ν is the cosine of the angle between the fluid velocity and direction of the observer, Γ the Lorentz factor the fluid and β its velocity in units of c . For each cell in each snapshot, the arrival time of the photons emitted in by this cell is given by:

$$t_{\text{obs}} = (1 + z)(t - r\mu), \quad (2.59)$$

with t the time in the lab frame, r the radial coordinate in the spherical coordinates system as defined at the beginning of this chapter, μ the cosine of the angle ϑ between \vec{r} and the line of sight, and z the redshift of the source. A schematic representation of these quantities is given in figure 2.9. Careful, $\vartheta \neq \theta$ in the general case, with $\vartheta = \theta$ only when the observer is aligned with the axis $\{\theta = 0\}$ in the spherical system of coordinates used for the dynamical simulations. Assuming that the medium is optically thin, we can eventually express the observed spectral flux density as:

$$F_\nu(\nu, t_{\text{obs}}) = \frac{1 + z}{4\pi d_L^2} \int_0^{2\pi} d\varphi \int_{-1}^1 d\mu \int_0^\infty r^2 dr \frac{P'_{\nu'}(r, t_{\text{obs}} + r\mu, \varphi)}{\Gamma^2(1 - \beta\mu)^2}. \quad (2.60)$$

In this expression we have used φ instead of ϕ to make the distinction with the spherical coordinate system used in the simulations which is not a priori aligned. From this expression, two different approaches can be taken, both of which are subsequently applied in chap. 3 and chap. 4, respectively.

The first approach can only be applied in an optically thin medium and consists in summing over the contributions of all the snapshots for the whole light curve for a given ν_{obs} . We first split the target light-curve in a number of bins. We then compute the arrival time of each cell, and simply add the contribution from the integrand in the in each bin. This approach has the advantage of being very straightforward to implement. However, absorption along the photon paths cannot be implemented with

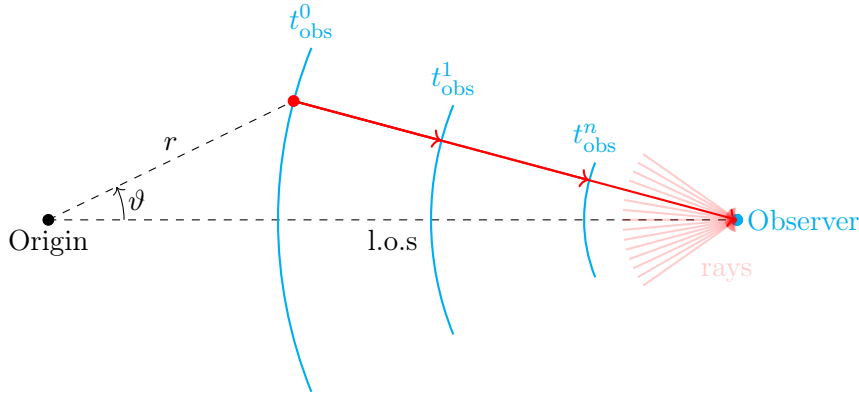


Figure 2.9: Schematic representation of the linear flux integration process. For each observer time, the emissivity is computed from each snapshot at the intersections between pre-specified rays and the EDS (curved blue surfaces). This schematic representation is valid $\forall\varphi$. Again we caution the reader that the system of coordinates **is not** the one used in the dynamical simulation (the simulation could actually be carried out in Cartesian or cylindrical coordinates too).

in this context.

Even though we do not include the effects of synchrotron self-absorption (SSA) in our simulations yet⁹, we intend for future work to include its effects, and we make use in chapter 4 of the code from [van Eerten & Wijers \(2009\)](#) which uses a linear radiative transfer approach which we describe here. Figure 2.9 gives a schematic representation. In this approach, the domain is traversed by a number of rays converging on the observer and covering the simulation domain. For each snapshot (and corresponding lab time), it is possible to define and *equidistant surface* (EDS). For a given lab time t and observer time t_{obs} , the EDS equation is obtained by re-writing eq. 2.59:

$$r = \frac{1}{\mu} \left(t - \frac{t_{\text{obs}}}{1+z} \right), \quad \mu \neq 0. \quad (2.61)$$

All the photons emitted from this surface will reach the observer at the same specified t_{obs} . The emissivity is evaluated at the intersection between this EDS and the collection of rays. The snapshots are then considered in increasing order of lab times and the flux is integrated along the rays before the resulting contributions from each rays are summed up. This approach presents the advantage of allowing for the implementation of absorption along each ray which we will not detail in this thesis.

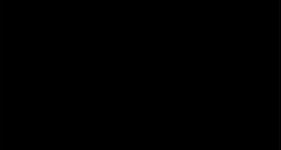
⁹SSA will be discussed in more detail in chapter 6 and will be included in future simulations

Late X-ray Flares from the
Interaction of a Reverse Shock with
a Stratified Ejecta in GRB
Afterglows: Simulations on a
Moving Mesh

Eliot H. Ayache, Hendrik J. van Eerten, Frédéric Daigne (2020)
MNRAS 495 (3), 2979–2993.

*Aujourd'hui, le monde est devenu trop complexe pour se contenter d'approximations,
d'explications floues, ou de remarques vagues.*

— JEAN-PAUL DUBOIS, Tous les hommes n'habitent pas le monde de la même façon

This declaration concerns the article entitled:			
Late X-ray Flares from the Interaction of a Reverse Shock with a Stratified Ejecta in GRB Afterglows: Simulations on a Moving Mesh			
Publication status (tick one)			
Draft manuscript <input type="checkbox"/> Submitted <input type="checkbox"/> In review <input type="checkbox"/> Accepted <input type="checkbox"/> Published <input checked="" type="checkbox"/>			
Publication details (reference)	Ayache et al. 2020, Monthly Notices of the Royal Astronomical Society, Volume 495, Issue 3, July 2020, Pages 2979–2993, https://doi.org/10.1093/mnras/staa1397		
Copyright status (tick the appropriate statement)			
I hold the copyright for this material <input checked="" type="checkbox"/> Copyright is retained by the publisher, but I have been given permission to replicate the material here <input type="checkbox"/>			
Candidate's contribution to the paper (provide details, and also indicate as a percentage)	<p>This project constituted the starting point of my Ph.D. studies. As such, I was the primary person working on the project full-time. It is not part of any other degree attainment.</p> <p>Formulation of ideas: I formulated my own ideas for the progress of the project, aided by useful input during my supervisory meetings with Dr. Hendrik van Eerten. (65%)</p> <p>Design of methodology: The main contribution of the paper is the confirmation of the viability of the reverse shock scenario for GRB afterglow flares. I designed the setups used to put the scenario to the test. (65%)</p> <p>Experimental work: My contributions included: writing the 1D Lagrangian dynamical simulation code, writing the radiative transfer code for synthetic light curve generation. I carried out testing of both of these codes. I set up and ran the simulations, post-processing of the output and analysis of the results. (90%)</p> <p>Presentation of data in journal format: I designed all the figures and wrote the manuscript draft, whilst benefitting from feedback by Dr. Hendrik van Eerten. I then received further comments from collaborators, which I implemented. (90%)</p>		
Statement from Candidate	This paper reports on original research I conducted during the period of my Higher Degree by Research candidature.		
Signed		Date	08/07/2021

Preamble

In this chapter I present the first application of the methods described in chapter 2. The objective here is to tackle from a new angle a long-standing question in GRB afterglow research, the origin of flares, made possible thanks to the benefits of the moving-mesh and local cooling approaches combined. Indeed, this particular problem requires the ability to model complex dynamics and identify multiple synchrotron emission sites in a relativistic outflow. With the goal of providing answers on the mechanism responsible for such flares, we use this project to highlight the benefits of the moving mesh and local cooling approaches in a simple one-dimensional setup. This is the first extensive study of the validity of the reverse shock flaring scenario which was made possible by the first implementation of local cooling on a moving mesh.

In the context of this thesis, the presentation of this work is also a great opportunity to give a more intuitive understanding of GRB afterglow dynamics and emission processes, and the workings of the moving mesh and local cooling methods, in a simple one-dimensional setup, before presenting multi-dimensional studies in chapter 4. Since this work was published in [Ayache et al. \(2020\)](#), I choose to report in the rest of the chapter the contents of the paper as published, making this chapter entirely self-contained. However, some of the introductory material in the paper has already been presented in chapter 2. As such, the reader will encounter repetitions in §3.2.1 and §3.4.1 when presenting these methods in the 1D case, which they might choose to skim over. At the end of the paper, I provide a additional information which was not published as well as a general conclusion to this paper in the context of the thesis (§3.8).

Abstract

Late activity of the central engine is often invoked in order to explain the flares observed in the early X-ray afterglow of gamma-ray bursts, either in the form of an active neutron star remnant or (fall-back) accretion onto a black hole. However, these scenarios are not always plausible, in particular when flares are delayed to very late times after the burst. Recently, a new scenario was proposed that suggests X-ray flares can be the result of the passing of a long-lived reverse shock through a stratified ejecta, with the advantage that it does not require late-time engine activity. In this work, we numerically demonstrate this scenario to be physically plausible, by performing one dimensional simulations of ejecta dynamics and emission using our novel moving-mesh relativistic hydrodynamics code. Improved efficiency and precision over previous work enables the exploration of a broader range of setups. We can introduce a more physically realistic description of the circumburst medium mass density. We can also locally trace the cooling of electrons when computing the broadband emission from these setups. We show that the synchrotron cooling timescale can dominate the flare decay time if the stratification in the ejecta is constrained to a localised angular region inside the jet, with size corresponding to the relativistic causal connection angle, and that it corresponds to values reported in observations. We demonstrate that this scenario can produce a large range of observed flare times, suggesting a connection between flares and initial ejection dynamics rather than with late-time remnant activity.

3.1 Introduction

Gamma-Ray Bursts (GRBs) are the most luminous explosions in the Universe. They are the result of the collapse of a massive star (long GRBs) (Woodsley, 1993; MacFadyen & Woodsley, 1999) or of the merger of two Neutron Stars (NS) or a NS with a black hole (Short GRBs) (Eichler et al., 1989; Mochkovitch et al., 1995), a scenario spectacularly confirmed three years ago with the joint detection of GW170817 and GRB170817a (Abbott et al., 2017a,b; Goldstein et al., 2017; Savchenko et al., 2017; Troja et al., 2017; Hallinan et al., 2017). These explosions give rise to a collimated ultra-relativistic jetted outflow typically observed on-axis. In the first milliseconds to a few seconds, an initial burst of gamma-rays (the prompt emission) can be observed, followed after a few hundred seconds by an afterglow (at larger wavelengths). The afterglow, originally peaking at X-ray energies, decreases in luminosity and frequency with time until it disappears.

The launch of the *Neil Gehrels Swift* observatory (Gehrels et al., 2004) in 2004, ded-

icated to GRB detection and early X-ray/optical afterglow observations, showed the great variability in the light curve at early times. For 15 years now, *Swift* has been detecting GRBs and measuring the properties and spectra of their early X-ray afterglow at a rate of around 90 detections a year (Evans et al., 2009), revealing flaring and re-brightening behaviors. These flares are detected in about a third of GRBs (Burrows et al., 2005b; Falcone et al., 2007; Chincarini et al., 2010; Margutti et al., 2011; Yi et al., 2016) and display a characteristic shape with a sharp jump in luminosity followed by a smoother decay, eventually going back to the original luminosity level (Chincarini et al., 2007). They can happen at any time during the afterglow, from 10^2 to 10^5 s after the prompt emission, growing longer with time following $\Delta t_{\text{flare}}/t_{\text{flare}} \sim 0.1 - 0.3$ (e.g. Burrows et al., 2005b). Margutti et al. (2011) showed that the average isotropic equivalent energy of flares also decreased with time as $E_{\text{iso,flare}} \propto t_{\text{obs,flare}}^{-1.7}$, albeit with a very large scatter.

Several works have shown that the external forward shock (FS) cannot produce flares with the correct timescale and flux variability (Ioka et al., 2005; Nakar & Granot, 2007; van Eerten et al., 2009), and the currently accepted paradigm involves late-time activity of the central engine (Burrows et al., 2005b; Chincarini et al., 2010; Margutti et al., 2011) or late-time fallback accretion onto the remnant (King et al., 2005; Perna et al., 2006; Proga & Zhang, 2006; Lee et al., 2009; Cao et al., 2014). This scenario, though, requires the central engine to be active on the same timescale in the lab frame as that of the occurrence of the flare (Kobayashi et al., 2007), implying that the engine has not yet collapsed to a black hole in cases where fallback accretion is unlikely to play a role as well (e.g. at very late timescales). It also requires this surge of activity to obey the constraint $\Delta t/t \sim 0.1$, putting an intrinsic constraint on the variability timescale of the activity of the central engine up to very late times. Consequently, having a model that relaxes the constraints on the central engine is a step towards better understanding of late-time variability in X-ray afterglows.

In order to relieve the constraints on the central engine, Hascoët et al. (2017) proposed an alternate mechanism in which flares can arise from the interaction of a long-lived reverse shock (RS) with a stratified ejecta produced by a gradual and non-monotonic shutdown of the central engine right after the initial ejection phase, and tested this scenario using a ballistic model. Indeed, Uhm & Beloborodov (2007) and Genet et al. (2007) showed that the emissivity of the RS can dominate over that of the FS. A dominating RS is also able to reproduce most of the other canonical features of the early X-ray afterglow (Uhm et al., 2012; van Eerten, 2014b). Lamberts & Daigne (2018) (hereinafter LD18) further investigated this approach by running complete hydrodynamical simulations using the relativistic version of the adaptive mesh refinement

(AMR) hydrodynamics code RAMSES (Teyssier, 2001; Lamberts et al., 2013). They were able to reproduce in principle flaring behavior and validate the ballistic model of Hascoët et al. (2017). But even with using a moving grid where cells were deleted behind the ejecta to be reused upstream, they were limited by the fixed resolution of their numerical hydrodynamics code. As a result they were constrained to very dense uniform cirumburst environment (density $n_0 \sim 10^3 \text{ cm}^{-3}$). Additionally, they were not able to directly trace the impact of synchrotron cooling on electron populations as fluid zones advect away from the shocks. Finally, the study was limited in the range of observer times for flares it could demonstrate.

In this work, we expand the approach of LD18 to more realistic dynamical initial conditions. We use a newly developed moving mesh special relativistic hydrodynamics code that allows for improved numerical accuracy and computational efficiency. We improve the radiative prescription by implementing local cooling, by tracing the electron Lorentz factors bracketing the accelerated electron population through the fluid (Downes et al., 2002; van Eerten et al., 2010b).

The hydrodynamics code we used and the simulation setup are described in §3.2. The dynamical evolution is described in §3.3. We explain our emission prescription and discuss flare production in §3.4.

3.2 Numerical Methods

3.2.1 Relativistic hydrodynamics on a moving mesh

The simulations were ran using our own numerical dynamics code (see appendix 3.7.1 for code validation). Similarly to the codes from Kobayashi et al. (1999), Daigne & Mochkovitch (2000) and Duffell & MacFadyen (2011), our code uses a special relativistic hydrodynamics (SRHD) finite-volume Godunov prescription on a moving mesh in spherical coordinates (r, θ, φ) , solving the following system of conservation equations:

$$\partial_t \mathbf{U} + \nabla \mathbf{F}(\mathbf{U}) = \mathbf{S}, \quad (3.1)$$

where \mathbf{U} and $\mathbf{F}(\mathbf{U})$ are the vector of conserved variables and the corresponding flux vector, respectively and \mathbf{S} is the source term. \mathbf{U} and $\mathbf{F}(\mathbf{U})$ are given by:

$$\mathbf{U} = \begin{pmatrix} D \\ m \\ E \end{pmatrix} \equiv \begin{pmatrix} \rho\Gamma \\ \rho h\Gamma^2 v \\ \rho h\Gamma^2 - p \end{pmatrix} \quad \begin{array}{l} \text{(Rest-mass density)} \\ \text{(Momentum)} \\ \text{(Energy)} \end{array}, \quad (3.2)$$

$$\mathbf{F}(\mathbf{U}) = \begin{pmatrix} Dv \\ mv + p \\ m \end{pmatrix}, \quad (3.3)$$

where the primitive variables ρ, v, p are the rest-mass density, the fluid velocity and the fluid pressure in the comoving frame, respectively, h is the specific enthalpy, Γ the Lorentz factor of the fluid, and the speed of light $c = 1$. The spherical coordinates formulation of these equations includes a non-zero source term $\mathbf{S} = (0, 2p/r, 0)^T$.

The system of equations is closed using an ideal monoatomic fluid equation of state:

$$p(\rho, \epsilon) = \rho\epsilon(\gamma - 1), \quad (3.4)$$

where ϵ is the specific internal energy density, and γ the adiabatic index of the fluid set to $\gamma = 4/3$ in the ultra-relativistic case.

The 1D version of the code involves a grid of N cells $(\mathcal{C}_i)_{i \in \llbracket 0, N-1 \rrbracket}$ along the r direction, for which the cell-centered vector of conserved variables is written \mathbf{U}_i , and $N - 1$ interfaces $(\mathcal{I}_j)_{j \in \llbracket 1/2, N-1-1/2 \rrbracket}$ between these cells. As in any Godunov approach, computing the evolution of the fluid involves determining the fluxes at each interface by solving a Riemann problem at a given time. The code is built on an Arbitrary Lagrangian-Eulerian (ALE) approach where the interfaces are allowed to move at arbitrary velocity (provided that it does not exceed the speed of light c). We set this velocity to the velocity of the contact discontinuity in the Riemann fan at each interface. This makes the code purely Lagrangian. The fluxes are then computed by solving the Riemann problem in the frame of reference of the interface. We then transform these fluxes to the lab frame before updating the cell averages.

We use a HLLC Riemann solver (Harten et al., 1983; Mignone & Bodo, 2006) and linear spatial reconstruction with a minmod slope limiter. Time integration is done using a third order Runge-Kutta prescription which has the advantage of being total variation diminishing, with a Courant-Friedrich-Lewy condition of 0.2.

The moving-mesh approach introduces the need for re-gridding. Cells that become too small will hinder computational efficiency by driving down the time-step, while we might lose crucial resolution in other areas because of expanding cells. The former issue is addressed by merging neighbouring cells while the latter is solved by splitting cells following a linear interpolation with a minmod slope limiter to ensure conservation. Re-gridding criteria are twofold: first, a maximum and minimum cell aspect ratio¹

¹The aspect ratio (a.r.) is the ratio of the spatial extent of the cell in the first dimension over the

constrain resolution for a given radius (a cell gets refined when its aspect ratio exceeds the upper bound, and de-refined when it drops below the lower bound); second, we enforce boundaries on primitive variables spatial second derivatives in order to increase the resolution of regions with small-scale variability. Mesh regularity is enforced by splitting any cell becoming more than three times as big as one of its neighbours, provided that the two previous criteria are respected. All these parameters can be updated on the fly when experimenting with new setups, by taking advantage of the code to start from any previous data dump. The re-gridding parameters we used in our simulations are described in §3.2.2.

Computational efficiency in the GRB setup is further improved by introducing a moving outer boundary traveling at the speed of light ahead of the forward shock. The right-most cell \mathcal{C}_{N-1} is split if $\Delta r_{N-1} > 2\Delta r_0 \times \frac{r_{N-1}}{r_{N-1}(t=0)}$, thus resulting in a dynamically produced logarithmic grid ahead of the FS.

We assess the code accuracy and stability on standard test setups for which we are able to compute the exact solution and show that we achieve second order convergence for smooth flows while conserving accurate shock descriptions and evolution. The tests and the associated results are described in detail in appendix 3.7.1. As a result, we can confidently use the results of the dynamical simulations in more elaborate cases.

The computation of radiative emission relies on shock detection in the dynamics of the blast-wave. We choose to use a modified version of the shock detector used in LD18 based on the method introduced in Rezzolla et al. (2003a) and described in Zanotti et al. (2010), that evaluates the nature of the waves in the Riemann fan for all interfaces of the grid based on the calculation of limiting relative velocities \tilde{v}_{12} . These waves can either be rarefaction waves or shocks. Physical shocks will be signaled by shocks waves emerging from these interfaces with relative velocity $v_{12} > \tilde{v}_{12}$. In practice, we place shocks at the locations of local maxima of $S = v_{12} - \tilde{v}_{12}$. This method, however, can lead to the spurious detection of weak shocks. LD18 address this issue by smoothing S . The intense re-gridding used in our approach introduces occasional additional spurious variability in the value of S for which the smoothing approach is unsatisfying. However, the 1D aspect of our simulation makes the implementation of the full method from Rezzolla et al. (2003a) rather straightforward. This method, which we implemented successfully, tightens the shock detection threshold by also taking into account the limiting relative velocity corresponding to the 2-shock Riemann fan. The calculation of the limiting relative velocities is described in appendix 3.7.2, along with the treatment

spatial extent in the second dimension (a.r. = dx/dy in cartesian coordinates (x, y, z) , a.r. = $dr/rd\theta$ in spherical coordinates (r, θ, φ)).

of weak shocks.

3.2.2 Simulation setup

Our approach follows that of [LD18](#), that we describe in this section before introducing the improvements we carried out. We emulate the behavior of the central engine during ejection by setting up a slab of ejecta, shortly after breakout, in which we set up a variable initial radial velocity profile. We will consider a constant power of the central engine during the ejection phase, meaning that faster material will also be more diffuse. A gradual shutdown can then be represented by slower material towards the back of the ejecta. The chaotic aspect of that shutdown is tackled by introducing non-monotone radial variability of the velocity in this region of the fluid.

In this approach, the initial state is characterized by a cold ejecta with variable Lorentz factor radial profile $\Gamma(r)$. The total isotropic equivalent energy of the blast wave is set to $E = 10^{53}$ erg and the initial ejection happens between $t_0 = 0$ s and $t_w = 100$ s, bringing the constant isotropic power of the ejection to $\dot{E} = 10^{51}$ erg.s⁻¹. The ejecta being cold, the thermal pressure p is set by $\eta = p/\rho c^2 = 10^{-3}$, where the rest-mass density profile is expressed as a function of \dot{E} and $\Gamma(r)$ as follows:

$$\rho(r) = \frac{\dot{E}}{4\pi r^2 v(r) \Gamma^2(r) c^2 \left[1 + \eta \left(\frac{\gamma}{\gamma-1} - \frac{1}{\Gamma^2(r)} \right) \right]}, \quad (3.5)$$

where $v(r)$ is the velocity of the fluid.

Until the starting time of the dynamical simulation $t_{\text{ini}} = 200$ s, the ejecta is assumed to follow a ballistic evolution, allowing to compute the corresponding positions of the external and internal edges of the ejected shell, respectively R_0 and R_Δ (with Lorentz factors Γ_0 and Γ_Δ)², such that:

$$R_0 = \left(1 - \frac{1}{\Gamma_0^2} \right)^{1/2} c(t_{\text{ini}} - t_0), \quad (3.6)$$

$$R_\Delta = \left(1 - \frac{1}{\Gamma_\Delta^2} \right)^{1/2} c(t_{\text{ini}} - t_w - t_0). \quad (3.7)$$

Since \dot{E} is set to a constant value and the ejecta is cold, the initial radial profile can be fully described by a single physical quantity. Here we follow [LD18](#) and set the value of the Lorentz factor $\Gamma(r)$. The shell will be characterized by an outer flat head region with Lorentz factor Γ_0 and a region of decreasing velocity (the tail region) all the way

²Careful, R_Δ here should not be confused with the reverse shock crossing radius defined in §1.3.1.

to engine shutdown at Lorentz factor Γ_Δ . The initial Lorentz factor profile is given by:

$$\Gamma(r) = \begin{cases} 1 & \text{if } 0 < r \leq R_\Delta, \\ [\Gamma_\Delta + (\Gamma_0 - \Gamma_\Delta)x][1 + f(x)] & \text{if } R_\Delta < r \leq r_\alpha, \\ \Gamma_0 & \text{if } r_\alpha < r \leq R_0, \\ 1 & \text{if } R_0 < r, \end{cases} \quad (3.8)$$

with,

$$x = \frac{r - R_\Delta}{r_\alpha - R_\Delta}, \quad (3.9)$$

where $r_\alpha = R_\Delta + \alpha(R_0 - R_\Delta)$ sets the limit between the head and tail regions of the ejecta (α is the ratio of tail to head). $f(x)$ is the profile of the perturbation responsible for the stratification of the ejecta and emanating from a chaotic shutdown of the central engine. In [LD18](#), f is given by:

$$f(x) = A \sin(2\pi x), \quad A \in [0, 1], \quad (3.10)$$

where A is the amplitude of the perturbation.

We run SRHD simulations for various values of A and α (reported in table 3.1), with the corresponding profiles drawn in figure 3.1. These values are the same as in [LD18](#) to allow for comparison. Run1 is a test of our setup for a canonical reverse shock (RS) propagating inside a homogeneous shell of ejecta. Run2 simulates the propagation of a long-lived RS (LLRS) with a significant "tail" in the ejecta, corresponding to the gradual shutdown of the central engine. Run3 produces a flare as a result of its non-monotonic tail (corresponding to non-monotonic central engine shutdown) that produces stratification in the ejecta. The initial profile parameters are summarized in table 4.4.

The grid has outflow boundary conditions on both sides. The choice of AMR criteria is driven by both the need for high resolution downstream of the shocks, as we expect very short synchrotron cooling timescales (see §3.4.1), and by the need for computational efficiency. These criteria will be different for the ejecta, the external medium, and the material behind the ejecta. For this reason we track different regions of the fluid using a passive scalar. The upper and lower limits on aspect ratio for each part of the fluid are reported in table 3.3. We find a good balance between FS resolution and efficiency for a higher bound decreasing with r in the circumburst medium and adjust the power-law index manually. We also add in this part of the flow a de-refinement criterion based

Run	α	A	Description
run1	0	0	homogeneous
run2	0.5	0	tail
run3	0.5	0.6	perturbed

Table 3.1: Run Parameters

Parameter	Notation	Value	Unit
Injected kinetic power	\dot{E}	10^{51}	erg/s
Burst Lorentz Factor	Γ_0	100	
Tail Lorentz Factor	Γ_Δ	10	
Burst starting time	t_0	0	s
Duration of ejection	t_w	100	s
Initial time of simulation	t_{ini}	200	s
External medium number density	n_0	1	cm^{-3}
Ratio between pressure p and ρc^2	η	10^{-3}	

Table 3.2: Initial parameters

on the derivative of the synchrotron cooling rate downstream of the FS to improve efficiency that we also adjust manually.

We run simulations starting with 1200 cells in the ejecta and 100 in the external medium. Depending on the setup, the total number of cells at the end of the simulations is usually contained between 3000 and 5000.

3.3 Hydrodynamical evolution

In this section, we comment on the behavior of the fluid resulting from the various setups we introduced. The results are in accordance with [LD18](#) and we refer the reader to this paper for a more detailed discussion of the dynamics.

The dynamical evolution of run1 ("homogeneous shell") is reported in fig. 3.2. In order to make dynamical evolution figures more easily readable, we plot physical quantities as a function of cumulated mass M defined as follows:

$$M(r) = \frac{1}{M_0} \int_{R_\Delta}^r 4\pi\rho\Gamma(r')^2 dr', \quad (3.11)$$

Fluid material	Lower bound	Higher bound
ejecta	10^{-10}	5×10^{-4}
circumburst medium	10^{-9}	$5 \times 10^{-5} \times (r/R_0)^{-0.1}$

Table 3.3: Adaptive mesh refinement aspect ratio criteria

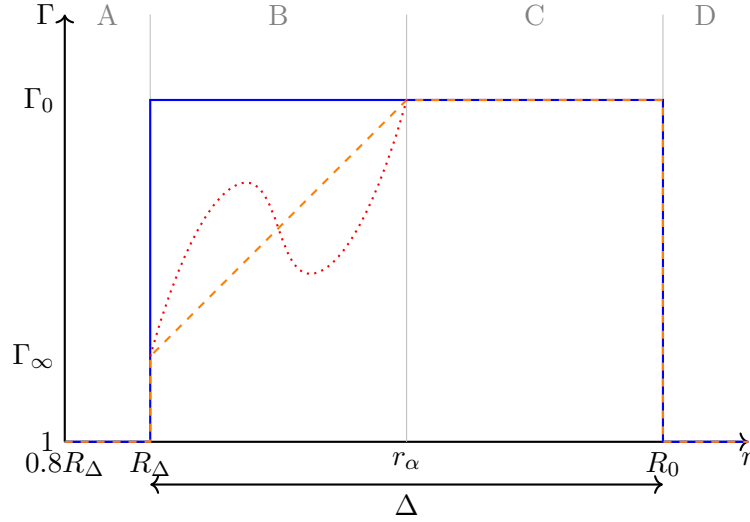


Figure 3.1: Schematic representation of the initial profile of the Lorentz factor Γ as a function of the radius r . The solid blue line represents the *pulse* profile with constant Γ throughout all the ejection. The dashed orange line represents the case with a tail of Lorentz factor Γ (progressive shutdown of the central engine). The dotted red line is the case with a non-monotonic progressive shutdown, expected to lead to the formation of internal shocks in the tail.

where M_0 is the initial total mass of the ejecta. As expected, one can observe the formation of a reverse shock propagating leftwards in the fluid frame (blue curve at 1.5×10^5 s), with a crossing time of $t_{\text{cross}} < 3.50 \times 10^6$ s. In their simulations, [Lamberts & Daigne](#) were limited in the spatial scale they could cover and thus discarded the tail of the ejecta as the shocked medium grew in mass so as to keep a constant total simulated mass. Thanks to our numerical prescription, we are able to keep all the initial material in the simulation. This additional material at the back of the ejecta is responsible for the formation of a spurious internal reverse shock, visible here at $M \sim 0.05$, $t_{\text{lab}} = 5.15 \times 10^6$ s (green curve), after the external reverse shock has crossed the ejecta. After deceleration, a forward shock starts to form ahead of the ejecta ($M > 1$) as the blast wave sweeps up some circumburst medium material.

Fig. 3.3 shows the dynamical results for run2 ("decreasing tail"). The initial profile of velocity increasing with r is responsible for the tail expanding, as is visible in the density profile (lower pane) where the density decreases in the tail ($M \lesssim 0.7$) as the blast wave moves to larger radii. This causes the RS to take longer to traverse the ejecta, thus giving rise to a long-lived reverse shock. Indeed, the crossing time is increased to $t_{\text{cross}} > 1.3 \times 10^7$ s in this case, thus giving rise to a long-lived RS.

The results of run3 are shown in fig. 3.4. The important feature in this run is the presence of a non-monotonic radial Lorentz factor profile in the tail of the ejecta, akin

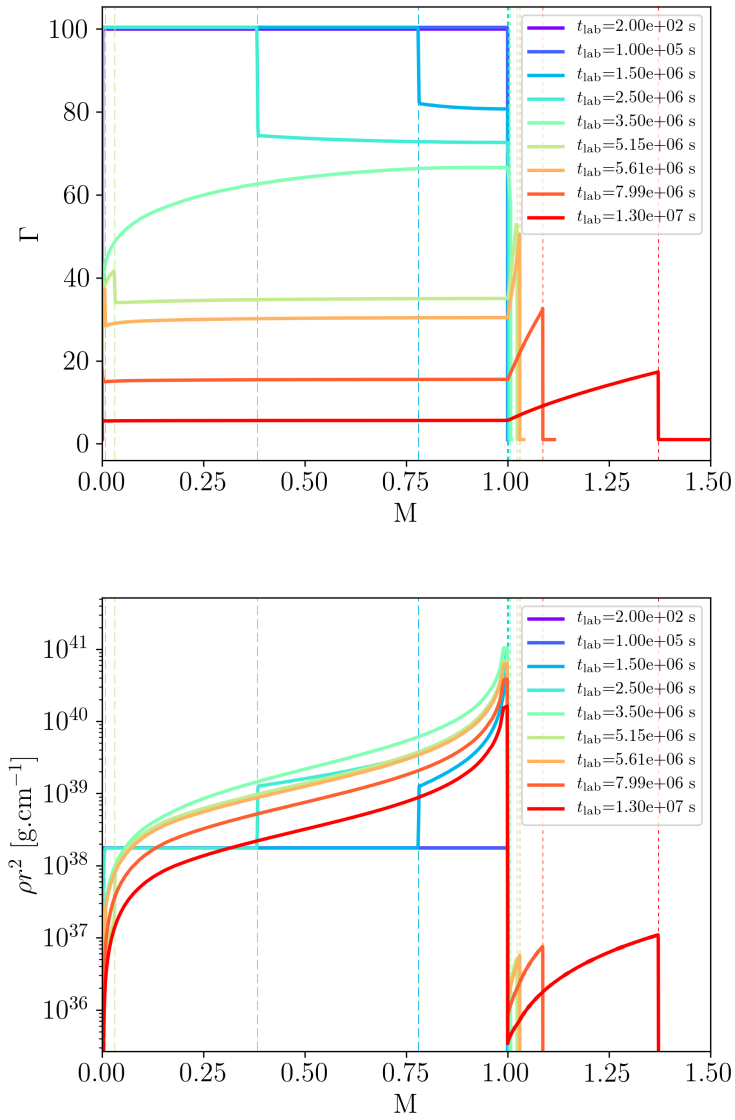


Figure 3.2: Lorentz factor (top) and density (bottom) as a function of cumulative mass for run1 (homogeneous ejecta). Dashed vertical lines show the positions of reverse shocks and dotted vertical lines the positions of forward shocks.

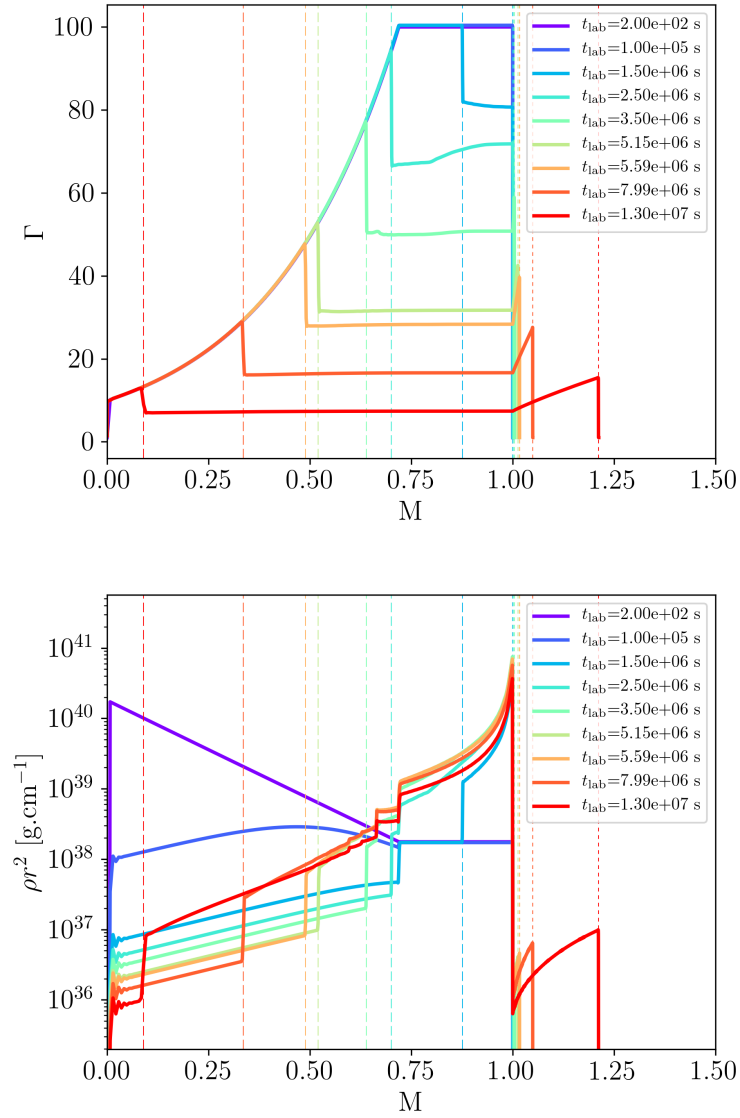


Figure 3.3: Lorentz factor (top) and density (bottom) as a function of cumulative mass for run2 (gradual shut down of the central engine leading to a region of decreasing Lorentz factor at the back of the ejecta). Dashed vertical lines show the positions of reverse shocks and dotted vertical lines the positions of forward shocks.

to the ballistic simulations of [Hascoët et al. \(2017\)](#), and run 4 in [LD18](#). The faster material at smaller radii eventually catches up with the slower material ahead, creating a first internal forward shock / reverse shock system (IFS/IRS) that delimits the boundaries of a dense shell of ejecta, with significantly higher rest-mass density (dark blue curve at $t_{\text{lab}} = 1.00 \times 10^5$ s). The shocked material displays a centered spike in density that delimits the position of the contact discontinuity between "forward-shocked" and "reverse-shocked" material. This spike is not visible in the simulations of [LD18](#), probably because of a lack of sufficient resolution, and is the result of the compression of the fluid ahead of shock formation because of the smooth velocity gradient in the initial setup. A similar feature has been predicted by numerical Lagrangian simulations and analytical calculations ([Daigne & Mochkovitch, 2000](#); [van Eerten, 2014a](#), respectively) and we can recover it here thanks to the moving-mesh approach. As the external RS enters the dense shell, it is partially reflected into a forward shock (light green curve, $t_{\text{lab}} = 5.15 \times 10^6$ s) that eventually catches up with the external FS (yellow curve, $t_{\text{lab}} = 5.59 \times 10^6$ s). As the RS progresses through the dense shell, it eventually interacts with the contact discontinuity density spike leading to the formation of an additional reflected forward shock that will eventually catch up with the previous one and strengthen it. We show however in §3.4.4 that this feature does not influence the general shape of the light-curve and thus validate the results from [LD18](#). Subsequently, the RS keeps traveling through the dense shell until it eventually leaves it before crossing the ejecta altogether for $t_{\text{cross}} > 1.3 \times 10^7$ s.

All three setups display dynamical features similar to [LD18](#), thus providing additional support to the idea that flares can be produced from the interaction of a LLRS with a stratified ejecta. §3.4 focuses on the radiative prescription necessary to produce synthetic light-curves, and shows how run3 can be responsible for flaring behavior in GRB afterglows, while providing a better understanding of the spectral evolution of flares associated with this setup, thanks to the local cooling approach we implemented.

3.4 Emission - Flares from a LLRS in a stratified ejecta

3.4.1 Radiative prescription - local cooling

Afterglow emission can be modeled by synchrotron radiation from electrons accelerated in shocks. In our situation, we can neglect self-absorption as we are only interested in the X-ray and optical afterglow. We ignore inverse Compton scattering for the sake of simplicity. We approximate the population of accelerated electrons by a truncated

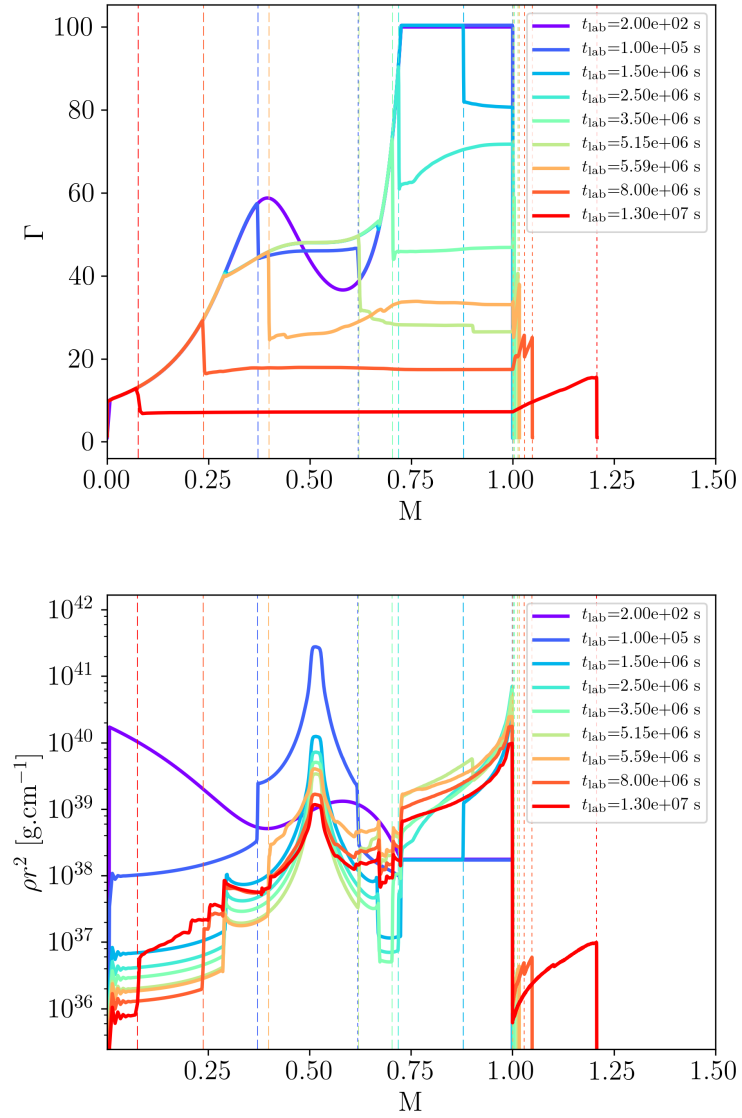


Figure 3.4: Lorentz factor (top) and density (bottom) as a function of cumulative mass for run3 (chaotic shut down of the central engine leading to a region of negative velocity gradient in the trail of the ejecta. Dashed vertical lines show the positions of reverse shocks and dotted vertical lines the positions of forward shocks.)

power-law:

$$n'(\gamma'_e) = \begin{cases} (\gamma'_e)^{-p} & \text{if } \gamma_m < \gamma'_e < \gamma_M, \\ 0 & \text{otherwise,} \end{cases} \quad (3.12)$$

with $p = 2.3$ and γ_m the energy of the bulk of the population, and γ_M the evolving cut-off due to localised electron cooling, where the $'$ notation denotes quantities in the fluid frame. We consider that a fraction $\zeta = 0.1$ of electrons present in the fluid are accelerated by any shock and that a fraction $\epsilon_e = 0.1$ of the internal energy density $e = \rho\epsilon$ is transferred to these electrons. Similarly, a fraction $\epsilon_B = 0.1$ of the internal energy density powers the tangled magnetic field needed for synchrotron radiation. The choice of $\zeta = 0.1$ differs from the canonical $\zeta = 1$ commonly used. However, since we neglect in this work synchrotron self-absorption, as well as the limited contribution to radiation from the thermalised non-accelerated electron population [Ressler & Laskar \(2017\)](#), ζ is a degenerate parameter, meaning that identical results can be obtained for a different value of ζ by adjusting \dot{E} , n_0 , ϵ_e and ϵ_B ([Eichler & Waxman, 2005](#)). Moreover, particle-in-cell simulations suggest that ζ is most likely closer to 0.01 than unity ([Spitkovsky, 2008](#)). In the simulations presented later, $\zeta = 0.01$ led to fast-cooling spectra which made interpretation less straightforward and we chose $\zeta = 0.1$ instead. Electron cooling is driven by the adiabatic expansion and synchrotron cooling as shown by the following equation:

$$\frac{d\gamma'_e}{dt'} = -\frac{\sigma_T(B')^2}{6\pi m_e c} (\gamma'_e)^2 + \frac{\gamma'_e}{3\rho} \frac{d\rho}{dt'}, \quad (3.13)$$

with σ_T the Thomson cross-section, m_e the electron mass and $B' = \sqrt{8\pi\epsilon_B e}$ the magnetic field intensity. γ_m and γ_M follow this evolution. Since, our setups involve fast-cooling populations of electrons for which synchrotron losses need to be taken into account, we cannot compute γ_m a posteriori and we apply the same method for the calculation of the local evolution of γ_m and γ_M . Most works implement the global cooling approximation ([Granot & Sari, 2002](#); [van Eerten et al., 2010a](#)) that is based on assumptions on the dynamics downstream of the shock, or assume a single uniform electron population across the shocked fluid. The complex dynamics of our system prevents us from using this approximation as some regions of the fluid will be shocked multiple times. In their work, [LD18](#) approximate the cooling frequency by assuming it decreases with the dynamical timescale in the co-moving frame of the shocked region which approximates the time since a fluid parcel has been shocked. Our improved dynamical numerical scheme actually allows us to directly trace the local numerical evolution of γ_m and γ_M , as long as we allow the resolution to increase sufficiently

downstream of the shocks thanks to the compression of the mesh. Indeed, equation 4.17 can be rewritten in the following advection equation form (Downes et al., 2002; van Eerten et al., 2010b):

$$\frac{\partial}{\partial t} \left(\frac{\Gamma \rho^{4/3}}{\gamma_e'} \right) + \frac{\partial}{\partial x^i} \left(\frac{\Gamma \rho^{4/3}}{\gamma_e'} v \right) = \frac{\sigma_T}{6\pi m_e c} \rho^{4/3} (B')^2. \quad (3.14)$$

The two boundaries of the electron population are thus simply handled as tracers during the hydrodynamical evolution. We reset their value every time a cell is shocked. In theory, the value of γ_M directly downstream of a shock set by the acceleration timescale and can be taken to be infinity for sufficiently large p . In practice, we set γ_M to 10^8 when crossed by a shock, such that the induced frequency cutoff for the radiation from each individual shock is placed above 1keV in the observer frame. γ_m is initialised by normalising the integrated energy of the electron population by the total available energy.

The improved resolution downstream of the shocks, along with the fact that grid zones are co-moving with the fluid lift the constraints linked to the very short cooling time of the accelerated electrons and enables the implementation of local cooling with accurate treatment of new source term on the right-hand side of eq. 4.18.

Figure 3.5 shows the values of γ_M as a function of M during the propagation of the reverse shock in the ejecta for run3 (perturbed setup). To begin with, the profile shows a complex pattern of multiple acceleration sites that cannot be modeled with a simple analytical approach. Second, γ_M drops by several orders of magnitude over a very small number of cells downstream of each shock formed in the setup. This highlights the need for very high resolution, provided by the moving mesh, downstream of shocks for accurate calculation of the evolution of γ_M . Additionally, because of this very steep drop, the region contributing to X-ray emission downstream of the shocks is extremely narrow, adding an additional constraint on resolution in order to reconstruct the light-curve accurately. The region contributing to optical is wider, which is responsible for a smoother variations of the flux than in X-ray.

Once the energy distribution of electrons is known, we can compute the spectral volumetric emitted power P'_ν for any region of the flow downstream of a shock. Let $\nu_{\text{syn}}(\gamma_e) = \frac{3q_e B'}{16m_e c} (\gamma_e')^2$ be the frequency of the synchrotron radiation from a single electron with energy $\gamma_e' m_e c^2$ in the frame of the fluid, with q_e the charge of the electron. We can associate a synchrotron frequency to any γ_e such that $\nu'_m = \nu_{\text{syn}}(\gamma'_m)$ and

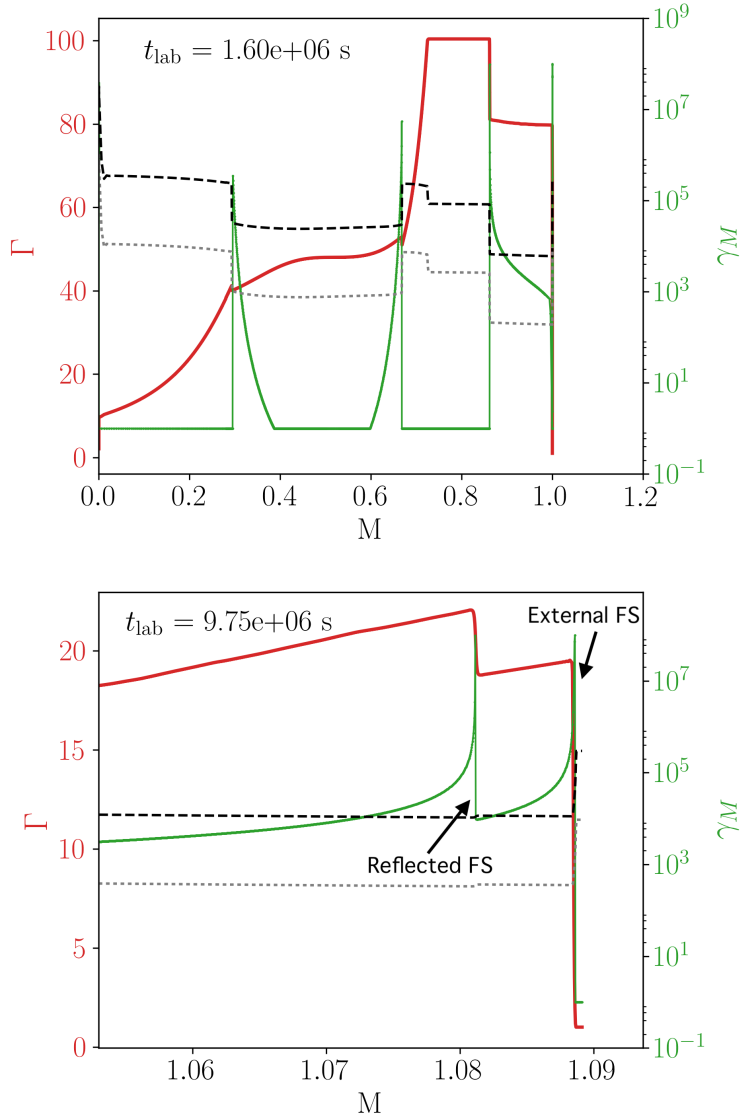


Figure 3.5: Snapshot of run3 at $t_{\text{lab}} = 1.60 \times 10^6$ s (top panel) and $t_{\text{lab}} = 9.75 \times 10^6$ s (bottom panel) showing the Lorentz factor (red) and γ_M (green) as a function of cumulative mass M . In this figure $\epsilon_{B,FS} = 0.1$. The black (grey) dashed line is the minimum value of γ_M for which the synchrotron emission can contribute to X-rays (optical) in the observer frame. The bottom panel is zoomed in on the external medium to show the discrepancy between dynamical and synchrotron cooling timescale.

$\nu'_M = \nu_{\text{syn}}(\gamma'_M)$. P'_ν is thus given by:

$$P'_\nu = \begin{cases} P'_{\nu, \text{max}} \left(\frac{\nu}{\nu'_m} \right)^{1/3}, & \nu < \nu'_m, \\ P'_{\nu, \text{max}} \left(\frac{\nu}{\nu'_m} \right)^{-(p-1)/2}, & \nu > \nu'_m, \end{cases} \quad (3.15)$$

$$\text{with } P'_{\nu, \text{max}} = \frac{4(p-1)}{3p-1} \times n' \sigma_T \frac{4}{3} \frac{B'}{6\pi} \frac{16m_e c}{3q_e}. \quad (3.16)$$

Above the maximum frequency ν'_M the emitted power follows an exponential cut-off. We set $P'_\nu = 0$ if $\nu > \nu'_M$ for the sake of simplicity.

We then integrate this power over the whole fluid using equation:

$$F(\nu, t_{\text{obs}}) = \frac{1+z}{2d_L^2} \int_{-1}^1 d\mu \int_0^\infty r^2 dr \frac{P'_{\nu'}(r, t_{\text{obs}} + r\mu)}{\Gamma^2(1 - \beta\mu)^2}. \quad (3.17)$$

This integration assumes that the fluid is optically thin, a reasonable assumption above radio frequencies. For every cell in the volume, and a given lab time, we compute the arrival time for a redshift $z = 1$, where we place the observer along the axis of the jet. The latter assumption allows to generalise the results to an observer within the opening angle of the flow, with the only difference being the nature of the jet break transition of the underlying non-flaring continuum. In practice, and since we only run 1D simulations, we divide the jet opening angle in 500 angular directions and compute the arrival times and radiative contribution for each cell in each one of these directions. The contributions from all cells for a given observer time bin are then summed to build the light-curve. As a sanity check, We verify a posteriori that we have taken into account the contributions from all the lab times corresponding to a given observer time by plotting the contribution to the total final light-curve for every snapshot.

3.4.2 Synthetic light-curves and spectra

Figure 3.6 shows the spectral energy distribution (SED) for the forward and the reverse shock for run1 (homogeneous). The slopes are in good agreement with analytical modeling of shock emission (Sari et al., 1998) and thus validate our radiative prescription. The slight deviation for the slopes of the FS decreases with increasing resolution downstream of the shock, at the expense of computational efficiency. We also confirm that the frequency cut-off resulting from our choice of initial value for γ_M is also located above 10^{20} Hz for the FS and 10^{24} Hz for the RS. With observer time, this frequency cut-off decreases but we check that it always remains above X-ray frequencies,

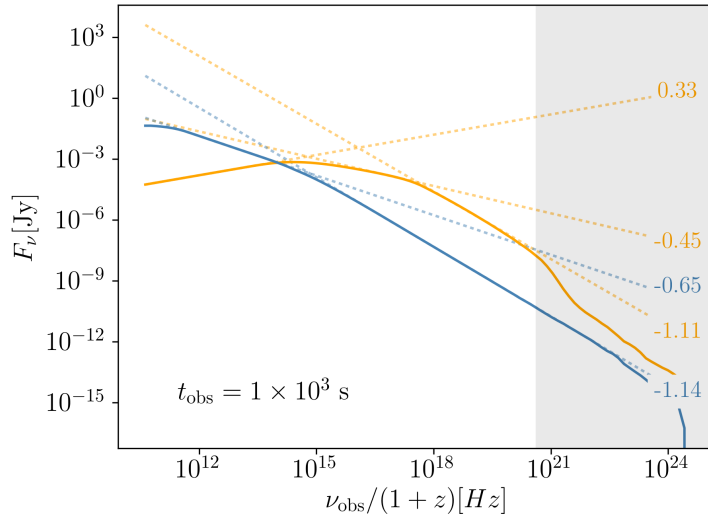


Figure 3.6: Spectral energy distribution for run1 (homogeneous) for the FS (orange) and the RS (blue). We fit each regime of these SEDs in log space and report the slope with the dotted lines. The choice of γ_M directly downstream of the shocks causes the numerical solution to deviate from the expected slope at high energies beyond those that we model (shaded region).

confirming the validity of our approach for light-curve calculations at 1keV.

In figure 3.7 we show the X-ray light-curves at 1 keV obtained in the case of a spherical outflow and isotropic local emission for run2 (tail) and run3 (non-monotonic). These are in very good agreement with the results from LD18. The emission is computed with the same value of $\epsilon_e = 0.1$ and $\zeta = 0.1$ in the FS and RS, but $\epsilon_B = 0.1$ in the RS and $\epsilon_B = 10^{-6}$ in the radiatively inefficient FS. We discuss in §3.4.4 the validity of the choice of values for the FS. The lower emission at very early times compared to LD18 before 100 s in our simulations is due to our decision not to include the variable "head" region that they use in their simulations, as it is not linked to the flaring phenomenon. We obtain very similar results displaying a first spike at ~ 160 seconds corresponding to emission from the internal shocks as the dense shell is being formed (we do not include prompt emission or a steep decay phase at this time in our synthetic light curves. The visibility of this first spike would directly depend on the characteristics of those features). Indeed, fig. 3.8 reports the contribution of all lab times to the final light-curve and shows that all the radiation in this first spike is emitted mostly between $t_{\text{lab}} \sim 4 \times 10^4$ s and $t_{\text{lab}} \sim 5 \times 10^5$ s, the time of the formation of the dense shell in our dynamical simulations (recall fig. 3.4). The arrival time of this spike is comparable to the time at which the corresponding emitting material was ejected by the central engine in the lab frame, in the same fashion as the internal shock mechanism

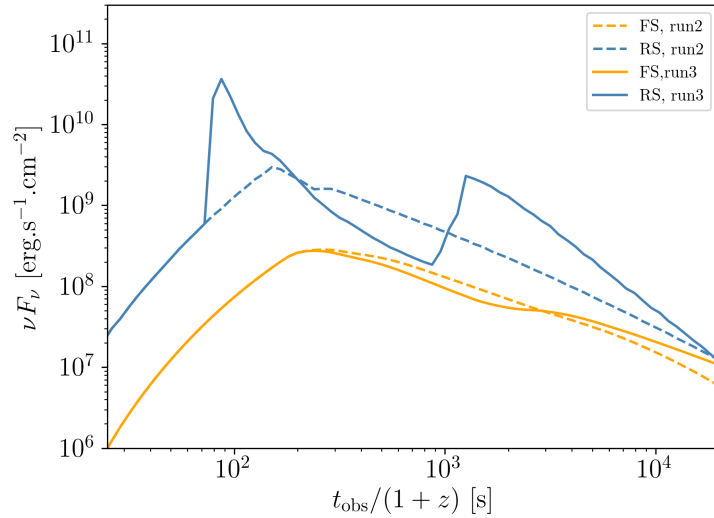


Figure 3.7: X-ray light-curves for the FS (orange) and RS (blue) at 1 keV for run2 (gradual central engine shutdown) and run3 (chaotic central engine shutdown) for a non-jetted outflow. The RS displays flaring behavior in run3 at $t_{\text{obs}} \sim 3 \times 10^3$ s. The FS shows a rebrightening at similar times, due to refueling by reflected forward shocks. The spike in the RS at $t_{\text{obs}} \sim 160$ s is associated with the internal shocks and akin to prompt emission mechanisms.

invoked for burst emission (Rees & Mészáros, 2000; Zhang & Meszaros, 2002). A second bump is visible in the light curve at $t_{\text{obs}} \sim 3 \times 10^3$ s and corresponds to increased emission from the RS as it traverses the dense shell. Again, this is highlighted by the contributions map showing that this radiation is now only produced at very late lab times corresponding to the RS crossing the dense region. This emission will be able to peak above a radiatively inefficient FS in a flare-like manner. Allowing the microphysics to differ in the ejecta and the external medium thus makes it possible for flares to have a RS origin. The FS emission eventually displays a rebrightening occurring just after the flare. This rebrightening is expected as a consequence of the reflected FS formed by the interaction of the RS with the dense layer and is stronger in our simulations than in that of LD18 because of the second forward reflected shock. However, we will see in §3.4.3 that the rebrightening actually completely disappears when taking into account the constraints on flare timescale in jet setups with an angular patch, side-stepping the potential shortcoming of this scenario that would have associated flares with rebrightenings in GRB afterglows.

Thanks to our emission calculation prescription, we are able to produce accurate synthetic broadband SED for the afterglow emission. Figure 3.9 shows the FS and RS spectra for run2 (tail) and run3 (non-monotonic). As expected for early times, we

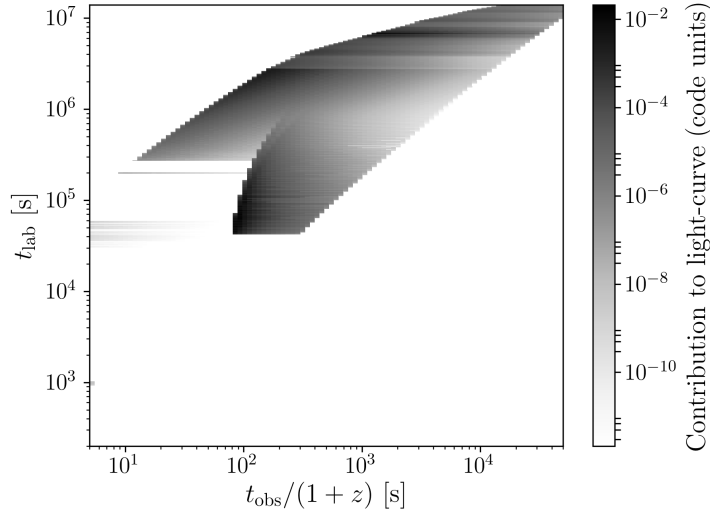


Figure 3.8: Normalised contribution of every data dump to the light curve for run3. The light-curve is simply the stack of all these contributions.

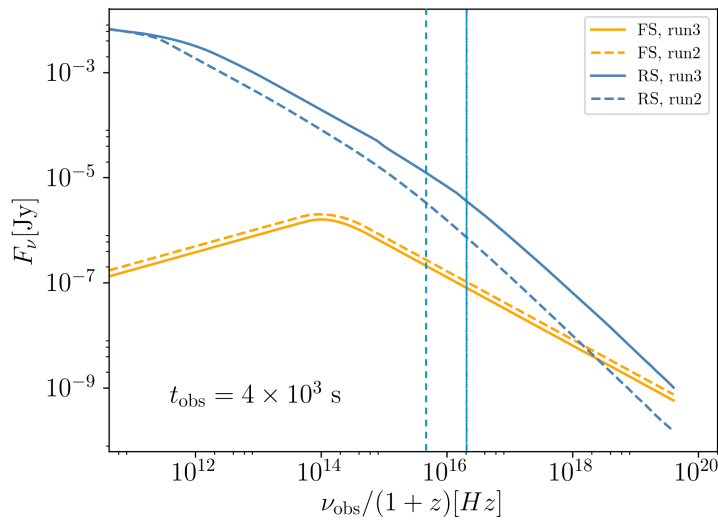


Figure 3.9: Spectral energy distribution for run2 and run3 at the time of the flare $t_{\text{obs}} = 4 \times 10^3$ s. In this figure, $\epsilon_{B,RS} = 0.1$ and $\epsilon_{B,FS} = 10^{-6}$. Careful, the scale in the horizontal axis has been changed from figure 3.6. The vertical lines show the approximate positions of the cooling break in both cases. We can see that this characteristic cooling frequency increases from run2 to run3.

get a harder spectrum for the FS than for the RS, with a dominating RS at low frequencies. From these SEDs, we can see that the emission increases for all frequencies in the RS at the time of the flare. However, the cooling break also increases from $\nu_{c,\text{run2}} \sim 6 \times 10^{15}$ Hz to $\nu_{c,\text{run3}} \sim 3 \times 10^{16}$ Hz. As a result, the relative flux change in optical is smaller than the change in X-ray, as optical frequencies are placed below the cooling break, and X-ray above. Depending on how radiatively efficient the FS is, it could allow the flare to dominate in X-ray, but not in optical, as suggested by observations. Finally, it appears that the rebrightening FS in X-ray is linked to a second radiating component with a very high cooling frequency. However, as mentioned before, we will show later that this emission can be totally suppressed if the dynamical perturbation is constrained to a small opening angle.

3.4.3 Short flares from a localised angular emission region

As mentioned in [LD18](#) and shown in the previous section, the timescale of this flare is longer than observed, with $\Delta t_{\text{flare}}/t_{\text{flare}} \sim 1$ instead of the $\Delta t_{\text{flare}}/t_{\text{flare}} \sim 0.1 - 0.3$ reported by [Chincarini et al. \(2010\)](#). [LD18](#) choose to invoke anisotropy of the emission in the co-moving frame in order to reconcile simulations with observations, essentially limiting the emission to a smaller solid angle. However, this constraint could very well be produced by the geometry of the jet itself. We present here a different approach that avoids having to introduce additional constraints on the microphysics of emission. Here, the short timescale of flares translates into constraints on the spatial extent of the emitting region. In the late activity of the central engine scenario, this constraint is satisfied as the emission is taking place at very small radii close to the remnant, such that the timescale of the flare is directly proportional to the variability timescale of the activity of the central engine. As a result, it is possible to reach the small values of $\Delta t_{\text{flare}}/t_{\text{flare}}$ observed rather easily, but it is more difficult to justify the ad hoc requirement of an evolving timescale for the central engine activity ([Kobayashi et al., 2007](#)). In the reverse shock scenario, the criterion on spatial extent can be fulfilled in the angular direction. The variability of the initial ejection can leave an imprint on the radial as well as the angular velocity profile of the ejecta. In this situation, an over-dense region of material could form only in a "filament" of ejecta in a small angular region, with which the RS would eventually interact.

We investigate this possibility by limiting the perturbed dynamical setup to a small angular region at the initial state. The angular setup is described in figure 3.10. We expect this setup to allow the cooling timescale to dominate the flare decay time, suppressing the curvature effect. We show that the reverse shock scenario can produce flares in filaments away from the line of sight as well as on the line of sight, before

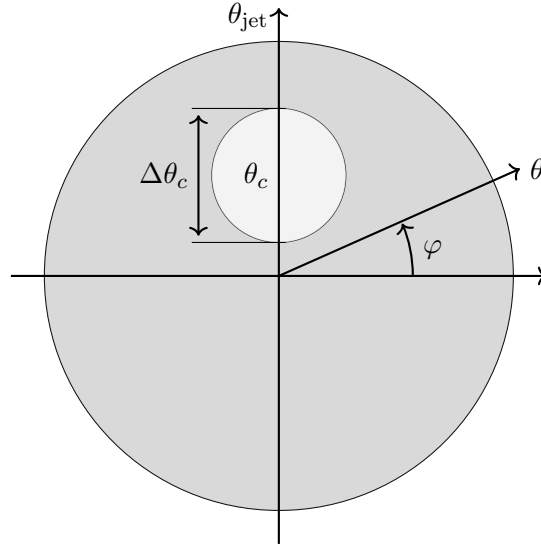


Figure 3.10: Schematic representation of the angular setup for the jet viewed on-axis. The shaded region represents the non-perturbed dynamics, whereas the white region corresponds to the perturbed "filament" responsible for the flare.

focusing on flaring behavior aligned with the observer.

In practice, we use the dynamics results of run2 and run3 and assign them to different angles in the light-curve and spectral reconstruction, to form a non-perturbed (NP) and a perturbed (P) region, respectively. Later in this work, we will assign different dynamics outputs to the P region and will refer to the integrated light-curve and spectra over P and NP by the name of that dynamical output (since NP is unchanged and remains run2). In the on-axis ($\theta_c = 0$) case, the dynamics $\mathcal{D}(\theta)$ eventually come down to:

$$\mathcal{D}(\theta) = \begin{cases} \mathcal{D}_P, & 0 \leq \theta < \Delta\theta_c \\ \mathcal{D}_{NP}, & \Delta\theta_c \leq \theta < \theta_{\text{jet}} \end{cases}, \quad (3.18)$$

with $\Delta\theta_c$ the opening angle of the P region and θ_{jet} the jet opening angle. As a first approach, and provided that $\Delta\theta_c$ is sufficiently large, we can thus limit ourselves to post-processing of 1D dynamical simulations as we expect the P region to be non-causal at least until the reverse shock has crossed the dense shell. The NP region that constitutes the bulk of the jet is also non-causal as we model its evolution pre-jet break. From these considerations on the validity of our setup, we extract the following

constraints:

$$\Delta\theta_c \gtrsim 0.01 \text{ rad}, \quad (3.19)$$

$$\theta_{\text{jet}} \lesssim 0.1 \text{ rad}. \quad (3.20)$$

In the results presented in fig. 3.11, we chose $\Delta\theta_c = 0.015$ and $\theta_{\text{jet}} = 0.1$. The value of θ_{jet} corresponds to a canonical observed jet opening angle (Ryan et al., 2015). As expected, we observe a decrease of the flare decay time, in better accordance with observations. We can then empirically derive a final constraint on $\Delta\theta_c$ corresponding to the maximum value it can take in order to retrieve the flare timescales measured from observations. From our simulations, we record that $\Delta t_{\text{flare}}/t_{\text{flare}}$ starts increasing for $\Delta\theta_c \gtrsim 0.01$ rad, which actually corresponds to the maximum expected size for the patches allowed by transverse causal contact $1/\Gamma$. This limit supports the validity of our scenario since flares with longer timescales than that observed can't actually be produced.

Fig. 3.12 also shows that this setup can produce X-ray flares with perturbations away from the line of sight, as visible when offsetting the P region by an angle $\theta_c = 0.02$. Due to curvature effects, the timescale of the flare increases when moved to higher angles. However, the flux of the the flare also decreases in that case due to simple Doppler beaming effects. As the flare coming from the RS needs to peak above the FS emission, this latter effect is also responsible for a decrease in timescale. It also means that perturbations away from the line of sight will sometimes not give rise to flares at all, causing concerns about the timescales of flaring behavior to be irrelevant in these directions. Additionally, this effect can be responsible for the large scatter in $\Delta F/F$ measured in observations (Chincarini et al., 2010; Margutti et al., 2011).

Figure 3.13 shows the contributions of the P and NP regions to the spectral energy distribution for the case aligned with the observer at the time of the flare. Just like in the spherical blast-wave case (fig. 3.9), the X-ray flare is due to an increase in both the peak frequency and the cooling frequency in the radiation from the P component. The significant increase in the cooling frequency in the P component is responsible for a stronger flare signature above the cooling break. This is responsible for the flare being much smaller in optical than in X-ray.

3.4.4 Evolution and influence of the shocked external medium

We presented here the first set of simulations with a realistic treatment of the external medium density for $n_0 = 1 \text{ cm}^{-3}$. Even though the RS is weaker than for larger

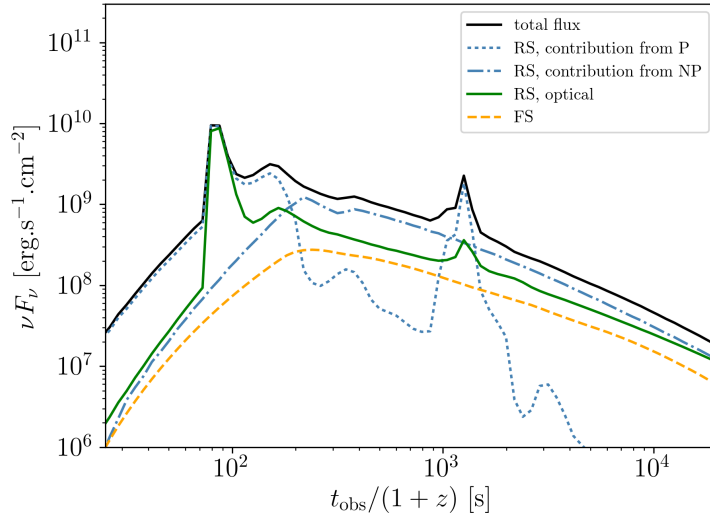


Figure 3.11: X-ray light-curves (black, blue, orange) at 1keV and optical light-curve (green) for a jet perturbed in an angular patch ($\theta_{\text{jet}} = 0.1$ rad, $\theta_c = 0$, $\Delta\theta_c = 0.015$ rad, black solid curve) and for a non-perturbed jet (black dashed curve). The blue dashed and dot-dashed curves are the contributions to the RS from the NP and P regions respectively. The solid green curve is the optical light-curve for the flaring setup. The timescale of the flare is significantly reduced in comparison with globally perturbed setups.

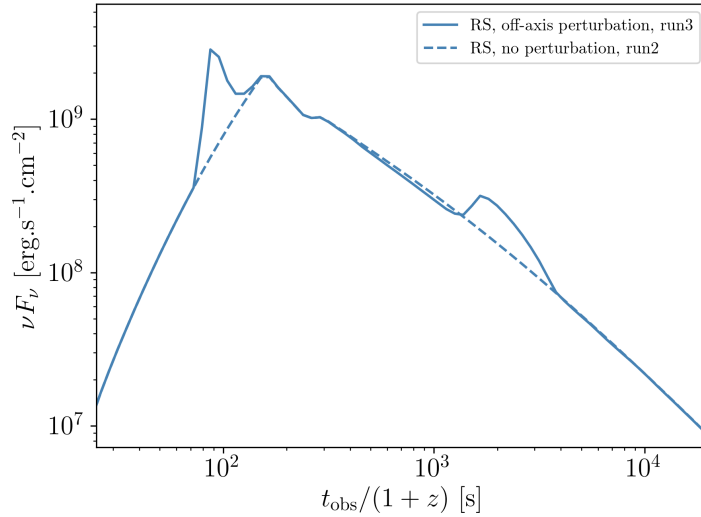


Figure 3.12: X-ray light-curves at 1keV for a jet with a perturbed angular patch away from the line of sight ($\theta_{\text{jet}} = 0.1$ rad, $\theta_c = 0.02$, $\Delta\theta_c = 0.03$ rad, blue solid curve).

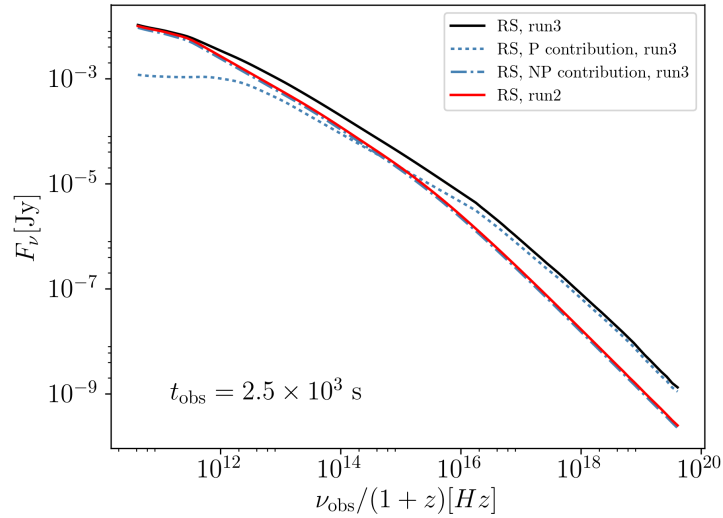


Figure 3.13: Simulated RS spectra at the flaring observer time $t_{\text{obs}} = 2500\text{s}$ for the flaring (solid black line) and non-flaring (solid red line). The dotted and dash-dotted blue lines show the contributions of the P and NP regions to the total RS spectrum in the flaring setup.

values of n_0 , these simulations first show that the setup still produces flares for a more diffuse external environment and is not dependent on the very high density of previous simulations. Moreover, the lower density causes the reverse shock to form later in the lab frame, causing the flares to appear later in the observer frame. This is a first encouraging result towards the ability of this setup to produce late flares. We study late flares in more detail in §3.4.5

Flares can peak over the FS thanks to the difference in radiative efficiency between the ejecta and the external medium. In our simulations, we chose $\epsilon_{B,\text{RS}} = 0.1$ and $\epsilon_{B,\text{FS}} = 10^{-6}$. Even though a change in the value of ϵ_e would yield the same result, the constraints are more stringent on this parameter with $\epsilon_e \sim 0.13 - 0.15$ (Beniamini & van der Horst, 2017). On the contrary, Santana et al. (2014) measure a wide scatter of $\epsilon_B \sim 10^{-8} - 10^{-3}$ in the FS, with a median for $\epsilon_B \sim 10^{-5}$. This coincides with our choice of value of ϵ_B . The discrepancy in the values of ϵ_B between the FS and the RS could be explained by a difference in the intensity of the seed magnetic field eventually compressed in the shock, where the ejecta may be more magnetised than the circumburst medium.

As mentioned in the previous section, the interaction of the RS with the dense region in the tail of the ejecta is responsible for a rebrightening in the FS at the observer time of the flare. As it turns out, and is shown in fig. 3.11, the rebrightening is strongly

suppressed when constraining the perturbation to a small angular region, for various reasons. First, the increased emission now comes from a smaller region, causing the total flux to be lower. Second, the region being narrow, the rebrightening is only visible while the beaming angle is smaller than the perturbed region opening angle. When this is not the case anymore, a break in the contribution of the perturbed region to the light-curve causes its emission to drop below the underlying non-perturbed jet emission.

The fact that the rebrightening disappears in the case of a narrow emitting region supports the validity of our setup, as it would otherwise imply that all flares have to be associated with a subsequent rebrightening.

3.4.5 Late flares

The currently accepted paradigm for X-ray flares in GRB light curves invokes late activity of the central engine, either from late-time fallback accretion, or from energy injection from a NS remnant. Various works have shown the ability of this model to reproduce the observed flare properties. However, a significant number of GRBs display flares at times as late as 10^5 s after the burst (Burrows et al., 2005b). The scenario involving late activity of the central engine runs into a limitation there as the timescale on which the flare shows in observer time is equal to that over which the central engine reactivates. This puts severe constraints on the nature and stability of the remnant. Piro et al. (2019) show a rebrightening around 160 days at 3.2σ in the X-rays relative to the underlying broadband continuum for the famous gravitational counterpart afterglow of GRB170817A (the significance decreases to 2.8σ if the X-rays are analysed in isolation (Piro et al., 2019; Hajela et al., 2019)). They suggest energy injection from a hypermassive NS, which further emphasizes the need for an explanation for flares at very late time that does not rely on assumptions about the nature of the remnant. In this section, we show how a LLRS can be responsible for flares at early and late times.

We investigate how our setup can reproduce flares at later times by modifying the previous dynamical setup as follows: The radial Lorentz factor profile still displays a flat head region, followed by a smoothly decreasing region corresponding to gradual shutdown of the central engine. The chaotic shutdown of the engine is now modeled by a Gaussian profile added to the gradual shutdown. This is done by replacing $f(x)$ in eq. 3.8 by $g(x)$ such that:

$$g(x) = Ae^{\left(\frac{x-x_0}{\sigma_0}\right)^2}. \quad (3.21)$$

Run	A	x_0	σ_0	Description
run4	8	0.01	0.005	early bump
run5	8	0.001	0.005	late bump

Table 3.4: Run Parameters for late flare setups.

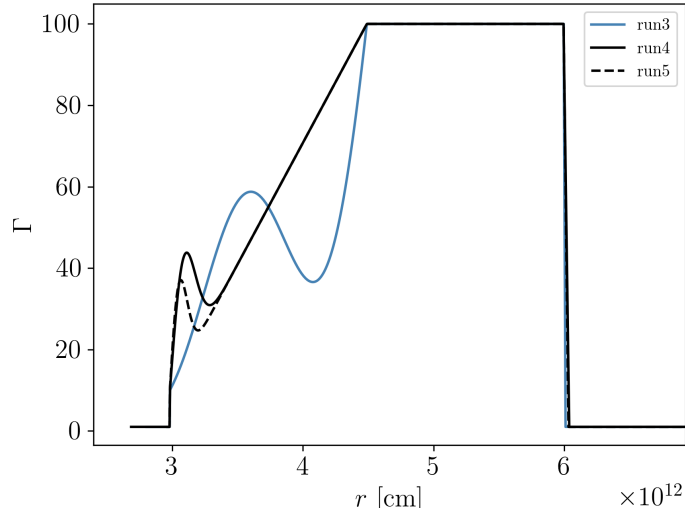


Figure 3.14: Initial Lorentz factor radial profile for run4 and run5. The gaussian bump is moved further at towards the back of the ejecta in comparison to the oscillation visible in run3.

This bump can be moved left or right to model earlier or later ejection times by changing the value of $x_0 \in [0, 1]$, with σ_0 controlling the width of the bump. The Lorentz factor initial radial profiles are shown in fig. 3.14 and the corresponding parameters are reported in table 3.4. A and σ_0 are kept the same in both run so as to investigate whether x_0 would have an influence on its own on $\Delta F/F$ for the produced X-ray flare. The strength of this approach lies in that the shell still has the same width of 100 light-seconds. The late variability in the afterglow can then be imprinted onto the dynamics at the time of the ejection and does not rely on late activity of the central engine.

The dynamics are very similar to the dynamics described in §3.3 and are shown in figures 3.15 and 3.16. As in previous simulations, the region of negative velocity gradient in the tail leads to the formation of a dense region of ejecta surrounded by two internal shocks. Again, the RS emission is powered up as it traverses this shell and is responsible for a flare. Fig. 3.17 shows the synthetic X-ray light-curves for this setup for various values of x_0 . As expected smaller values of x_0 lead to later peak times of the produced flares. The significant result of these simulations is that the timescale ratio of the flares remains the same, independent of the value of x_0 , showing that the cooling timescale remains the

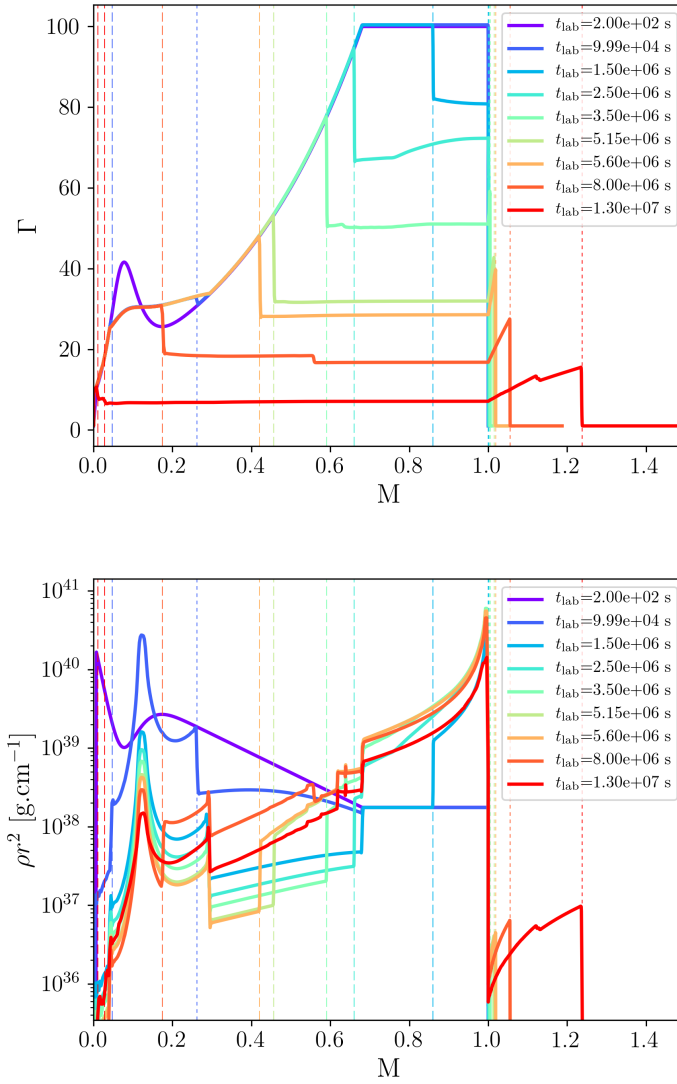


Figure 3.15: Lorentz factor (top) and density (bottom) as a function of cumulative mass for run4 (chaotic shut down of the central engine leading to a region of negative velocity gradient in the trail of the ejecta. Dashed vertical lines show the positions of reverse shocks and dotted vertical lines the positions of forward shocks.)

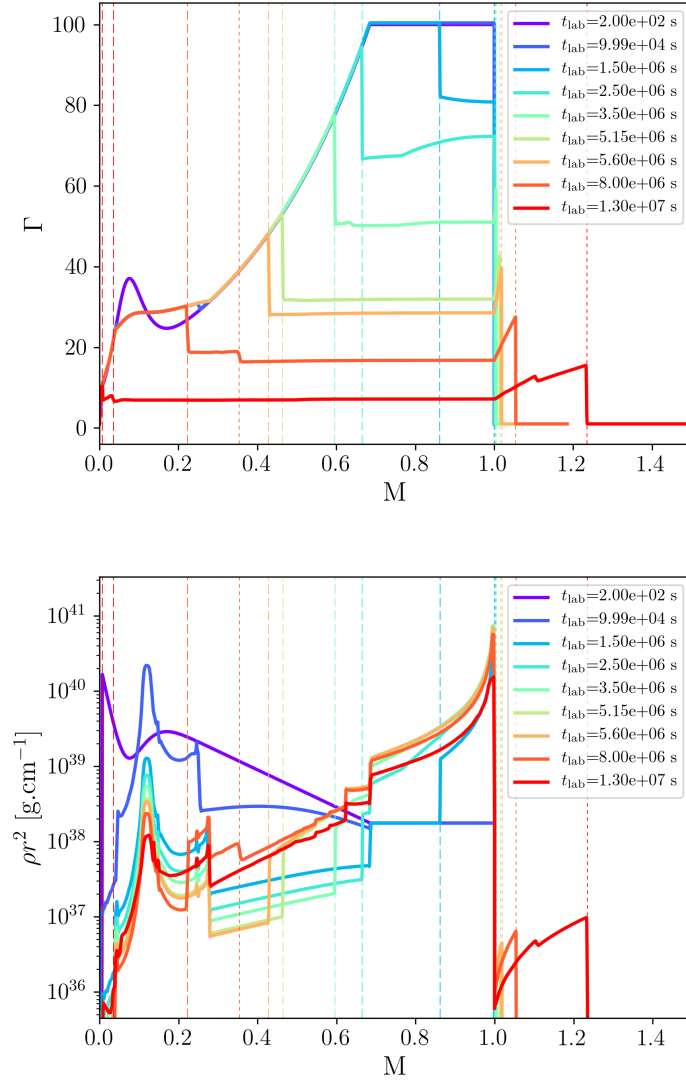


Figure 3.16: Lorentz factor (top) and density (bottom) as a function of cumulative mass for run5 (chaotic shut down of the central engine leading to a region of negative velocity gradient in the trail of the ejecta. Dashed vertical lines show the positions of reverse shocks and dotted vertical lines the positions of forward shocks.)

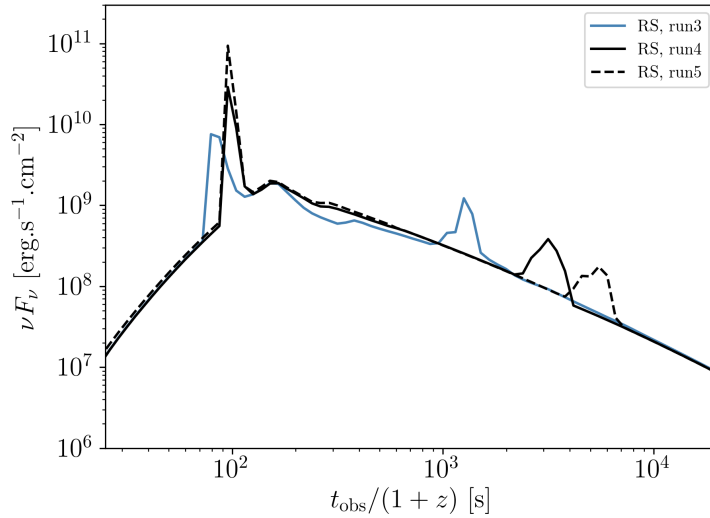


Figure 3.17: X-ray light-curves for run3, run4, run5. The flare moves to later observer times as non-monotonic region of velocity is moved further at the back of the ejecta.

same regardless of the arrival time of the flare, making the reverse-shock scenario for flares all the more robust. Another striking feature is that the flux variability $\Delta F/F$ is the same for run4 and run5, for flares occurring at different times, in accordance with observations. This suggests that it is possible to produce flares up to an arbitrarily long time after the burst if one considers a gradual shutdown of the central engine all the way to Lorentz factors of order unity, over a timescale consistent with a short-lived central engine, while still fulfilling the flux variability and flare timescale requirements.

3.5 Discussion

We demonstrated the ability of the RS to produce flares at both early and late times as it interacts with a dense region in the ejecta created by the non-monotonic initial radial velocity profile. These flares can arise both in a direction aligned and non-aligned with the line of sight and satisfy the timescale constraints given by observations provided that the region producing them is narrow enough. However, some aspects remain to be investigated.

3.5.1 Limitations to dynamical simulations

Even though we offer significant improvement over previous studies thanks to the moving mesh approach, both in terms of efficiency and accuracy, because we are able to run

more simulations with a wider range of more realistic parameters, our description of the dynamics still relies on a number of simplifying hypotheses. First, we are running 1D-simulations that ignore all lateral motion. This is a good approximation at early times as the jet is non-causal but becomes less valid as the blast-wave decelerates at later times, leading to spreading and growing shear-driven lateral instabilities. However, since we are mostly interested in the dynamics of the reverse shock at Lorentz factors of a few tens, 1D simulations remain a good approximation all the way to crossing time. Still, given the complexity of the dynamics involved, and the need to introduce angular structure to explain the observed timescale for flares, we expect that this study will benefit from comparison with 2D simulations in the future.

Second, we neglect in these simulations the dynamical effect of potential magnetic fields and assume a low magnetisation of the ejecta. At late stages following launching, magnetic fields are not expected to be dynamically dominant (see e.g. [Granot et al., 2015](#), for a recent review). We consider residual magnetic fields that are small enough such that they do not influence the strength of the reverse shock, as a strong magnetisation would hinder the propagation of the RS, making this scenario unviable ([Giannios et al., 2008](#); [Mimica et al., 2009](#)). While the observation of reverse shock signatures (the optical flash (e.g. [Akerlof et al., 1999](#)) and radio flare (e.g. [Frail et al., 2000](#))) in several afterglows, as well as low polarisation upper limits and detections (e.g. [Mundell et al., 2007](#); [Laskar et al., 2019](#)) are in favour of our assumption, other detections of more strongly linearly polarised reverse shocks ([Mundell et al., 2013](#)) show that low magnetisation cannot always be assumed. Measured polarisation is also strongly dependent on the spatial scale of the ordering of the magnetic field, and low polarisation does not necessarily entail low magnetisation. Future work could include investigating whether flares appear in highly polarised afterglows.

3.5.2 Validity of the flaring setup

Some aspects of our setup itself still need to be investigated. To begin with, the flux variability of the flares is loosely constrained, for two main reasons. First, the flux variation is a measurement of how high the flare from the RS can peak over the FS. This is directly driven by the ratio in radiative efficiency between the FS and the RS, decided by the values of ϵ_e and ϵ_B in the FS, and the RS respectively. The timescale $\Delta t_{\text{obs}}/t_{\text{obs}}$ of the flare also depends on this ratio, as a better radiative efficiency of the FS will cause a shorter Δt_{obs} . Improving the constraints on the microphysics of emission in the ejecta and the circumburst medium constitutes a crucial step towards validating the approach presented here. Moreover, this dependency on the relative radiative efficiency between FS and RS could cause flares to be more frequent in dimmer afterglows with this model.

It would be interesting to investigate whether such correlation exists in observations. This effect could however be cancelled out by potential correlation between intrinsic GRB energy and the level of variability observed in the ejecta dynamics.

Second, the scope of this article focuses on cases in which the jet axis is aligned with the line of sight. We observe that, even though perturbations away from the line of sight give rise to flares with longer timescales than aligned perturbations, they also display smaller peak fluxes simply because of Doppler beaming effects. This gives rise to a range of values for $\Delta F/F$ for patches at arbitrary angles and can actually completely suppress the flare for high angles as the flux variability from the RS becomes unable to peak above the FS emission. As a result, we expect to mostly be seeing flares coming from perturbations aligned with the line of sight. More evidence is also being accumulated in favor of structured jets (e.g. [Abbott et al., 2017b](#); [Troja et al., 2017](#); [Kasliwal et al., 2017](#); [Kathirgamaraju et al., 2017](#); [Lazzati & Perna, 2019](#); [Troja et al., 2019](#)) with less energetic sides and domination by the central material, further advocating for more variability coming from the central region. These aspects in turn favour the associated values of $\Delta t_{\text{obs}}/t_{\text{obs}} \sim 0.1 - 0.3$ corresponding to observations.

These flares however can only fulfill the timescale requirements if the perturbed region remains sufficiently narrow. We observe that longer flares arise if the curvature effect starts to dominate the decay time, which can happen in the perturbed region becomes too wide. We find empirically that the timescale starts to increase for $\Delta\theta_c \gtrsim 0.01$ rad. Actually, this constraint corresponds to the value of $1/\Gamma$ for $\Gamma = 100$ and is the expected size of angular perturbations due to transverse causal contact across the ejecta. As a result, we do not expect to see these longer flares, in accordance again with observations. This proves the robustness of this mechanism which does not rely on fine-tuning of the angle, nor the size of the patch in order to produce flares with the correct timescale, arrival time and flux variability.

Finally, this mechanism relies on the formation of a dense shell associated with radiating internal shocks in the ejecta, responsible for a first spike in the X-ray light-curve. One might wonder whether these internal shocks can directly contribute in gamma-rays. We do not expect that this is the case as the Lorentz factors involved in the tail of the ejecta are too small to shield the corresponding radiation from $\gamma\gamma$ annihilation. As a result, we expect these spikes not to be detectable in the prompt phase and to be only visible in cases where X-ray observations start very early, for which they can be interpreted as late prompt emission or early flares (such as some sometimes seen during the early steep decay phase). Our afterglow model thus does not depend on any prompt mechanism but merely requires the launch of a relativistic ejecta.

3.6 Conclusions

In this paper, we present one-dimensional SRHD numerical simulations of GRB afterglow blast waves. These simulations are carried out using our new moving-mesh code, improving both resolution and efficiency. We apply them to a novel scenario (Hascoët et al., 2017; Lamberts & Daigne, 2018) for the origin of flares in the X-ray afterglow that involves the interaction of a long-lived reverse shock with a stratified ejecta. We implement numerical tracing of the boundaries of the local particle population and present the first broadband study of such scenario.

By exploring a larger parameter space than previous works, and by considering a more realistic description of the circumburst medium density, we are able to confirm that a chaotic shutdown of the central engine produces X-ray flares in the afterglow at an arbitrary long time after the burst.

In order to do so, the initial dynamics of the ejecta must include the following features:

- A region (tail) of decreasing velocity as we move further towards the back of the ejecta, responsible for its expansion as it travels outwards, and delaying the interaction of a reverse shock with potential embedded features.
- Variations of the Lorentz factor in the tail. Each region of negative velocity gradient in this tail will be responsible for the formation of a dense shell as the faster material catches up with the slower material ahead, and later a flare when it is crossed by the RS. The number of flares in a single afterglow depends on the variability in the tail.

This model also relies on the assumption that the radiative efficiency of the forward shock needs to be smaller than that of the reverse shock, by means of a smaller value of ϵ_B , such that flares from the RS can peak over the FS emission. Depending on the variability of the tail and the ratio of radiative efficiencies, a fraction of weak flares might go undetected.

The light curve displays two new features in comparison with a uniform profile. First, a spike is produced by the internal shocks at early times, reminiscent of the mechanisms involved for prompt emission. The second feature is the result of the interaction of the RS with the dense region. The peak frequency and the cooling break of the RS both increase, leading to a flare in X-ray and a smaller bump in optical.

In order to retrieve the timescale flares expected from observations, we constrain the perturbation responsible for the flaring behavior to a small angular patch and show

that the width of this patch actually naturally falls below the expected size derived by causal contact arguments as the cooling timescale needs to dominate over the curvature effect.

We show that this model produces flares at an arbitrarily long time after the burst if the perturbation in the gradual engine shutdown happens just before the complete end of its activity. This delays the interaction of the reverse shock with the resulting dense shell and produces flares with the same timescale and flux variability, but at later times.

Eventually, our moving mesh approach to the simulation of the dynamics is sufficiently efficient that we can expect to carry out additional simulations in a relatively short amount of time. Moving to two dimension would allow us to simulate the dynamics past jet spreading, and to study the link between flaring behavior and late evolution of the afterglow light-curve.

3.7 Article appendix

3.7.1 Code validation

First, the stability and accuracy of the code are tested on standard shock-tube setups. Fig. 3.18 shows an example in cartesian coordinates in which the numerical solution is able to resolve the shock fronts and the contact discontinuity with high precision. The spike at the contact discontinuity is a resolution-dependent numerical oscillation linked to the initial transient state and is different from the physical density spike described in §3.3. Fig. 3.19 shows an example in spherical coordinates in which the numerical evolution is in good agreement with the exact solution. We tested the code on several other shock-tube setups that all yielded satisfying results but are not reported here.

We assess the accuracy of our code for smooth parts of the flow by testing the evolution of an isentropic wave in cartesian coordinates, following the setup presented in [Zhang & MacFadyen \(2006\)](#) and find that our code achieve the expected second order convergence in these cases, as is shown in figures 3.20 and 3.21. Further testing is carried out by reproducing the Blandford-McKee (BM) setup ([Blandford & McKee, 1976](#)) akin to the propagation of a spherically symmetric relativistic blast-wave in the ISM. The results are shown in fig. 3.22 and show again that the code behaves as expected, even at significantly high Lorentz factors and with realistic values of circumburst medium number density $n_0 = 1 \text{ cm}^{-3}$.

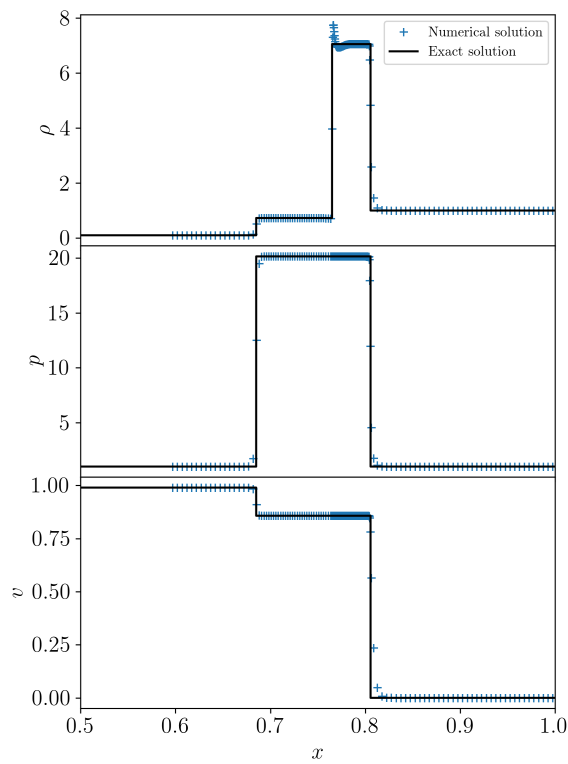


Figure 3.18: Shock tube in cartesian coordinates. $t = 0.6$. Initial discontinuity at $x = 0.25$. Left state: $\rho = 0.1$, $p = 1$, $v = 0.99 \times c$. Right state: $\rho = 1$, $p = 1$, $v = 0$. Initial resolution is 200 cells.

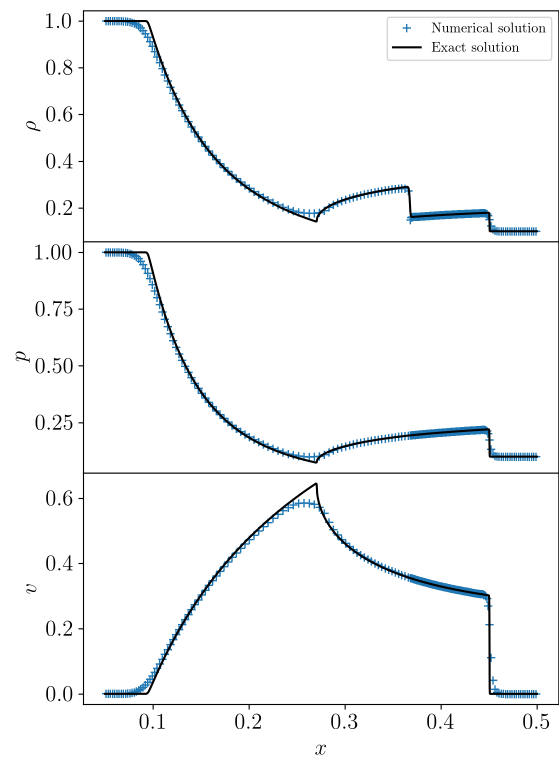


Figure 3.19: Shock tube in spherical coordinates. $t = 0.3$. Initial discontinuity at $x = 0.25$. Left state: $\rho = 1$, $p = 1$, $v = 0$. Right state: $\rho = 0.1$, $p = 0.1$, $v = 0$. Initial resolution is 200 cells.

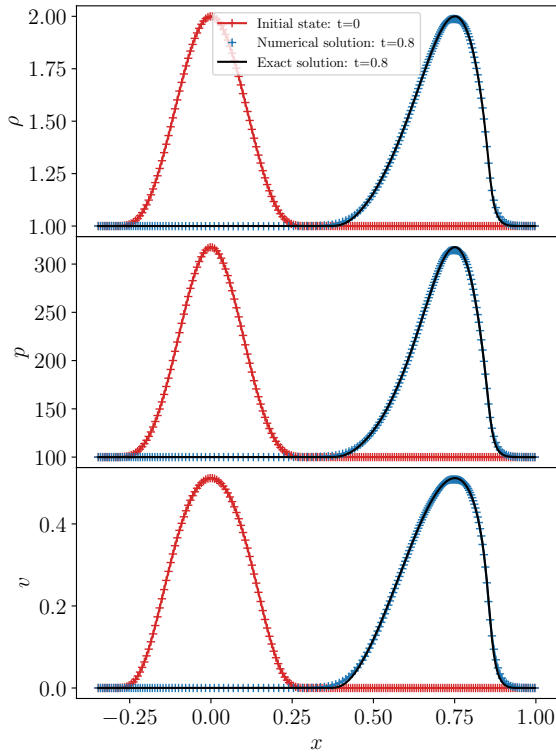


Figure 3.20: Isentropic wave test output for primitive variables. We plot the initial (left wave) and final state (right wave) on the same graph here. The numerical results at $t=0.8$ (blue crosses) are in very good agreement with the exact solution (black solid curve).

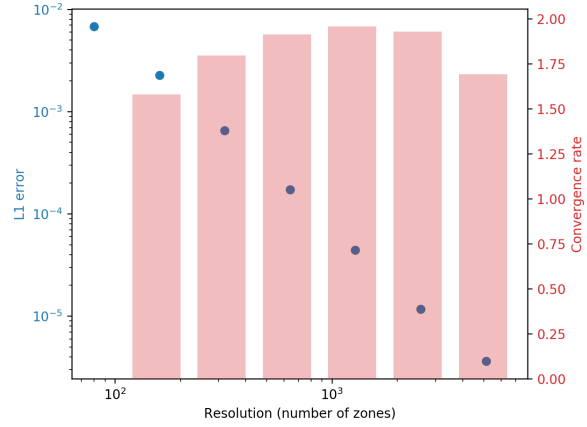


Figure 3.21: Convergence rate and L1 error for the isentropic wave test.

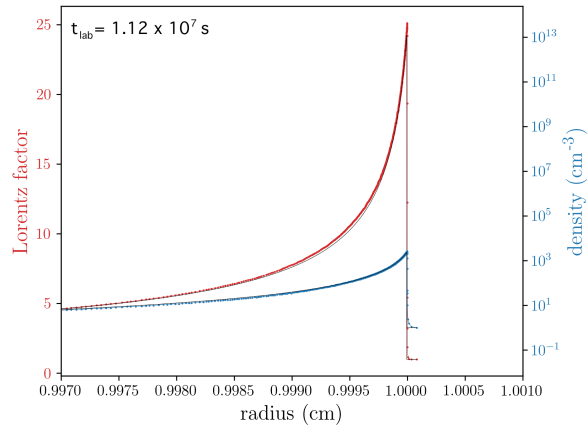


Figure 3.22: Validation of the moving-mesh code against the Blandford-McKee analytical evolution of a spherical blast-wave ($E_{\text{iso}} = 10^{53}$ erg, $n_0 = 1 \text{ cm}^{-3}$). Here we show the normalized density and Lorentz factor as a function of radius at the deceleration time. Then numerical solution (blue and red dots) is in very good agreement with the analytical Blandford-McKee solution (solid black curve).

3.7.2 Shock detection algorithm

Shock detection methods usually rely on measuring gradients in the fluid state. However, these methods are only efficient for strong shocks and often fail to detect internal shock in our setups (Lamberts & Daigne, 2018). As a result, we follow the more robust method introduced in Rezzolla et al. (2003a) and described in Zanotti et al. (2010), that evaluates nature of the waves in the Riemann fan for all interfaces of the grid based on the calculation of limiting relative velocities. Indeed, in the absence of a magnetic field, a discontinuity between two regions of fluid with different thermodynamical values will decay into two waves propagating on both sides of a contact discontinuity (jump in density). These waves can either be rarefaction waves or shocks. As described above, we use this behavior to compute the dynamical evolution of our fluid by solving the Riemann problem at every interface between the cells of our grid. We can simply detect the shocks in our fluid by checking whether the wave pattern at each of these interfaces will contain a shock or not. A shock will appear if the relative velocity between neighbouring cells exceeds a threshold dependent on the fluid states.

The 1D aspect of our simulations allows us to compute the limiting relative velocities of each case of the Riemann problem rather efficiently. We report here the procedure presented in Rezzolla et al. (2003a) to compute the limiting relative velocity in the Shock-Rarefaction (\mathcal{SR}) and 2-Shock ($2\mathcal{S}$) cases.

One Shock - One Rarefaction wave case ($1\mathcal{R}_{\leftarrow}3\mathcal{C}3'\mathcal{S}_{\rightarrow}2$)

The Riemann fan produced at the interface between two neighbouring cells will contain at least a shock if the relative velocity between these cells v_{12} is greater than a limiting velocity $(\tilde{v}_{12})_{\mathcal{SR}}$ given by

$$(\tilde{v}_{12})_{\mathcal{SR}} = \frac{1 - A_+(p_3)}{1 + A_+(p_3)} \Big|_{p_3=p_2}, \quad (3.22)$$

with

$$A_+(p_3) \equiv \left[\left(\frac{(\gamma - 1)^{1/2} - c_s(p_3)}{(\gamma - 1)^{1/2} + c_s(p_3)} \right) \left(\frac{(\gamma - 1)^{1/2} + c_s(p_1)}{(\gamma - 1)^{1/2} - c_s(p_1)} \right) \right]^{2/(\gamma-1)^{1/2}}, \quad (3.23)$$

with $c_s(p_i)$ the sound speed in region i .

A very straightforward shock detection method would consist in comparing the relative velocities and limiting relative velocities at each interface, flagging a shock if:

$$v_{12} > (\tilde{v}_{12})_{\mathcal{SR}}. \quad (3.24)$$

However, this method detects shocks of any strength, and we are only interested in the strongest shocks responsible for particle acceleration. A nice workaround involves the calculation of the limiting relative velocities in the $2\mathcal{S}$ case.

Two-shock case ($1\mathcal{S}_{\leftarrow}3\mathcal{C}3'\mathcal{S}_{\rightarrow}2$)

The fan will display two shocks if:

$$v_{12} > (\tilde{v}_{12})_{2\mathcal{S}} = \sqrt{\frac{(p_1 - p_2)(\hat{e} - e_2)}{(\hat{e} + p_2)(e_2 + p_1)}}, \quad (3.25)$$

with

$$\hat{e} = \hat{h} \frac{\gamma p_1}{(\gamma - 1)(\hat{h} - 1)} - p_1, \quad (3.26)$$

where \hat{h} is the only positive root of the Taub adiabat (Taub, 1948). In order to relax the our shock-detection criterion, we set the threshold for shock detection to a intermediate value between both relative velocity limits:

$$(\tilde{v}_{12}) = (\tilde{v}_{12})_{\mathcal{SR}} + \chi[(\tilde{v}_{12})_{2\mathcal{S}} - (\tilde{v}_{12})_{\mathcal{SR}}], \quad (3.27)$$

where the value of χ is arbitrarily chosen between 0 and 1. In our simulations, choosing $\chi = 0.1$ gives satisfying results.

Acknowledgements

We address special thanks to Geoffrey Ryan and Tanmoy Laskar for their respective help in setting up the moving-mesh code and the observational insight into GRB afterglow behaviour that they provided.

3.8 Additional information

3.8.1 Implementation specifics

The code is implemented in C/C++ with an object oriented approach. It makes use of the GNU scientific library for root finding operations. Data inputs and outputs are structured using HDF5. The code can restart from any outputted snapshot in order for the user to resume computation if stopped too early. This also allows users to adjust numerical ad hoc parameters during simulations. The calculation is parallelised with a shared memory approach using OpenMP.

The code is one-dimensional but includes solvers in cartesian, cylindrical and spherical coordinates. The Riemann solvers implemented are HLL and HLLC with the possibility to set up criteria on the choice of solver at runtime. Shock detection and particle injection and cooling can be turned on or off. To compute synthetic light curves and spectra from dynamical snapshots, the radiative calculation module can be compiled from the same source as the dynamical simulation code as a lot of their functions overlap.

3.8.2 Flux integration

As explained in §2.4.3, there are two approaches to computing the observed flux at a given observer time t_{obs} . Contrary to the linear radiative transfer method described in chapter 2, the method used in this chapter consists in summing the contribution of the cells from each snapshot to each observer time considered in the calculation of the light curve. This approach obviously relies on the assumption that the medium is optically thin, which is the case above radio frequencies. For a given observer frequency ν_{obs} , the calculation is done as follows:

1. We split the observer time range in a series of bins in log space.
2. For each snapshot, we compute the arrival time for each cell. Each cell is thus attributed a bin to which it will contribute.
3. We compute the emissivity in each of these cells at the frequency corresponding to the observer frequency but in the frame co-moving with the fluid. This relies on our knowledge of the local micro-physical quantities.
4. The contribution of the cell to its associated bin is a function of the cell position, velocity and the time between data dumps. To simplify the calculation, for each snapshot at lab time t_d we assume that each cell contributes up to the following

data dump at t_{d+1} and integrate the power over $\Delta t_d = (t_{d+1} - t_d)$. With this approach, the contribution to the light curve is:

$$\Delta F_{\text{cell}}(\nu, t_{\text{obs}}) = \frac{1+z}{2d_L^2} \times \frac{P'_{\nu}|_{\text{cell}}}{\Gamma^2(1-\beta\mu)^2} \times \Delta\mu r^2 \Delta r \frac{\Delta t_d}{\Delta t_{\text{obs}}}, \quad (3.28)$$

where Δr and $\Delta\mu$ are the radial and polar extent of the cell, and Δt_{obs} the observer time bin size.

This approach forces us to arbitrarily declare a bin size even when computing spectral energy distributions. However, it allows us to create maps of light-curve contribution and identify the various emission sites. An example of how these contribution maps can be used is shown in figure 3.8 in which we plot the integrated contribution from each snapshot to the total light-curve, allowing us to connect features in observer time with events in lab time. These steps were implemented in a module added to the one-dimensional hydrodynamics code which can be called after the dynamics run to compute light curves or SEDs for any combination of parameters.

General conclusion

In this chapter, we have shown the importance of accurately capturing the dynamics and emission from relativistic astrophysical transients in order to better understand their complex features. Using the improved dynamical and radiative simulation tools I developed, we showed that the flaring mechanism involving the interaction of a long-lived reverse shock with a stratified ejecta naturally reproduces observed flare characteristics in the whole range of values covered by their observables. This result came from our ability to run more simulations thanks to the increased computational efficiency from the moving mesh. Comparison between x-ray and optical bands was only possible thanks to the local cooling.

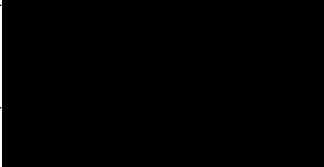
Overall, this project highlights the benefits of the methods described in chapter 2 even when constraining them to a simple 1D approach. The important results obtained provide backing the idea of applying such methods to full multi-dimensional simulations in order for us to learn about the full trans-relativistic radiative evolution of the blast wave, which I develop in chapter 4. While chapter 3 how local cooling helped in identifying multiple emission sites, the next chapter will show how crucial an accurate description of synchrotron cooling is in order to conduct broadband analysis of non-thermal emission from relativistic transients.

GAMMA: A New Method for Modeling Relativistic Hydrodynamics and Non-thermal Emission on a Moving Mesh

Eliot H. Ayache, Hendrik J. van Eerten, Rupert W. Eardley (in review)

*We are all adventurers here, I suppose, and wild doings in wild countries appeal to us
as nothing else could do. It is good to know that there remain wild corners of this
dreadfully civilised world.*

— ROBERT FALCON SCOTT, Scott's Last Expedition

This declaration concerns the article entitled:			
GAMMA: A New Method for Modeling Relativistic Hydrodynamics and Non-thermal Emission on a Moving Mesh			
Publication status (tick one)			
Draft manuscript	<input type="checkbox"/>	Submitted	<input type="checkbox"/>
In review	<input checked="" type="checkbox"/>	Accepted	<input type="checkbox"/>
Published	<input type="checkbox"/>		
Publication details (reference)	Ayache, E., Van Eerten, H., Eardley, R. (in review) Submitted to Monthly Notices of the Royal Astronomical Society		
Copyright status (tick the appropriate statement)			
I hold the copyright for this material		<input checked="" type="checkbox"/>	Copyright is retained by the publisher, but I have been given permission to replicate the material here
Candidate's contribution to the paper (provide details, and also indicate as a percentage)		<p>I predominantly contributed to this research which constituted the core of my Ph.D. project. As such, I was the primary person working on the project full-time.</p> <p>Formulation of ideas: I formulated my own ideas for the progress of the project, aided by useful input during my supervisory meetings with Dr. Hendrik van Eerten. I drove the design choices of the code and decided on the simulation setups in close discussion with my supervisor. (65%)</p> <p>Design of methodology: The main contribution of the paper is the public release of a code for simulating non-thermal emission from relativistic hydrodynamics. The projects main scientific result is the discovery of a difference in the spectral behaviour at the jet break from previous works. I contributed to the choice of setups to run. I actively participated in the design of the local cooling prescription we use in close discussion with my supervisor. (65%)</p> <p>Experimental work: My contributions included: writing the multi-dimensional dynamical simulation code from scratch, interfacing it with the radiative transfer code for synthetic light curve generation from Van Eerten & Wijers (2009). I carried out testing at the output of the simulation code and the radiation code. I set up and ran the simulations (except the RT instability setups), post-processing of the output and analysis of the results. (85%)</p> <p>Presentation of data in journal format: I designed all the figures and wrote the manuscript draft, whilst benefitting from feedback by Dr. Hendrik van Eerten. I then received further comments from collaborators, which I implemented. (90%)</p>	
Statement from Candidate	This paper reports on original research I conducted during the period of my Higher Degree by Research candidature.		
Signed			Date
			08/07/2021

Preamble

Following the first results obtained from 1D simulations on GRB afterglow phenomenology, we carry out a full implementation of the code in multi-dimensions. The paper reported in this chapter presents the full description of this new code, **GAMMA**, in the context of the study of the full GRB afterglow blast-wave evolution. As later shown in this chapter, GRB afterglows in the trans-relativistic regime are an inherently multi-dimensional phenomena, with crucial features in the light curve directly depending on our ability to accurately capture the transverse jet evolution.

Just like in chapter 3, I report the contents of the paper as submitted for publication. This means that this chapter is self-contained and can be read independently from the rest of the thesis. Some repetition of the introductory concepts from chapter 2 can be found in §4.2.1 and §4.2.2 (dynamics), and in §4.4.1 and §4.4.2 (radiation). Additional information not included in the submitted paper is reported in §4.7. §4.7.2 summarises the results introduced in this chapter in the general context of the thesis.

Abstract

In recent years, dynamical relativistic jet simulation techniques have progressed to a point where it is becoming possible to fully numerically resolve gamma-ray burst (GRB) blast-wave evolution across scales. However, the modeling of emission is currently lagging behind and limits our efforts to fully interpret the physics of GRBs. In this work we combine recent developments in moving-mesh relativistic dynamics with a local treatment of non-thermal emission in a new code: **GAMMA**. The code involves an arbitrary Lagrangian-Eulerian approach only in the dominant direction of fluid motion which avoids mesh entanglement and associated computational costs. Shock detection, particle injection and local calculation of particle evolution including radiative cooling are done at runtime. The dynamical evolution is adiabatic. Even though **GAMMA** has been designed with GRB physics applications in mind, it is modular such that new solvers and geometries can be implemented easily with a wide range of potential applications. In this paper, we demonstrate the validity of our approach and compute accurate broadband GRB afterglow radiation from early to late times. Our results show that the spectral cooling break shifts by a factor of ~ 40 compared to existing methods. Its temporal behavior also significantly changes from the previously calculated temporary steep increase after the jet break. Instead, we find that the cooling break does not shift with time between the relativistic and Newtonian asymptotes when computed from our local algorithm. **GAMMA** is publicly available at: <https://github.com/eliotayache/GAMMA>.

4.1 Introduction

The simulation of gamma-ray-burst (GRB) afterglow evolution is a particularly challenging multiscale numerical problem (Granot, 2007; van Eerten, 2018). These collimated relativistic jets produced by the collapse of a massive star (long GRBs) (Woosley, 1993; MacFadyen & Woosley, 1999) or a compact binary merger (short GRBs) (Eichler et al., 1989; Mochkovitch et al., 1995) exhibit features crucial to our understanding of their behaviour over several orders of magnitude in time and space. Various analytical and semi-analytical models for the lateral spreading of afterglow jets based on single shell models exist in the literature (Rhoads, 1999b; van Eerten et al., 2010a; Wygoda et al., 2011; van Eerten & MacFadyen, 2012; Granot & Piran, 2012; van Eerten & Macfadyen, 2013; Duffell & Laskar, 2017; Ryan et al., 2020). However, even when calibrated on simulations these do not capture the full radial and angular profiles computed by simulations. In the last 20 years, dynamical simulations of GRB blast waves have evolved from one-dimensional (1D) Lagrangian computations of the evolution of spher-

ically symmetric fireballs (Kobayashi et al., 1999; Daigne & Mochkovitch, 2000), to state-of-the-art two-dimensional (2D) and three-dimensional (3D) Eulerian simulations (Kumar & Granot, 2003; Cannizzo et al., 2004; Zhang & MacFadyen, 2009; van Eerten et al., 2010a; Meliani & Keppens, 2010; De Colle et al., 2011; Wygoda et al., 2011; van Eerten et al., 2012). The latter can simulate the sideways interaction of collimated jets with the circumburst (CSM) medium and provide insight in the stability of the ejecta-CSM interface. Unfortunately, these approaches remain particularly computationally expensive. They rely on intense adaptive mesh refinement (AMR) procedures in order to capture the extreme resolution needed to properly resolve the head of the jet and converge before the onset of the jet’s sideways expansion. As it is notoriously difficult to resolve jet spreading behavior in the lab frame even with AMR, a first successful approach improving convergence and computational efficiency has been to move the computation in a Lorentz-boosted frame (van Eerten & Macfadyen, 2013). Moving at fixed velocity along the jet axis, this frame minimises the Lorentz-contraction of the blast-wave and relaxes the resolution constraints.

The use of arbitrary Lagrangian-Eulerian (ALE) methods helps to improve the numerical resolution of simulations of astrophysical flow, as has been demonstrated for Newtonian dynamics by e.g. AREPO (Springel, 2010; Weinberger et al., 2020). In this finite-volume approach, the mesh edges can be moved arbitrarily during the dynamical evolution. In practice, matching the mesh motion to that of the fluid provides significant improvement in terms of time-stepping and resolution around shocks as the numerical prescription effectively becomes pseudo-Lagrangian. Duffell & MacFadyen (2011) implemented this approach in the special relativistic context in their code TESS, finally opening the door to numerically capturing the trans-relativistic evolution of GRB jets across scales from the ultra-relativistic stage to the deceleration. Furthermore, in cases in which fluid motion is dominant in one direction, further progress was made by sidestepping the need for computationally expensive re-gridding operations usually associated with moving meshes. JET (Duffell & MacFadyen, 2013) and DISCO (Duffell, 2016) take advantage of this directionality and model the dynamics on parallel ‘tracks’ along which fluid zones can move freely, leading to a significant increase in computational efficiency.

As a result, the bottleneck for accurate modeling of highly energetic transients currently lies in the calculation of associated radiative emission. GRB afterglows are the result of synchrotron emission from shocks forming in the head of the jet as it interacts with the CSM (Rees & Meszaros, 1992; Meszaros & Rees, 1997). Current numerical radiative prescriptions rely on approximations of the evolution of the micro-physical state in the fluid downstream of these shocks. The widely used global cooling approximation

assumes a single micro-physical state across the whole fluid profile that evolves globally with time since the explosion (Sari et al., 1998). While this conserves the scalings and closure relations in each regime of the resulting spectra, this approximation is known to produce errors in the absolute flux level by up to a decade, as well as an incorrect position of the characteristic spectral break frequencies (van Eerten et al., 2010a; Guidorzi et al., 2014). This makes any broadband interpretation of the data across timescales very difficult. While analytical solutions locally calculating the micro-physical states have been used for 20 year now (Granot & Sari, 2002) and produce satisfying results in the ultra-relativistic limit of top-hat jets observed on-axis, an accurate description across all stages of jet evolution is still missing. Having at our disposal a numerical tool capable of computing such radiation accurately, efficiently and with precision promises to finally allow broadband fitting of afterglow light-curves and spectra. This toolkit could achieve this by refining the current templates and providing benchmarking opportunities for more efficient semi-analytical approaches, while also allowing for the accurate study of edge cases involving complex dynamics and multiple radiation emission sites.

In this work, we present a new numerical code, **GAMMA**, and use it to show the striking difference obtained in the radiative evolution in the trans-relativistic phase of the jet's life compared to previous approaches. In order to achieve this calculation, **GAMMA** combines the moving mesh approach to multi-dimensional dynamical simulations seen in JET and DISCO with a local calculation of the micro-physical accelerated particle population evolution. The local cooling approach is possible thanks to the increased resolution from the moving mesh around the shocks that allows accurate computation of the rapidly evolving particle energy distribution. In §4.2 we describe the dynamical part of the code. §4.3 is dedicated to standard tests of the dynamics. We also investigate the code's ability to capture complex dynamics by reproducing results from a study of Rayleigh-Taylor (RT) instabilities at the contact discontinuity between ejecta and CSM (Duffell & MacFadyen, 2013). We then describe the local cooling prescription in §4.4. Finally, in §4.5 we present the calculation of accurate synthetic afterglow light-curves and spectra from early to late times from the forward shock (FS) from 2D axisymmetric simulations of a GRB jet. A discussion of the implications and limitations of our work is presented in §4.6.

4.2 Code description

GAMMA uses a Godunov scheme to solve hyperbolic systems of partial differential equations (PDEs) in one and two dimensions (3-dimensional evolution will be implemented

at a later stage). The solvers currently implemented correspond to special relativistic hydrodynamics (SRHD). New solvers (e.g magneto-hydrodynamics) can be added easily. The code follows the same approach as JET and DISCO (Duffell & MacFadyen, 2013; Duffell, 2016) with the addition of the radiation module and a treatment of parallelisation that takes advantage of shared memory architectures. In this section we describe the numerical approach to the dynamics. The radiative local particle acceleration and cooling and the associated radiation are described in §4.4.

4.2.1 Special relativistic hydrodynamics

The fluid can be described by a state vector of *primitive variables* $\mathbf{V} = (\rho, \vec{v}, p)^T$, where ρ and p are the rest-mass density and pressure in the co-moving frame, and \vec{v} is the fluid velocity in the lab frame. We solve the following system of equations:

$$\partial_t \mathbf{U} + \nabla \mathbf{F}(\mathbf{U}) = \mathbf{S}, \quad (4.1)$$

Where \mathbf{U} and $\mathbf{F}(\mathbf{U})$ are the vector of *conserved variables* and the corresponding flux vector, respectively, and \mathbf{S} is the source term. ∇ is the divergence operator broadcast on all spatial vector components of $\mathbf{F}(\mathbf{U})$. \mathbf{U} and $\mathbf{F}(\mathbf{U})$ are expressed in terms of primitive variables as follows:

$$\mathbf{U} = \begin{pmatrix} D \\ \vec{m} \\ \tau \end{pmatrix} \equiv \begin{pmatrix} \rho\Gamma \\ \rho h\Gamma^2 \vec{v} \\ \rho h\Gamma^2 - p - D \end{pmatrix} \quad \begin{array}{l} \text{(Rest-mass density)} \\ \text{(Momentum)} \\ \text{(Energy)} \end{array}, \quad (4.2)$$

$$\mathbf{F}_i(\mathbf{U}) = \begin{pmatrix} Dv_i \\ \vec{m}v_i + p\hat{i} \\ m_i - Dv_i \end{pmatrix}, \quad \forall i \in \{x, y, z\}, \quad (4.3)$$

where \hat{i} is the unit vector in the i -direction, h is the specific enthalpy including rest-mass energy in the co-moving frame, Γ is the Lorentz factor, and the speed of light is set to $c = 1$. The SRHD equations can be cast in their angular momentum conserving form identical to eq. 4.1 for cylindrical (r, θ, z) and spherical (r, θ, ϕ) coordinates (Mignone & McKinney, 2007). This requires that we replace, in the conservation equation, the θ component of linear momentum m_θ in \mathbf{U} with the the angular momentum rm_θ , and the flux of the θ momentum $F_{i\theta} = m_\theta v_i + p\delta_\theta^i$ with $rF_{i\theta}$. With this form of the equations,

the following source terms appear in 2D:

$$\text{cylindrical} \quad \mathbf{S} = (0, p/r, 0, 0)^T, \quad (4.4)$$

$$\text{spherical} \quad \mathbf{S} = (0, (\rho h \Gamma^2 v_\theta^2 + 2p)/r, p/\tan \theta, 0)^T, \quad (4.5)$$

where the pressure terms compensate our inclusion of p in the divergence and the other term is a "geometrical" source term. The calculation of the geometrical source terms for the linear momentum conserving form, for any set of orthogonal curvilinear coordinates, is presented in the appendix of [Mignone et al. \(2005\)](#). The corresponding derivation in the case of SRHD is reported in the appendix of [Zhang & MacFadyen \(2006\)](#), which is equivalent to our approach. The full conservation equations can also be derived in any curved metric using the "Valencia formulation" ([Banyuls et al., 1997](#)) against which we compared our expressions.

We close the system of equations with the Synge-like ideal mono-atomic fluid equation of state (EOS) from [Meliani et al. \(2004\)](#) based on the relativistic perfect gas law ([Synge, 1957](#); [Mathews, 1971](#)):

$$p(\rho, \epsilon) = \rho \epsilon (\gamma_{\text{eff}} - 1), \quad (4.6)$$

where ϵ is the specific internal energy and γ_{eff} the effective polytropic index of the fluid given by:

$$\gamma_{\text{eff}} = \gamma - \frac{\gamma - 1}{2} \left(1 - \frac{1}{e^2} \right). \quad (4.7)$$

$\gamma = 5/3$ is the fixed adiabatic index of the fluid in the non-relativistic (cold) case, and e the specific internal energy including rest-mass. γ_{eff} is dependent on the fluid temperature such that $\gamma_{\text{eff}} = 4/3$ in the ultra-relativistic case and $\gamma_{\text{eff}} = 5/3$ in a non-relativistic fluid and allows for a trans-relativistic description of the evolution. This description is a very good approximation to the Synge gas equation and avoids the costly evaluation of associated Bessel functions.

4.2.2 Riemann solver

The code is based on a finite-volume Godunov scheme. The simulation domain is divided in discrete volumes, or cells in which the local fluid state is averaged. To evolve the system we solve a Riemann problem at each interface by calculating the corresponding Riemann fan of waves emerging from the discontinuity and the associated fluxes. At this stage, **GAMMA** includes the HLLC ([Mignone & Bodo, 2006](#)) solver for

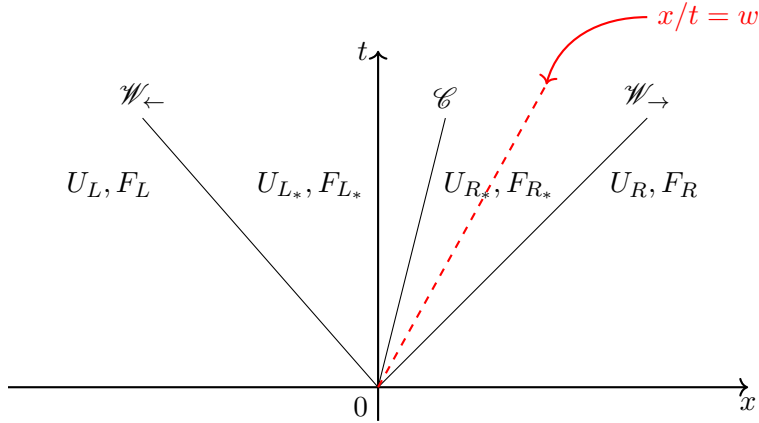


Figure 4.1: Schematic representation of a Riemann problem. The dashed red line shows the movement of the interface at velocity w . The flux across the interface, and the state chosen to correct for the motion of the interface, will be F_{R^*} and U_{R^*} , respectively.

relativistic hydrodynamics. This solver builds on the two-wave HLL solver (Harten et al., 1983) by adding a calculation of the wavespeed of the contact discontinuity (CD). As explained in the next section, we set the interface velocity to that of the CD and thus require the use of a complete three-wave solver.

GAMMA follows an arbitrary Lagrangian-Eulerian approach (ALE). This means that it can compute inter-cell fluxes for arbitrary interface velocities, in any direction. Figure 4.1 describes a Riemann problem for a moving interface with velocity w . For the HLLC hydrodynamics solver, three waves (W_{\leftarrow} , C , W_{\rightarrow}) emerging from the discontinuity split the fluid in 4 regions (L , L_* , R_* , R). The flux across the interface is given by $F = F_{\text{Riemann}} - wU_{\text{Riemann}}$, where F_{Riemann} and U_{Riemann} are the flux and state vectors of the fluid in the region in which sits this interface (region R_* in the situation depicted in figure 4.1).

4.2.3 Moving mesh and parallelisation

Moving meshes provide several advantages to simulate the evolution of GRB afterglows, but more broadly to simulate dynamics over a wide range of scales. First, the time-step can be increased for smooth regions of high velocity, where it is essentially limited by the speed of sound, in comparison to fixed-mesh approaches where the bulk velocity is the limiting factor. This is of particular interest to us as we look to maximising the resolution downstream of shocks to capture local cooling accurately. Second, a moving mesh matching the fluid velocity ends up naturally refining the regions of strong gradients as the fluid zones pile-up in compression waves and shocks. Because we are

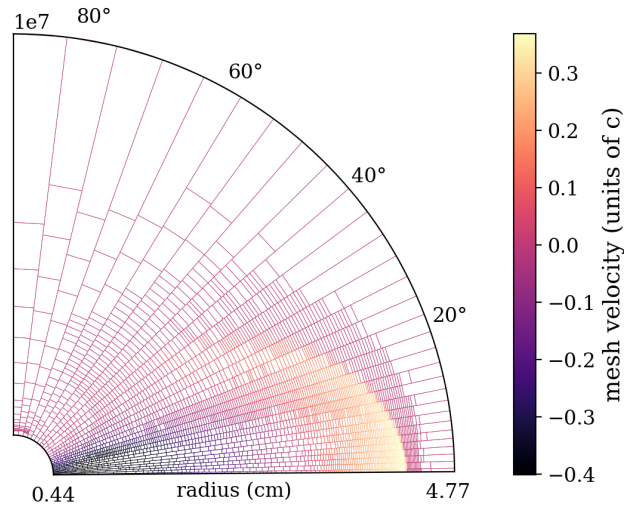


Figure 4.2: Mesh radial velocity and interface positions for a low-resolution example of a relativistic GRB jet. Axi-symmetry at $\theta = 0$ and planar symmetry at $\theta = 90$ deg allow us to restrict the simulation to $\theta \in [0, \pi/2]$. The resolution naturally increases at the shock without the need for active adaptive mesh refinement.

trying to capture the very fast evolving particle population downstream of shocks, a pseudo-Lagrangian approach is ideal.

The mesh is allowed to move in one direction, that we will assume to be the x -direction for the rest of this section. The transverse direction will be called y as the treatments remain the same in 2D or 3D. The simulation grid is built as a set of tracks along which the interfaces between the cells are allowed to move at arbitrary velocity. This frees us from the re-gridding operations associated with mesh entanglement, and ensures that interfaces remain orthogonal to the coordinate system basis vectors. In practice, to maximise mass conservation in a given cell, we set interface velocity to the contact discontinuity velocity (\mathcal{C} wave in the Riemann fan). Figure 4.2 illustrates how the mesh moves following these tracks. Allowing the mesh to move forces us to re-compute the geometry of the interfaces between tracks for each time-step. For two neighbouring tracks, since the number of interfaces between them can significantly vary during the simulation, we allocate new interface objects in the code at each time-step, instead of evolving an array of interfaces from one time-step to another. While this approach is more computationally expensive, it is much easier to implement and less demanding in terms of memory.

We use a hybrid OpenMP/MPI approach to parallelisation in order to make use of

shared memory on a single node. This gives us more flexibility when dealing with variable numbers of cells per track. The simulation domain is cut in the y direction into a number N_{nodes} of regions containing an equal number of neighboring tracks, each region sent to a single node. Ultimately, depending on the number of nodes, tracks per node, and cells per track, the user will be able to choose to parallelise the computation in each region using OpenMP either in the moving x direction (for a given track, cell are distributed over the available cores) or in the fixed y direction (for a given region, track are distributed over the available cores). Parallelising in x minimises the number of cores in an idle state in a node, but runs into the risk of false sharing¹ for tracks with very few cells compared to the number of cores available, which is why we first implemented the parallelisation in y with the x version available soon. One limitation to our approach is when the average number of cells per track varies strongly from region to region (typical case in figure 4.2), which leads to some nodes having much fewer cells to evolve and sit idle. At this stage we compensate this by giving more tracks to these nodes to compute. Further improvements on parallelisation are expected in future versions of GAMMA.

4.2.4 Spatial reconstruction

GAMMA currently includes piecewise linear spatial reconstruction. Figure 4.3 shows a schematic representation of gradient calculation in two dimensions. In the x -direction, the reconstruction can be done independently in each track as the cell centers and the center of the interface between cells are aligned. we store the slope-limited gradients in the x -direction for use in the y -direction gradient calculation. Indeed, for reconstruction across tracks, we follow the procedure from Duffell (2016). The gradient \vec{w} inside a given cell is calculated using the following steps. First, for every interface i between two cells at (x_i, y_i) coordinate, we compute an associated gradient in the y -direction $w_{y,i}$ across this interface:

$$w_{y,i} = [\mathbf{W}^+(x_i) - \mathbf{W}^-(x_i)] / (y^+ - y^-) \quad (4.8)$$

$$\text{with } \mathbf{W}^\pm(x) = \mathbf{W}_0^\pm + \mathbf{w}_x^\pm(x - x_0^\pm) \quad (4.9)$$

where the $+$ and $-$ exponents denote the cell above and below the interface, respectively (see figure 4.3), \mathbf{W}_0^\pm is the cell-centered primitive fluid state and \mathbf{w}_x^\pm the gradient in

¹False sharing happens when several threads are trying to update independent variables on the same cache line at the same time (a cache line is a collection of neighbouring memory addresses loaded together by the processor when carrying out an operation on even only one address). Each thread must wait for the cache to be freed by competing processes in order to make their update. This makes the set of operations that should have been run in parallel actually occur linearly. To avoid false sharing, separate processes should be working on distant memory locations.

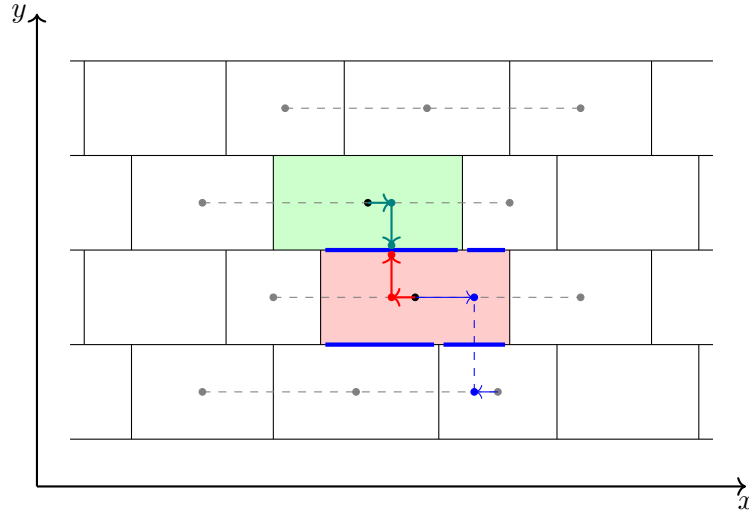


Figure 4.3: Schematic representation of the procedure to reconstruct the states left and right of the interface between the red and green cells. For example for the red cell, the first step is to compute the transverse gradients for all the y -interfaces of the cell (marked in blue). These gradients are measured between states projected on the x coordinate corresponding the center of the interface using the x gradients already computed (gray dashed lines) We then compute the average gradient for the cell and apply the slope limiter. Using this gradient for each cell, it's possible to reconstruct the red and green states.

the x -direction. We then compute an averaged gradient $\bar{\mathbf{w}}_y$ for the considered cell from the gradients associated with all the interfaces composing its two y -faces, weighted by their respective surface areas $A_{y,i}$:

$$\bar{\mathbf{w}}_y = \frac{\sum_{i \in \{\text{interfaces}\}} \mathbf{w}_{y,i} A_i}{\sum_{i \in \{\text{interfaces}\}} A_i} \quad (4.10)$$

To avoid spurious oscillations we apply a minmod slope limiter such that the final gradient value in the y -direction is:

$$\mathbf{w}_y = \text{minmod}(\bar{\mathbf{w}}_y, (\mathbf{w}_{y,i})_{i \in \{\text{interfaces}\}}), \quad (4.11)$$

Once the gradients have been computed in all directions for every cell, it is then possible to finally compute the fluid states on either sides of every interface by interpolating from the cells centers:

$$\mathbf{W}(\vec{r}_i) = \mathbf{W}_0 + \vec{r}_i \cdot \vec{\mathbf{w}}, \quad (4.12)$$

where \vec{r}_i is the interface coordinate calculated from the cell centroid to ensure quantity conservation during spatial reconstruction. Indeed, this method returns a single gradi-

ent to be used to reconstruct the states at all interfaces of a given cell. Even though this gradient is a quantity averaged from all the gradients with neighbouring cells, the Riemann solver will then use the reconstructed states on each side of each interface to compute the inter-cell flux, which enforces strict mass and energy conservation, even at higher orders.

4.2.5 Time-stepping and adaptive mesh refinement

The cell conserved quantities are updated by summing over all fluxes across their associated interfaces in all directions, for each time-step (method of lines), while accounting for potential source terms. The moving interface positions are updated according to their measured velocities during this time-step too, which leads to minimum fluxes (and zero flux in mass) across them when setting their velocity to that of the CD. The time-integration can be chosen between Euler time-stepping and third order Runge-Kutta, which has the advantage of being total-variation-diminishing. We use an adaptive time-step based on a Courant-Friedrich-Lewy (CFL) condition ([Courant et al., 1928](#)). This introduces issues when combined with a moving mesh as compressed fluid cells will lead to a detrimental decrease in time-step if no lower bound is chosen for their size. We implement the ability for the user to set up their own criteria for adaptive mesh refinement and include in the code methods to split and merge cells together on a single track. The code offers two different modes for re-gridding: a "runaway" mode in which the total number of cells on a given track is only constrained by a maximum value, and a "circular" mode in which every call of the merge/split function calls an instance of the split/merge function on a cell in the same track based on a calculation of its "re-gridding score" that can also be set by the user. This "circular" mode ensures that the total number of cells on a single track is constant throughout the simulation.

The new physical state in cells post-merger are averaged over the two states in the cells prior to merger, ensuring quantity conservation. Cell-splitting follows linear interpolation of the conserved variables from the new cells centroids. We apply the same slope limiter as in the spatial reconstruction on the gradient used for the interpolation. This ensures quantity conservation and limits oscillations around shock fronts.

4.3 Tests

We evaluate the accuracy and convergence of the code on a range of standard tests. All tests are carried out with a CFL condition of 0.4 unless stated otherwise.

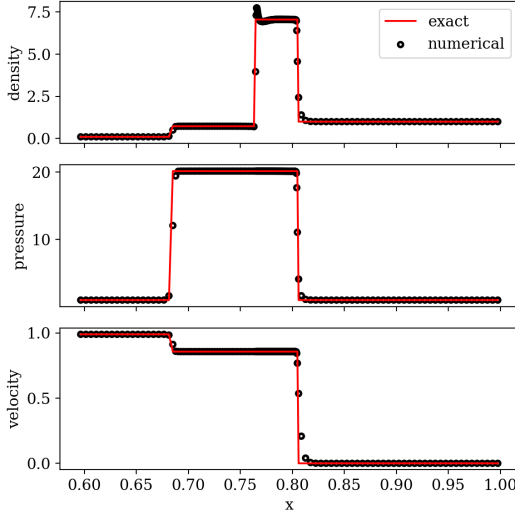


Figure 4.4: Shock tube in Cartesian coordinates. $t = 0.6$. Initial discontinuity at $x = 0.25$ (outside of the range in x shown here, the waves having moved towards increasing x). Left state: $\rho = 0.1$, $p = 1$, $v = 0.99 \times c$. Right state: $\rho = 1$, $p = 1$, $v = 0$. Ideal EOS with $\gamma = 4/3$. Initial resolution is 200 cells

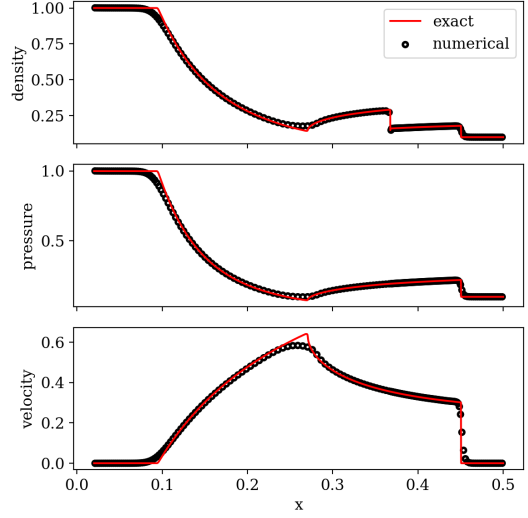


Figure 4.5: Shock tube in spherical coordinates. $t = 0.3$. Initial discontinuity at $x = 0.25$. Left state: $\rho = 1$, $p = 1$, $v = 0$. Right state: $\rho = 0.1$, $p = 0.1$, $v = 0$. Ideal EOS with $\gamma = 4/3$. Initial resolution is 200 cells

4.3.1 1D relativistic shock tubes

In figure 4.4 we show the result of a relativistic 1D shock tube in cartesian coordinates with the following parameters:

$$(\rho, v, p) = \begin{cases} (0.1, 0.99, 1) & \text{for } x \leq 0.25, \\ (1, 0, 1) & \text{for } x > 0.25, \end{cases} \quad (4.13)$$

where v is in units of c . We also choose a fixed adiabatic index $\gamma = 4/3$. In figure 4.5 we test our correct implementation of spherical coordinates and show the result of a relativistic 1D shock tube with parameters:

$$(\rho, v, p) = \begin{cases} (1, 0, 1) & \text{for } x \leq 0.25, \\ (0.1, 0, 0.1) & \text{for } x > 0.25. \end{cases} \quad (4.14)$$

In both systems of coordinates, the code is able to properly capture the shock positions as well as the contact discontinuity. The motion of the interfaces at the fluid velocity allows us to resolve contact discontinuity with only a couple of zones in these tests.

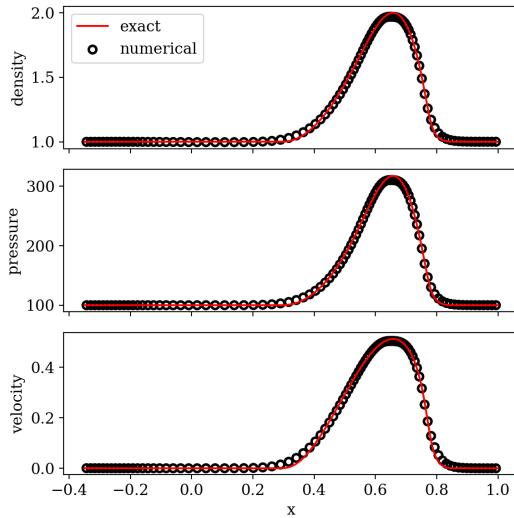


Figure 4.6: 1D Isentropic wave test output for primitive variables with 100 fluid zones. The numerical results at $t = 0.7$ (black circles) are in very good agreement with the exact solution (red solid curve)

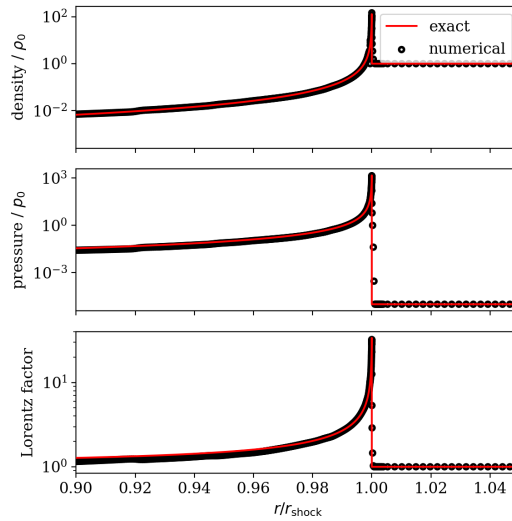


Figure 4.7: Blandford-McKee blast-wave output at $t = 8.81 \times 10^6$ s. $E_{\text{iso}} = 10^{53}$ erg, initial peak fluid Lorentz factor $\Gamma = 100$, CSM number density $n_0 = 1 \text{ cm}^{-3}$.

4.3.2 Isentropic wave

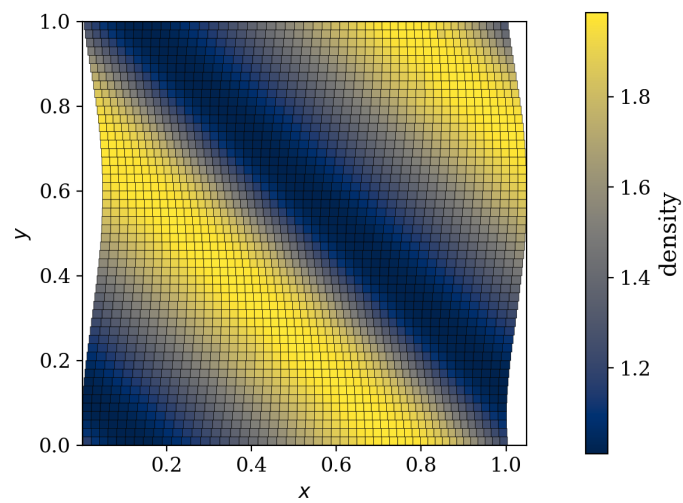
We test the accuracy of our code for smooth regions of the flow by simulating the evolution of a 1D isentropic wave in cartesian coordinates. The setup we use is identical to that of [Zhang & MacFadyen \(2006\)](#). We choose a fixed adiabatic index $\gamma = 5/3$ for this setup. A comparison of the exact solution and the numerical result is shown in figure 4.6. The convergence rates at different resolutions are reported in table 4.1. We nearly reach second order convergence for this test. We also assess the order of convergence of the code in two dimensions by running the isentropic wave in a direction diagonal to the initial grid in cartesian coordinates. This setup is identical to the one from [Duffell & MacFadyen \(2011\)](#). We choose periodic boundary conditions and fix the boundaries to a $[0, 1] \times [0, 1]$ box. We constrain the aspect ratio of the cells in the simulation domain to the $[0.5, 2]$ interval. A snapshot in which we have instead allowed the boundaries to move (with a periodic boundary condition still however), showing the distortion of the grid, is shown in figure 4.8. We report the convergence rates for the fixed boundaries case in table 4.2.

4.3.3 2D Riemann problem

To assess more complex 2D behavior of the code, we run a 2D Riemann problem with the same parameters as [Mignone & Bodo \(2006\)](#). This setup involves the interaction

Table 4.1: Convergence analysis for the 1D isentropic wave test

Resolution	L1 error	Convergence rate
100	4.41e-3	
316	5.87e-4	1.85
1000	6.15e-5	1.92
3160	6.92e-6	1.89

**Figure 4.8:** 2D isentropic wave test at $t = 0.7$ with initial uniform grid of resolution of 50×50 . In this case, the mesh is allowed to move the x direction and distorts with the waves. The waves remain diagonal to the grid directions and follow the expected theoretical evolution, propagating towards increasing x and y .**Table 4.2:** Convergence analysis for the 2D isentropic wave test

Resolution	L1 error	Convergence rate
20x20	1.93e-2	
50x50	3.71e-3	1.80
100x100	1.18e-3	1.65
300x300	3.46e-4	1.12

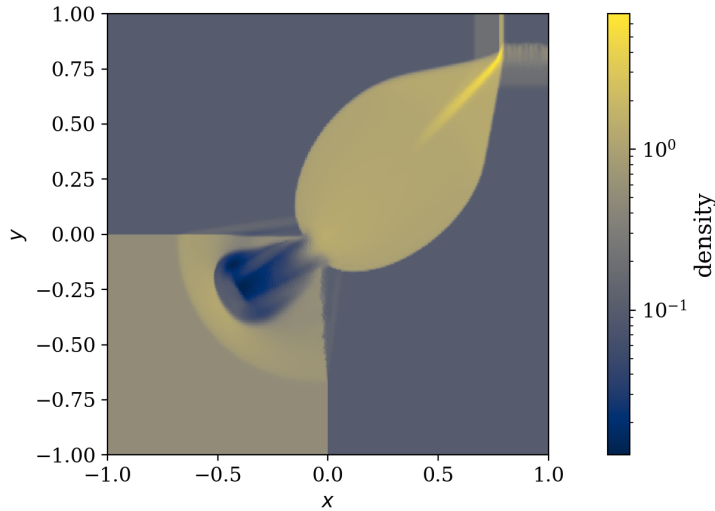


Figure 4.9: Density output for the 2D Riemann problem at $t = 0.8$. Initial uniform grid of resolution 300×300 . The mesh moves in the y direction. Even though the mesh only moves in one direction, we observe a symmetrical evolution where the only difference between the x and y directions is the higher diffusion around the shocks in the non-moving direction.

of four elementary waves formed at the interfaces between four initial different fluid states. On a square domain spanning $[-1, 1] \times [-1, 1]$, their setup is the following:

$$(\rho, v_x, v_y, p) = \begin{cases} (0.1, 0, 0, 0.01) & \text{for } x, y > 0 \\ (0.1, 0.99, 0, 1) & \text{for } x < 0 < y \\ (0.5, 0, 0, 1) & \text{for } x, y < 0 \\ (0.1, 0, 0.99, 1) & \text{for } y < 0 < x \end{cases}. \quad (4.15)$$

In our setup, we use a resolution of 300×300 and allow the mesh to move in the x direction and constrain the aspect ratio in the interval $[0.2, 3]$. We show the output density at final time $t_f = 0.8$ in figure 4.9. This test confirms the accuracy of the code in both the directions aligned and transverse to the mesh motion. It also highlights the increase in precision around shocks parallel to the mesh motion as features in the x direction are more diffuse. The slight asymmetry in the region of lowest density is attributed to the difference in treatments between the x and y directions and nicely confirms the improvement in the direction of mesh motion. This region also particularly suffers from a high frequency of de-refinement operations on the lower-right edge, which is responsible for the loss in precision.

4.3.4 1D GRB jet - Blandford Mckee blast wave profile

A first application of this code to one-dimensional GRB blast wave simulations is done in [Ayache et al. \(2020\)](#). It is important for any code applied to ultra-relativistic blast waves to demonstrate its ability to properly capture dynamics in these extreme regimes. As such an very important test is the comparison with the analytical solution for a relativistic point-like explosion, the Blandford-McKee (BM) solution ([Blandford & McKee, 1976](#)). GRB blast waves transition to this asymptotic solution as they sweep up CSM material and it is surprisingly hard for fixed mesh AMR codes to properly capture the peak of the blast-wave, where particle acceleration happens. Here, we set up a BM solution at time t_0 (corresponding to an initial Lorentz factor Γ_0) and check that our numerical solution still matches the expected radial profile for the fluid quantities for $t > t_0$. We set up a blast wave with isotropic equivalent energy $E_{\text{iso}} = 10^{53}$ erg and CSM uniform number density $n_0 = 1\text{cm}^{-3}$ at an initial peak fluid Lorentz factor $\Gamma_0 = 100$ (initial time $t_0 = 4.36 \times 10^6$ s). Figure 4.7 shows the radial profile of primitive variables at $t = 8.81 \times 10^6$ s. The code accurately captures the shock position and the radial profile of the blast wave. Our code also fully captures the time evolution of the peak Lorentz factor at the shock front, which we demonstrate for two dimensions in §4.5.3. The peak four-velocity directly downstream of the shock u_{Peak} follows the expected evolution $u_{\text{Peak}} \propto t^{-3/2}$ (fig. 4.13) very closely until the onset of transverse motion (jet spreading). In this 1D test, we use the same AMR criteria as in the 2D simulations described §4.5.2, using a fiducial angular track width $d\theta = \pi/2000$. We can see the advantage of the moving mesh approach where we can resolve the blast wave with little added computational cost as the region limiting the time-step is situated just ahead of the shock.

4.3.5 2D GRB jets - Rayleigh-Taylor instabilities in afterglows

Moving to two dimensions, we show the ability of the code to capture complex dynamics by investigating the growth of Rayleigh-Taylor (RT) instabilities at the contact discontinuity between the ejecta and the CSM. [Duffell & MacFadyen \(2013\)](#) (hereinafter [DM13](#)) have already shown that RT instabilities can appear at the contact discontinuity in GRB afterglows by running moving mesh dynamical simulations. We reproduce here their approach and compare our results with those obtained using their code JET.

Initial setup

We implement the fireball model ([Kobayashi et al., 1999](#)) in which we input a given amount of energy E_{iso} and mass M into a small sphere of radius R_0 placed in a uniform

Table 4.3: Initial parameters for the 2D GRB RT simulations

Parameter	Notation	Value	Unit
Equivalent Isotropic Energy	E_{iso}	10^{52}	erg
Coasting Lorentz factor	Γ	30;100	
Initial radius of the fireball	R_0	100;0.4	l.s.
CSM number density	n_0	1	cm^{-3}
Temperature of CSM ($p/\rho c^2$)	η	10^{-5}	

CSM of mass density ρ_0 . At the initial time, the velocity of the fluid is 0 in the whole system. The thermal energy in the hot fireball is then converted to kinetic energy and the resulting blast wave will coast with fluid Lorentz factor $\Gamma = E_{\text{iso}}/M$. Like DM13 we place ourselves in the *thin shell* limit where the initial structure of the fireball does not influence the evolution after $t_\gamma = (M/\Gamma\rho_0)^{1/3}$. This is done by choosing R_0 small enough in order for the coasting and spreading phases to happen long before the deceleration phase: $\Gamma^2 R_0 \ll t_\gamma$ (Kobayashi et al., 1999). We run two simulations with $\Gamma \equiv 30$ (run30) and $\Gamma \equiv 100$ (run100). Setting $E_{\text{iso}} \equiv 10^{52}$ erg determines the corresponding value of M . The rest of the initial parameters are reported in table 4.3.

1D early run and grid parameters

All simulations are carried out in axisymmetric spherical coordinates (r, θ, ϕ) . For the sake of computational efficiency, we first run 1D simulations of the acceleration and coasting phases of the fireball, before deceleration. 1D simulations are sufficient in this regime since the collimated jet is not yet causally connected and we can thus assume spherical symmetry. Transverse motion will appear with the instabilities after the deceleration time and we will need to transition to 2D before then. We initialise the fireball on a logarithmic radial grid with 600 cells. The inner boundary is initially placed at $0.01 R_0$ and set to reflective boundary conditions. After the acceleration phase, we set the inner boundary velocity to $0.5 c$ and outflow boundary conditions to reduce the computation grid size. The outer boundary moves at $1.05 c$ throughout the whole simulation. We call r_{max} this increasing outer radius. In the 2D stage, we set reflective boundary conditions at $\theta = 0$ and $\theta = \theta_{\text{simu}}$.

We transition to the 2D simulations at $t \sim 0.5 t_\gamma$, by broadcasting the result of the 1D solution onto $N_\theta \equiv 200$ radial tracks evenly distributed in the interval $\theta \in [0, \theta_{\text{simu}} \equiv \pi/32]$. Since our simulation domain is half as wide, this corresponds to the 400 tracks case in DM13. We run the simulation until $t_M = (M/\rho_0)^{1/3}$ which is the time at which the blast-wave becomes non-relativistic. In both the 1D and 2D stages, the radial resolution is governed for each cell by a modified cell aspect ratio criterion $\hat{a} = dr/(r_{\text{max}}d\theta)$. We choose to use \hat{a} instead of the actual aspect ratio $a = dr/(rd\theta)$ to

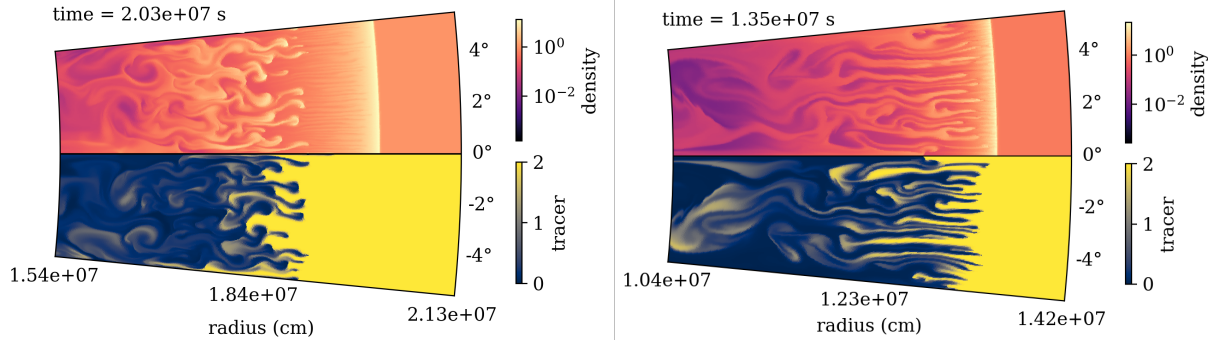


Figure 4.10: 2D Snapshots at $t = t_M$ of run30 (left) and run100 (right). The density is normalised by ρ_0 . The tracer highlights the mixing between ejecta material (tracer=0) and CSM material (tracer=2).

prevent the time-step from being limited by the cells located at small radii at later stages of the evolution. For each cell, \hat{a} is allowed to vary in the interval $\hat{a} \in [0.2, 5]$. We normalise the pressure and density by ρ_0 and $\eta\rho_0c^2$, respectively. Throughout the evolution we floor the normalised density and pressure to 10^{-10} .

Results

Snapshots at t_M for run30 and run100 are shown in figure 4.10 and the corresponding radial profiles are reported in figure 4.11. We obtain very similar results to DM13. The radial profiles in 2D were obtained by averaging the fluid quantities over the θ direction weighing track contributions by their respective volumes. We also ran 1D simulations up to t_M to compare with the results from the 2D runs. First looking at these radial profiles, our forward shock (FS) closely coincides with the FS in the simulations of DM13. However, we notice a discrepancy in the reverse shock (RS) position and a difference in the rest-mass density behind the ejected material. This not linked to our different choice of EOS (they use an ultra-relativistic ideal gas with fixed $\gamma = 4/3$, as opposed to our trans-relativistic EOS) as the difference is still visible when switching to their fluid description. We have confirmed that mass was conserved in the ejecta using the passive scalar tracer we have set up. Finally we ran the code for various values of R_0 and noticed no significant difference between our runs. DM13 do not specify the treatment of their inner boundary.

The 2D runs exhibit the same features as those found in DM13. We observe Rayleigh-Taylor instability at the contact discontinuity growing from the numerical noise without the need for seeding. We can also confirm the influence of this instability on the position of the RS. As the instability grows, the turbulence is able to reach the RS and pushes it faster towards the back of the ejecta. This effect is particularly well visible

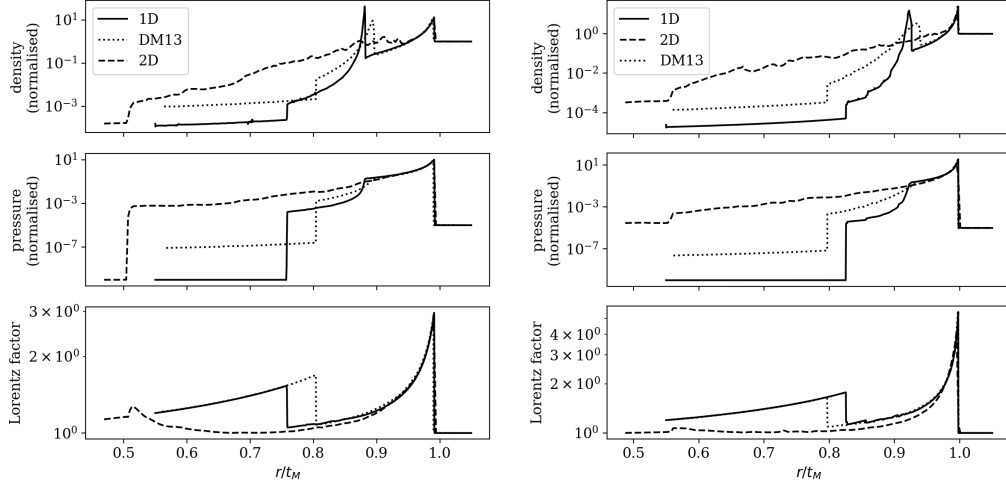


Figure 4.11: Radial profiles at $t = t_M$ for run30 (left) and run100 (right). Density and pressure are normalised by the external medium density value. The DM13 curve is their 1D solution. In all cases, the forward shock is very accurately captured. In 2D, the RT instabilities push the reverse shock further at the back of the ejecta.

in run30 in figure 4.11 and so strong in run100 that the RS has actually already left the simulation domain at t_M . In order to properly quantify this effect, we would need to run higher resolution simulations like in DM13 as the transverse size of the tracks currently prevents the instability from growing properly. While sufficient resolution is almost achieved in run30, we do not observe the smaller scales expected at higher Lorentz factors. In run100 the maximum angular size at which RT instability can develop is $1/150$ rad, corresponding to 13.6 angular track widths. It is therefore likely that smaller scale instability was not sufficiently resolved.

These results confirm the ability of the code to properly capture complex relativistic dynamics on a moving mesh. They also confirm that the CD can be unstable in the afterglow. Since this particular phenomenon has previously been explored in the literature, we refer the reader to DM13 for more in depth analysis, where they show that the instability does not affect the forward shock emission, but causes the reverse shock contribution to peak later and the corresponding flash to be narrower.

4.4 Local synchrotron cooling

We have shown in the previous two sections that our code is able to properly capture complex relativistic hydrodynamics on a moving mesh. In this section, we describe our approach to implementing local tracing and radiation of particles accelerated at the

shock fronts in the fluid.

4.4.1 Tracing of accelerated particles

We follow the prescription first described in [Downes et al. \(2002\)](#) and [van Eerten et al. \(2010b\)](#) and implemented on a moving mesh in one dimension in [Ayache et al. \(2020\)](#). We expand on this previous implementation by including a description of the spectral evolution of the particle population that depends on shock velocity.

Shock waves are responsible for the acceleration of electrons that radiate in synchrotron across the whole electromagnetic spectrum. We model this accelerated population with a truncated power-law in energy ([Sari et al., 1998](#); [Wijers & Galama, 1999](#)):

$$n'(\gamma'_e) \propto \begin{cases} (\gamma'_e)^{-p} & \text{if } \gamma_{\min} < \gamma'_e < \gamma_{\max}, \\ 0 & \text{otherwise,} \end{cases} \quad (4.16)$$

where primed quantities are expressed in the co-moving frame. n' is the spectral number density as a function of γ'_e the Lorentz factor of an electron. γ_{\min} is the minimum Lorentz factor (of the bulk of the population) and γ_{\max} is the maximum Lorentz factor that decreases as the population cools. p is the spectral index (power-law slope of this population). The distribution is normalised by considering that a fraction ζ of electrons are accelerated and carry a fraction ϵ_e of the internal energy density $e = \rho\epsilon$. The cooling of these electrons is driven by synchrotron losses and adiabatic expansion:

$$\frac{d\gamma'_e}{dt'} = -\frac{\sigma_T(B')^2}{6\pi m_e c} (\gamma'_e)^2 + \frac{\gamma'_e}{3\rho} \frac{d\rho}{dt'}, \quad (4.17)$$

with $B' = \sqrt{8\pi\epsilon_B e}$ the local magnetic field intensity derived from magnetic energy expressed as a fraction ϵ_B of internal energy. m_e and σ_T are the electron mass and the Thompson cross section, respectively. This expression can be re-cast into an advection equation:

$$\frac{\partial}{\partial t} \left(\frac{\Gamma\rho^{4/3}}{\gamma'_e} \right) + \frac{\partial}{\partial x^i} \left(\frac{\Gamma\rho^{4/3}}{\gamma'_e} v^i \right) = \frac{\sigma_T}{6\pi m_e c} \rho^{4/3} (B')^2, \quad (4.18)$$

that the hydrodynamics solver can treat as a passive scalar with a source term. The bounds of the population of accelerated electrons are locally evolved downstream of shocks following this procedure. Particle injection at shock fronts is simply done by resetting the values of γ_{\max} and γ_{\min} . γ_{\max} directly downstream of the shock is theoretically set by the acceleration time-scale. For sufficiently large p it can be taken to be infinity. In practice, we just set $\gamma_{\max} = 10^8$ to a high enough value such that the

frequency cut-off in the observer frame is higher than 10^{18} Hz, the highest frequency at which we compute the radiation. γ_{\min} is set by normalising the total available energy over the electron population.

We have also added in the radiative code the possibility of using a local value of p . Indeed, most works currently assume fixed spectral index $p \sim 2 - 2.5$. However, we expect shock strength to vary during the dynamical evolution, which leads to a varying spectral index in the accelerated population. To evaluate the effect of this evolution we implement this in our shock detector and subsequently advect the spectral index value p as a simple passive scalar field:

$$\frac{\partial}{\partial t}(\Gamma \rho p) + \frac{\partial}{\partial x^i}(\Gamma \rho p v^i) = 0. \quad (4.19)$$

The initial value of p is chosen following [Kirk et al. \(2000\)](#) and [Keshet & Waxman \(2005\)](#) (see e.g. [Sironi et al. \(2015\)](#) and [Marcowith et al. \(2020\)](#) for recent reviews on particle acceleration in relativistic shocks), where we have identified the upstream fluid velocity with the bulk fluid velocity. This approximation greatly simplifies the implementation and is acceptable as we will only be interested in forward shock emission from GRB afterglows in this work, but a different approach would be needed for e.g. reverse shock contribution or internal shocks. The dependency of p on the upstream fluid four-velocity u is approximated by the following expression in our code (which is a rough fit to [Kirk et al. \(2000\)](#), sufficient as a first approach):

$$p = 2.11 + 0.11 \times \tanh(\log_{10}(u/3.16)). \quad (4.20)$$

We thus have $p \rightarrow 2$ and $p \rightarrow 2.22$ in the Newtonian and relativistic limits, respectively. It should be pointed out at this stage that this addition leads to issues in the initialisation of the accelerated particles. In short, decreasing values of p lead to decreasing values of γ_{\min} . If γ_{\min} gets too close to 1, our description of the particle population as a power-law in energy breaks down. In keeping with the mainstream approach, we focus on converting the total available energy in radiation and allow for values of $\gamma_{\min} < 1$. In the results we focus on the radiation at high energies around the cooling break. This issue and potential solutions are discussed in more details in §4.6.

4.4.2 Radiative flux calculation

To calculate the corresponding flux, we have adapted the linear radiative transfer approach and corresponding code from [van Eerten & Wijers \(2009\)](#) using the same simplified connected power-law description for synchrotron emission as in [van Eerten et al.](#)

(2010a). We intend to upgrade the code in the future with more a elaborate description including a treatment of the transition between these power-law regimes as described in van Eerten & Wijers (2009). For the sake of simplicity we neglect self-absorption here and focus on frequencies above the radio band.

The frequency at which a single electron with energy $\gamma'_e m_e c^2$ in the co-moving frame produces synchrotron radiation is $\nu_{\text{syn}}(\gamma'_e) = \frac{3q_e B'}{16m_e c} (\gamma'_e)^2$ with q_e the charge of the electron. We can now write $\nu'_{\text{min}} = \nu_{\text{syn}}(\gamma'_{\text{min}})$, and $\nu'_{\text{max}} = \nu_{\text{syn}}(\gamma'_{\text{max}})$. The spectral volumetric power for an emitting region of the fluid is given by:

$$P'_\nu = \begin{cases} P'_{\nu, \text{max}} \left(\frac{\nu}{\nu'_{\text{min}}} \right)^{1/3}, & \nu < \nu'_{\text{min}}, \\ P'_{\nu, \text{max}} \left(\frac{\nu}{\nu'_{\text{min}}} \right)^{-(p-1)/2}, & \nu > \nu'_{\text{min}}, \end{cases} \quad (4.21)$$

$$\text{with } P'_{\nu, \text{max}} = \frac{4(p-1)}{3p-1} \times n' \sigma_T \frac{4}{3} \frac{B'}{6\pi} \frac{16m_e c}{3q_e}. \quad (4.22)$$

where n' is the accelerated electron number density in the co-moving frame.

To account for local cooling, we implement a simple sharp cut-off in the spectral emissivity for frequencies above ν'_{max} in the fluid frame. In theory the emitted radiation follows and exponential cutoff that will be implemented in the future. We expect from our prescription a small underestimation of the true flux above the cooling break. This does not change the interpretation of the results from §4.5 as we will see the flux is generally higher with our approach compared to previous prescriptions. Eventually, once having taken into account the proper beaming factors depending on μ the cosine of the angle between the fluid velocity and the observer, and accounting for photon arrival times, the flux received at a given observer time t_{obs} for a given frequency ν can be integrated following:

$$F(\nu, t_{\text{obs}}) = \frac{1+z}{2d_L^2} \int_{-1}^1 d\mu \int_0^\infty r^2 dr \frac{P'_{\nu'}(r, t_{\text{obs}} + r\mu)}{\Gamma^2(1 - \beta\mu)^2}, \quad (4.23)$$

with d_L the luminosity distance and z the redshift.

4.4.3 Shock detection algorithm

This radiative prescription relies on accurate detection of the shock positions in the fluid. While Ayache et al. (2020) make use of a shock detector based on the calculation of the limiting relative velocities at cell interfaces in 1D from Rezzolla et al. (2003b) and Zanotti et al. (2010), we use in this work the more complex multi-dimensional version

of this detector, introduced by the same authors, that we describe in this section.

Let us consider a candidate discontinuity in fluid quantities in which we observe a jump in density, pressure and velocity between two regions denoted 1 and 2. This is the setup of a local Riemann problem for which we can compute a criterion on the relative velocity orthogonal to the discontinuity $v_{12} \equiv (v_1 - v_2)/(1 - v_1 v_2)$ for the formation of one shock and one rarefaction (\mathcal{SR}), or two shocks ($2\mathcal{S}$) in the resulting Riemann fan. By checking for this criterion on all the interfaces of the grid we can map the location of the shocks in all directions.

In the \mathcal{SR} case, the criterion is given by:

$$v_{12} > (\tilde{v}_{12})_{\mathcal{SR}} = \tanh \left(\int_{p_1}^{p_2} \frac{\sqrt{h^2 + \mathcal{A}_1^2(1 - c_s^2)}}{(h^2 + \mathcal{A}_1^2)\rho c_s} dp \right), \quad (4.24)$$

where c_s is the speed of sound and $\mathcal{A}_1 \equiv h_1 \gamma_1 v_1^t$, with v_1^t the transverse velocity. We compute $(\tilde{v}_{12})_{\mathcal{SR}}$ by numerical integration.

In this simple form, the algorithm does not discriminate on shock strength and can lead to the spurious detection of weak shocks. This can be adjusted by computing the limiting relative velocity for the $2\mathcal{S}$ case:

$$v_{12} > (\tilde{v}_{12})_{2\mathcal{S}} = \frac{(p_1 - p_2)(1 - v_2 \bar{V}_s)}{(\bar{V}_s - v_2)\{h_2 \rho_2 \gamma_2^2 [1 - v_2^2] + p_1 - p_2\}}. \quad (4.25)$$

We refer the reader to (Rezzolla et al., 2003b) for the explicit expression of \bar{V}_s which is the velocity of $\mathcal{S}_{\rightarrow}$ in the Riemann fan $\{1\mathcal{S}_{\leftarrow} 3\mathcal{C}3'\mathcal{S}_{\rightarrow}2\}$ in the limit case where $p_3 \rightarrow p_1$.

The shock detection threshold is adjusted by computing a new limit $(\tilde{v}_{12})_{\text{eff}}$ with adjustable parameter $\chi \in [0, 1]$ such that a shock is detected for:

$$v_{12} > (\tilde{v}_{12})_{\text{eff}} = (\tilde{v}_{12})_{\mathcal{SR}} + \chi[(\tilde{v}_{12})_{2\mathcal{S}} - (\tilde{v}_{12})_{\mathcal{SR}}]. \quad (4.26)$$

We find $\chi = 0.5$ produces satisfactory results in all the applications presented in this paper.

This procedure can be generalized to any spacetime metric (or system of coordinates) by projecting the velocities into a local tetrad following $v^{\hat{i}} = M_j^{\hat{i}} v^j$ (Pons et al., 1998). In this work we are only interested in spherical coordinates for which the projection simply reduces to $M_j^{\hat{i}} = \text{diag}(1, r, r \sin \theta)$.

Table 4.4: Initial parameters for the 2D GRB jet local cooling simulation

Parameter	Notation	Value	Unit
Dynamics:			
Equivalent Isotropic Energy	E_{iso}	10^{53}	erg
CSM number density	n_0	1	cm^{-3}
Initial peak Lorentz factor	$\Gamma_{\text{peak},0}$	100	
Corresponding initial time	t_0	4.36×10^6	s
Jet half-opening angle	θ_{jet}	0.1	rad
Temperature of CSM ($p/\rho c^2$)	η	10^{-5}	
Micro-physics:		slow / fast	
Fraction of accelerated e^-	ζ	1 / 0.1	
Electron energy	ϵ_e	0.1 / 0.1	
Magnetic energy	ϵ_B	0.01 / 0.1	

4.5 Synthetic GRB afterglow light curves with local cooling

4.5.1 Initial setup

We run simulations of spreading top-hat jets with local and global cooling. The setups are similar to those from [van Eerten et al. \(2012\)](#). We start from a BM solution constrained to a small opening angle. This ensures that the results can be re-scaled making use of scale invariance with regard to the ratio of burst energy over circumburst medium density. The initial time t_0 is chosen such that the peak fluid Lorentz factor of the outflow is set to $\Gamma_{\text{peak}} = 100$. We run two simulations with the same dynamical parameters but different micro-physical parameters leading to a slow-cooling and fast-cooling early times case for us to analyse. Since we locally compute the microphysics these parameters indeed need to be specified before the dynamical simulation. Of course, the fast-cooling case is expected to transition to slow-cooling at later times and these different sets of micro-physical parameters are only selected to make our interpretation more straightforward. All the initial parameters in these simulations are reported in table 4.4. The simulation final time t_f is determined by the time spanned by the synthetic light-curve. In practice, we choose $t_f = 3.33 \times 10^8$ s and we check that the last snapshot does indeed not contribute to the emission at the final observer time $t_{\text{obs},f} = 10^8$ s.

4.5.2 Grid parameters

The grid contains $N_\theta = 300$ tracks in the interval $\theta \in [0, \pi/2]$. Initially we set the grid radial width as a function of initial shock Lorentz factor Γ_s such that the radial bounds

are equal to $r_{\min,0} = r_s - 50/\Gamma_s^2$ and $r_{\max,0} = r_s + 50/\Gamma_s^2$, where r_s is the initial shock position as given by the BM solution. Each track contains $N_{r,0} = 5000$ cells of equal dr initially (except for $r > r_s$ where dr is multiplied by a factor 10 only in the initial grid to make sure the blast-wave does not outrun the moving outer boundary in the first few time-steps) so as to resolve the blast wave correctly and ensure the energy contained in the grid is as close to the expected $E_{\text{iso}}/(1 - \cos \theta_{\text{jet}})$ as possible. The number of cells per track quickly decreases due to the AMR criteria described in the next paragraph. During the simulation, we move the outer boundary such that the shock front on the jet axis is always located at $0.9r_{\max}$. New cells are simply created from this moving boundary by the AMR methods implemented in the code. All boundaries apart from the outer one are reflective to ensure energy conservation in the grid (inner boundary), model potential interaction with the counter-jet (boundary at $\theta = \pi/2$), and comply with axisymmetry (boundary at $\theta = 0$).

The resolution is determined as follows. The radial resolution is governed for each cell by a special "re-gridding score" $S_{\text{regrid}} = \hat{a} \times \Gamma^{3/2}$ where \hat{a} is the modified aspect ratio described in §4.3.5 and Γ the fluid Lorentz factor at the cell location. S_{regrid} increases with Lorentz factor such that smaller aspect ratios are allowed for highly relativistic cells. This ensures that the blast wave is better resolved at the shock position where the velocity is the highest. We ran simulations with varying exponent values and found $\Gamma^{3/2}$ to give satisfying convergence of the light-curves. We also multiply S_{regrid} by a factor 10 in the few cells around the onset of the forward shock to further increase the resolution there. S_{regrid} is allowed to vary in the interval $[0.1, 3]$ leading to aspect ratios ranging from 10^{-4} to 3 in practice. The re-gridding mode is set to "runaway". In order to improve the resolution close to the jet axis, we use a variable-size track width where the position of interface $j - 1/2$ between tracks $j - 1$ and j is set by:

$$\theta_{j-1/2} = \frac{\pi}{2} \left(0.3 \frac{j}{N_\theta} + 0.7 \left(\frac{j}{N_\theta} \right)^3 \right), \quad (4.27)$$

where N_θ is the number of tracks. This means that the radial resolution is also higher closer to the jet axis. The number of cells on track 0 varies from ~ 450 to ~ 1500 throughout the simulation. The dynamical simulations run in 7 hours on 384 Marvell ThunderX2 ARM cores distributed over 12 nodes.

The synchrotron emission is computed following the method described in section 4.4 with a small modification. The the larger size of the cells ahead of the blast wave leads to shock diffusion over the same scale as that of the hot region, and thus a wide region ahead of the blast wave is marked as "shocked" by the shock detector. We

decide to turn off the emissivity in all the cells neighbouring a detected shock, and only sum over the emission from the cells in the process of cooling. This does not hinder the ability of the computed light curves to converge since the resolution directly downstream of the shocks is sufficient to allow for this approximation. We check that the light curves obtained are indeed converged by running simulations with varying radial and transverse resolutions (see fig. 4.17, light curve with 600 tracks).

4.5.3 Results

Snapshots in the slow-cooling case at $1.6 \times t_0$, spreading time t_s and close to final time $t \lesssim t_f$ are reported in figure 4.12. For better readability, these snapshots are truncated at $\theta = 0.5$ rad. We observe the expected behavior where the first stages of the evolution follow the BM solution as the jet lacks transverse causal connection. The jet eventually starts spreading at:

$$t_s = \left(\frac{17E_{\text{iso}}\theta_{\text{jet}}^2}{4\pi n_0 m_p c^5} \right)^{1/3} = 3.22 \times 10^7 \text{s}, \quad (4.28)$$

where it transitions to the spherical evolution stage in which we choose to stop the simulation at t_f . In figure 4.14 we show that at t_s the blast wave still follows the BM solution. this figure also highlights the very high resolution needed to properly resolve the hot region where γ_{max} quickly decreases downstream of the shock. In figure 4.13 we show that our simulation accurately follows the expected BM evolution until spreading by plotting the fluid Lorentz factor at the shock position as a function of lab time. Figure 4.15 shows the peak value for γ_{min} (directly downstream of the shock) as a function of lab time in three different directions. Here too, we recover the expected evolution pre-jet break except near the outer edge of the jet where interaction with the CSM influences γ_{min} from the start. This figure highlights the transition to the spherical expansion phase when γ_{min} adopts the same evolution in all plotted directions for $t > 10^8 \text{s}$. At these late times, with our description of the particle population, we enter the regime in which $\gamma_{\text{min}} < 1$. We report in the figures the limit observer time $t_{\text{lim}} \sim 10^7 \text{s}$ above which regions of the fluid with such low values of γ_{min} start contributing to the light-curves and caution against interpretation of the radiation evolution after t_{lim} , especially at the lowest frequency end of the spectrum. Figure 4.16 shows the evolution the spectral index p directly downstream of the shock with lab time, in the case where we allow it to vary. We can notice it does not evolve significantly before the jet break at $t_{\text{lab}} = t_s = 3.2 \times 10^7 \text{s}$ and undergoes a sharp decrease as the jet decelerates post-jet break. This is easily explained by the direct dependency of p on the upstream fluid velocity.

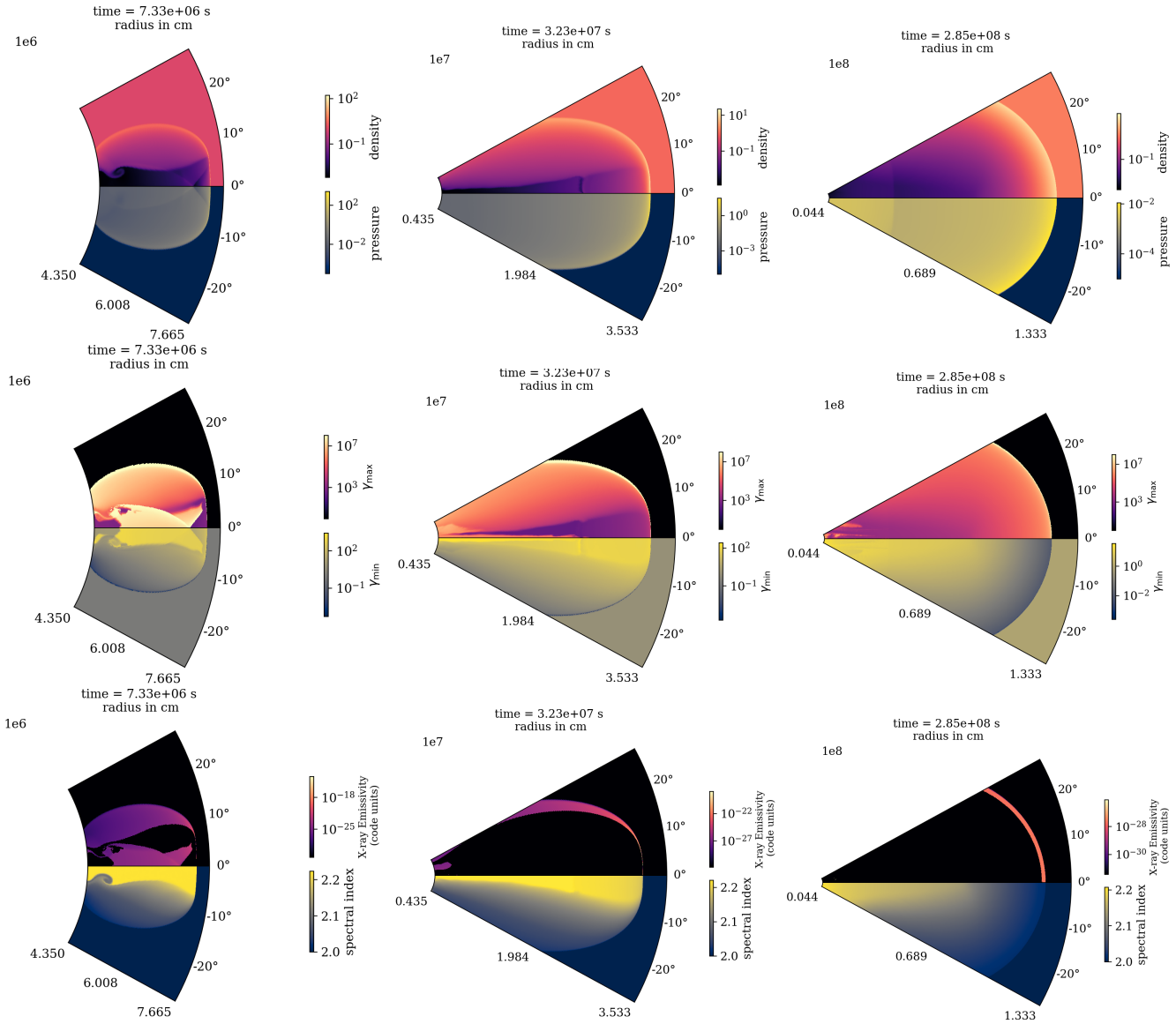


Figure 4.12: Snapshots in the slow-cooling case before spreading (left column), at t_s (center column), and at the end of the simulation (right column). The bottom line shows the x-ray emissivity (positive angles) as seen from an on-axis static observer. Since we use a log color scale, we floor the emissivity to the lowest measured non-zero value in the grid. This quantity allows us to map the emission sites in the jets and verify that the contribution to X-ray from the early re-collimation shock in the evolution is negligible in our simulation, as the density downstream of these shocks is very low compared to the FS. This shock propagates from the edge of the edge of the jet head towards the jet axis as a result of the jets sideways expansion, and is reflected on the jet axis, creating a V-like feature in the γ_{\max} snapshot at $t = 7.33$ s.

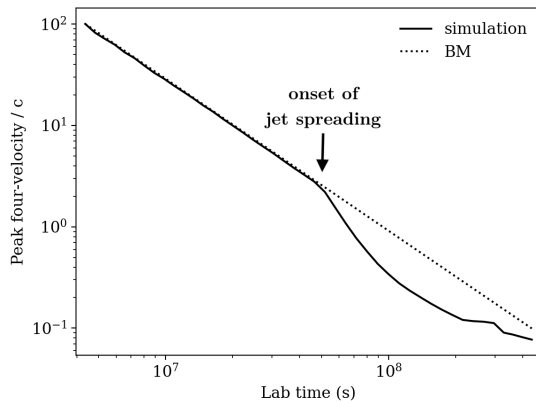


Figure 4.13: Four-velocity $\Gamma\beta$ directly downstream of the shock. We obtain this value by simply measuring the maximum radial velocity in the simulation domain. Our dynamical simulation very accurately follows the BM solution $\Gamma\beta \propto t^{-3/2}$ before jet spreading at $t_s = 3.22 \times 10^7$ s.

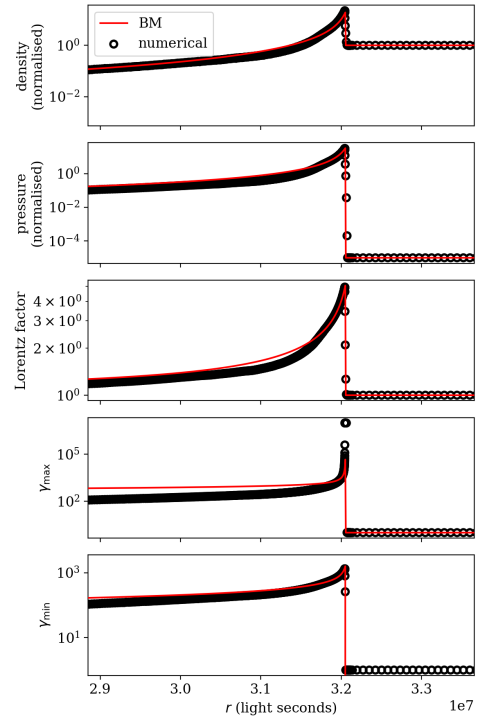


Figure 4.14: Radial profile at t_s in the fast-cooling case for $\theta = 0$. The jet still follows the BM solution at this stage. Density and pressure are normalised by $m_p n_0$ and $m_p \eta n_0 c^2$, respectively.

The synthetic light curves and spectra are reported in figures 4.17-4.18 (slow-cooling) and 4.19-4.20 (fast-cooling). All light-curves exhibit a jet break at $t_{\text{obs}} = t_{\text{break}} \sim 10^5$ s corresponding to the spreading time t_s in the lab frame. In both cases, we observe pre-jet break a very good match with the expected BM flux computed with local cooling (Granot & Sari, 2002), which confirms the validity of our approach. Post-jet break, the BM solution diverges from the true solution as it does not take into account jet spreading and the associated deceleration. As expected, we observe a steeper decrease post-jet break when accounting for jet spreading and deceleration in our numerical solution.

We can now compare the light curves and spectra to those obtained with the global cooling approximation. Let us first consider the slow-cooling case. We can observe a discrepancy of factor ~ 5 in flux levels between the global cooling and local cooling approaches after the cooling break. This is explained by the difference in the position of the cooling break in the spectrum, which has a direct influence on the overall flux level in the light-curves at higher frequencies. Now considering the fast-cooling case,

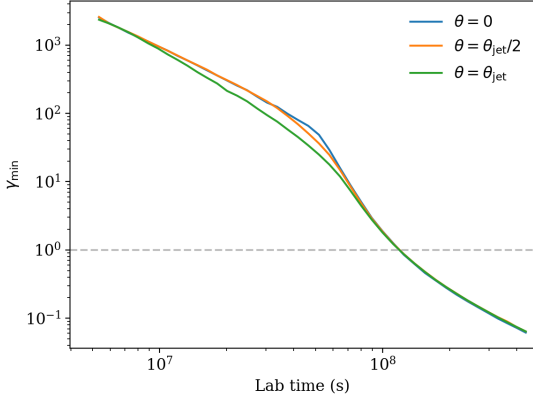


Figure 4.15: Slow-cooling case, fixed spectral index p . Lower bound γ_{\min} of the accelerated electron population directly downstream of the shock for different directions (jet axis $\theta = 0$, jet half-opening angle $\theta = \theta_{\text{jet}}$, and halfway $\theta = \theta_{\text{jet}}/2$). As expected γ_{\min} decreases faster from the beginning due to jet edge effects. All evolutions rejoin when the jet enters the spherical expansion phase in the Newtonian regime. Eventually we encounter the known issue with describing the accelerated particles as a power-law in energy as γ_{\min} moves below 1 (dashed gray line) at very late times.

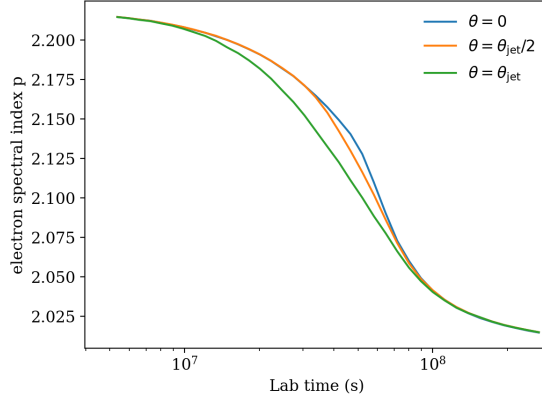


Figure 4.16: Slow-cooling case, variable spectral index p . Spectral index p directly downstream of the shock for different directions (jet axis $\theta = 0$, jet half-opening angle $\theta = \theta_{\text{jet}}$, and halfway $\theta = \theta_{\text{jet}}/2$). p undergoes a fast transition during jet spreading. This explains why the light-curves and spectra are identical in the variable and fixed p cases in our figures.

we see that the change in cooling break frequency influences all parts of the spectrum as γ_{\min} is now also subject to cooling. The light curves flux level at frequencies below ν_c is thus also affected in this case. These strong differences highlight the clear need to include local cooling in the modeling tools currently used by the community.

Locally tracing the particle population offers several opportunities regarding the study of the evolution for the emission post-jet break. We can for the first time accurately capture the radiative transition from the ultra-relativistic BM solution to the Newtonian ST solution. In figure 4.21 we report the evolution of the cooling break ν_c with observer time t_{obs} . Firstly, we find that our simulations using the global cooling approach are in good agreement with previous trans-relativistic simulation works (van Eerten & MacFadyen, 2012; van Eerten & Macfadyen, 2013). We find the expected $-1/2$ slope in the ultra-relativistic limit and observe the same turnover at t_{break} . Secondly, with local cooling, ν_c follows the same slope for $t_{\text{obs}} < t_{\text{break}}$, but offset by a factor ~ 40 . This offset was expected as pointed out by previous works (van Eerten et al., 2010a; Guidorzi et al., 2014). Post-jet break, we observe a striking difference between the two approaches. While $\nu_{c,\text{global}}$ sharply increases, $\nu_{c,\text{local}}$ transitions to a plateau stage from $t_{\text{obs}} \sim 3 \times 10^5 \text{s}$ to $t_{\text{obs}} \sim 3 \times 10^7 \text{s}$. As the jet transitions to the

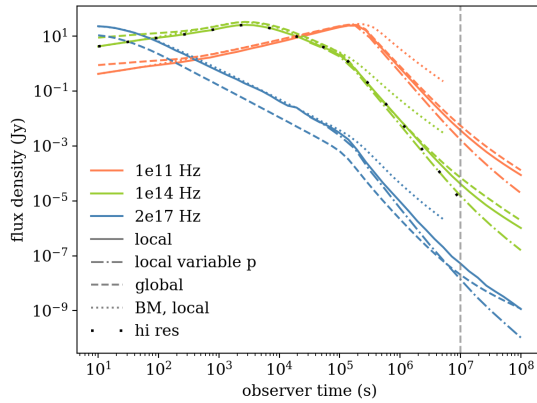


Figure 4.17: Light curves in the slow-cooling case in far IR (orange), optical (green) and x-ray (blue). The BM solution is not computed after 10^7 s as is outside its region of validity then. As expected, it diverges from the true solution after the jet break at $t_{\text{obs}} \sim 10^5$ s. The difference between local and global cooling at early times for optical and far IR is due to the fact that the system is still fast-cooling then. As it transitions to slow-cooling the light-curves rejoin. At later times, the effect of local cooling starts to show on γ_{min} that decreases faster than in the global cooling case, leading to lower fluxes above the injection break. After $t_{\text{obs}} \sim 10^7$ s (dashed gray vertical line), some of the contributing regions of the blast-wave see $\gamma_{\text{min}} < 1$ in the variable p case and we caution against interpretation of the corresponding dot-dashed curves at later times. The loosely dotted black line shows the optical light-curve for a local, variable p run at higher transverse resolution (600 tracks). Other frequencies are not shown for readability but we confirmed convergence there too.

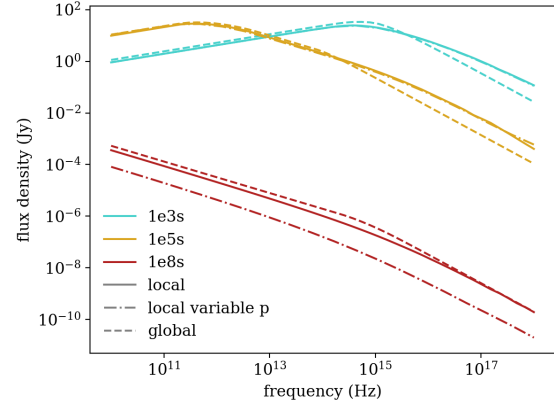


Figure 4.18: Slow-cooling spectra. Line styles match those of fig 4.17. Since this is slow cooling, the cooling break ν_c is easily identified as the right-most break in each spectrum. The injection break ν_m is the left-most break (not apparent in the late spectra at 10^8 s in this figure) The difference in the cooling break position is responsible for the difference in flux density at high frequencies.

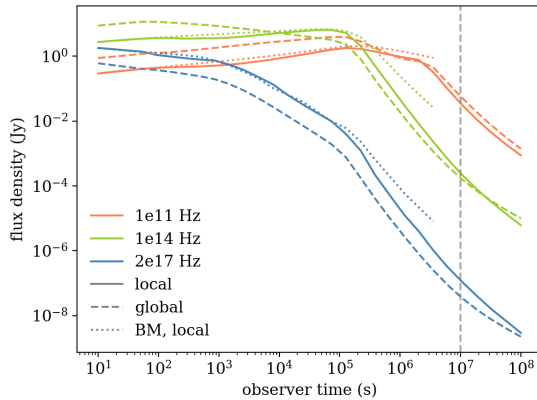


Figure 4.19: Same as figure 4.17 but in the fast-cooling case. We do not show the variable p light curve in this case which is discussed instead in the slow-cooling case. As in slow cooling all curves exhibit a jet break at $t_{\text{obs}} \sim 10^5$ s. Just like in slow-cooling, the x-ray light-curve shows a factor ~ 5 difference pre-jet break as this frequency is placed above the cooling break throughout the whole evolution.

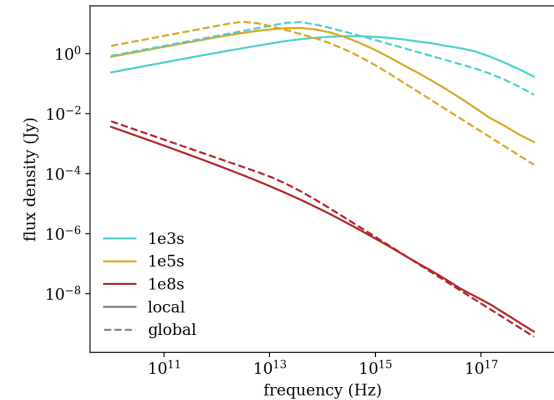


Figure 4.20: Fast-cooling spectra. Line styles match those of fig 4.17. The cooling break is the left-most break in the blue curves, and the only break visible in the red curves. At the time of the yellow curves, the injection and cooling break are superimposed and it is difficult to identify their exact positions (transition from fast to slow-cooling).

Newtonian phase, ν_c resumes decreasing. In figure 4.21 we show the asymptotic $-1/5$ slope expected for this phase. Unfortunately, our simulations did not run long enough to allow us to model the radiation at later times yet and we cannot confirm at this stage that ν_c will settle on this asymptote from this simulation. In this particular setup the global and local calculations of ν_c meet up at late times. Investigating whether this phenomenon happens for all explosion parameters or has a physical explanation is left to future work.

In all the figures describing the radiation from our the slow-cooling case, we also show the evolution of ν_c in the case where the spectral index p varies following the approach described in §4.4. We observe further differences from the case where $p = 2.22$ is kept to a fixed value. As can be seen in figure 4.17, for $t_{\text{obs}} > t_{\text{break}}$, the flux decreases faster at all frequencies when p is allowed to vary. This is also seen in the slow-cooling spectra, at $t_{\text{obs}} = 10^8$ s, where the spectrum in the "variable p " case lies below the spectra in other cases. As supported by these spectra, where the synchrotron regimes are conserved, this decline in flux can be explained by the sharper decrease of γ_{min} associated with decreasing spectral index after t_s , as is visible in the snapshots in figure 4.12.

The evolution of the cooling break position also changes and we observe in figure 4.21 that the plateau at the jet break time present with a fixed spectral index disappears with a variable value for p , showing a steady decrease similar to the pre-jet break regime. This effect is visible in light curves and spectra and provides a potential avenue to investigate the theoretical processes involved in particle acceleration at shock fronts.

4.6 Discussion

In this work, we present a 2D relativistic hydrodynamics code that includes a local calculation of particle population evolution. While the use of a moving mesh offers significant improvements in terms of efficiency over fixed mesh approaches, the immediate downside of the local cooling approach is the necessity to run separate expensive dynamical simulations for each set of micro-physical parameters, increasing the number of runs necessary to explore the parameter space in comparison to global cooling approaches.

Regarding our jet simulations, we assume either sphericity or axi-symmetry and run 2D calculations. We do not expect 3D effects to strongly influence our synthetic light-curve calculations, however, the study of the Rayleigh-Taylor instabilities at the contact discontinuity in the afterglow would benefit from a 3D approach as this could have important consequences on the rate of propagation of the reverse shock in the ejecta.

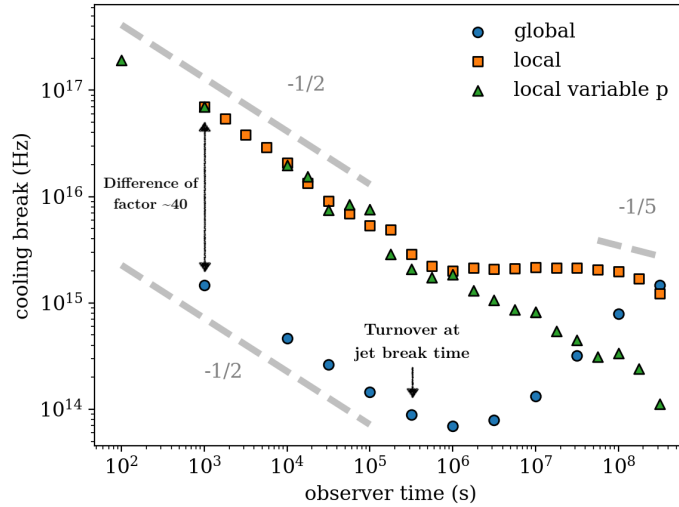


Figure 4.21: Evolution of the cooling break position with observer time. The dashed segments represent the asymptotic slopes expected in the relativistic ($-1/2$) and Newtonian ($-1/5$) limits. The global cooling results match those from [van Eerten & MacFadyen \(2012\)](#) and [van Eerten & Macfadyen \(2013\)](#) with a temporary sharp increase of ν_c . The local cooling approach displays a very different behavior with constant ν_c for at least two decades in observer time from the jet break onwards.

We also consider in these simulations the magnetisation to be small enough that it does not influence the general dynamics of the jet, which is expected at late stage of the evolution post-deceleration (for a recent review, see e.g. [Granot et al., 2015](#)).

The light curves and spectra presented in this work are all calculated for top-hat jets for an on-axis observer. Since GRBs are sources at cosmological distances, they are typically observed near on-axis or at least within the jet half-opening angle ([Ryan et al., 2015](#)), a situation for which angular structure of the jet has a negligible influence on the light-curve shape ([Rossi et al., 2002](#); [Kumar & Granot, 2003](#); [Ryan et al., 2020](#)). These results can thus already be applied to the bulk of GRB afterglow observations. The influence of local cooling on structured jets observed off-axis will be the focus of a future study.

In section 4, we mention our simplified approach to the cut-off of local emissivity above ν_{\max} . Since the slope above the cooling break in the observed spectrum is the result of this cut-off being placed at different frequencies in the observer frame depending on the emitting region of the blast-wave, a sharp cut-off will have a tendency to underestimate the flux received above ν_c . However, this can be compensated by increased resolution in the emitting region, and we actually observed a very good agreement between

our numerical approach and analytical solutions before the jet break. Our main results remain valid at later times too since what we observe is a significant increase in the observed flux with local cooling.

As also pointed out in §4.4, our treatment of the variable spectral index leads to a breakdown of our assumptions for accelerated particle injection when the jet transitions to the Newtonian phase after $t_{\text{obs}} = 10^7$ s, when we can no longer model the accelerated particle population as a power-law in energy. As p and the bulk Lorentz factor Γ of the blast-wave decrease, the total available energy for radiation cannot be stored into the electron population while keeping $\gamma_{\text{min}} \gg 1$. [van Eerten et al. \(2010b\)](#) handle this problem with a varying fraction of accelerated electron. In theory, the electron population should be described in the Newtonian phase by a powerlaw in momentum ([Bell, 1978](#); [Blandford & Ostriker, 1978](#); [Blandford & Eichler, 1987](#)) which has been implemented by [Sironi & Giannios \(2013\)](#). An accurate initialisation of γ_{min} in the deep Newtonian phase will be implemented in a future version of the code. This requires that we re-write eq. 4.18 to account for non-relativistic energies. Let us also point out that this issue is not as pronounced when keeping a fixed value of $p = 2.22$. Nevertheless, the difference in flux between variable and fixed p starts showing as soon as the jet break time, when our approach still holds. This makes a strong case for this effect to be taken into account in the radiative modeling. Finally, we also expect in the deep Newtonian phase contribution from the thermal population of electrons ([Eichler & Waxman, 2005](#)). However, we expect this part of the population to mostly impact the radio emission, both in absorption and emission, and we have restricted ourselves to higher frequencies in our study. An accurate treatment of the thermal emission would also require that we implement absorption in our radiative transfer approach, which is outside of the scope of this paper.

In conclusion, this work provides a solution to the current pitfalls of numerical modeling of afterglow light-curves thanks to an improved numerical approach that accounts for the local variability of the emissivity in the fluid. The striking difference in cooling break behaviour across the jet break between local and global cooling approaches implies that it is not sufficient to merely apply a fixed correction factor to a global cooling approach in order to match the more physically realistic local cooling results. Nevertheless, the cooling break evolution curve remains completely scale invariant in the manner first described by [van Eerten & MacFadyen \(2012\)](#) even across the trans-relativistic stage.

Recent discoveries associated with the multi-messenger detection of 170817 ([Abbott et al., 2017b,a](#); [Goldstein et al., 2017](#); [Hallinan et al., 2017](#); [Savchenko et al., 2017](#); [Troja et al., 2017](#)) have given new impetus for the development of more accurate numerical

models. These are needed for us to be able understand the added complexity (jet structure, off-axis observer, kilonova contribution, interaction with a dynamical ejecta) from these ongoing observations observations (e.g Troja et al., 2019; Hajela et al., 2019; Troja et al., 2020). While the simulations presented here are a textbook case of top-hat on-axis GRB afterglow evolution, GAMMA now provides the basis for the implementation of more complex micro-physical descriptions for the emission and GRB dynamics which will be explored in future works.

Acknowledgements

This work used the Isambard 2 UK National Tier-2 HPC Service (<http://gw4.ac.uk/isambard/>) operated by GW4 and the UK Met Office, and funded by EPSRC (EP/T022078/1). This research made use of the Balena High Performance Computing (HPC) Service at the University of Bath. H. J. van Eerten acknowledges partial support by the European Union Horizon 2020 Programme under the AHEAD2020 project (grant agreement number 871158).

Data Availability

The data underlying this article will be shared on reasonable request to the corresponding author.

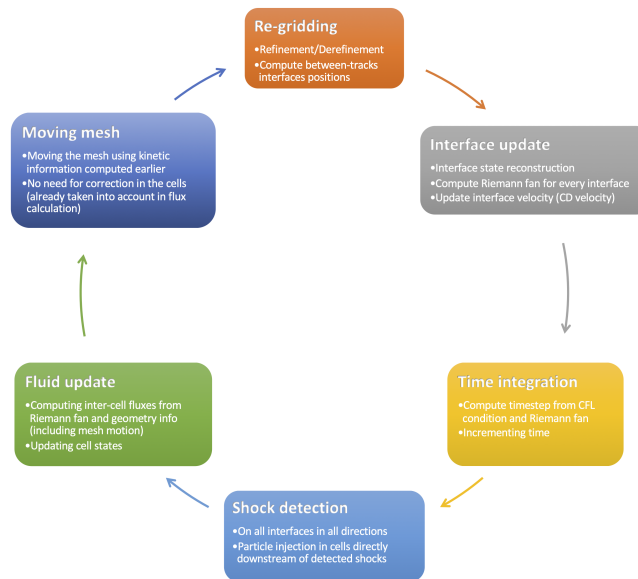


Figure 4.22: General algorithmic progression of the code. The first iteration starts with the re-gridding step. The shock detection can be activated or not depending on the needs of the simulation. When using higher order time-stepping, the first order partial time integration involves all steps apart from the re-gridding operations that are only carried out between full time increments.

4.7 Additional information

4.7.1 Implementation specifics

Even though the methods presented here are built on those introduced in the 1D case in chapter 3, these methods are implemented in a new separate code. Several reasons justify writing a new code: the parallelisation approach described in §4.2.3 differs from that of the code in chapter 3 and involves a significant re-write; the public access of the code also requires a more modular structure. The main algorithmic progression of GAMMA is summarised in figure 4.22, while the high-level flowchart of the code, which highlights the relationships between computational operations, is shown in figure 4.23.

Languages and libraries: GAMMA is implemented in C/C++. Compiled languages offer better performance than interpreted languages for highly intensive calculations. We also take advantage of C++ object-oriented capabilities which helps with code modularity. We make use of the GNU scientific library for root-finding operations. Data inputs and outputs (IO) are in pure text form so far. In the future, and like the code presented in chapter 3, handling of IO files in the Hierarchical Data Format (HDF5) should be implemented, if not because it is more flexible, then simply because it offers faster (parallel) output writing capabilities. For now, we have written a simple

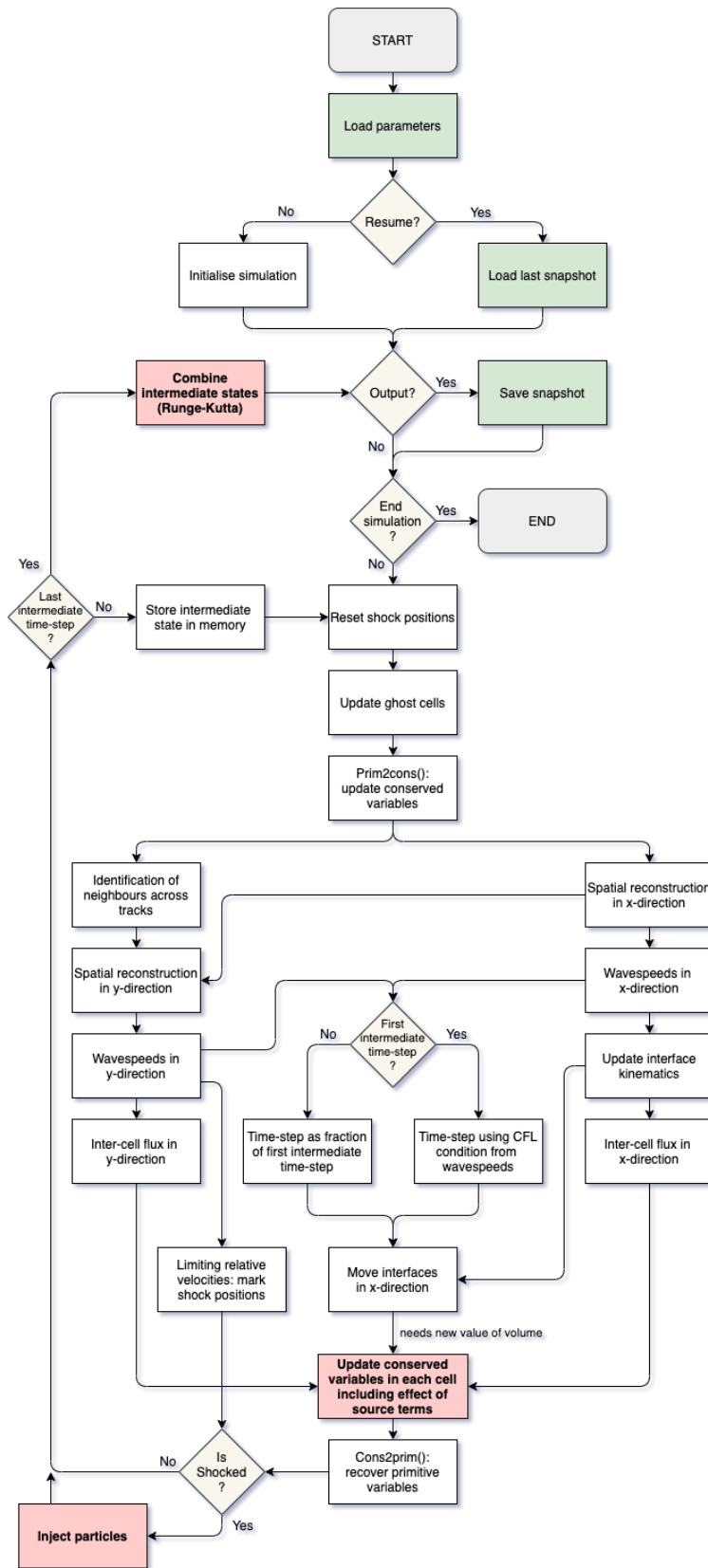


Figure 4.23: Flowchart of GAMMA. Parallelisation operations are ignored in this representation. In green are I/O operations. In red are fluid state update operations. The simulation ends when one of the user-specified criteria is verified. "Intermediate time-steps" are the multiple time integrations in a single Runge-Kutta time-step. The x and y directions are the moving and fixed directions, respectively.

Python tool which converts text files into the input HDF5 format for radiative post-processing (described later in this section).

Setting up simulations: A large number of hydrodynamics codes publicly available unfortunately suffer from their user-unfriendliness. While **GAMMA** does not offer (yet) an elaborate, easy to use, python wrapper like e.g. **PLUTO** (Mignone et al., 2007), the code was designed with this constraint in mind. Additionally, we strived towards giving maximum flexibility to the user in setting up their scientific simulation problems. This means that all the problem-specific functions (initial grid geometry and fluid state, refinement criteria, mesh motion control, source terms, boundary conditions, frequency of output) can be edited in a single file overriding their default versions. Even though the parallelisation procedure splits the domain in various slices in one of the dimensions (recall §4.2.3), we wanted this aspect to be imperceptible to the user when possible and the initialisation of grid geometry and fluid state is done on a domain that is then automatically distributed among processes. Other runtime functions unfortunately still have to be written taking parallelisation into account. A great improvement on accessibility would be to provide wrapping functions available to the user. More detailed instructions, including the list of user functions and compilation options are included in appendix A.

4.7.2 Interfacing with radiation code

Unlike in chapter 3, we did not write our own radiative transfer code to process the dynamical output of **GAMMA**. Instead, we adapted the in-house code **blast** (methods described in van Eerten & Wijers (2009)) by including the processing of local cooling from simulation snapshots which was not yet fully functional. **blast** uses the radiative transfer methods described in §2.4.3 and includes three different modes: (1) flux from analytical BM solution only, (2) from simulation snapshots only, (3) from analytical BM solution up to a given lab time followed by simulation snapshots. All three modes can now be used with local or global cooling. In practice, we use mode 3 since the simulations cannot start too early (the time-step at small radii becomes prohibitive). However this approach is still valid as long as we switch to simulation snapshots before any influence from transverse motion starts to show (which is not expected before the jet becomes causally connected). In this chapter, we presented simulations where the accelerated population of electrons has a variable local spectral index p . **blast** offers the possibility to pass additional local variables to the local fluid state when loading these from a simulation snapshot and we simply adapt the emissivity calculation to take into account this variable spectral index, instead of using the default one specified

in the `blast` parameter file.

`blast` uses the Hierarchical Data Format (HDF5) to load simulation snapshots. HDF5 allows one to load in memory only the spatial slices of interest, contributing to the observer time considered, in each snapshot. Considering that we loop over all snapshots for each observer time, this offers a significant increase in performance. Even though we run 2D hydrodynamical simulations, `blast` computes the emissivity in a 3D space by assuming axisymmetry of the simulation domain. As stated earlier, the text outputs from `GAMMA` are converted to the HDF5 format before use in `blast` using a simple Python tool we have written. This tool outputs the geometrical description of each cell as well as its corresponding fluid and micro-physical state. Ultimately, `GAMMA` will directly output files in the HDF5 format removing this extra step in the synthetic light curve calculation.

General conclusion

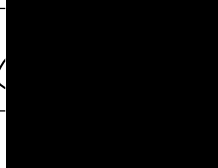
In this chapter, we presented our results improving the accuracy of the modeling of synchrotron emission from relativistic transients. These results were obtained by building on the latest developments in numerical relativistic hydrodynamics which allowed for the accurate calculation of the local emissivity. These improvements are combined and presented in the form of a new turnkey numerical code `GAMMA` which is the main contribution of this thesis work. Straight out of the gate, this code is able to produce significant results. In chapter 3 we use the code's ability to compute radiation produced at multiple emission sites to investigate an alternative flaring mechanism. In this chapter, the full blown multi-dimensional modeling allows us to finally start to pin down the trans-relativistic evolution of the broadband spectrum. The study of the late-time evolution of GRB afterglows needs to rely on improved prescriptions of the synchrotron emissivity calculation in comparison with the methods currently in use.

Machine Learning Insights into Gamma-ray Burst X-ray Emission

Eliot H. Ayache, Tanmoy Laskar & Hendrik, J. van Eerten (in prep.)

*Good and bad, I define these terms quite clear, no doubt, somehow,
Ah, but I was so much older then I'm younger than that now.*

— BOB DYLAN, My Back Pages

This declaration concerns the article entitled:			
Machine-Learning Insights into Gamma-ray Burst X-Ray Emission			
Publication status (tick one)			
Draft manuscript <input checked="" type="checkbox"/> Submitted <input type="checkbox"/> In review <input type="checkbox"/> Accepted <input type="checkbox"/> Published <input type="checkbox"/>			
Publication details (reference)	Ayache, E., Laskar, T., Van Eerten, H. (in prep) to be submitted to Monthly Notices of the Royal Astronomical Society		
Copyright status (tick the appropriate statement)			
I hold the copyright for this material <input checked="" type="checkbox"/> Copyright is retained by the publisher, but I have been given permission to replicate the material here <input type="checkbox"/>			
Candidate's contribution to the paper (provide details, and also indicate as a percentage)	<p>I considerably contributed to this research project. This project is the outcome of a joint interest in machine learning (ML) from Dr. Tanmoy Laskar and me. We jointly identified an avenue to provide physical insights into the GRB afterglow phenomenon in a data-driven approach. This project is not part of any other degree attainment.</p> <p>Formulation of ideas: Ideas were formulated together with Dr. Laskar and benefitted from some useful input from Dr. Hendrik Van Eerten. I participated in identifying the science question: Is the variability in light curve morphology the signature of the presence of different classes of objects, or a change of regime in the same phenomenon? (50%)</p> <p>Design of methodology: I actively participated in the exploration phase of to select the Convolutional Variational Autoencoder (CVAE) approach. I experimented with other methods (Recurrent Neural Networks, beta-VAE...). I designed together with Dr. Laskar the data pre-processing pipeline, as well as the post-processing and analysis tools (latent space visualisation, template generation, unsupervised clustering with DBSCAN). I also explored ways to improve on the work presented here with variational deep embedding mentioned in the discussion section. (55%)</p> <p>Experimental work: My contributions included: writing part of the ML algorithm, fetching and preparing the data for pre-processing, amending the code provided by Dr. Van Eerten for the production of synthetic data, producing the synthetic data. I co-supervised (main supervisor: Dr. Van Eerten, co-supervisor: Dr. Tanmoy Laskar) a Bachelor project of 2 students who experimented with an image-based approach to this problem. (50%)</p> <p>Presentation of data in journal format: I designed part of the figures and wrote this manuscript draft in full, whilst benefitting from feedback by Dr. Laskar and Dr. Van Eerten. (80%)</p>		
Statement from Candidate	This paper reports on original research I conducted during the period of my Higher Degree by Research candidature.		
Signed		Date	08/07/2021

Preamble

The numerical simulations presented earlier allow us to conduct analysis of either theoretical setups, or individual events, by fitting these models to observations. The theory, however, relies on information at the population level, and models can only be built by identifying the characteristic features of a population. This raises the age-old question whether differences in features between events can be explained by the same model or it is a marker of differences in the phenomenology, and thus separates two populations. In this chapter we adopt a data-driven approach to modeling GRB afterglow X-ray light curves and question whether the physics responsible for differing temporal behaviours signal a difference in phenomenology or a simple gradual change of regime. In order to do this we apply advanced unsupervised machine learning methods to GRB afterglow data and study the latent structure of the information it contains, to inform the validity of the categories traditionally used for afterglow light curve classification. This completes our set of numerical approaches to investigating GRB afterglow phenomenology in this thesis.

Abstract

As a data-driven science, astrophysics has tremendous potential as both driver and consumer of machine-learning (ML) applications. In particular, astrophysicists glean significant insight on the generalisation potential of their models from large-scale, population-based studies, where ML techniques can be used to great advantage for dimensionality reduction, generative modeling, and inference. Recent work in ML has made significant strides in both image-domain and time-series techniques. We present a case study at the intersection of both techniques using variational autoencoders (VAEs), applied to X-ray observations of Gamma-ray bursts (GRBs) from the *Neil Gehrels Swift* Observatory. We explore prospects for acquiring physical inference from ML models by clustering light curves in an unsupervised manner, and investigate the resulting level of segregation in the dataset. We find that the data creates over-densities in the latent-space suggesting the presence of dominant light curve types. However, the observed gradual transition in between unifies the prevalent classification of GRBs based on their X-ray data into a single continuum, supporting the idea that light curves of different types should be unified under a single model.

5.1 Introduction

For the last 17 years, the *Neil Gehrels "Swift" Observatory* (Gehrels et al., 2004) has been detecting and measuring emission from gamma-ray bursts (GRBs) and their associated afterglow. Today, over 1500 GRBs have been observed. Observations by the *Swift* X-ray telescope (XRT, Burrows et al., 2005a) revealed the high variability and complexity of the early X-ray afterglow. In particular, X-ray light curves (lcs) display differences in the succession of regimes with time since the burst. Ignoring the well known divide between long and short bursts and the associated differences in afterglow properties (short GRBs are less energetic, less luminous and decay faster, Margutti et al. (2012)), we investigate whether these different light curve (lc) "morphologies" form distinct classes of objects.

Recent years have seen massive progress in unsupervised machine learning (ML) methods for data visualisation. Dimensionality reduction techniques have been used to extract the most important features, or investigate the significant similarities between samples inside astrophysical datasets. Dimensionality reduction allows one to identify underlying classes in the population. For example, Garcia-Dias et al. (2018) use K-means¹ to identify spectral classes in the APOGEE survey. Jespersen et al. (2020)

¹K-means is a clustering method where each sample belongs to the cluster with the nearest mean.

recently used t-distributed stochastic neighbour embedding (t-SNE, [Van Der Maaten & Hinton, 2008](#))² to unambiguously classify short and long GRBs on a two-dimensional space.

For several years now artificial neural networks (ANN, [Rosenblatt, 1957](#)) have shown a great capacity in mimicking complex non-linear functions. More particularly, convolutional neural networks (CNN, [LeCun et al., 1989](#)) have shown their ability to extract the most significant features of samples of high-dimension (e.g. images, regularly sampled time-series) for classification and regression problems. ANNs have also been used for dimensionality reduction in the form of autoencoders ([LeCun, 1987](#); [Bourlard & Kamp, 1988](#); [Hinton & Zemel, 1994](#)). Autoencoders use two separate regression models trained together to compute latent variables in a lower-dimensional space. One model, the encoder, maps the input onto this lower-dimensional latent space. The other one, the decoder, re-computes the input from the latent variables³. More recently, this dimensionality reduction technique has been applied to classification problems by introducing variational inference in the encoding process ([Kingma & Welling, 2013](#); [Blei et al., 2017](#)). This means that we optimise an approximate posterior distribution (usually a multivariate distribution) for the latent variables at the output of the encoder. Thanks to this approach, variational autoencoders (VAEs) acquire a generative capacity in which it becomes possible to sample the latent space to produce new inputs. This property leads to clustering in the latent space as inputs from a training sample now carry a "region of influence" in the latent space where decoded samples have to be similar. The simplest VAE uses a unit Gaussian prior distribution in the latent space. However, new more elaborate methods, such as variational deep embedding (VaDE, [Jiang et al., 2017](#)) have been applied to astrophysical samples (e.g. [Spindler et al., 2021](#)). This method operates like a VAE with the difference that it uses a mixture-of-Gaussians as a prior, meaning that the latent space is forced to arrange itself in a specified number of clusters.

In this paper, we investigate the presence of different classes of GRB afterglow X-ray lcs by carrying our unsupervised classification using a convolutional variational autoencoder (CVAE) on *Swift*-XRT data. The objective is to identify intrinsic classes (or lack

It is an iterative algorithm that requires that the number of clusters to find, K , is specified.

²t-SNE assigns a probability to all pairs of points in the high-dimensional sample based on their similarity (points close-by get a higher probability, which requires the choice of a distance measure). It also defines a probability distribution over pairs in the low-dimensional space. It then minimises the Kullback-Leibler divergence between the distributions, which minimises the loss of information in the low-dimensional distribution with respect to the high-dimensional sample.

³Separating the encoder and decoder is not necessary mathematically, as this is just an optimisation problem in which we fit the model parameters to operate a two-way mapping between input and latent space, but it gives a more intuitive interpretation of the training process.

thereof) in the light curve population using advanced data-visualisation techniques. In §5.2 we describe the *Swift*-XRT dataset, as well as the pre-processing we carry out on the data before training. §5.3 describes our neural network and the related training algorithm. §5.4 presents our preliminary results. We discuss avenues for improvements of these results in §5.5.

5.2 Data description

5.2.1 *Swift*-XRT light curves

We focus our analysis on the *Swift*-XRT afterglow light curve sample⁴ (Evans et al., 2007, 2009) (hereinafter E07; E09). In this sample, light curves comprise of photon count rates in the energy range 0.3-10 keV binned by time. The time binning of the data given by the XRT data reduction pipeline is irregular. It is based on the number of counts in a given bin to ensure that short-timescale features are resolved in the early afterglow, while still allowing for late-time detection of the afterglow when it fades. This target number of photons per bin varies with the photon count rate. In window timing (WT) mode, maximising time resolution, the photon count per bin is at least $C = 30$ for a count rate of 1 to 10 photons/second. In photon count (PC) mode, $C = 20$ for a rate of 1 to 10. C increases by a factor 1.5 with increasing decades of photon rate (e.g. $C = 45$ for $10 \leq \text{rate} < 100$ in WT mode). The photon count in a bin can however be higher as each bin has to reach 3σ detection limit. The bin time is the average photon arrival time, which is naturally offset from the center of the bin.

In Evans et al. (2009), lcs observed in log - log space are split into 5 morphological categories depending on the succession of their power-law decay slopes: "canonical", "no break", "one break - steep first", "one break - shallow first", "oddball". Canonical lcs display at least 2 breaks with a "steep - shallow - steep" decay succession and an eventual final steepening (the jet break) (see also Nousek et al., 2006). The other categories are self-explanatory. Racusin et al. (2009) also classify light curves based on a similar power-law fit approach. They assume that all lcs intrinsically follow the canonical shape from Nousek et al. (2006) (steep decay, plateau, normal decay, jet break) and split them into 4 categories depending on whether we observe the full lc (canonical including jet break), only the beginning (no observed jet break), only the end (plateau to normal decay, or normal decay to jet break), or only one regime (single power-law). More recently, Margutti et al. (2013) (hereinafter M13) have conducted a comprehensive statistical analysis of *Swift*-XRT lcs. They also identify

⁴https://www.swift.ac.uk/xrt_curves/

different categories of lcs depending on the number of breaks and slopes (figure 1 in their paper):

- 0: no breaks,
- Ia: one break, shallow first,
- Ib: one break, steep first,
- IIa: two breaks, steep - shallow - steep,
- IIb: two breaks, shallow - steep - shallow,
- III: three breaks.

These categories match those from E09, with "canonical" corresponding to "IIa", and "oddball" encompassing "IIb" and "III". In the rest of this paper, we adopt the nomenclature from M13 as it is more informative, and includes a larger dataset than Racusin et al. (2009). However, since the regularly updated *Swift*-XRT repository follows the procedure from E09, we will not discriminate between "IIb" and "III" and will combine these classes into "oddballs".

Our dataset (case A) comprises of 1222 *Swift*-XRT afterglow light curves observed between December 2004 and November 2019 (517 type 0, 144 type Ia, 107 type Ib, 307 type IIa, 147 type "oddballs"). This dataset contains bin locations t_{bin} , bin upper extent Δt_{upper} , bin lower extent Δt_{lower} (negative value), count rate r , count rate upper extent Δr_{upper} , count rate lower extent Δr_{lower} (negative value) for each lc. We discard any light curve that displays a single measurement only.

In order to evaluate the influence of the presence of short-timescale features such as flares and rebrightenings, we also produce a dataset in which the data points from flaring features are simply removed (case B). The flares are identified in each lc in the *Swift*-XRT dataset (E07; E09). However, the procedure presented in E09 does not carry out model fitting to evaluate flare candidates and the approach has been improved since, making use of the functional form from Willingale et al. (2007) to fit the lc, including separate components for prompt and afterglow contributions. Flares are identified by iteratively fitting the Willingale et al. components to the lc, and marking data points that lie above the model as candidate flare data points. For each point the significance is defined as (Data-Model)/(Error on data). The point is categorised as a flare if the significance exceeds a threshold defined as follows:

- If within 3ks of the trigger, the threshold is set to 8 if applied to an isolated flare point candidate, or to 6 if the flare candidate spans at least 5 light curve bins.
- If more than 3ks after the trigger, the threshold is set to 10 if applied to an isolated flare point candidate, or to 8 if the flare candidate spans at least 5 light

curve bins.

This process is repeated until no new point is excluded. This information contained in these lcs is thus identical to that used for the fitting of multiple power-law components.

5.2.2 Synthetic light curves

In order to evaluate our model capacity to identify different lc types, we will make use of synthetic lcs alongside real observed lcs. These synthetic observations mimic *Swift*-XRT observations of lcs of the types described in M13 (0, Ia, Ib, IIa, IIb and III). We will follow the procedure from Curran et al. (2008), making use of the code applied in van Eerten et al. (2010a). For each class, the lcs are described by a set of break times $(t_b^i)_{0 < i \leq N_t}$ and power-law decay slopes $(\alpha_i)_{0 < i \leq N_t+1}$, where N_t is the number of breaks in the lc (the number in the class label). The lcs are modelled by a succession of broken power laws such that the count rate as a function of time $r(t)$ is given by:

$$r(t) = \begin{cases} Nt^{\alpha_1}, & t < t_b^1 \\ N(t_b^1)^{\alpha_1} \left(\frac{t}{t_b^1}\right)^{\alpha_2}, & t_b^1 \leq t < t_b^2 \\ N(t_b^1)^{\alpha_1} \left(\frac{t_b^2}{t_b^1}\right)^{\alpha_2} \left(\frac{t}{t_b^2}\right)^{\alpha_3}, & t_b^2 \leq t < t_b^3 \\ N(t_b^1)^{\alpha_1} \left(\frac{t_b^2}{t_b^1}\right)^{\alpha_2} \left(\frac{t_b^3}{t_b^2}\right)^{\alpha_3} \left(\frac{t}{t_b^3}\right)^{\alpha_4}, & t_b^3 \leq t \end{cases} \quad (5.1)$$

where N is the normalisation constant, t the observer time and t_b^i the break times in the lc. This expression is general, meaning that we can model lcs with strictly fewer than 3 breaks simply by setting the last break times to infinity or setting consecutive slopes to the same value. The net advantage of these synthetic lcs is that they are much better sampled than raw *Swift*-XRT observations, and are devoid flares and other short timescale variability that were excluded in the fitting procedures from E07; E09; M13. We do account however for the noise and orbital gaps in the observations.

From a set of (t_b^i) and (α_i) , reconstructing the lcs requires that we iteratively compute the variable bin size as it is dependent on count rate. All lcs will start at $t_{\text{ini}} = 10\text{s}$ after prompt emission and be modeled up to $t_{\text{end}} = 10^7\text{s}$ unless they fall below the detection threshold before this time. For each bin starting at time t , the count rate is computed using eq. 5.1. The bin size Δt is computed assuming that the count rate remains equal to $r(t)$ (the count rate at the beginning of the bin) throughout the bin width, following the criteria given in §5.2.1, meaning that bin locations correspond to bin centers. After one day the fractional exposure of the source f drops from 1 to 0.1. Meaning that the general expression for the bin size is $\Delta t = C_{\text{target}}/(rf)$, where C_{target} is the target count per bin. The count rates are then scattered following a 1σ error of fractional

value 0.25 which corresponds to the error measured on well sampled *Swift*-XRT lcs. The perturbation is sampled from a normal distribution with standard deviation $\sigma = 0.25r$ and applied to the previously computed count rate. We take the 47-minute orbital gap into account, during which no synthetic data is created. The time of first occurrence is sampled randomly from a uniform distribution in range $[0, T/2]$ where $T = 94$ min is the *Swift* orbital period (low Earth orbit means that the occultation time is $T/2$). We resume sampling after the occultation and apply the gap periodically from then on. We stop computing the lc after t_{end} , or if the count rate falls below the sensitivity limit for *Swift*-XRT $r_{\text{lim}} = 10^{-4}$ cts/s.

We create 2 synthetic light curve datasets that serve distinct purposes.

- The first synthetic dataset (case C) consists in synthetic lcs generated from the parameters reported in M13 fitted to 437 observed *Swift*-XRT afterglows. Their sample comprises of fits to light curves starting 60s after the burst. They also selected well-sampled enough events such that flux light-curves could be calculated. As mentioned before, our synthetic lcs do not display any flares or short timescale variability and are better sampled than raw XRT observations. They offer a homogeneous complete sample improving training efficiency. This dataset allows us to evaluate the influence of the short timescale variability on training. However, the limited sample size hinders our ability to carry out robust interpretation of the results from its analysis.
- A second synthetic dataset (case D) is used to evaluate the capacity of the network to cluster known groups of lc morphologies. This will allow us to confirm that the presence of (engineered) structure in the high-dimensional does lead to clustering in the lower-dimensional space. We produce between 100 and 1000 samples of each class, depending on their relative weight in the sample from M13 (1000 type 0, 500 type Ia, 500 type Ib, 500 type IIa, 500 type IIb, 100 type III). For each lc, we sample the break times and slopes from uniform distributions, while ensuring that the relative succession of slope values depending on the lc type is respected. The bounds of the distributions used are reported in table 5.1. We make sure that these are similar to the mean values measured by M13. For all types, the last regime of the lc is a normal decay with slope $\in [-2, -1.2]$. The uniform distributions are chosen to increase the variability in lc morphologies that the network will have to model. The ranges in the slope distributions are constrained by the necessity of the absence of overlap between classes, which entails a varying slope value from one regime to the next. For simplicity, we set the normalisation to $N = 10^5$ cts/s, which is the count rate at 1s after the burst,

Table 5.1: Bounds of the uniform distributions from which parameters of case D are sampled.

Type	Break times $\log t_b^i/[1s]$	Slopes α_i
0	n/a	[-2, -1.2]
Ia	[1.2, 4]	[-0.8, 0.2], [-2, -1.2]
Ib	[1.2, 2.5]	[-4.4, -3.6], [-2, -1.2]
IIa	[1.2, 2.5], [3, 4]	[-4.4, -3.6], [-0.8, 0.2], [-2, -1.2]
IIb	[1.2, 2], [2, 2.5]	[-0.8, 0.2], [-4.4, -3.6], [-2, -1.2]
III	[1.2, 2], [2, 2.5], [3, 4]	[-0.8, 0.2], [-4.4, -3.6], [-0.8, 0.2], [-2, -1.2]

Table 5.2: Description of datasets used in this study

Case	Number of samples	Description
A	1222	<i>Swift</i> -XRT full lcs
B	1222	<i>Swift</i> -XRT lcs with flares removed
C	437	Synthetic lcs produced from M13 measured parameters
D	3100	Synthetic lcs produced from sampled parameters (see table 5.1)

except for classes Ib, IIa and III which display an early steep decay and for which $N = 10^9$ cts/s. This second value is chosen to ensure the count rate does not fall below the detection threshold before the first break time. Higher values of N are also measured for these classes in M13.

The lcs can then undergo the same pre-processing as the real data, which is described in the following section. All the datasets used in this work are reported in table 5.2. Examples of samples from each case A and B are shown in figure 5.1. An example of a synthetic light curve is shown in figure 5.2.

5.2.3 Sample pre-processing

The irregular binning of the data represents added complexity for a machine learning model for unsupervised time-series classification. As we only focus on identifying the dominant lc morphology, we decide to re-bin the lcs on a regular grid of 40 evenly spaced bins in log space, which is chosen as it is close to the median value of 46 bins measured in our sample extracted from the *Swift*-XRT dataset. This simplifies the design of our ML model, avoiding the need for e.g. recurrent neural networks (Elman, 1990), which require more time for training and offer less opportunity for interpretability. It also simplifies the calculation of our cost function which will be used to train the network, as all bins now have equal weight in this function and all inputs have the same number of bins (see the description of the variational autoencoder in §5.3). An example of the comparison between raw and pre-processed lc for a well sampled afterglow is shown in figure 5.3. Intuitively, the new rate values can be set to the average of the values in the initial bins that overlap with the new bin, weighted by the size of this overlap.

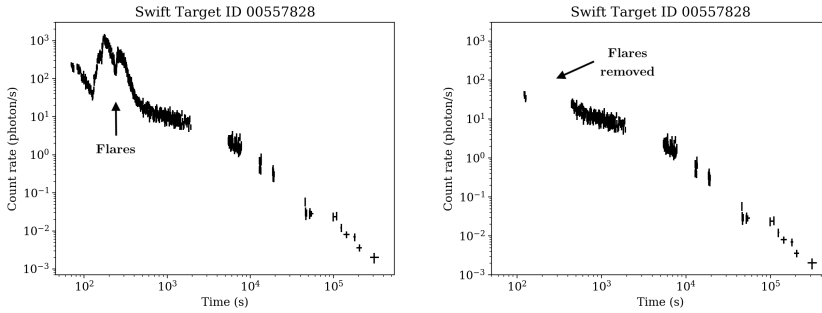


Figure 5.1: Raw *Swift*-XRT light curve (left) from case A showing flares between 100s and 400s and the corresponding case B light curve (right) where the flare has been removed.

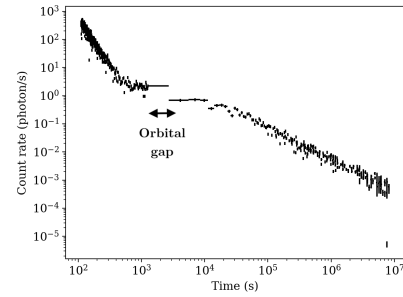


Figure 5.2: Raw synthetic *Swift*-XRT light curve in case C (type IIa, canonical). Our approach produces large temporal uncertainties at the orbital gaps which is different from the absence of data reported in the *Swift* sample. This has no influence on our model as the pre-processing only accounts for the bin center position.

However, this can lead to pathological morphologies in poorly sampled lcs with very large initial bins, where we then observe a large succession of bins with the same count rate (large flat succession of points). We choose instead to compute the average over the count rates of the initial bin centers located in the new bin. This approach leads to more gaps in the lc since new bins that do not overlap with any raw XRT bin center will then have a zero flux. The lc morphology is well conserved with this approach. We choose to treat empty bins as missing data and flag them by setting them to a constant value of -1. We explain later how we ignore the contribution of these bins in the objective function used for training.

In order to focus on lc morphology, we stretch the lcs so that the first photon detection corresponds to the first bin, and the last detection to the last bin. The bins thus lose absolute time information. For each sample, the log count rate is normalised by the mean log count rate value of the lc. This ensures that the network does not encode for the absolute flux level, and that the values passed to the network are of order of magnitude of unity which is crucial for efficient training.

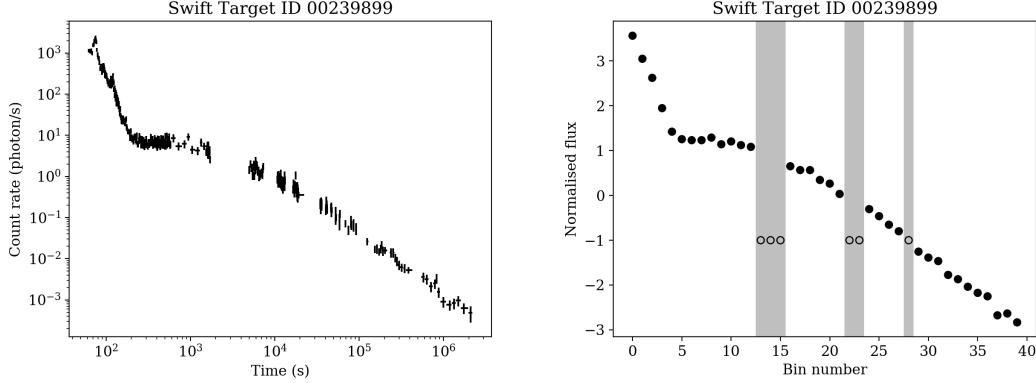


Figure 5.3: Pre-processing on a canonical *Swift*-XRT lc. On the left is the corrected data from the *Swift* sample. On the right is the pre-processed lc used as input to our model. The orbital gaps (shaded regions) lack data, which we impute to -1 (unfilled data points). Points within machine precision of -1 are not taken into account in our objective function.

5.3 Convolutional variational autoencoder

We design a CVAE for time-series analysis. An autoencoder is composed of an encoder E_ϕ and decoder D_θ .

$$E_\phi(\mathbf{x}) = \mathbf{z} \quad (5.2)$$

$$D_\theta(\mathbf{z}) = \hat{\mathbf{x}}, \quad (5.3)$$

where \mathbf{x} is the input, \mathbf{z} the corresponding latent representation, and $\hat{\mathbf{x}}$ the output estimating \mathbf{x} . ϕ and θ are the parameters of the encoder and decoder, respectively. These correspond to the trained weights in both ANNs. This sets up a regression problem in which the full network learns a latent representation \mathbf{z} of the inputs at the bottleneck between encoder and decoder. As with any ANN, the weights are updated during training using backpropagation of the error (Rumelhart et al., 1986). This means that we define a cost function (also called loss, or objective function) at the output layer, $\mathcal{L}(\hat{\mathbf{x}}, \mathbf{x})$, which will depend on the problem we are solving (regression or classification).

For each update during training, we compute the output $\hat{\mathbf{x}}$ of the network and the corresponding loss, for a batch of samples. We then compute the partial derivatives of this loss with respect to the weights. Let us note w_{ij}^l the weight between neuron i and j from layers l and $l - 1$ respectively. In a given layer l each neuron j outputs the weighted sum of inputs (the outputs of neurons from the previous layer) to which it

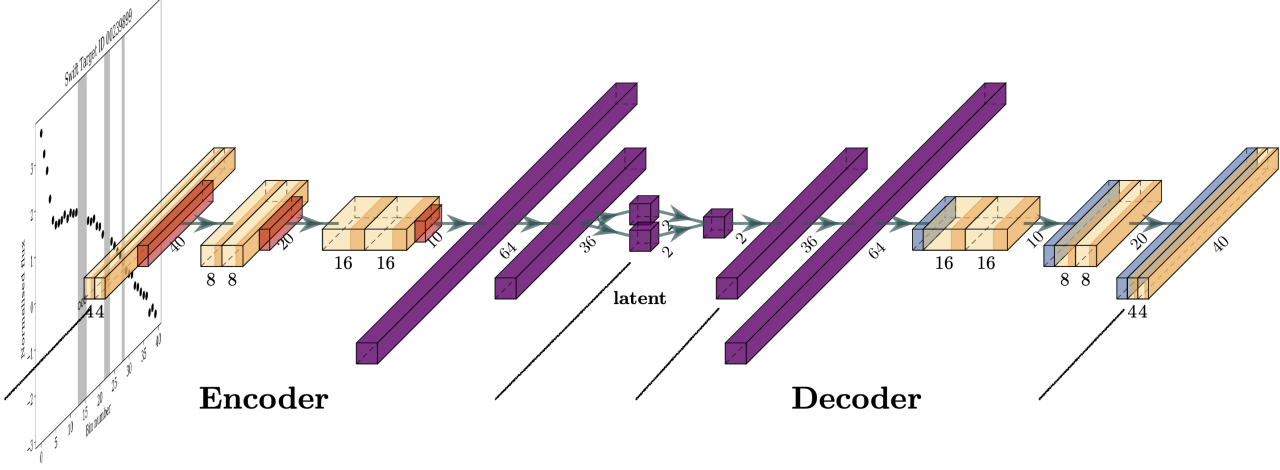


Figure 5.4: Architecture of our CVAE. Forward pass from left to right. Purple layers are dense layers. Convolutional blocs are in yellow. Orange layers are max-pooling operations. In blue are upsampling layers. The width of each convolutional block corresponds to the number of filters used. The depth corresponds to the number of neurons in each layer. The transition from/to convolutional block to/from dense layer is done by flattening/reshaping the activation maps. The 1D aspect of our data (time-series, as opposed to 2D images) is responsible for the elongated aspect of the blocks as we only apply 1D convolutions here.

applies an activation function ϕ :

$$o_j = \phi \left(\sum_i w_{ij} o_i \right) = \phi(s_j). \quad (5.4)$$

After a bit of algebra, the partial derivative of the loss with regards to the weights is given by:

$$\frac{\partial \mathcal{L}}{\partial w_{ij}} = o_i \delta_j, \quad (5.5)$$

with:

$$\delta_j = \begin{cases} \frac{\partial \mathcal{L}}{\partial o_j} \frac{d\phi(s_j)}{ds_j}, & \text{if } j \text{ is an output neuron,} \\ (\sum_{l \in L} w_{jl} \delta_l) \frac{d\phi(s_j)}{ds_j}, & \text{if } j \text{ is an inner neuron,} \end{cases} \quad (5.6)$$

where L is the set of neurons directly connected to the output o_j of neuron j . This expression highlights the recursive character of backpropagation in which the derivatives

with respect to inner layers depend on the derivatives closer to the output. Once the gradients have been calculated, the weights are updated following:

$$\Delta w_{ij}^l = -\eta \frac{\partial \mathcal{L}}{\partial w_{ij}^l}, \quad (5.7)$$

where η is the learning rate that we set manually in this work. This gradient descent minimises the loss $\mathcal{L}(\hat{\mathbf{x}}, \mathbf{x})$ for the batch of samples at each iteration. ANNs however need multiple epochs (loop over the whole training sample) in order to for the training to converge.

Variational inference is introduced at the bottleneck in VAEs where the encoder now learns the posterior latent distribution $q_\phi(\mathbf{z}|\mathbf{x})$. The decoder in turn now learns the distribution $p_\theta(\mathbf{x}|\mathbf{z})$. The latent prior is set to a unit Gaussian $p(\mathbf{z}) = \mathcal{N}(0, 1)$. In our VAE the posterior distribution is approximated by a Gaussian multivariate distribution such that:

$$E_\phi(\mathbf{x}) = \mathcal{N}(\boldsymbol{\mu}_z, \boldsymbol{\sigma}_z^2) \sim q_\phi(\mathbf{z}|\mathbf{x}). \quad (5.8)$$

This introduces a difficulty in the training of this network as back propagation of the error in the stochastic gradient descent, used to update the network weights and biases, is now impossible because of the non-differentiable random sampling carried out in the encoder during the forward pass. This can be solved using the "re-parametrisation trick" (Kingma & Welling, 2013) consisting in realising that $\mathcal{N}(\boldsymbol{\mu}_z, \boldsymbol{\sigma}_z^2) = \boldsymbol{\mu}_z + \boldsymbol{\sigma}_z \odot \mathcal{N}(0, 1)$ (\odot is the element-wise product), where the unit Gaussian sampling is now an input to the decoder and does not need to be differentiated. The training is thus a Monte-Carlo (MC) process in which we estimate the objective function by drawing from this distribution. In practice however, since the dataset is usually large and since we train for many epochs, only one sample is drawn from $E_\phi(\mathbf{x})$, and then passed to the decoder.

Training requires that we define a cost function. We use the evidence lower bound (ELBO) objective function which is a combination of a reconstruction term (forcing the output to match the input) and a regularisation term (forcing the distribution of \mathbf{z} to match the specified prior). The ELBO is given by:

$$\text{ELBO}(\theta, \phi) = -\text{KL}[q_\phi(\mathbf{z}|\mathbf{x})||p_\theta(\mathbf{z})] + \mathbb{E}_{q_\phi(\mathbf{z}|\mathbf{x})} \log p_\theta(\hat{\mathbf{x}}|\mathbf{z}), \quad (5.9)$$

where KL is the Kullback-Leibler divergence measuring the dissimilarity between the posterior approximation and prior distribution (variational loss), and the second term

the log-likelihood (reconstruction loss), where we denote the expectation of a distribution with \mathbb{E} . The reconstruction loss is set as the mean squared error (MSE) between input and output multiplied by the input dimensionality N_{bins} :

$$\mathcal{L}_{\text{recon}} = \text{MSE}(\mathbf{x}, \hat{\mathbf{x}}) \times N_{\text{bins}}. \quad (5.10)$$

With our description the variational loss becomes:

$$\mathcal{L}_{\text{var}} = -KL[\mathcal{N}(\boldsymbol{\mu}_{\mathbf{z}}, \boldsymbol{\sigma}_{\mathbf{z}}^2) || \mathcal{N}(0, 1)] \quad (5.11)$$

$$= -\frac{1}{2} \sum_j [1 + (\log \sigma_j)^2 - \mu_j^2 - \sigma_j^2], \quad (5.12)$$

where the subscript j denotes each element of the vectors in the latent space, and we have dropped the subscript \mathbf{z} for clarity. The total loss is then simply:

$$\mathcal{L} = \mathcal{L}_{\text{recon}} + \mathcal{L}_{\text{var}}. \quad (5.13)$$

We caution here however that the introduction of regularisation in the model decreases the fidelity of reconstruction, potentially leading to more scattering in the latent space. Improvements can be expected by adjusting the relative influence of both terms with a parameter β in so-called β -VAEs:

$$\mathcal{L} = \mathcal{L}_{\text{recon}} + \beta \mathcal{L}_{\text{var}}. \quad (5.14)$$

A larger beta will favor minimization of the variational loss, leading to stronger clustering, but worse reconstruction. Clusters will be comprised of less similar light curves as a result. Even though we implemented this method, we did not carry out systematic parameter exploration for β and all the results presented in this work made use of $\beta = 1$.

Our network architecture is shown in figure 5.4. The encoder and decoder are both CNNs with 3 convolutional blocks and 2 dense layers. We set up a latent space of dimension 2 to help with data visualisation. We use the rectified linear unit (ReLU) activation function for all convolutional layers. At the bottleneck of the network, $\mu_{\mathbf{z}}$ and $\sigma_{\mathbf{z}}$ are set as the outputs of two separate dense layers with linear activation functions. The output layer also uses a linear activation function. As mentioned in §5.2.3, we suffer from an incomplete dataset where some of our samples are missing datapoints. We choose to input a constant value for these datapoints and set them to -1 in the standardised dataset. We also ignore their contribution to the objective function. The network automatically learns to ignore these datapoints and does not try to match the

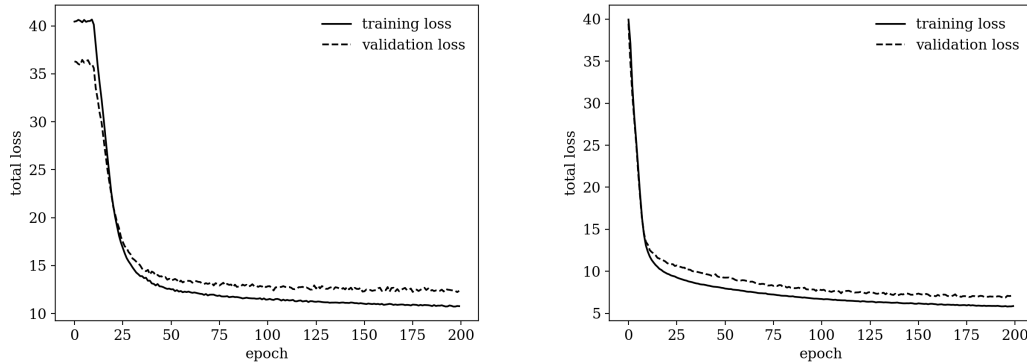


Figure 5.5: Convergence during training of our model for case A (left) and case D (right). We stop training before the validation loss starts increasing again, which would mark the onset of significant overfitting.

-1 value.

Hyper-parameters (batch size, learning rate) are set after manual adjustments to maximise validation accuracy. The learning rate is set to $l.r. = 0.0001$ and the batch size to 64. A larger batch size improves training efficiency and accuracy but increases overfitting. A larger learning rate improves training efficiency but can fail to converge. We use the Adaptive Moment Estimation (ADAM) (Kingma & Ba, 2015) gradient descent algorithm for training.

5.4 Preliminary Results

For each dataset, we train the network for 200 epochs. Convergence plots of the model applied to cases A and D are shown in figure 5.5, where we have randomly selected 15% of the dataset for validation. The difference in validation loss and training loss shows that our model is marginally overfitted. However, the fact that the training loss keeps decreasing up to the 200th epoch suggest that this is probably linked to the small size of our dataset, and that the training set is not completely representative of the validation set, since reconstruction keeps improving for unseen samples. The autoencoder performs well and offers good reconstruction capability. In figure 5.6 we show a few examples of lc reconstructions for case A. As expected the regularisation in our objective function causes a general smoothing of the reconstructed lc in comparison to the input, but well sampled lcs are accurately reconstructed. Flares and poorly sampled lcs prove challenging for our model to reconstruct accurately, justifying both the use of datasets B (no flares), and C and D (synthetic lcs) in our study.

The latent space distributions and analysis are shown of each case in figures 5.7

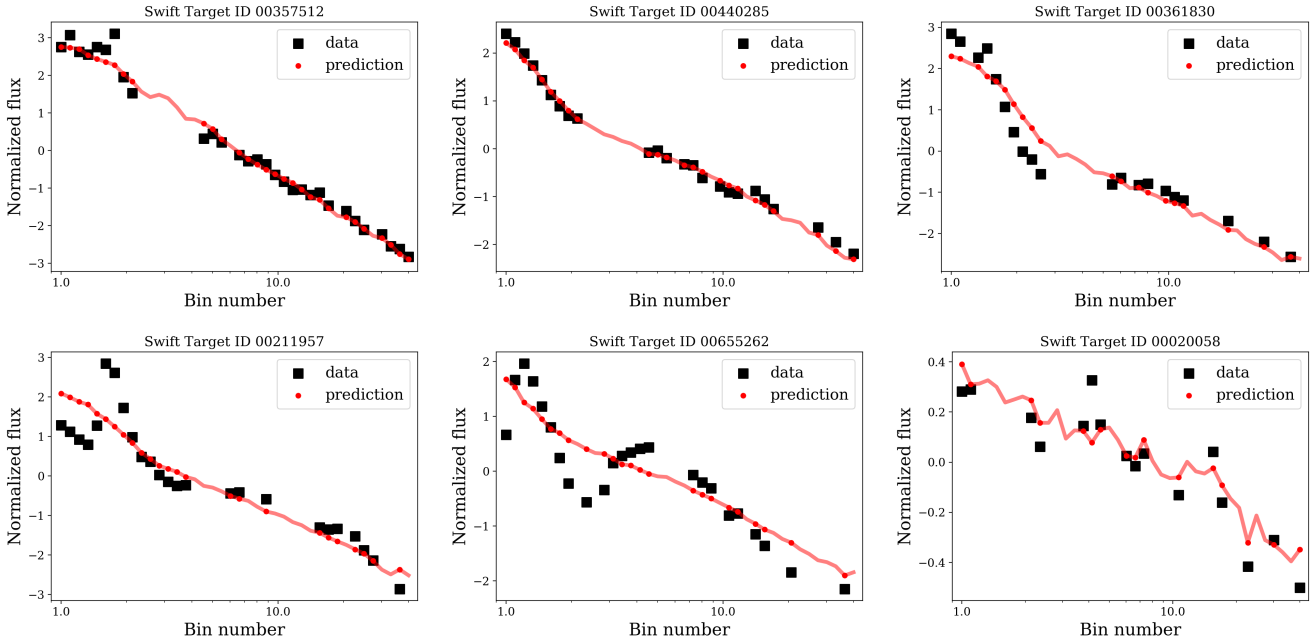


Figure 5.6: lc reconstruction examples. The black squares represent the pre-processed input data \mathbf{x} and the red dots the corresponding prediction $\hat{\mathbf{x}}$. The network is also able to predict values for missing points which is shown with the red line. Values are inputted where data is missing (red line). Upper row: well sampled inputs are accurately reconstructed, albeit with some smoothing introduced by the regularisation in the latent space. Lower row: flares and rebrightenings (left and center) are particularly challenging for model to reconstruct, as well as poorly sampled or noisy lcs (right).

(case A), 5.8 (case B), 5.9 (case C) and 5.10 (case D). In each case, we show on the top row the sample distribution in the latent space, colored by their type as reported in the *Swift*-XRT sample, and the corresponding kernel density estimation (KDE) using a Gaussian kernel and Scott's rule (Scott, 2015) to calculate the optimal bandwidth. This KDE analysis allows us to identify regions of over-density in the latent space and traces the location of cluster candidates. On the bottom row, we show on the left the result of a clustering analysis using the density-based spatial clustering of applications with noise (DBSCAN) algorithm (Ester et al., 1996). This approach presents the advantage of not relying on the user specifying a number of clusters to look for, but instead identifies clusters depending on the choice of parameters. These parameters are the neighbourhood size ϵ , which specifies the radius of the region around a point in which the algorithm will look for neighbours, and the minimum number of samples N_{\min} to be in that neighbourhood for this point to be identified as a core point. Core points that are in each other's neighbourhoods belong to the same cluster. Non-core points in the neighbourhood of a core point also belong to the cluster. Points outside of the

neighbourhood of any core point are labeled as noise points. For each dataset, we run DBSCAN for various combinations of parameters and show the most relevant result in this figure, with the objective to either identify the intrinsic number of clusters formed in the latent space. Strongest clustering is obtained when DBSCAN finds a reasonable number of clusters and few noise points. If, for all combinations of parameters, either the number of clusters, or the number of noise points is large, the distribution is poorly separated. More accurate measures exist of how representative of the population a clustering result is, such as the silhouette score of the Calinsky-Harabasz index (Calinski & Harabasz, 1974). These methods will be used in future work, in combination with deep embedding, to accurately measure the number of clusters in the population. Note that in our current approach, since we find poor clustering, the clusters identified by DBSCAN should not be interpreted as the intrinsic cluster in the dataset and do not highlight a particular light curve type.

In order to interpret the distribution of the data in the latent space, we make use of the generative character of our model and produce lc templates generated by sampling the latent space on a regular grid and decoding this each latent representation. The results are shown in the bottom right corner panel of the figure and shows the templates arranged on this grid. Thanks to the variational aspect of our model, these lc morphologies are representative of the general shape of the outputs generated from a latent representation in the vicinity of this sample, and thus of the general shape of the input encoded at this latent location. The number of points nodes in the grid is chosen to facilitate readability of the figure. However, we inspected the latent space with finer template grids and found no smaller-scale features in the latent space than those shown in the figures. The variability scale in the latent space is also penalised towards smaller values because of the unit Gaussian prior we use.

Case A is reported in figure 5.7. First, we observe a segregated distribution of lc types. While showing some with overlap, type 0 lcs mainly populate the right-hand side of the graph (high z_1) while types IIa, IIb and III are on the left-hand side. Interestingly, Type Ia are the least segregated distribution. Type Ib fall in the central part of the graph, between 0 and IIa, IIb, III. This confirms the ability of the code to arrange samples in terms of similarity. Second, we observe light clustering. This is highlighted by the kernel density estimation where we observe 3-4 distinct over-density locations in the latent space, one of which is centered on the type 0 population (notice the elongated structure of the over-density at this location, suggesting potential further clustering, hence the tentative identification of 4 overdensities). The DBSCAN however is not capable of recovering distinct clusters for any choice of parameters, leading to either a very large number of clusters detected (shown in this figure) or a very large

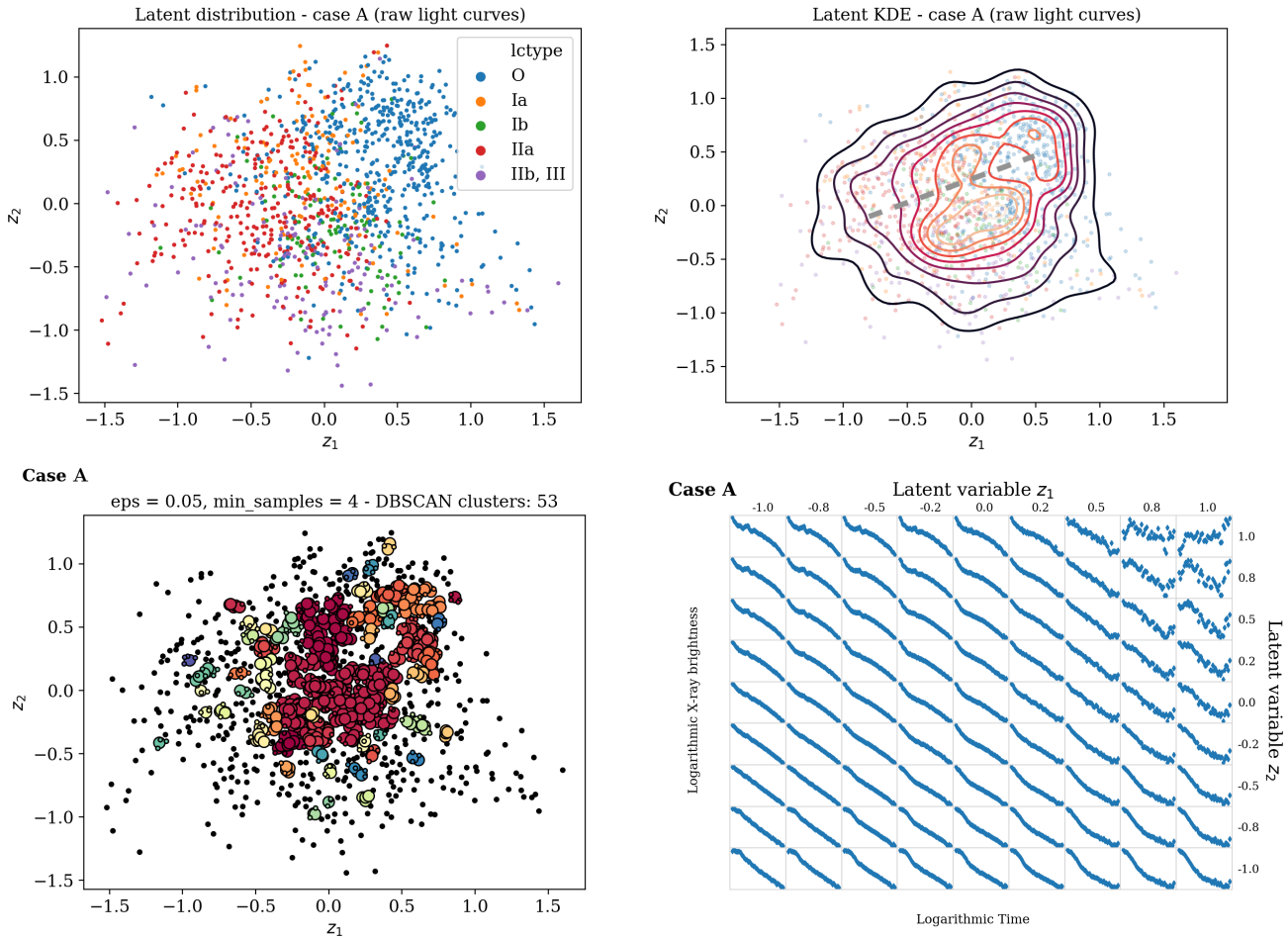


Figure 5.7: Case A: latent space distribution (sample distribution in upper left, sample density in upper right, DBSCAN clusters found in lower left, light curve templates in lower right). The description of these figures is given in the main text. We observe a separation (dashed grey segment in the KDE figure) between lcs with a flatter central regime (upper left corner), and those without (lower right corner). The unrealistic light curve templates in the upper right corner (bottom right=hand panel) do not correspond to light curves in the sample and are the result of sampling in a region of the latent space not used by the training set. No light curves from the validation set are found there either as shown in the latent distribution.

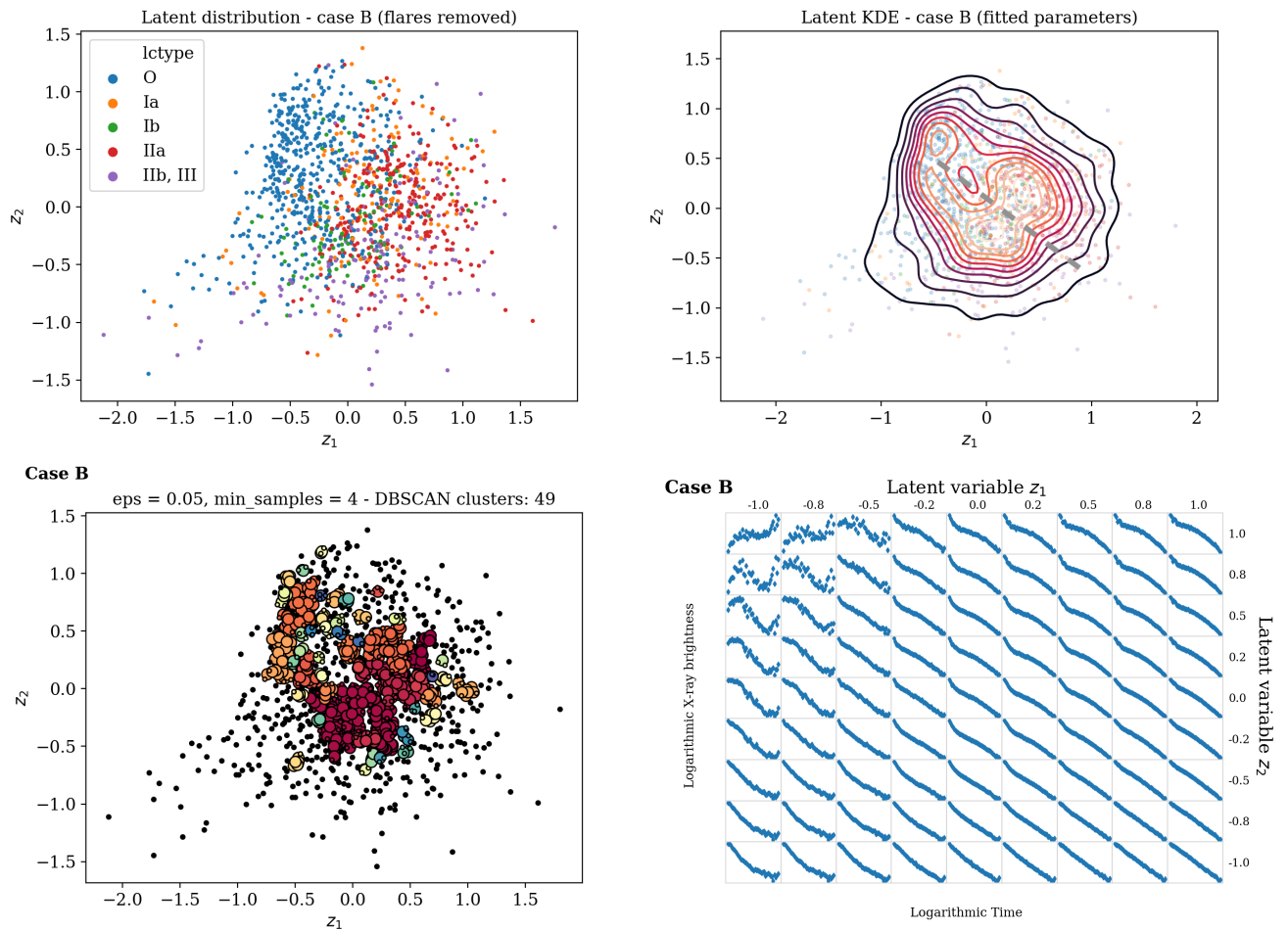


Figure 5.8: Case B: latent space distribution. (sample distribution in upper left, sample density in upper right, DBSCAN clusters found in lower left, light curve templates in lower right). The description of these figures is given in the main text. There is a separation (dashed grey segment in the KDE figure) between the lcs exhibiting a flatter central regime (upper right corner) and those devoid of such a phase (lower left corner). This separation is more visible than in case A.

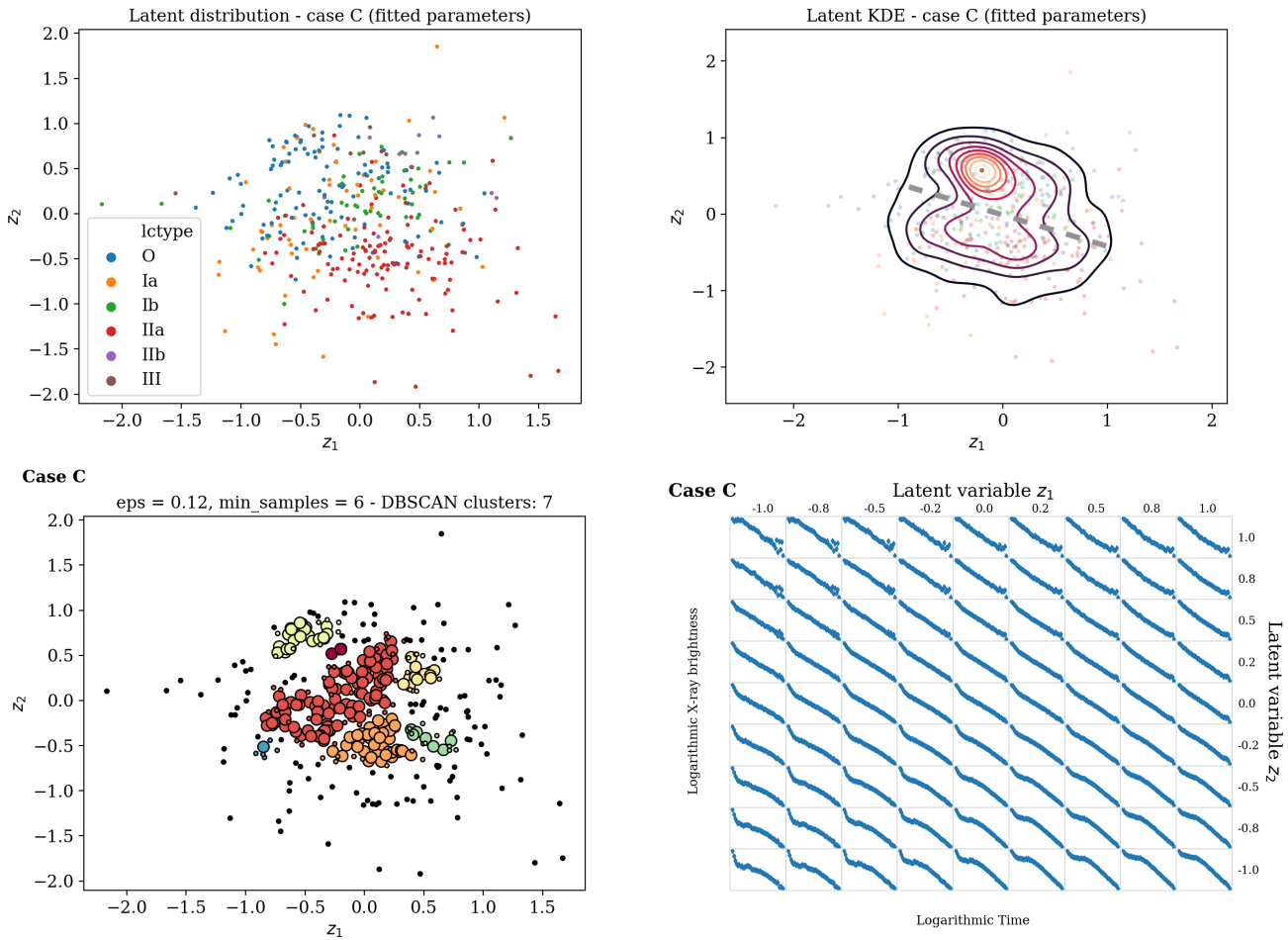


Figure 5.9: Case C: latent space distribution. (sample distribution in upper left, sample density in upper right, DBSCAN clusters found in lower left, light curve templates in lower right). The description of these figures is given in the main text. Here too, we observe a light separation (dashed grey segment, much less pronounced than in cases A and B) between lcs with a flatter central regime (lower left corner) and without (upper right corner). The latent space seems to be more clustered than in previous cases (A and B).

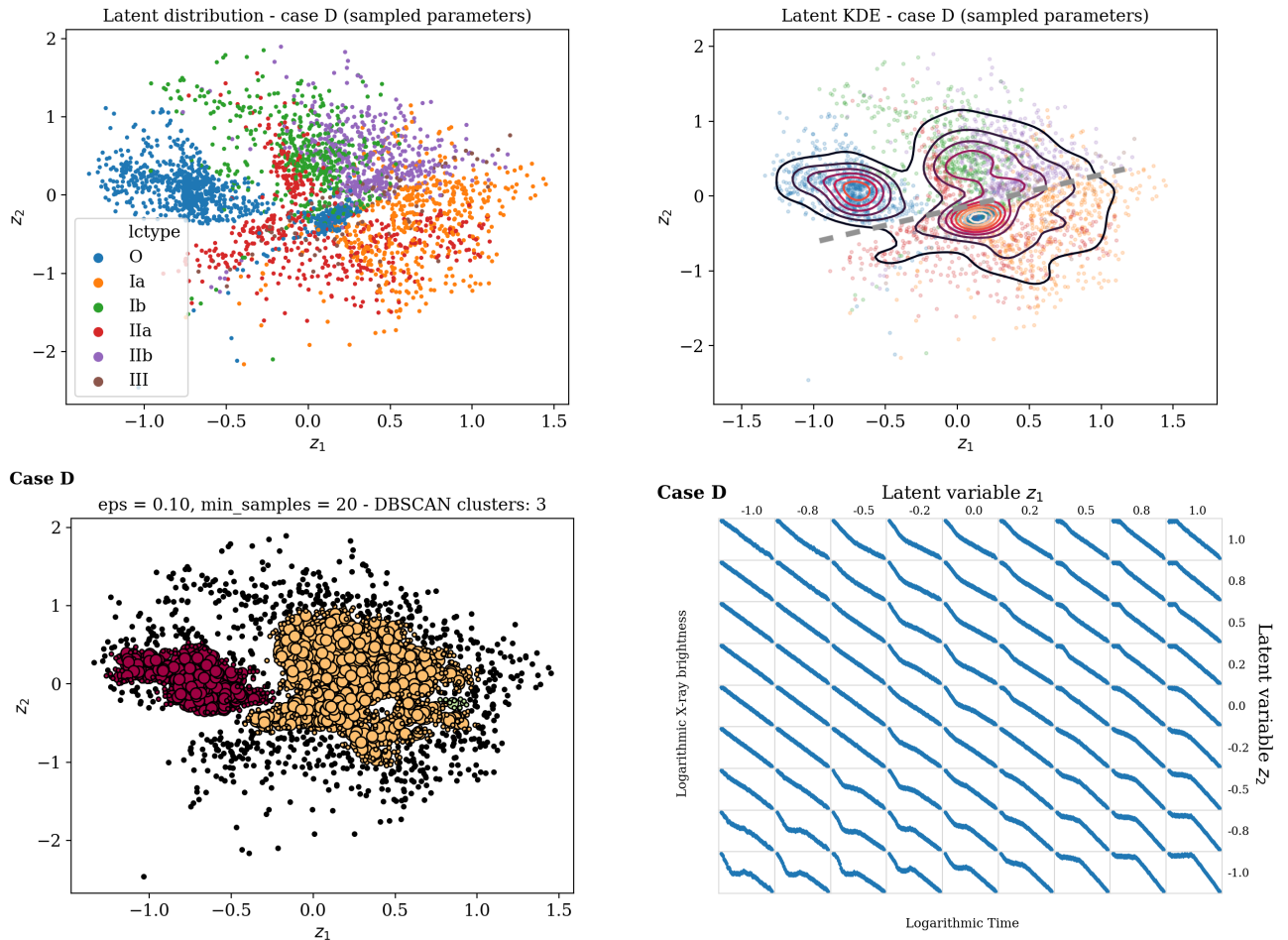


Figure 5.10: Case D: latent space distribution. (sample distribution in upper left, sample density in upper right, DBSCAN clusters found in lower left, light curve templates in lower right). The description of these figures is given in the main text. Three main clusters can be identified using the KDE (two type 0 clusters, one type Ib cluster), confirming the ability of the model to separated different lc morphologies. However, only two main clusters are recognised by DBSCAN. Type 0 lcs (single power-law) slope are clearly identified and separated from the rest of the dataset. Other smaller variability in the distribution suggest that the model has identified more discriminatory features in the lcs. Canonical lcs (IIa, red points) are placed at the bottom, with the increasing the level of the flatter central regime going towards the right side (seen in the templates). The separation between light curves with such flatter central regime and those without (dashed grey segment in KDE figure) is sharp but not wide. The over-densities on each side are quite pronounced however.

number of noise points and very poor completeness. One interesting feature however is a valley of lower density running from the lower-left to the upper-right corners, which disappears when encountering the type 0 population. When looking at the templates, we can observe that this feature separates two distinct types of lc morphology with light curves showing a flatter central regime phase in the upper-left corner (associated with the plateau phase of type IIa light curves), and lcs without such a regime in the lower-right corner. This valley disappears in the type 0 population which represents a "transition state" between the two cases. Interestingly however, some type IIa light curves are encoded on the side of the valley corresponding to no flatter central regime. This is either due to the incapacity of the network to properly reconstruct these light curves, or to other effects such as poor sampling of lcs, or very noisy signal, and needs to be investigated further. We also notice that the network is incapable of detecting the type Ia morphology which is absent from the templates and explains why type Ia lcs are scattered over the whole latent space. This needs more investigation to identify why the model presents such limitation.

As shown earlier, our ML model struggles in properly reconstructing lcs showing flares or rebrightenings. This is in part due to the regularisation in our objective function, but also to the very small dimensionality of the bottleneck of our autoencoder (two-dimensional latent space). Indeed, increasing the number of dimensions in the latent space consistently leads to better reconstruction, at the cost of interpretability however, since it becomes impossible to identify structure in the latent space with visual inspection. Carrying out analysis of a latent space of higher dimension can potentially lead one to identify more significant clustering but is left to future work at this stage. Instead, to improve reconstruction, we train the model on lcs where we have removed the short timescale variability (case B) and show the result in figure 5.8. We observe here the same segregation as in case A. However, the valley of lower density is more visible in this case and clearly separates lcs with a flatter central regime from those without (the valley runs in the upper-left to lower-right direction this time, the direction being arbitrary and only depending on the initial random state of the neural network). DBSCAN however does not display significant improvement, meaning that the gain from removing the variability in the lcs is potentially hindered by the creation of larger gaps and the loss of information. It is also possible that this variability is not the limiting factor of our approach.

An approach to removing this short timescale variability while avoiding the creation of gaps is to create synthetic light curves. In case C, we take the parameters measured by [M13](#) and create the corresponding synthetic light curves using the procedure described in §5.2.2. Unfortunately, this relatively old sample is much smaller than the current

sample of detected afterglows and training is more difficult as a result. Nevertheless, we get interesting insights from the graphs presented in figure 5.9. As for all previous cases, type 0 lcs are easily identified and clustered together (here in the upper-left corner). We also observe a clearer separation between type Ib and IIa, in a distribution that appears contain 3 clusters. Indeed, even though the KDE only shows 2 over-densities (most likely because one point in the latent space is much denser than the rest of the distribution and hides underlying structure), DBSCAN is this time able to identify 3 separate main clusters each corresponding to type 0, type Ib and type IIa light curves. Again, lcs with a flatter central regime (canonical type IIa) are separated from the rest of the sample. Here, the presence of less overlap between types in the latent space suggests that in cases A and B, the model was randomly reconstructing poorly sampled lcs, or lcs with gaps, with any morphology that fit satisfyingly, not taking into account Occam’s razor in doing so. The better sampling in case C potentially forces the model to adopt the correct morphology since many more bins are filled on average in each light curve. This could be verified by running the same analysis on well-sampled subsets of A and B.

So far, only light clustering has been observed in each latent distribution. We need to address whether this is due to the fact that, (i) even though we observe over-densities of single types of lcs, there is a smooth transition between lc morphologies, or (ii) the incapacity of our model to generate clusters in the first place. To do so, we use a final dataset (case D) in which we sample slopes and break times from arbitrary distributions (though similar to those measured for the same parameters in M13). In this new case, our CVAE is clearly able to single out type 0 light curves from the rest of the population, leading to the formation of 2 major clusters. Inside the right-hand side cluster, multiple over-densities suggest that the network is also able to separate the different lc types that display much less overlap than in previous cases, except for type IIa which can be mis-classified as Ia (orange) or Ib (green) if its early decay or plateau phase, respectively, is too short. Interestingly, the flatter central regime / no flatter central regime separation is clearly visible here again and runs from the lower-left to the upper-right corners in the templates. While this separation is sharp and is further highlighted by the fact that different light curve types sit on both sides, the gap observed is not as wide as in case B. Finally, part of the type 0 lcs actually sit at the boundary between all I, II, III types, allowing for a smooth transition in lc morphology from any type to any other. The results on this dataset thus show that the model is able to separate different morphologies, and that a short distance, or a smooth transition, between two populations, does suggest that there exists a whole range of hybrid morphologies in between.

5.5 Discussion

In this work, we set up and make use of a variational convolutional autoencoder to carry out unsupervised clustering of GRB afterglow light curves from *Swift*-XRT. We show that our model is capable of automatically clustering lcs of high similarity by producing a synthetic dataset. We apply our model to real data and find that light curves are segregated with observed types organising themselves in over-densities in the latent space. The smooth transition generally observed between types suggests that light curve morphologies actually span a continuum, and we do not recover the traditional light curve categories. In order to make sure that these categories are not lost because of the short timescale variability or poor sampling of part of the dataset, we carry out the same study on two additional datasets: (i) the real light curves where flares have been cut out, (ii) a synthetic dataset produced with parameters measured from real light curves. We find that the overlap is still significant in the first case, while the second case suggests the presence of clusters but necessitates a larger dataset to confirm. The presence in all cases, however, of a visible valley of lower density between lcs showing a flatter central regime and those without such flattening calls for further investigation. This can be carried out along two directions, either improving the clustering methods used, or expanding the dataset with new data collection.

Most importantly, we these qualitative results alone are not sufficient in order for us to conclude on the intrinsic number of light curve types and we require a quantitative measurement of cluster numbers. Indeed, visually observing clear clusters in the latent space of the real data would have confirmed supported the approach consisting in separating the on the *Swift*-XRT dataset in different light curve types, invalidating this hypothesis however requires us to quantitatively measure the level of clustering in the latent space in a noisy dataset. In this regard, unsupervised deep embedded clustering (DEC, [Xie et al., 2016](#)) represents a way to force the number of clusters the data has to form in the latent space. In order to retain the generative aspect of our current model, new methods, such as variational deep embedding (VaDE, [Jiang et al., 2017](#)) have been developed to combine the benefits in terms of interpretability that a VAE offers, with the control on the number of clusters formed of DEC. To do this, VaDE uses a mixture of Gaussians as prior, instead of a unit Gaussian, in the latent space of a VAE. Using this method would allow us to compare the posterior probabilities of models with varying numbers of clusters in a Bayesian model selection approach. Other metrics such as silhouette scores and the Calinsky-Harabasz index ([Calinski & Harabasz, 1974](#)) can help in identifying the most appropriate number of clusters to force the data into. These measures can also be directly applied to our

current latent representation when using other algorithms than DBSCAN, such as K-means and K-nearest neighbours, which will be done in the near future. Pre-processing of the lcs could also be simplified. Indeed, the role of the pre-processing is to prepare the data to allow convergence of a machine learning model and to remove the features of no interest (for example the absolute flux level). However, this process potentially introduces biases. Making use of recurrent neural networks simplifies the pre-processing and the risk of such biases appearing. This type of network is able to handle time-series data with variable number of data-points, by keeping a memory of the information previously seen by the network for each input time bin. The trade-off however is that that parallel back-propagation becomes impossible and the training time is significantly increased.

Acknowledgements

This work made use of data supplied by the UK Swift Science Data Centre at the University of Leicester.

Conclusion and Outlook

ANDERS: *Oh my God! Look at that picture over there!*

There's the Earth coming up. Wow, that's pretty.

BORMAN: *Hey, don't take that, it's not scheduled. (joking)*

ANDERS: *(laughs) You got a color film, Jim?*

Hand me that roll of color quick, would you...

LOVELL: *Oh man, that's great!*

— THE APOLLO 8 CREW, taking the picture 'Earthrise'

A lot of progress in our understanding of relativistic astrophysical transients is expected in the near future, thanks to a new generation of instruments and detectors opening new windows of observation. The Square Kilometer Array (Carilli et al., 2003) will significantly improve observations in the radio band. Radio afterglow emission can be detected at very late times and provides substantial information about the late stages of GRB evolution and inform the transition to non-relativistic dynamics. Where the current facilities can observe this transition only for a handful of events, SKA will observe up to a quarter of the detected GRB population at late times (Yuan et al., 2016). SKA will also observe afterglows below the synchrotron self-absorption break for longer. Additionally, polarisation measurements in radio allow us to probe the structure (or lack thereof) of the magnetic field in the ejecta and the surrounding medium.

Detection capabilities will be significantly enhanced by the launch of the Sino-French Space Variable Objects Monitor (SVOM, Schanne et al., 2010) dedicated to GRB detection and follow-up, whose one essential objective is to facilitate GRB redshift measurement and add to the detection capabilities of the current *Swift* telescope. Dedicated ground-based facilities ensure broadband observation of the detected GRBs. This instrument will require real-time modeling of afterglows for efficient resource observing time allocation. Indeed, the full power of SVOM will be unlocked when conducting follow-up operations with the new generation ground-based facilities such as the Cherenkov Telescope Array (CTA, Acharya et al., 2013) at very high energies, the Vera Rubin Large Synoptic Survey Telescope (LSST, Ivezić et al., 2019) in optical, and SKA in radio.

The forthcoming operations of CTA promise real advances in the understanding of the very high energy and particle acceleration processes at play in GRBs and GRB afterglows. The first TeV detections from the afterglows of GRB180720B and GRB190829A by the High-Energy Stereoscopic System (HESS, Hinton, 2004), and GRB190114C by the Major Atmospheric Gamma Imaging Cherenkov Telescopes (MAGIC, Barrio et al., 1998), the latter attributed to synchrotron self-Compton (SSC) processes, call for accurate incorporation of particle acceleration and scattering processes associated with emission. All these new facilities are of course expected to also inform us on the physics of other relativistic phenomena such as active galactic nuclei, tidal disruption events, etc.

As we expect these new facilities to reveal ever more complex features of the GRB afterglow phenomenon, the models describing the targeted transients have to be improved for (i) accurate description of new features, (ii) accurate real-time analysis of transients and prediction of flux evolution for resource allocation. This is particularly

important as the global temporal evolution results from the contribution of competing distinct components which dominate at different times. Only then is it possible to use these new observations to properly constrain the underlying physical mechanisms.

In this context, the questions driving the argument of this thesis have been the following:

- **How can we theoretically constrain the micro-physics of emission from GRB observations?**
- **How can we devise relevant and self-consistent numerical schemes to extract such information?**
- **What can we learn about the phenomenology of these events using this accurate modeling?**

With this underlying framework in mind, we decided to focus on three outstanding scientific questions regarding aspects of GRB phenomenology:

- In chapter 3 we investigated the origin of flares in the early X-ray afterglow. We showed that these flares can be the result of the interaction of a long-lived reverse shock with a stratified ejecta. This stratified ejecta can be the result of chaotic central engine shutdown imprinted into the ejecta during the progenitor collapse. Variability present at the back of a region of low velocity leads to flares at later times. These results lift the constraints on central engine activity long after prompt emission.
- In chapter 4 we focused on accurately modeling the trans-relativistic evolution of the blast wave when it decelerates to non-relativistic speeds. We found that the cooling break in the GRB afterglow spectrum does not shift with time during the jet break, in opposition to the temporary increase between the ultra-relativistic and Newtonian phases modeled in previous works, which bears strong implications on late-time interpretation of GRB afterglow observational data.
- In chapter 5 we investigated the variability in morphology in the current sample of X-ray afterglow light curves with the aim to investigate whether the GRB afterglow sample consists of separate classes or if all light curves should be interpreted using a unified model, with unsupervised dimensionality reduction machine learning techniques.

In order to be able to carry out accurate simulations of such situations we identified the need for a better handling of both the numerical hydrodynamics and radiative

prescriptions. The new set of methods we presented needed to accurately handle **complex dynamics leading to interacting radiating shocks** (i.e. multiple emission sites) and would need to provide an **accurate broadband synthetic flux** to reliably compare light curve features in different observing bands. These criteria can be met by carrying out numerical dynamical simulations on a moving mesh and by locally tracing the accelerated particle population downstream of radiating shocks. We implemented these features in a self-contained code, **GAMMA**, which is publicly available and can be used to carry out simulations of dynamics and emission from any relativistic astrophysical source.

In the applications of **GAMMA** presented in this thesis, we have focused on the high-energy end of the EM spectrum and ignored synchrotron self-absorption (SSA) which plays a significant part in the radio range. However, unlike cooling, SSA does not need to be implemented directly in the dynamical simulation and can simply be implemented during the linear radiative transfer phase (Granot et al. 1999; Granot & Sari 2002; more recently van Eerten et al. 2010b). This is actually already implemented in the code **blast** and will be used in future studies. The addition of SSA leads to an additional break frequency ν_a in the spectrum of a radiative shock, below which the emitting fluid becomes optically thick. Below ν_a , only the front of the blast-wave is visible to the observer. Similarly to the change in peak flux in the fast-cooling case with no SSA, we also expect new regimes to appear below ν_a in the fast-cooling case with SSA. These aspects are important to take into account when analysing the early radio emission from afterglows, especially when trying to disentangle RS and FS contributions, which will become crucial with SKA observations.

Having such a code at our disposal, we can apply it to some outstanding questions in GRB research such as the flattening of the light-curve in GRB170817A which could potentially be a manifestation of a change in particle index p (Troja et al., 2020). Our local description of the micro-physics allows us to investigate such a situation. Additionally, as we expect potential contribution from the associated kilonova afterglow, only an accurate calculation of the absolute flux from the GRB afterglow can allow us to accurately extract the KN contribution.

With new facilities starting operations in the near future, the numerical work we carried out can now be expanded upon in various ways. An application of great potential of the code is to develop a fitting tool based on templates simulated with **GAMMA**, along the lines of the work carried out by van Eerten et al. (2012). This tool will provide both improvements in terms of precision, thanks to the moving mesh, but also in terms of accuracy as the spectra were previously obtained using the "hybrid" global cooling

approximation, introducing an offset in the position of the cooling break. In the era of SVOM, this tool would allow real-time modeling of light curves and consequently help with resource allocation with an unprecedented level of accuracy. Another avenue to explore involves the recent TeV detections from GRB afterglows, which will only become more frequent with the first observations from CTA. In this regard, it is crucial that we investigate how relativistic explosions can produce such high-energy emission and pin down the radiative efficiency of the processes involved (e.g. synchrotron self-Compton). A code that provides a local treatment of particle evolution can serve as a test-bench for particle acceleration and light-matter interaction theory, as well as turbulent magnetic field generation, as it becomes possible to experiment with various local physical prescriptions. Continuing in this direction, the implementation of a magnetohydrodynamical (MHD) module can be a way to link polarisation measurements with magnetic field geometry and behavior. It also opens the door to applications in other fields such as AGN physics where magnetic fields play a major role with regards to jet stability.

Bibliography

- Abbott, B. P., Abbott, R., Abbott, T. D., et al. (2017). Gravitational Waves and Gamma-Rays from a Binary Neutron Star Merger: GW170817 and GRB 170817A. *The Astrophysical Journal letters*, 848(2):L13.
- Abbott, B. P., Abbott, R., Abbott, T. D., et al. (2017a). GW170817: Observation of Gravitational Waves from a Binary Neutron Star Inspiral. *Physical Review Letters*, 119(16):30–33.
- Abbott, B. P., Abbott, R., Abbott, T. D., et al. (2017b). Multi-messenger Observations of a Binary Neutron Star Merger. *The Astrophysical Journal Letters*, 848(2):L12.
- Acharya, B., Actis, M., Aghajani, T., et al. (2013). Introducing the CTA concept. *Astroparticle Physics*, 43:3–18.
- Akerlof, C., Balsano, R., Barthelmy, S., et al. (1999). Observation of contemporaneous optical radiation from a γ -ray burst. *Nature*, 398(6726):400–402.
- Andrade, U., Bengaly, C. A. P., Alcaniz, J. S., et al. (2019). Revisiting the statistical isotropy of GRB sky distribution. *Monthly Notices of the Royal Astronomical Society*, 490(4):4481–4488.
- Ayache, E. H., van Eerten, H. J., Daigne, F. (2020). Late X-ray flares from the interaction of a reverse shock with a stratified ejecta in GRB afterglows: simulations on a moving mesh. *Monthly Notices of the Royal Astronomical Society*, 495(3):2979–2993.
- Banyuls, F., Font, J. A., Ibanez, J. M., et al. (1997). Numerical $\{3 + 1\}$ General Relativistic Hydrodynamics: A Local Characteristic Approach. *The Astrophysical Journal*, 476(1):221–231.
- Barniol Duran, R. (2014). Constraining the magnetic field in GRB relativistic collisionless shocks using radio data. *Monthly Notices of the Royal Astronomical Society*, 442(4):3147–3154.

- Barrio, J., et al. (1998). Design report on magic. *MPI-PhE/98-5:11–27*.
- Bell, A. R. (1978). The acceleration of cosmic rays in shock fronts - I. *Monthly Notices of the Royal Astronomical Society*, 182(2):147–156.
- Beniamini, P., van der Horst, A. J. (2017). Electrons' energy in GRB afterglows implied by radio peaks. *Monthly Notices of the Royal Astronomical Society*, 472(3):3161–3168.
- Berger, E. (2013). Short-Duration Gamma-Ray Bursts. *Annu. Rev. Astron. Astrophys.*, 52:43 – 105.
- Bhat, P. N., Meegan, C. A., von Kienlin, A., et al. (2016). The Third Fermi GBM Gamma-ray Burst Catalog: The First Six Years. *The Astrophysical Journal Supplement Series*, 223(2):28.
- Bissaldi, E., von Kienlin, A., Kouveliotou, C., et al. (2011). First-year Results of Broad-band Spectroscopy of the Brightest Fermi-GBM Gamma-Ray Bursts. *Astrophysical Journal*, 733(2):97.
- Blandford, R., Eichler, D. (1987). Particle acceleration at astrophysical shocks: A theory of cosmic ray origin. *Physics Reports*, 154(1):1–75.
- Blandford, R., Meier, D., Readhead, A. (2019). Relativistic Jets from Active Galactic Nuclei. *Annual Review of Astronomy and Astrophysics*, 57(1):467–509.
- Blandford, R. D., McKee, C. F. (1976). Fluid dynamics of relativistic blast waves. *Physics of Fluids*, 19(8):1130.
- Blandford, R. D., Ostriker, J. P. (1978). Particle acceleration by astrophysical shocks. *The Astrophysical Journal*, 221:L29.
- Blei, D. M., Kucukelbir, A., McAuliffe, J. D. (2017). Variational Inference: A Review for Statisticians. *Journal of the American Statistical Association*, 112(518):859–877.
- Bloom, J. S., Frail, D. a., Kulkarni, S. R. (2003). Gamma-Ray Burst Energetics and the Gamma-Ray Burst Hubble Diagram: Promises and Limitations. *The Astrophysical Journal*, 594(2):674–683.
- Bodenheimer, P., Laughlin, G., Rozyczka, M., et al. (2007). *Numerical Methods in astrophysics: An Introduction*.
- Boella, G., Butler, R. C., Perola, G. C., et al. (1997). BeppoSAX, the wide band mission

- for X-ray astronomy. *Astronomy and Astrophysics Supplement Series*, 122(2):299–307.
- Bourlard, H., Kamp, Y. (1988). Auto-association by multilayer perceptrons and singular value decomposition. *Biological Cybernetics*, 59(4-5):291–294.
- Briggs, M. S., Paciesas, W. S., Pendleton, G. N., et al. (1996). BATSE Observations of the Large-Scale Isotropy of Gamma-Ray Bursts. *The Astrophysical Journal*, 459:40.
- Burrows, D. N., Hill, J. E., Nousek, J. A., et al. (2005a). The Swift X-Ray Telescope. *Space Science Reviews*, 120(3-4):165–195.
- Burrows, D. N., Romano, P., Falcone, A., et al. (2005b). Astrophysics: Bright X-ray flares in gamma-ray burst afterglows. *Science*, 309(5742):1833–1835.
- Calinski, T., Harabasz, J. (1974). A dendrite method for cluster analysis. *Communications in Statistics - Theory and Methods*, 3(1):1–27.
- Cannizzo, J. K., Gehrels, N., Vishniac, E. T. (2004). A Numerical Gamma-Ray Burst Simulation Using Three-Dimensional Relativistic Hydrodynamics: The Transition from Spherical to Jetlike Expansion. *The Astrophysical Journal*, 601(1):380–390.
- Cao, X., Liang, E. W., Yuan, Y. F. (2014). Episodic jet power extracted from a spinning black hole surrounded by a neutrino-dominated accretion flow in gamma-ray bursts. *The Astrophysical Journal*, 789(2).
- Carilli, C. L., Ivison, R. J., Frail, D. A. (2003). Variability of Submillijansky Radio Sources. *The Astrophysical Journal*, 590(1):192–196.
- Chincarini, G., Mao, J., Margutti, R., et al. (2010). Unveiling the origin of X-ray flares in gamma-ray bursts. *Monthly Notices of the Royal Astronomical Society*, 406(4):2113–2148.
- Chincarini, G., Moretti, A., Romano, P., et al. (2007). The First Survey of X-Ray Flares from Gamma-Ray Bursts Observed by Swift : Temporal Properties and Morphology. *The Astrophysical Journal*, 671(2):1903–1920.
- Costa, E., Frontera, F., Heise, J., et al. (1997). Discovery of an X-ray afterglow associated with the γ -ray burst of 28 February 1997. *Nature*, 387(6635):783–785.
- Courant, R., Friedrichs, K., Lewy, H. (1928). Über die partiellen Differenzgleichungen der mathematischen Physik. *Mathematische Annalen*, 100(1):32–74.
- Curran, P. A., Van Der Horst, A. J., Wijers, R. A. (2008). Are the missing X-ray

- breaks in gamma-ray burst afterglow light curves merely hidden? *Monthly Notices of the Royal Astronomical Society*, 386(2):859–863.
- Daigne, F., Mochkovitch, R. (1998). Gamma-ray bursts from internal shocks in a relativistic wind: Temporal and spectral properties. *Monthly Notices of the Royal Astronomical Society*, 296(2):275–286.
- Daigne, F., Mochkovitch, R. (2000). Gamma-ray bursts from internal shocks in a relativistic wind: an hydrodynamical study. *Astronomy and Astrophysics*, 358(3):1157–1166.
- d’Avanzo, P., Salvaterra, R., Bernardini, M., et al. (2014). A complete sample of bright swift short gamma-ray bursts. *Monthly Notices of the Royal Astronomical Society*, 442(3):2342–2356.
- Davis, S. F. (1988). Simplified Second-Order Godunov-Type Methods. *SIAM Journal on Scientific and Statistical Computing*, 9(3):445–473.
- De Colle, F., Granot, J., López-Cámara, D., et al. (2012). Gamma-ray Burst Dynamics And Afterglow Radiation From Adaptive Mesh Refinement, Special Relativistic Hydrodynamic Simulations. *The Astrophysical Journal*, 746(2):122.
- De Colle, F., Ramirez-Ruiz, E., Granot, J., et al. (2011). Simulations of GRB Jets in a Stratified External Medium: Dynamics, Afterglow Lightcurves, Jet Breaks and Radio Calorimetry:1–11.
- Djorgovski, S. G., Metzger, M. R., Kulkarni, S. R., et al. (1997). The optical counterpart to the γ -ray burst GRB970508. *Nature*, 387(6636):876–878.
- Downes, T. P., Duffy, P., Komissarov, S. S. (2002). Relativistic blast waves and synchrotron emission. *Monthly Notices of the Royal Astronomical Society*, 332(1):144–152.
- Duffell, P. C. (2016). DISCO: A 3D Moving-mesh Magnetohydrodynamics Code Designed For The Study Of Astrophysical Disks. *The Astrophysical Journal Supplement Series*, 226(1):2.
- Duffell, P. C., Laskar, T. (2017). On the Deceleration and Spreading of Relativistic Jets I: Jet Dynamics. *The Astrophysical Journal*, 865(2):94.
- Duffell, P. C., MacFadyen, A. I. (2011). TESS: A Relativistic Hydrodynamics Code on a Moving Voronoi Mesh. *The Astrophysical Journal Supplement Series*, m(1995).

- Duffell, P. C., MacFadyen, A. I. (2013). Rayleigh-Taylor Instability in a Relativistic Fireball on a Moving Computational Grid. *The Astrophysical Journal*, 775(2):87.
- Eichler, D., Livio, M., Piran, T., et al. (1989). Nucleosynthesis, neutrino bursts and γ -rays from coalescing neutron stars. *Nature*, 340(6229):126–128.
- Eichler, D., Waxman, E. (2005). The Efficiency of Electron Acceleration in Collisionless Shocks and Gamma-Ray Burst Energetics. *The Astrophysical Journal*, 627(2):861–867.
- Elman, J. (1990). Finding structure in time. *Cognitive Science*, 14(2):179–211.
- Ester, M., Kriegel, H.-P., Sander, J., et al. (1996). A Density-Based Algorithm for Discovering Clusters in Large Spatial Databases with Noise. *Proceedings of the 2nd International Conference on Knowledge Discovery and Data Mining*:226–231.
- Evans, P. A., Beardmore, A. P., Page, K. L., et al. (2007). An online repository of Swift/XRT light curves of γ -ray bursts. *Astronomy and Astrophysics*, 469(1):379–385.
- Evans, P. A., Beardmore, A. P., Page, K. L., et al. (2009). Methods and results of an automatic analysis of a complete sample of Swift-XRT observations of GRBs. *Monthly Notices of the Royal Astronomical Society*, 397(3):1177–1201.
- Falcone, A. D., Morris, D., Racusin, J., et al. (2007). The First Survey of X-Ray Flares from Gamma-Ray Bursts Observed by Swift: Spectral Properties and Energetics. *The Astrophysical Journal*, 671:1921.
- Frail, D. A., Kulkarni, S. R., Sari, R., et al. (2001). Beaming in Gamma-Ray Bursts: Evidence for a Standard Energy Reservoir. *The Astrophysical Journal*, 8(1):55–58.
- Frail, D. A., Waxman, E., Kulkarni, S. R. (2000). A 450 Day Light Curve of the Radio Afterglow of GRB 970508: Fireball Calorimetry. *The Astrophysical Journal*, 537(1):191–204.
- Fruchter, A. S., Levan, A. J., Strolger, L., et al. (2006). Long gamma-ray bursts and core-collapse supernovae have different environments. *Nature*, 441(May):463–468.
- Fynbo, J. P. U., Jakobsson, P., Prochaska, J. X., et al. (2009). Low-resolution Spectroscopy Of Gamma-ray Burst Optical Afterglows: Biases In The Swift Sample And Characterization Of The Absorbers. *The Astrophysical Journal Supplement Series*, 185(2):526–573.

- Galama, T. J., Vreeswijk, P. M., Van Paradijs, J., et al. (1998). An unusual supernova in the error box of the γ -ray burst of 25 April 1998. *Nature*, 395(6703):670–672.
- Garcia-Dias, R., Prieto, C. A., Almeida, J. S., et al. (2018). Machine learning in APOGEE: Unsupervised spectral classification with K-means. *Astronomy and Astrophysics*, 612.
- Gehrels, N., Chincarini, G., Giommi, P., et al. (2004). The Swift Gamma-Ray Burst Mission. *The Astrophysical Journal*:1005–1020.
- Genet, F., Daigne, F., Mochkovitch, R. (2007). Can the early X-ray afterglow of gamma-ray bursts be explained by a contribution from the reverse shock? *Monthly Notices of the Royal Astronomical Society*, 381(2):732–740.
- Ghirlanda, G., Ghisellini, G., Salvaterra, R., et al. (2013). The faster the narrower: Characteristic bulk velocities and jet opening angles of gamma-ray bursts. *Monthly Notices of the Royal Astronomical Society*, 428(2):1410–1423.
- Giannios, D., Mimica, P., Aloy, M. A. (2008). On the existence of a reverse shock in magnetized gamma-ray burst ejecta. *Astronomy and Astrophysics*, 478(3):747–753.
- Gleeson, L. J., Legg, M. P. C., Westfold, K. C. (1974). Synchrotron Emission from Particles Having A Truncated Power-law Energy Spectrum. *Monthly Notices of the Royal Astronomical Society*, 168(2):379–397.
- Godunov, S. K. (1959). A difference method for numerical calculations of discontinuous solutions of the equations of hydrodynamics. *Mat. Sb. (N.S.)*, 47(89)(3):271 – 306.
- Goldstein, A., Veres, P., Burns, E., et al. (2017). An Ordinary Short Gamma-Ray Burst with Extraordinary Implications: Fermi-GBM Detection of GRB 170817A. *The Astrophysical Journal Letters*, 848(2):L14.
- Goodman, J. (1986). Are gamma-ray bursts optically thick? *The Astrophysical Journal*, 308:L47.
- Granot, J. (2007). The structure and dynamics of GRB jets. *Revista Mexicana de Astronomia y Astrofisica: Serie de Conferencias*, 27:140–165.
- Granot, J., Piran, T. (2012). On the lateral expansion of gamma-ray burst jets. *Monthly Notices of the Royal Astronomical Society*, 421(1):570–587.
- Granot, J., Piran, T., Bromberg, O., et al. (2015). Gamma-Ray Bursts as Sources of Strong Magnetic Fields. *Space Science Reviews*, 191(1-4):471–518.

- Granot, J., Piran, T., Sari, R. (1999). Images and Spectra from the Interior of a Relativistic Fireball. *The Astrophysical Journal*, 513(2):679–689.
- Granot, J., Piran, T., Sari, R. (2000). The Synchrotron Spectrum of Fast Cooling Electrons Revisited. *The Astrophysical Journal*, 534(2):L163–L166.
- Granot, J., Sari, R. (2002). The Shape of Spectral Breaks in Gamma-Ray Burst Afterglows. *The Astrophysical Journal*, 568(2):820–829.
- Gruber, D., Goldstein, A., von Ahlefeld, V. W., et al. (2014). The Fermi GBM Gamma-ray Burst Spectral Catalog: Four Years Of Data. *The Astrophysical Journal Supplement Series*, 211(1):12.
- Guidorzi, C., Mundell, C. G., Harrison, R., et al. (2014). New constraints on gamma-ray burst jet geometry and relativistic shock physics. *Monthly Notices of the Royal Astronomical Society*, 438(1):752–767.
- Hajela, A., Margutti, R., Alexander, K. D., et al. (2019). Two Years of Nonthermal Emission from the Binary Neutron Star Merger GW170817: Rapid Fading of the Jet Afterglow and First Constraints on the Kilonova Fastest Ejecta. *The Astrophysical Journal*, 886(1):L17.
- Hallinan, G., Corsi, A., Mooley, K. P., et al. (2017). A radio counterpart to a neutron star merger. *Science*, 358(6370):1579–1583.
- Harten, A., Lax, P. D., van Leer, B. (1983). On Upstream Differencing and Godunov-Type Schemes for Hyperbolic Conservation Laws. *SIAM Review*, 25(1):35–61.
- Hartmann, D., Blumenthal, G. R. (1989). Angular clustering properties of gamma-ray bursts and quantitative constraints on their distances. *The Astrophysical Journal*, 342:521.
- Hartmann, D. H., Linder, E. V., Blumenthal, G. R. (1991). Fuzzy correlations of gamma-ray bursts. *The Astrophysical Journal*, 367:186.
- Hascoët, R., Beloborodov, A. M., Daigne, F., et al. (2017). X-ray flares from dense shells formed in gamma-ray burst explosions. *Monthly Notices of the Royal Astronomical Society: Letters*, 472(1):L94–L98.
- Hinton, G. E., Zemel, R. S. (1994). Autoencoders, Minimum Description Length and Helmholtz Free Energy. *Proceedings of the 6th International Conference on Neural Information Processing Systems*.

- Hinton, J. (2004). The status of the HESS project. *New Astronomy Reviews*, 48(5-6):331–337.
- Hjorth, J., Sollerman, J., Møller, P., et al. (2003). A very energetic supernova associated with the gamma-ray burst of 29 March 2003. *Nature*, 423(6942):847–850.
- Hou, T. Y., Le Floch, P. G. (1994). Why Nonconservative Schemes Converge to Wrong Solutions: Error Analysis. *Mathematics of Computation*, 62(206):497.
- Ioka, K., Kobayashi, S., Zhang, B. (2005). Variabilities of Gamma Ray Burst Afterglows: Long acting Engine, Anisotropic Jet, or Many Fluctuating Regions? *The Astrophysical Journal*, 631(1):429–434.
- Ivezić, Ž., Kahn, S. M., Tyson, J. A., et al. (2019). LSST: From Science Drivers to Reference Design and Anticipated Data Products. *The Astrophysical Journal*, 873(2):111.
- Jakobsson, P., Levan, A., Fynbo, J. P. U., et al. (2006). A mean redshift of 2.8 for Swift gamma-ray bursts. *Astronomy & Astrophysics*, 447(3):897–903.
- Jespersen, C. K., Severin, J. B., Steinhardt, C. L., et al. (2020). An Unambiguous Separation of Gamma-Ray Bursts into Two Classes from Prompt Emission Alone.
- Jiang, Z., Zheng, Y., Tan, H., et al. (2017). Variational Deep Embedding: An Unsupervised and Generative Approach to Clustering. In *Proceedings of the Twenty-Sixth International Joint Conference on Artificial Intelligence (IJCAI-17)*.
- Kann, D. A., Klose, S., Zhang, B., et al. (2010). The Afterglows of Swift-era Gamma-ray Bursts. I. Comparing pre-Swift and Swift-era Long/Soft (Type II) GRB Optical Afterglows. *The Astrophysical Journal*, 720(2):1513–1558.
- Kasliwal, M. M., Nakar, E., Singer, L. P., et al. (2017). Illuminating gravitational waves: A concordant picture of photons from a neutron star merger. *Science*, 358(6370):1559–1565.
- Kathirgamaraju, A., Duran, R. B., Giannios, D. (2017). Off-axis short GRBs from structured jets as counterparts to GW events. *Proceedings of Science*, 2017-Octob.
- Keshet, U., Waxman, E. (2005). Energy Spectrum of Particles Accelerated in Relativistic Collisionless Shocks. *Physical Review Letters*, 94(11):111102.
- King, A., Brien, P. T. O., Goad, M. R., et al. (2005). Gamma-ray bursts: Restarting the engine. *The Astrophysical Journal*, (630):L113–L115.

- Kingma, D. P., Ba, J. L. (2015). Adam: A method for stochastic optimization. *3rd International Conference on Learning Representations, ICLR 2015 - Conference Track Proceedings*:1–15.
- Kingma, D. P., Welling, M. (2013). Auto-Encoding Variational Bayes.
- Kirk, J. G., Guthmann, A. W., Gallant, Y. A., et al. (2000). Particle Acceleration at Ultrarelativistic Shocks: An Eigenfunction Method. *The Astrophysical Journal*, 542(1):235–242.
- Klebesadel, R. W., Strong, I. B., Olson, R. A. (1973). Observations of Gamma-Ray Bursts of Cosmic Origin. *The Astrophysical Journal*, 182:L85.
- Kobayashi, S. (2000). Light Curves of Gamma-Ray Burst Optical Flashes. *The Astrophysical Journal*, 545(2):807–812.
- Kobayashi, S., Piran, T., Sari, R. (1997). Can Internal Shocks Produce the Variability in Gamma-Ray Bursts? *The Astrophysical Journal*, 490(1):92–98.
- Kobayashi, S., Piran, T., Sari, R. (1999). Hydrodynamics of a Relativistic Fireball: The Complete Evolution. *The Astrophysical Journal*, 513:669–678.
- Kobayashi, S., Zhang, B., Meszaros, P., et al. (2007). Inverse Compton X-Ray Flare from Gamma-Ray Burst Reverse Shock. *The Astrophysical Journal*, 655(1):391–395.
- Kouveliotou, C., Meegan, C. A., Fishman, G. J., et al. (1993). Identification of two classes of gamma-ray bursts. *The Astrophysical Journal*, 413:L101.
- Kumar, P., Granot, J. (2003). The Evolution of a Structured Relativistic Jet and Gamma-Ray Burst Afterglow Light Curves. *The Astrophysical Journal*, 591(2):1075–1085.
- Lamberts, A., Daigne, F. (2018). Relativistic simulations of long-lived reverse shocks in stratified ejecta: the origin of flares in GRB afterglows. *Monthly Notices of the Royal Astronomical Society*, 474(2):2813–2827.
- Lamberts, A., Fromang, S., Dubus, G., et al. (2013). Simulating gamma-ray binaries with a relativistic extension of RAMSES. *Astronomy & Astrophysics*, 560:A79.
- Laskar, T., Alexander, K. D., Gill, R., et al. (2019). Alma detection of a linearly polarized reverse shock in grb 190114c. *The Astrophysical Journal Letters*, 878(1):L26.
- Lax, P. D., Wendroff, B. (1960). Systems of conservation laws. *Communications on Pure and Applied Mathematics*, 13(2):217–237.

- Lazzati, D., Perna, R. (2019). Jet-Cocoon Outflows from Neutron Star Mergers: Structure, Light Curves, and Fundamental Physics. *The Astrophysical Journal*, 881(2):89.
- LeCun, Y. (1987). *Modèles Connexionnistes de l'Apprentissage*. Ph.D. thesis.
- LeCun, Y., Boser, B., Denker, J. S., et al. (1989). Backpropagation Applied to Handwritten Zip Code Recognition. *Neural Computation*, 1(4):541–551.
- Lee, W. H., Ramirez-Ruiz, E., López-Cmara, D. (2009). Phase transitions and he-synthesis-driven winds in neutrino cooled accretion disks: Prospects for late flares in short gamma-ray bursts. *The Astrophysical Journal*, 699(2 PART 2):93–96.
- LeVeque, R. (1998). Nonlinear conservation laws and finite volume methods. *Computational methods for astrophysical fluid flow*, M:1–159.
- LeVeque, R. J. (1992). *Numerical Methods for Conservation Laws*, vol. 57.
- MacFadyen, A. I., Woosley, S. E. (1999). Collapsars: Gamma-Ray Bursts and Explosions in “Failed Supernovae”. *The Astrophysical Journal*, 524(1):262–289.
- Marcowith, A., Ferrand, G., Grech, M., et al. (2020). Multi-scale simulations of particle acceleration in astrophysical systems.
- Margutti, R., Bernardini, G., Duran, R. B., et al. (2011). On the average gamma-ray burst X-ray flaring activity. *Monthly Notices of the Royal Astronomical Society*, 410(2):1064–1075.
- Margutti, R., Zaninoni, E., Bernardini, M. G., et al. (2012). A comprehensive statistical analysis of Swift X-ray light-curves: the prompt-afterglow connection in Gamma-Ray Bursts.
- Margutti, R., Zaninoni, E., Bernardini, M. G., et al. (2013). The prompt-afterglow connection in gamma-ray bursts: a comprehensive statistical analysis of Swift X-ray light curves. *Monthly Notices of the Royal Astronomical Society*, 428(1):729–742.
- Martí, J. M., Ibáñez, J. M., Miralles, J. A. (1991). Numerical relativistic hydrodynamics: Local characteristic approach. *Physical Review D*, 43(12):3794–3801.
- Martí, J. M., Müller, E. (1994). The analytical solution of the Riemann problem in relativistic hydrodynamics. *Journal of Fluid Mechanics*, 258:317–333.
- Martí, J. M., Müller, E. (2003). Numerical hydrodynamics in special relativity. *Living Reviews in Relativity*, 2:1–100.

- Mathews, W. G. (1971). The Hydromagnetic Free Expansion of a Relativistic Gas. *The Astrophysical Journal*, 165:147.
- Meegan, C. A., Fishman, G. J., Wilson, R. B., et al. (1992). Spatial distribution of gamma-ray bursts observed by BATSE. *Nature*, 355:143–145.
- Meliani, Z., Keppens, R. (2010). Dynamics and stability of relativistic gamma-ray-bursts blast waves. *Astronomy and Astrophysics*, 520(20):1–4.
- Meliani, Z., Keppens, R., Casse, F., et al. (2007). AMRVAC and relativistic hydrodynamic simulations for gamma-ray burst afterglow phases. *Monthly Notices of the Royal Astronomical Society*, 376(3):1189–1200.
- Meliani, Z., Sauty, C., Tsinganos, K., et al. (2004). Relativistic parker winds with variable effective polytropic index. *Astronomy and Astrophysics*, 425(3):773–781.
- Mészáros, P., Laguna, P., Rees, M. J. (1993). Gasdynamics of Relativistically Expanding Gamma-Ray Burst Sources: Kinematics, Energetics, Magnetic Fields and Efficiency. *The Astrophysical Journal*, 415(1):181–190.
- Meszáros, P., Rees, M. J. (1993). Relativistic fireballs and their impact on external matter - Models for cosmological gamma-ray bursts. *The Astrophysical Journal*, 405:278.
- Meszáros, P., Rees, M. J. (1997). Optical and Long-Wavelength Afterglow from Gamma-Ray Bursts. *The Astrophysical Journal*, 476(1):232–237.
- Metzger, M. R., Djorgovski, S. G., Kulkarni, S. R., et al. (1997). Spectral constraints on the redshift of the optical counterpart to the γ -ray burst of 8 May 1997. *Nature*, 387(6636):878–880.
- Mignone, A., Bodo, G. (2006). An HLLC Riemann solver for relativistic flows - I. Hydrodynamics. *Monthly Notices of the Royal Astronomical Society*, 368:1040–1054.
- Mignone, A., Bodo, G., Massaglia, S., et al. (2007). PLUTO: A Numerical Code for Computational Astrophysics. *The Astrophysical Journal Supplement Series*, 170(1):228–242.
- Mignone, A., McKinney, J. C. (2007). Equation of state in relativistic magnetohydrodynamics: Variable versus constant adiabatic index. *Monthly Notices of the Royal Astronomical Society*, 378(3):1118–1130.
- Mignone, A., Plewa, T., Bodo, G. (2005). The Piecewise Parabolic Method for Mul-

- tidimensional Relativistic Fluid Dynamics. *The Astrophysical Journal Supplement Series*, 160(1):199–219.
- Mignone, A., Zanni, C., Tzeferacos, P., et al. (2012). The PLUTO code for adaptive mesh computations in astrophysical fluid dynamics. *Astrophysical Journal, Supplement Series*, 198(1):34.
- Mimica, P., Giannios, D., Aloy, M. A. (2009). Deceleration of arbitrarily magnetized GRB ejecta: the complete evolution. *Astronomy & Astrophysics*, 494(3):879–890.
- Misner, C., Thorne, K., Wheeler, J. (1973). *Gravitation*. W.H. Freeman, San Francisco.
- Mochkovitch, R., Hernanz, M., Isern, J., et al. (1995). Gamma-ray bursts from relativistic beams in neutron star mergers. *Astronomy & Astrophysics*, 293:803–809.
- Mundell, C. G., Kopač, D., Arnold, D. M., et al. (2013). Highly polarized light from stable ordered magnetic fields in GRB 120308A. *Nature*, 504(7478):119–121.
- Mundell, C. G., Steels, I. A., Smith, R. J., et al. (2007). Early optical polarization of a gamma-ray burst afterglow. *Science*, 315(5820):1822–1824.
- Nakar, E., Granot, J. (2007). Smooth light curves from a bumpy ride: Relativistic blast wave encounters a density jump. *Monthly Notices of the Royal Astronomical Society*, 380(4):1744–1760.
- Nool, M., Keppens, R. (2002). Amrvac: A multidimensional grid-adaptive magnetofluid dynamics code. *Computational Methods in Applied Mathematics*, 2(1):92–109.
- Nousek, J. A., Kouveliotou, C., Grupe, D., et al. (2006). Evidence for a Canonical Gamma-Ray Burst Afterglow Light Curve in the Swift XRT Data. *The Astrophysical Journal*, 642:389.
- Paczynski, B. (1986). Gamma-ray bursters at cosmological distances. *The Astrophysical Journal*, 308:L43.
- Panaitescu, A., Kumar, P. (2003). Properties of Gamma-Ray Burst Jets Obtained from Afterglow Modelling. In G. R. Ricker, R. K. Vanderspek, eds., *Gamma-Ray Burst and Afterglow Astronomy 2001: A Workshop Celebrating the First Year of the HETE Mission*, vol. 662 of *American Institute of Physics Conference Series*. pp. 305–312.
- Pe’er, A. (2015). Physics of Gamma-Ray Bursts Prompt Emission. *Advances in Astronomy*, 2015:907321.
- Perley, D. A., Krühler, T., Schulze, S., et al. (2016). The Swift Gamma-ray Burst

- Host Galaxy Legacy Survey. I. Sample Selection And Redshift Distribution. *The Astrophysical Journal*, 817(1):7.
- Perna, R., Armitage, P. J., Zhang, B. (2006). Flares in Long and Short Gamma-Ray Bursts: A Common Origin in a Hyperaccreting Accretion Disk. *The Astrophysical Journal*, 636(1):L29–L32.
- Piran, T. (1996). Relativity at action or gamma-ray Bursts. *General Relativity and Gravitation*, 28(12):1421–1426.
- Piran, T. (2005). The physics of gamma-ray bursts. *Reviews of Modern Physics*, 76(4):1143–1210.
- Piran, T., Shemi, A., Narayan, R. (1993). Hydrodynamics of Relativistic Fireballs. *Monthly Notices of the Royal Astronomical Society*, 263(4):861.
- Piro, L., Troja, E., Zhang, B., et al. (2019). A long-lived neutron star merger remnant in GW170817: constraints and clues from X-ray observations. *Monthly Notices of the Royal Astronomical Society*, 483(2):1912–1921.
- Pons, J. A., Font, J. A., Ibáñez, J. M., et al. (1998). General relativistic hydrodynamics with special relativistic Riemann solvers. *Astronomy and Astrophysics*, 339(2):638–642.
- Pons, J. A., Martí, J. M., Müller, E. (2000). The exact solution of the Riemann problem with non-zero tangential velocities in relativistic hydrodynamics. *Journal of Fluid Mechanics*, 422:125–139.
- Preece, R. D., Briggs, M. S., Mallozzi, R. S., et al. (1998). The Synchrotron Shock Model Confronts a “Line of Death” in the BATSE Gamma-Ray Burst Data. *The Astrophysical Journal Letters*, 506(1):L23–L26.
- Proga, D., Zhang, B. (2006). The late time evolution of gamma-ray bursts: ending hyperaccretion and producing flares. *Monthly Notices of the Royal Astronomical Society: Letters*, 370(1):L61–L65.
- Qin, Y., Liang, E. W., Liang, Y. F., et al. (2013). A comprehensive analysis of fermi gamma-ray burst data. III. energy-dependent T90 distributions of GBM GRBs and instrumental selection effect on duration classification. *Astrophysical Journal*, 763(1):15.
- Racusin, J. L., Liang, E. W., Burrows, D. N., et al. (2009). Jet breaks and energetics of swift gamma-ray burst X-ray afterglows. *The Astrophysical Journal*, 698(1):43–74.

- Rees, M., Meszaros, P. (1994). Unsteady Outflow Models for Cosmological Gamma-Ray Bursts. *The Astrophysical Journal Letters*, 430:L93–L96.
- Rees, M. J., Meszaros, P. (1992). Relativistic fireballs: energy conversion and time-scales. *Monthly Notices of the Royal Astronomical Society*, 258(1):41P–43P.
- Rees, M. J., Mészáros, P. (2000). Fe / K α Emission from a Decaying Magnetar Model of Gamma-Ray Bursts. *The Astrophysical Journal*, 545(2):L73–L75.
- Ressler, S. M., Laskar, T. (2017). Thermal Electrons in Gamma-Ray Burst Afterglows. *The Astrophysical Journal*, 845(2):150.
- Rezzolla, L., Zanotti, O. (2013). *Relativistic Hydrodynamics*. Oxford University Press.
- Rezzolla, L., Zanotti, O., Pons, J. A. (2003a). An improved exact Riemann solver for multi-dimensional relativistic flows. *Journal of Fluid Mechanics*, 479(479):199–219.
- Rezzolla, L., Zanotti, O., Pons, J. A. (2003b). An Improved Exact Riemann Solver for Relativistic Hydrodynamics with non-zero tangential velocities. *Journ. of Fluid Mech.*, 479(1959):199.
- Rhoads, J. E. (1999a). Gamma-ray burst beaming constraints from afterglow light curves. *Astronomy and Astrophysics Supplement Series*, 138(3):539–540.
- Rhoads, J. E. (1999b). The Dynamics and Light Curves of Beamed Gamma-Ray Burst Afterglows. *The Astrophysical Journal*, 525(2):737–749.
- Rosenblatt, F. (1957). A Perceiving and Recognizing Automaton - Project Para. Tech. rep., Cornell Aeronautical Laboratory.
- Rossi, E., Lazzati, D., Rees, M. J. (2002). Afterglow light curves, viewing angle and the jet structure of γ -ray bursts. *Monthly Notices of the Royal Astronomical Society*, 332(4):945–950.
- Rumelhart, D. E., Hinton, G. E., Williams, R. J. (1986). Learning representations by back-propagating errors. *Nature*, 323(6088):533–536.
- Ryan, G., van Eerten, H., MacFadyen, A., et al. (2015). Gamma Ray Bursts Are Observed Off-Axis. *The Astrophysical Journal*, 799(1):3.
- Ryan, G., van Eerten, H., Piro, L., et al. (2020). Gamma-Ray Burst Afterglows in the Multimessenger Era: Numerical Models and Closure Relations. *The Astrophysical Journal*, 896(2):166.

- Rybicki, G. B., Lightman, A. P. (1979). Radiative Processes in Astrophysics. *Physics of the Earth and Planetary Interiors*, 25(4):432.
- Santana, R., Barniol Duran, R., Kumar, P. (2014). Magnetic fields in relativistic collisionless shocks. *The Astrophysical Journal*, 785(1).
- Sari, R., Piran, T. (1995). Hydrodynamic Timescales and Temporal Structure of Gamma-Ray Bursts. *The Astrophysical Journal*, 455(2):143–146.
- Sari, R., Piran, T., Halpern, J. P. (1999). Jets in Gamma-Ray Bursts. *The Astrophysical Journal*, 519(1):L17–L20.
- Sari, R., Piran, T., Narayan, R. (1998). Spectra and Light Curves of Gamma-Ray Burst Afterglows. *The Astrophysical Journal*, 497(1):L17–L20.
- Savchenko, V., Ferrigno, C., Kuulkers, E., et al. (2017). INTEGRAL Detection of the First Prompt Gamma-Ray Signal Coincident with the Gravitational Wave Event GW170817. *The Astrophysical Journal Letters*, 848(2):L15.
- Schady, P. (2017). Gamma-ray bursts and their use as cosmic probes. *Royal Society Open Science*, 4(7).
- Schanne, S., Paul, J., Wei, J., et al. (2010). The future Gamma-Ray Burst Mission SVOM.
- Scott, D. W. (2015). *Multivariate Density Estimation*. Wiley Series in Probability and Statistics. Wiley.
- Sedov, L. I. (1946). Propagation of strong shock waves. *Journal of Applied Mathematics and Mechanics*, 10:241 – 250.
- Shemi, A., Piran, T. (1990). The appearance of cosmic fireballs. *The Astrophysical Journal*, 365:L55.
- Sironi, L., Giannios, D. (2013). A late-time flattening of light curves in gamma-ray burst afterglows. *The Astrophysical Journal*, 778(2):1–8.
- Sironi, L., Keshet, U., Lemoine, M. (2015). Relativistic Shocks: Particle Acceleration and Magnetization. *Space Science Reviews*, 191(1-4):519–544.
- Spindler, A., Geach, J. E., Smith, M. J. (2021). AstroVaDEr: astronomical variational deep embedder for unsupervised morphological classification of galaxies and synthetic image generation. *Monthly Notices of the Royal Astronomical Society*, 502(1):985–1007.

- Spitkovsky, A. (2008). Particle Acceleration in Relativistic Collisionless Shocks: Fermi Process at Last? *The Astrophysical Journal*, 682(1):L5–L8.
- Springel, V. (2010). E pur si muove: Galilean-invariant cosmological hydrodynamical simulations on a moving mesh. *Monthly Notices of the Royal Astronomical Society*, 401(2):791–851.
- Synge, J. (1957). *The Relativistic Gas*. North-Holland Amsterdam.
- Taub, A. H. (1948). Relativistic Rankine-Hugoniot Equations. *Physical Review*, 74(3):328–334.
- Tegmark, M., Hartmann, D. H., Briggs, M. S., et al. (1996). The Angular Power Spectrum of BATSE 3B Gamma-Ray Bursts. *The Astrophysical Journal*, 468:214.
- Teyssier, R. (2001). Cosmological Hydrodynamics with Adaptive Mesh Refinement: a new high resolution code called RAMSES. *Astronomy & Astrophysics*, 385(1):337–364.
- Toro, E. F. (2009). *Riemann Solvers and Numerical Methods for Fluid Dynamics: A Practical Introduction*. Springer.
- Troja, E., Piro, L., van Eerten, H., et al. (2017). The X ray counterpart to the gravitational wave event GW170817. *Nature*, 551(7678):71–74.
- Troja, E., van Eerten, H., Ryan, G., et al. (2019). A year in the life of GW170817: The rise and fall of a structured jet from a binary neutron star merger. *Monthly Notices of the Royal Astronomical Society*, 489(2):1919–1926.
- Troja, E., van Eerten, H., Zhang, B., et al. (2020). A thousand days after the merger: continued X-ray emission from GW170817. 000(June).
- Uhm, Z. L., Beloborodov, A. M. (2007). On the Mechanism of Gamma-Ray Burst Afterglows. *The Astrophysical Journal*, 665:L93–L96.
- Uhm, Z. L., Zhang, B., Hascoët, R., et al. (2012). Dynamics and afterglow light curves of gamma-ray burst blast waves with a long-lived reverse shock. *The Astrophysical Journal*, 761(2).
- Van Der Maaten, L., Hinton, G. (2008). Visualizing data using t-SNE. *Journal of Machine Learning Research*, 9:2579–2625.
- van Eerten, H. (2014a). Self-similar relativistic blast waves with energy injection. *Monthly Notices of the Royal Astronomical Society*, 442(4):3495–3510.

- van Eerten, H. (2018). Gamma-ray burst afterglow blast waves. *International Journal of Modern Physics D*, 27(13):1842002-314.
- van Eerten, H., Macfadyen, A. (2013). Gamma-ray burst afterglow light curves from a lorentz-boosted simulation frame and the shape of the jet break. *The Astrophysical Journal*, 767(2):1–17.
- van Eerten, H., Van Der Horst, A., MacFadyen, A. (2012). Gamma-ray burst afterglow broadband fitting based directly on hydrodynamics simulations. *The Astrophysical Journal*, 749(1).
- van Eerten, H., Zhang, W., MacFadyen, A. (2010a). Off-axis gamma-ray burst afterglow modeling based on a two-dimensional axisymmetric hydrodynamics simulation. *The Astrophysical Journal*, 722(1):235–247.
- van Eerten, H. J. (2014b). Gamma-ray burst afterglow plateau break time-luminosity correlations favour thick shell models over thin shell models. *Monthly Notices of the Royal Astronomical Society*, 445(3):2414–2423.
- van Eerten, H. J. (2015). Simulation and physical model based gamma-ray burst afterglow analysis. *Journal of High Energy Astrophysics*, 7:23–34.
- van Eerten, H. J., Leventis, K., Meliani, Z., et al. (2010b). Gamma-ray burst afterglows from transrelativistic blast wave simulations. *Monthly Notices of the Royal Astronomical Society*, 403(1):300–316.
- van Eerten, H. J., MacFadyen, A. I. (2012). Gamma-ray Burst Afterglow Scaling Relations For The Full Blast Wave Evolution. *The Astrophysical Journal*, 747(2):L30.
- van Eerten, H. J., MacFadyen, A. I. (2012). Observational implications of gamma-ray burst afterglow jet simulations and numerical light curve calculations. *The Astrophysical Journal*, 751(2):1–6.
- van Eerten, H. J., Meliani, Z., Wijers, R. A. M. J., et al. (2009). No visible optical variability from a relativistic blast wave encountering a wind termination shock. *Monthly Notices of the Royal Astronomical Society*, 398(1):L63–L67.
- van Eerten, H. J., Wijers, R. A. (2009). Gamma-ray burst afterglow scaling coefficients for general density profiles. *Monthly Notices of the Royal Astronomical Society*, 394(4):2164–2174.
- van Paradijs, J., Groot, P. J., Galama, T., et al. (1997). Transient optical emission from the error box of the γ -ray burst of 28 february 1997. *Nature*, 386(6626):686–689.

- von Kienlin, A., Meegan, C. A., Paciesas, W. S., et al. (2014). The Second Fermi GBM Gamma-ray Burst Catalog: The First Four Years. *The Astrophysical Journal Supplement Series*, 211(1):13.
- Weinberger, R., Springel, V., Pakmor, R. (2020). The AREPO Public Code Release. *The Astrophysical Journal Supplement Series*, 248(2):32.
- Wijers, R. A., Rees, M. J., Mészáros, P. (1997). Shocked by GRB 970228: The afterglow of a cosmological fireball. *Monthly Notices of the Royal Astronomical Society*, 288(4).
- Wijers, R. A. M. J., Galama, T. J. (1999). Physical Parameters of GRB 970508 and GRB 971214 from Their Afterglow Synchrotron Emission. *The Astrophysical Journal*, 523(1):177–186.
- Willingale, R., O’Brien, P. T., Osborne, J. P., et al. (2007). Testing the Standard Fireball Model of Gamma-Ray Bursts Using Late X-Ray Afterglows Measured by Swift. *The Astrophysical Journal*, 662(2):1093–1110.
- Wilson, J. R. (1972). Numerical Study of Fluid Flow in a Kerr Space. *The Astrophysical Journal*, 173(10):431.
- Woosley, S. E. (1993). Gamma-ray bursts from stellar mass accretion disks around black holes. *The Astrophysical Journal*, 405:273.
- Wygoda, N., Waxman, E., Frail, D. A. (2011). Relativistic jet dynamics and calorimetry of gamma-ray bursts. *Astrophysical Journal Letters*, 738(2).
- Xie, J., Girshick, R., Farhadi, A. (2016). Unsupervised deep embedding for clustering analysis. *33rd International Conference on Machine Learning, ICML 2016*, 1:740–749.
- Yi, S.-X., Xi, S.-Q., Yu, H., et al. (2016). Comprehensive Study of the X-Ray Flares From Gamma-Ray Bursts Observed By Swift. *The Astrophysical Journal Supplement Series*, 224(2):20.
- Yuan, W., Amati, L., Cannizzo, J. K., et al. (2016). Perspectives on Gamma-Ray Burst Physics and Cosmology with Next Generation Facilities. *Space Science Reviews*, 202(1-4):235–277.
- Zanotti, O., Rezzolla, L., Del Zanna, L., et al. (2010). Electromagnetic counterparts of recoiling black holes: general relativistic simulations of non-Keplerian discs. *Astronomy & Astrophysics*, 523:A8.

- Zhang, B. (2014). Gamma-ray Burst Prompt Emission. *International Journal of Modern Physics D*, 23(02):1430002.
- Zhang, B., Kobayashi, S. (2005). Gamma-Ray Burst Early Afterglows : Reverse Shock Emission. *The Astrophysical Journal*, (628):315–334.
- Zhang, B., Meszaros, P. (2002). Gamma-Ray Bursts with Continuous Energy Injection and Their Afterglow Signature. *The Astrophysical Journal*, 566(2):712–722.
- Zhang, F.-W., Shao, L., Yan, J.-Z., et al. (2012). Revisiting the Long/Soft-Short/Hard Classification of Gamma-Ray Bursts in the Fermi Era. *Astrophysical Journal*, 750(2):88.
- Zhang, W., MacFadyen, A. (2009). The dynamics and afterglow radiation of gamma-ray bursts. i. constant density medium. *The Astrophysical Journal*, 698(2):1261–1272.
- Zhang, W., MacFadyen, A. I. (2006). RAM: A Relativistic Adaptive Mesh Refinement Hydrodynamics Code. *The Astrophysical Journal Supplement Series*, 164(1):255–279.

A

GAMMA readme

This appendix is adapted from the documentation available at: <https://github.com/eliotayache/GAMMA/readme.md>.

GAMMA is a code for modeling relativistic hydrodynamics and non-thermal emission on a moving mesh. We provide here information on how to compile and run the test cases included with the code.

A.1 Requirements

- gnu scientific library
- OpenMP
- MPI

A.2 Installation

Clone this repository in a directory of your choice. Move to the directory and build the code.

```
git clone https://github.com/eliotayache/GAMMA/ dirname
cd dirname
make -B
```

A.3 Usage

A.3.1 running a simulation

Output is stored in ./results/Last. Before you can run calculations you need to create this directory.

```
mkdir -p results/Last
```

Use mpirun to launch computation.

```
mpirun -n N_nodes ./bin/GAMMA -w # to overwrite files in results/Last
mpirun -n N_nodes ./bin/GAMMA -r # to resume from the last file in results/Last
```

A.3.2 choice of module to use

The choice of geometry, time-integration, solver, dimensions are specified in ./Makefile

```
INITIAL      = Tests/BM1D      # Initial setup: .cpp file in src/Initial (see test examples)
TIMESTEP     = rk3             # euler / rk3
GEOMETRY     = spherical1D    # cartesian / spherical / spherical1D
HYDRO       = rel_sph        # rel_cart / rel_sph
RADIATION    = radiation_sph  # only one option for now
SOLVER       = hllc           # only one option for now
DIMENSIONS   = 1d             # 1d / 2d
IO           = text1d         # text1d / text2d
```

A.3.3 environment variables

A range of self-explanatory environment variables are specified in src/environment.h and should be set before running the code. The non-thermal particle population calculation switches are the following.

```
#define SHOCK_DETECTION_      ENABLED_
#define DETECT_SHOCK_THRESHOLD_ 0.01
#define LOCAL_SYNCHROTRON_    ENABLED_      # needs SHOCK_DETECTION_ ENABLED_
#define GAMMA_MAX_INIT_      (1.e8)
#define VARIABLE_PSPEC_      DISABLED_     # needs LOCAL_SYNCHROTRON_ and SHOCK_DETECTION_
```

A.3.4 initial setup

New initial setups can be created as new .cpp files in src/Initial. **These files should follow the same architecture as the example tests in src/Initial/Tests.** They

specify the initial grid geometry, the initial fluid values, the output times, the AMR criteria and other user-specified (override) functions.

The geometry and fluid state are initialised on a grid `Cinit`. After initialisation the calculation will be moved to the `Ctotgrid` that includes ghost cells. The relevant indices to move around the various grids involved in the code are all specified in `src/grid.h`. In `initialValues()` the fluid state should be specified in terms of primitive variables `S.prim[q]` with velocities in units of c .

The following functions have to be declared in this initial file:

```
void loadParams(s_par *par){}
int Grid::initialGeometry(){return(0);}
int Grid::initialValues(){return(0);}
void Grid::userKinematics(){}
void Cell::userSourceTerms(double dt){}
void Grid::userBoundaries(int it, double t){}
int Grid::checkCellForRegrid(int j, int i){return(skip_);}
void Cell::user_regridVal(double *res){}
void FluidState::cons2prim_user(double *rho, double *p, double *uu){}
void Simu::dataDump(){}
void Simu::runInfo(){}
void Simu::evalEnd(){}
```

A.4 License

MIT¹

A.5 Contact

Feel free to get in touch! e.h.r.ayache@bath.ac.uk

¹<https://choosealicense.com/licenses/mit/>